Star Formation in
Nearby Galaxies

By

George Philip Ford

A Thesis submitted to Cardiff University
for the degree of Doctor of Philosophy

14th August, 2014

DECLARATION OF AUTHORSHIP

- DECLARATION:
  This work has not previously been accepted in substance for any degree and is not concurrently submitted in candidature for any degree.

  Signed: .... (candidate) Date: ....

- STATEMENT 1:
  This thesis is being submitted in partial fulfillment of the requirements for the degree of Doctor of Philosophy (PhD).

  Signed: .... (candidate) Date: ....

- STATEMENT 2:
  This thesis is the result of my own independent work/investigation, except where otherwise stated. Other sources are acknowledged by explicit references.

  Signed: .... (candidate) Date: ....

- STATEMENT 3
  I hereby give consent for my thesis, if accepted, to be available for photo-copying and for inter-library loan, and for the title and summary to be made available to outside organisations.

  Signed: .... (candidate) Date: ....

Watch the stars and from them, learn.

ALBERT EINSTEIN

ACKNOWLEDGEMENTS

Having only been to Cardiff once before my interview for a PhD place, I was not sure what to expect from the Welsh capital. Nearly four years later I am pleased to say the decision to leave a pretty cushy job with no risk of redundancy and a house on the harbourside in the wonderful city of Bristol hasn't completely backfired, and that's largely down to these people:

Thanks to mother and father for supporting and encouraging me in all my endeavours for the best part of thirty years and for calling me a lazy git when required.

I'd like to thank Merryn Thomas and Matthew Smith for being great people to live with during my time in Cardiff, for very different reasons I hasten to add.

I'm grateful to Prof Elias Brinks and Prof Jon Davies for giving me a thorough grilling in my viva and providing suggestions for corrections which have undoubtedly resulted in a better thesis. Also thanks to Dr Pete Hargrave for sitting there quietly for three hours.

Huge thanks to my supervisors Prof Walter Gear and Prof Steve Eales for invaluable advice and discussion throughout my PhD. Walter was always available for a chat despite his many responsibilities as Head of School and commitment to the sport of golf, and visiting Steve was always a good boost to the ego as I knew my desk would never be as messy as his.

Naturally, over the three and a half years I had the odd computing issue to overcome. Now, I don't believe in God but thousands of years from now our machine overlords will be building giant statues of Richard Frewin, there was not one problem he couldn't solve.

I was very lucky to be a member of the Galaxies research group, sharing an office with two Matts, two Chrises, two Elizabeths, an Andreas, a Robbie, an Olivia and a Simon, with Dr Haley Gomez and Prof Mike Disney adding to group meetings in their own unique ways. Office discussions were extremely useful in developing a direction for my own research, overcoming technical hurdles, and musing over the regional accents of cattle across Europe.

One of the highlights of my time in Cardiff has been the opportunity to engage

with the public about science, something which I hope to continue in whatever branch of science I end up working. Among others I have TV's Chris North$^{\text{TM}}$ to thank for getting me involved.

Of course the life of a PhD student isn't all work, so for all of the coffee breaks that lasted a whole afternoon, the Christmas pool tournaments, the cake days, the pub trips, the all-you-can-eat buffets and the days I turned up in yesterday's clothes having not gone home, I thank you* all.

PUBLICATIONS

FIRST AUTHOR

- Ford, G. P., Gear, W. K., Smith, M. W. L., Eales, S. A. et al. 2013; Herschel Exploitation of Local Galaxy Andromeda (HELGA) III: The star formation law in M31; The Astrophysical Journal, 769:55 (11pp), 2013 May 20.

CONTRIBUTOR

- Fritz, J., Gentile, G., Smith, M. W. L., Gear, W. K. et al. 2012; Herschel Exploitation of Local Galaxy Andromeda (HELGA) I: Global far-infrared and sub-mm morphology; Astronomy and Astrophysics, 546, A34.

- Smith, M. W. L., Eales, S. A., Gomez, H. L., Roman-Duval, J. et al. 2013; Herschel Exploitation of Local Galaxy Andromeda (HELGA) II: Dust and gas in Andromeda; The Astrophysical Journal, 756:40 (17pp), 2012 September 1

- Kirk, J. M., Gear, W. K., Fritz, J., Smith, M. W. L., Ford, G. P. et al 2013; Herschel Exploitation of Local Galaxy Andromeda (HELGA) IV: The distribution and properties of molecular cloud associations in M31; The Astrophysical Journal

ABSTRACT

This work uses multiwavelength observations of nearby galaxies to explore the relationship between star formation and the interstellar medium in galaxies of various sizes and morphology.

Galaxies in the *Herschel* Reference Survey are divided into barred and unbarred spirals to test for differences in dust temperature, dust mass, star formation rate, far-infrared luminosity, NUV-r colour and stellar mass between the two populations. The only significant observed difference is with stellar mass, where barred spirals are generally less massive. I suggest this is due to the speed of bar creation depending on galaxy mass, although this is counter to some previous observations. Trends with Hubble-type and environment are consistent with previous work.

The resolved star formation law is studied in the two largest extragalactic sources in the local group, Andromeda (M31) and the Triangulum (M33). The two are measured to have global star formation rates (SFR) of $0.25\,\mathrm{M_\odot\,yr^{-1}}$ and $0.16\,\mathrm{M_\odot\,yr^{-1}}$ respectively using far-ultraviolet and $24\,\mu\mathrm{m}$ emission as star formation tracers. M33 has a higher mean surface density of star formation, as expected as it is later type than M31, and a higher star formation efficiency. Both galaxies appear consistent with the globally averaged SFR and gas surface density of normal spirals studied in previous work, with M31 at the low end in terms of SFR.

When looking at smaller scales, both galaxies show evidence of saturation of neutral monatomic hydrogen at $\Sigma_{\mathrm{Gas}} = 10\,\mathrm{M_\odot\,pc^{-2}}$ when looking at the star formation law with total gas. They also appear to follow close to linear star formation laws with molecular gas only, consistent with previous work on resolved galaxies. M31 shows evidence of a sub-linear star formation law with molecular gas, indicating that star formation efficiency is lower in the highest density regions. Testing the relationship in M31 on different pixel scales does not effect the measured Kennicutt-Schmidt index, as has been suggested in previous work.

M33 shows a significant portion of the galaxy has a relatively high SFR surface density, but little molecular gas as traced by CO. I suggest this could be evidence of CO-free molecular hydrogen in these regions.

CONTENTS

LIST OF FIGURES

LIST OF TABLES

George Philip Ford

1 INTRODUCTION

Was it really a big bang, or did it just seem big because there
wasn't anything else to drown it out at the time?

–KARL PILKINGTON

What we know about the physics of galaxy evolution has profound implications in all areas of astrophysics. Resolved observations and simulations of galaxies can help us deduce the processes that govern the formation of individual stars and planets, while global properties of galaxies measured at every observable epoch give us clues as to the evolution of the universe as a whole.

Recent advances in observational techniques and the building of ever more powerful telescopes have allowed us to study thousands of galaxies as resolved structures out to vast distances and in greater detail than ever before. Furthermore, the advent of infrared and sub-mm astronomy has allowed a truly panchromatic view of the universe, where we can study material that was previously invisible to us.

This work uses multi-wavelength observations of nearby galaxies to study their star formation properties and interstellar medium both globally and on a resolved basis. Here we hope to gain valuable insight into how galaxies have evolved but first I will give a brief history of extragalactic astronomy.

1.1 RECEDING HORIZONS

In the beginning, there was an infinitely dense point or 'Big Bang singularity' containing all of the energy that would go on to create our universe. This point rapidly expanded and over many billions of years evolved into the universe we see today. This current (somewhat condensed) understanding of how our universe came to be is easy to explain chronologically, from the 'Big Bang' to the current epoch and even into the future but it is not representative of how we came to understand our universe.

1.1.1 AN ISLAND UNIVERSE

It was not until Galileo looked to the heavens with his telescope in 1610 that it was realised that the large swathe of cloud across the sky, known as the Milky Way (Figure 1.1), was actually made up of thousands of faint stars. It was deduced by Thomas Wright in the 18th century that the reason we see a band across the sky is that we are sitting inside a flattened system of stars (Wright, 1750).

Objects that we now know to be external to our galaxy had soon been observed and mapped in the Messier catalogue and by Dreyer's New General Catalogue (NGC, Dreyer 1888) and Index Catalogue (IC, Dreyer 1895) which contain ∼13000 clusters and nebulae, including the Great Andromeda Nebula (Messier 31) and the Magellanic clouds. However, there was considerable debate as to whether these objects were part of the Milky Way, or external to it. The latter train of thought was named 'the island universe' hypothesis, an idea originating from Wright and the philosopher Immanuel Kant.

In the mid 19th century, Lord Rosse spotted spiral structures in some of the observed nebulae, including in what is now known as the 'Whirlpool,' M51. This was taken to mean these were nearby systems, of the type that many at the time thought would go on to form planets.

Soon afterwards, William Huggins added to the debate using the new technique of spectroscopy, where observed light is split into its constituent wavelengths. The bright spectral lines he observed seemed to indicate that many of the nebulae were in fact clouds of gas. The fact that they were only observed outside the plane of the Galaxy (Proctor, 1869) suggested that they were related to the Milky Way somehow and not randomly positioned external objects.
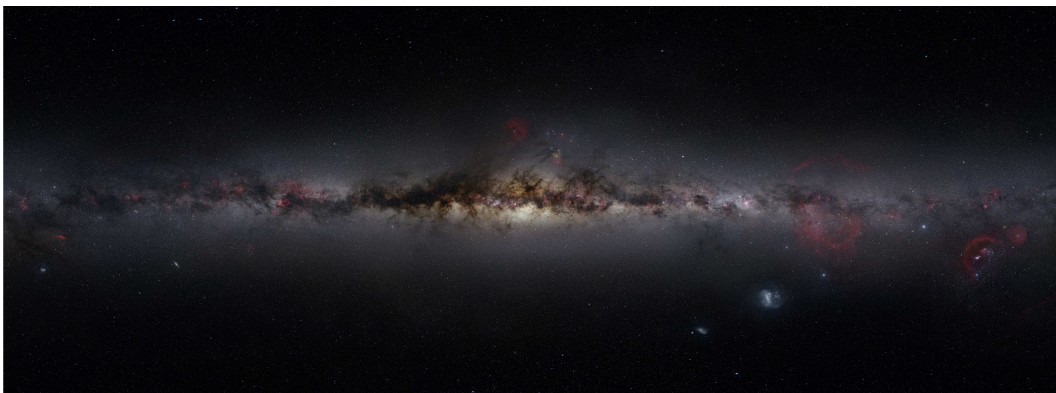
Figure 1.1 The Milky Way galaxy, as viewed from earth. The centre is the Galactic core, with the image showing a nearly 360° view around the Galactic plane. Image courtesy of Nick Risinger, *skysurvey.org*.

The 'island universe' advocates had further cause for concern in 1885 when a nova was observed in the Andromeda nebula that accounted for one-tenth of the nebula's total luminosity. Similar phenomena had been seen in our Galaxy and assuming the same approximate absolute luminosity for the nova in Andromeda placed it well within the Milky Way. However, subsequent discoveries of far fainter novæ, indicating far greater distances, lent support to the idea of a universe outside of our Galaxy.

1920 saw the 'Great Debate' between Heber Curtis, an 'island universe' proponent, and Harlow Shapley for the single 'metagalaxy.' Curtis addressed the brightness of the Andromeda nova by suggesting it was actually a 'supernova,' far more luminous than what was assumed. He also countered the argument from the distribution of gas clouds stating that their positions were not somehow physically connected to the Milky Way, but were only observable in polar regions of the Galaxy due to obscuration by interstellar dust (this is a very important point I will return to later).

Despite the 'island universe' hypothesis gaining favour with many astronomers at the time, a direct distance measurement was required to determine the truth beyond any doubt.

Determining the distance to a celestial body is one of the most fundamental measurements we can make in astronomy. Even now, distance measurements are invaluable for nearly all aspects of astrophysics. The first successful distance measurements using parallax were made in the 19$^{\text{th}}$ century, determining a distance to 61 Cygni of 3.5 pc (Bessel, 1838), but this method is limited by the length of the observer's baseline, the largest from Earth being the diameter of its orbit around the sun. Considering the estimated size of the Galaxy at that time was 5–10 kpc this is not sufficient to measure potentially extragalactic distances as was required to settle the 'Great Debate.'

The solution came as a result of a study on the Magellanic clouds (Leavitt, 1908). It was found that Cepheid variable stars in these clouds oscillated in brightness on a timescale that was directly related to their relative luminosities. As they could be assumed to be roughly the same distance away, the period of oscillation must be related to their absolute luminosity, also. It was the 'island universe' opponent Shapley who managed to determine the absolute luminosities of these objects and hence calibrate the period-luminosity (P–L) relation to determine distance. Once the timescale and observed brightness was known, the distance could be determined using the inverse square law, $F_* = L_*/4\pi D^2$. Shapley himself made measurements of globular clusters out to 50 kpc, but it was Edwin Hubble who put

the nail in the coffin with observations of M31. He used Shapley's Cepheid method to determine a distance to M31 of >300 kpc (Hubble, 1925) which, given the observed angular diameter of the Andromeda Nebula, is consistent with it having a similar size to the Milky Way. We had finally determined beyond doubt that there was a universe of galaxies outside our own.

1.1.2 GALAXIES

Galaxies come in a variety of morphologies and sizes from flat, disk-like spirals to giant red ellipticals. It was Edwin Hubble who came up with a way of classifying galaxies in terms of their morphology called the 'Hubble sequence' (Hubble, 1926) represented by the now famous 'tuning fork' diagram (Figure 1.2). Ellipticals (the bottom of the fork, as it is presented here) are often referred to as 'early-types' and spirals (top) are 'late-types.' The primary aim in the study of galaxy evolution is to determine how these different morphologies come to be. The traditional view is that most of the star formation occurs in spiral galaxies, with older big ellipticals containing little star formation as they have used up the requisite gas. But how did they get there in the first place?

The current best theory of galaxy evolution is based on the concordance model of cosmology or ΛCDM. Here, CDM stands for cold dark matter, which is thought to dominate the matter density of the universe and is the primary driver of the gravitational collapse of material into galaxies and galaxy clusters. Λ is the cosmological constant, the current most likely form of dark energy which drives the accelerated expansion of the universe, derived from Einstein's attempts to model a static universe with General Relativity.

In the ΛCDM model, overdensities in the early universe caused by quantum fluctuations during inflation were the seeds of structure formation. Contraction of these clumps under gravity would lead to the formation of galaxies and galaxy clusters. The earliest galaxies are predicted to be small, with overdensities of matter merging over time to form the larger galaxies we see today, hence the name 'hierarchical model of galaxy formation.' However, despite general agreement between simulations of galaxy formation and cosmology based on the ΛCDM paradigm, there are issues with the model, including the prevalence of smaller galaxies in the nearby universe, an issue known as 'downsizing.' It is possible that the discrepancy is due in part to our incomplete understanding of the baryonic physics going on in galaxies rather than a problem with ΛCDM, one reason why it is so important to understand the evolution of individual galaxies.

The immediate question to ask when studying galaxies is what do they look
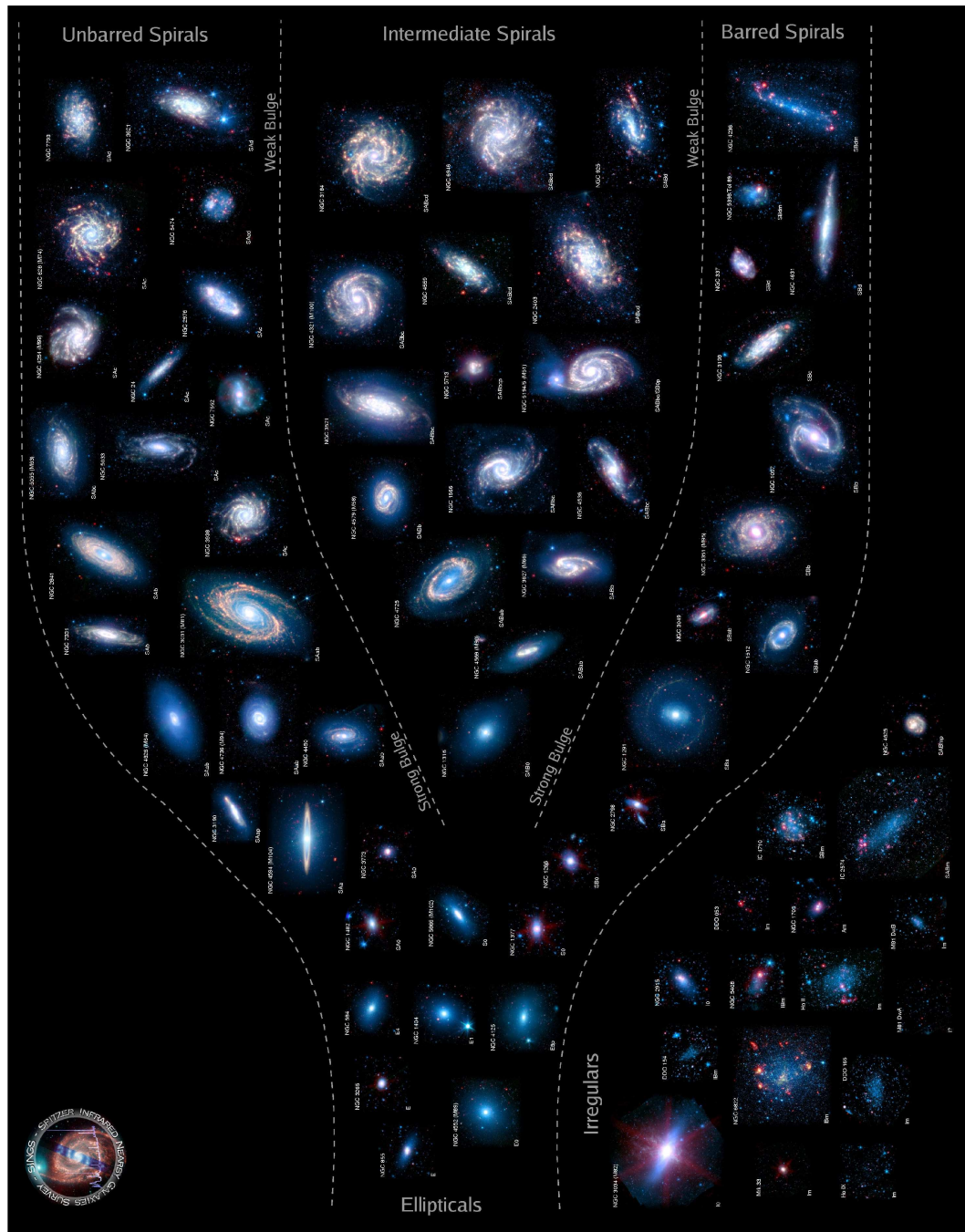
Figure 1.2 The tuning fork diagram of galaxy morphology, courtesy of the SINGS survey. Spheroidal elliptical galaxies (E0-7) are represented on the handle of the tuning fork (bottom). Towards the centre the ellipticals turn to the intermediate lenticular galaxies (S0) and then spiral galaxies (Sa-c, top) becoming less tightly wound. Spirals are split into two subclasses, barred (SB) and unbarred (SA). Galaxies to the left of the diagram are often referred to as 'early-types,' those on the right are 'late-types.' Image produced by Karl Gordon, Robert Hurt and the *Spitzer Science Centre*.

like? Elliptical galaxies are spheroidal stuctures dominated by old stars, giving rise to a red colour (see Figure 1.4). Spiral galaxies are generally observed to be bluer. They are made up of a central bulge and surrounding disc of spiral arms, often linked by a bar structure. The bulge tends to have properties similar to an elliptical galaxy, being dominated by an old stellar population, suggesting that this is the region where stars first formed in the galaxy. The disc contains younger bluer stars and the majority of the dust and gas. These emergent properties are all the result of star formation propagating through the galaxy.

1.2 GALACTIC SCALE STAR FORMATION

This brings us to star formation on galactic scales. As has been alluded to, cosmology, galaxy formation/evolution and the Hubble sequence are greatly influenced by the process of star birth, life and death. Star formation consumes gas in the interstellar medium (ISM); the stars, once ignited produce feedback through stellar winds and eventually supernovæ. With so many contributing factors, predicting how the star formation rate of a galaxy will change from region to region, and evolve over time is a complicated problem. Fortunately for observers, star formation on large scales appears to follow a series of tight empirical scaling relations, the most famous of which being the Kennicutt-Schmidt (K-S) star formation (SF) law, which I will discuss in detail later. Briefly, it is an empirical power law relationship between surface density of gas and surface density of star formation (Figure 1.3, Kennicutt & Evans 2012). However, the physical driver for this relation is largely unknown as many processes have to occur to lead to the formation of a star (e.g. McKee & Ostriker, 2007).

First gas must be accreted from the intergalactic medium (IGM), which may be especially important for the eventual global star formation rate (SFR) of the galaxy. The ISM must then become neutral which depends on the local gas density and ambient radiation. Following this, bound clouds must be formed, ensuring that the mass present is likely to collapse further. This gas will cool and become molecular providing the gas is optically thick to photodissociating ultraviolet (UV) photons. The final stage is the formation of a bound core which is presumed to lead invariably to the formation of a star. Determining how each stage affects galaxy-scale star formation has been a primary aim of astronomers working in the field, and is complicated by the possibility that the main driver may be dependent on the local environment and epoch.
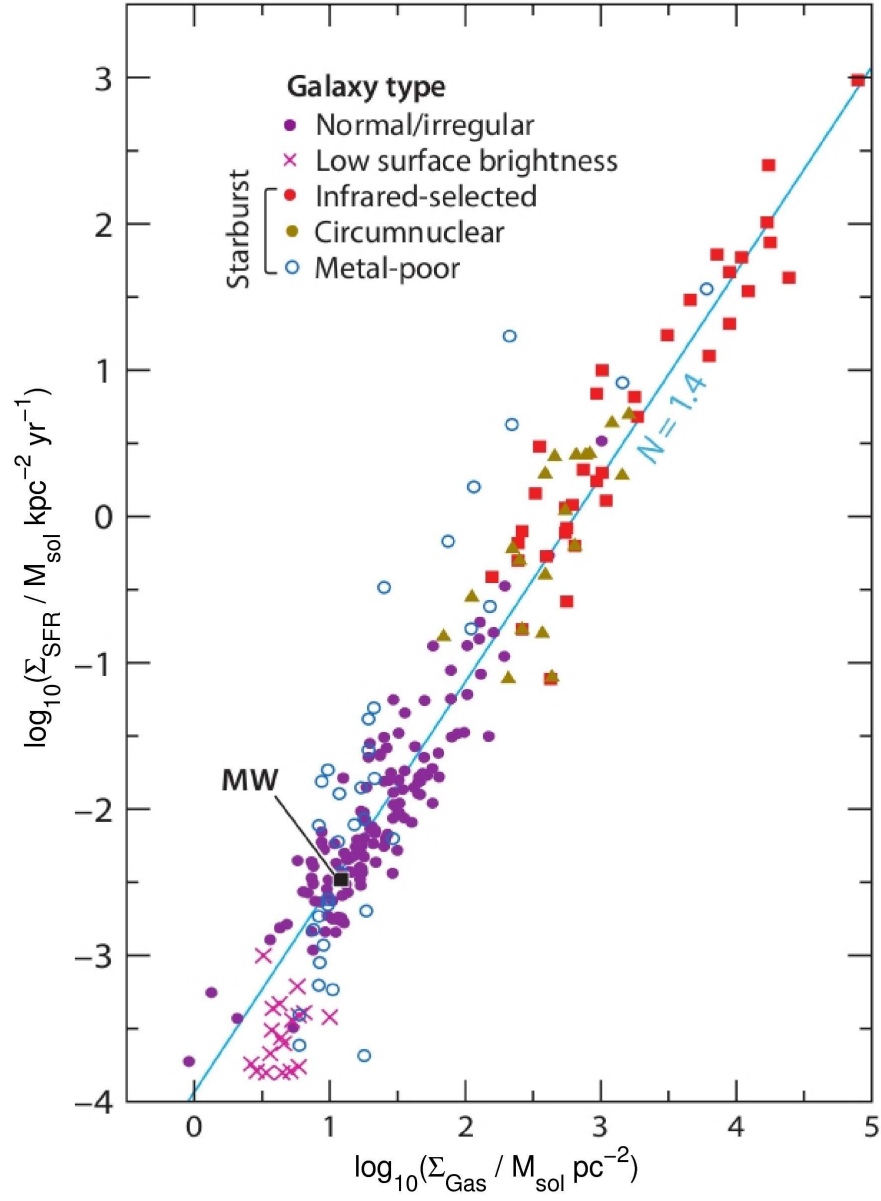
Figure 1.3 Surface densities of star formation and gas mass for the galaxies studied in Kennicutt (1998b) among others. The blue trendline assumes the relationship $\Sigma_{\text{SFR}} = A\,\Sigma_{\text{Gas}}^{N}$, with $N = 1.4$. Figure taken from Kennicutt & Evans (2012).

1.2.1 STAR FORMATION RATE INDICATORS

Star formation rate (SFR) is one of the most important parameters when quantifying galaxy evolution. SFR indicators of varying fidelity have existed for around 30 yrs but improvements in observations over the last decade have advanced the field significantly. Observatories like the *Hubble Space Telescope (HST)*, *Spitzer Space Telescope*, *Galaxy Evolution Explorer (GALEX)* and the *Herschel Space Observatory* provide high sensitivity and angular resolution to push calibration of SFR indicators to greater accuracy and ever smaller spatial scales with *GALEX*, *Spitzer* and *Herschel* having full-width half-maximum (FWHM) beamwidths of a few to tens of arcseconds, corresponding to the size of giant molecular cloud complexes and smaller in the nearest extragalactic sources (i.e. local group galaxies).

Usually when determining a rate in any scientific discipline, time must pass to make the measurement. In astronomy the timescales are far too large for this to be practical so some other approach is required. Invariably, a tracer assumed to be dominated by emission from the youngest stars is used. Figure 1.4 shows the Hertzsprung-Russell (H-R) diagram with stellar lifetime and mass indicated. A star of $0.1\,M_\odot$ can last for a trillion years while the sun's lifetime is approximately ten billion years. The most massive stars ($M_* > 10\,M_\odot$) only live for around ten million years as they burn their fuel incredibly quickly so where they are observed must be a site of recent star formation. The best bands in which to pick out these massive stars are the UV. However we must bear in mind that older stars emit in the UV too, but are relatively fainter at this wavelength.

Unfortunately not all UV from young stars can reach our telescopes directly. Some emission is absorbed by interstellar dust resulting in an underestimate of the SFR. This is common as dust is often co-distributed with areas of star formation because it helps drive the gravitational collapse of gas clouds due to its relatively high density. It also acts as a site for the formation of the molecular hydrogen which will go on to form stars (e.g. van de Hulst, 1948). Luckily the dust re-radiates at infrared wavelengths, meaning the obscured SFR can also be estimated. As with direct stellar emission, the dominant heating of dust is assumed to be due to the youngest brightest stars.

Obscured / embedded star formation tracers have become especially important since the discovery that much of the star formation occurring at redshifts of $z = 1\text{-}3$ is enshrouded in dust (e.g. Le Floc'h et al., 2005; Elbaz et al., 2011). There has been special interest in single band tracers which can be used in the same way as tracers of direct stellar emission. The advent of *Spitzer* and *Herschel* has allowed significant progress to be made in this area over the last decade especially with
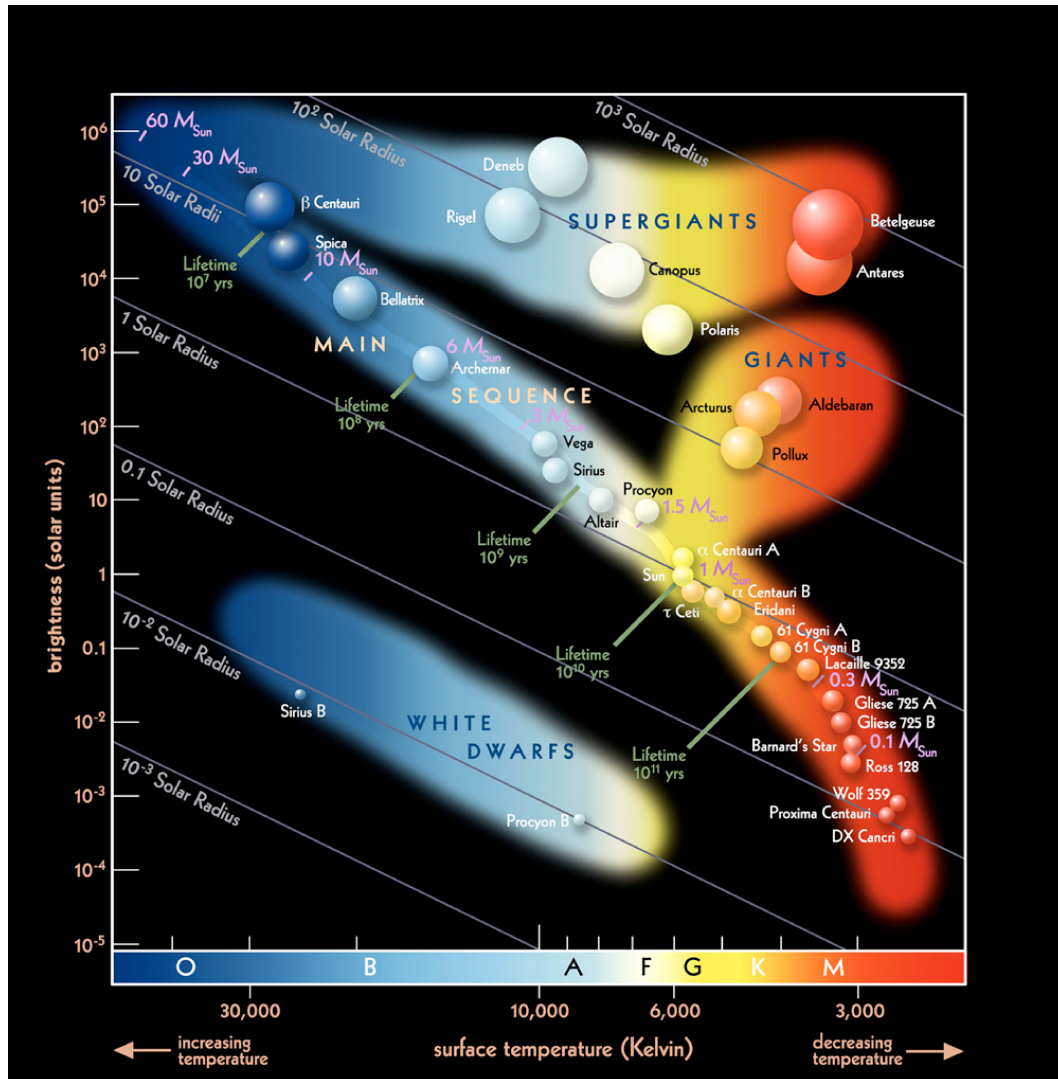
Figure 1.4 Hertzsprung-Russell diagram with indications of size and lifetime of stars along the main sequence. The longest lived stars are redder, with large blue (hot) stars using up their fuel more quickly. Image credit: *European Southern Observatory* (*ESO*)

Table 1.1 Star formation rate calibrations, reproduced and modified from Kennicutt & Evans (2012).

Band	τ / Myr[a]	L_x units	$\log C_x^{\text{b}}$	$\dot{M}_*/\dot{M}_*^{\text{c}}$	Reference(s)
Far-UV	0-10-100	erg s^{-1} (νL_ν)	43.35	0.63	Hao et al. (2011), Murphy et al. (2011)
Near-UV	0-10-200	erg s^{-1} (νL_ν)	43.17	0.64	Hao et al. (2011), Murphy et al. (2011)
Hα	0-3-10	erg s^{-1}	41.27	0.68	Hao et al. (2011), Murphy et al. (2011)
TIR[d]	0-5-100[e]	erg s^{-1}	43.41	0.86	Hao et al. (2011), Murphy et al. (2011)
24 μm	0-5-100[e]	erg s^{-1} (νL_ν)	42.69		Rieke et al. (2009)
70 μm	0-5-100[e]	erg s^{-1} (νL_ν)	43.23		Calzetti et al. (2010)
1.4 GHz	0-100	erg s^{-1} Hz^{-1}	28.20		Murphy et al. (2011)
2-10keV	0-100	erg s^{-1}	39.77	0.86	Ranalli et al. (2003)

[a] - lower limit-mean age-upper limit (below which 90% of emission is contributed).

[b] - Conversion factor between luminosity and SFR, given $\log(\dot{M}_* / M_\odot \text{ yr}^{-1}) = \log L_x - \log C_x$.

[c] - Ratio of SFR derived in this table, to that used in Kennicutt (1998a) using a Salpeter IMF.

[d] - Total far-infrared luminosity integrated over the range 3–1100 μm.

[e] - Age range sensitive to star formation history. Here continuous SF over 100 Myr is assumed.

GALEX providing high resolution and sensitivity for observations of unobscured star formation.

For the most nearby regions in our own Galaxy it is possible to obtain the SFR by counting the young stellar objects (YSOs), i.e. protostars. For unresolved regions however (applicable to all extragalactic sources) the luminosity must be converted to a star formation rate given certain assumptions (a sample of conversion factors is given in Table 1.1, Kennicutt & Evans 2012). The first is that the SFR is approximately constant over the timescale probed, τ, which depends on the tracer. When looking at constant star formation on timescales longer than 100 Myr changes in the conversion factor are small for the UV tracer, but considerably shorter timescales have a significant affect. For example, when using UV to trace star formation, timescales of 10 Myr and 2 Myr require a conversion factor $\sim$1.4 and $\sim$3.5 times higher than that for an assumed timescale of 100 Myr (Calzetti, 2013). If using total far-infrared (FIR) luminosity to trace star formation, much longer timescales also have a large affect on the conversion factor, with a 10 Gyr timescale reducing the conversion to $\sim$57% of that for $\tau = 100$ Myr.

The conversion factor also depends on the inital mass function (IMF), which is the distribution of masses of a population of stars, often given as a probability density function. This is important as more massive stars burn their fuel quickly, so tend to be more luminous. In order to glean a reliable rate, it is important that the assumed IMF is fully sampled, which can be an issue at the smallest scales and in

low-SFR regimes.

1.2.2 INTERSTELLAR GAS TRACERS

All chemicals, including those that make up the interstellar medium of a galaxy, have characteristic emission spectra. A spectral line is produced when an electron moves from one quantised energy state to a lower state, emitting a photon. The difference in the two energy states will correspond to the energy of the emitted photon and the frequency of the spectral line is proportional to the photon energy (Planck, 1901). One important caveat is that these lines will be doppler shifted for many astronomical objects so the observed frequency of the emission line will not necessarily correspond to that in the lab.

NEUTRAL ATOMIC HYDROGEN, H I

Hydrogen gas is the dominant constituent of the ISM in galaxies. Its neutral atomic phase is observationally inferred from an emission line that corresponds to a hyperfine transition in the ground state of the hydrogen atom originally predicted in van de Hulst (1945) and observed by Ewen & Purcell (1951).

Hyperfine splitting of the ground state is due to the hydrogen atom having a different energy depending on the relative spin of the proton and electron. When spins are parallel, the atom has slightly higher energy than when they are antiparallel due to magnetic interactions. Therefore, if an electron changes spin there will be a change in energy and a photon will be emitted. The energy difference between the hyperfine levels of the ground state of H I is $\sim 6\,\mu$eV. This corresponds to a frequency, ν of $1420\,$MHz and a wavelength ($\lambda = c/\nu$) of $21.11\,$cm. This transition is highly forbidden, with a probability of $2.9 \times 10^{-15}\,$s^{-1} meaning a single atom is only likely to undergo the process once in around ten million years. Due to the number of atoms in an interstellar gas cloud, however, it is easily observed in space with collisions with other atoms and interaction with background radiation increasing its liklihood.

MOLECULAR GAS

Recent studies suggest that molecular gas is the most important constituent of the ISM in terms of star formation (e.g. Bigiel et al., 2008, 2011; Rahman et al., 2012), so its observation is fundamental to the study of galaxy evolution. The most abundant molecule in the universe is molecular hydrogen, H_2. Unfortunately as the

molecule is symmetric and so light, its first excited rotational state occurs at $\sim$500 K whereas the temperature of interstellar clouds tends to be tens of degress Kelvin.

In lieu of a direct measurement we use the second most abundant molecule, Carbon Monoxide (CO), as a proxy. The rotational transitions J=1-0, J=2-1 and J=3-2 are most commonly used where the quantised rotational energy is given as,

$$E_{\rm rot,CO} = \frac{J(J+1)\hbar^2}{2I} \qquad J = 0, 1, 2... \tag{1.1}$$

where I is the moment of inertia of the molecule. Going from J to $J-1$ releases energy,

$$\Delta E_{\rm rot,CO} = [J(J+1) - (J-1)J]\frac{\hbar^2}{2I} = \frac{\hbar^2 J}{I}, \tag{1.2}$$

The energy released from a J=1-0 transition in ^{12}C^{16}O corresponds to a frequency of $\sim$115 GHz or $\lambda \sim$2.6 mm.

Another possible tracer of the dense gas in galaxies is dust. The following subsection will outline some of its important properties and how it can be observed.

1.2.3 DUST

Interstellar dust consists predominantly of silicates and graphites. These heavy elements are produced in the centre of stars by nuclear fusion. Dust is thought to enter the ISM via stellar winds from asymptotic giant branch (AGB) stars or ejection in supernovæ. Because of this, study of dust gives us clues as to the properties of the generations of stars that have come before. However, there is still some debate as to whether these processes are sufficient to account for the amount of dust observed, especially in the early universe (e.g. Morgan & Edmunds, 2003).

Dust has a significant affect on the surrounding gas by driving the collapse of clouds by radiating away heat and as a site for the production of molecular hydrogen (van de Hulst, 1948). As such it is very important for star formation.

Unfortunately dust is an observational hindrance at visible and UV wavelengths. It absorbs optical light which can be seen clearly in views of the Galactic centre (Figure 1.1). This information is not lost, however. The dust is heated so re-radiates at longer wavelengths (depending on the temperature of the grains) and this emission contributes a significant proportion of the total bolometric luminosity of a galaxy (Figure 1.5).

Emission from dust takes the form of a modified blackbody as interstellar dust has an emissivity ($Q_\nu = 1\text{-}e^{-\tau_\nu}$) less than unity. This is often called a greybody, with
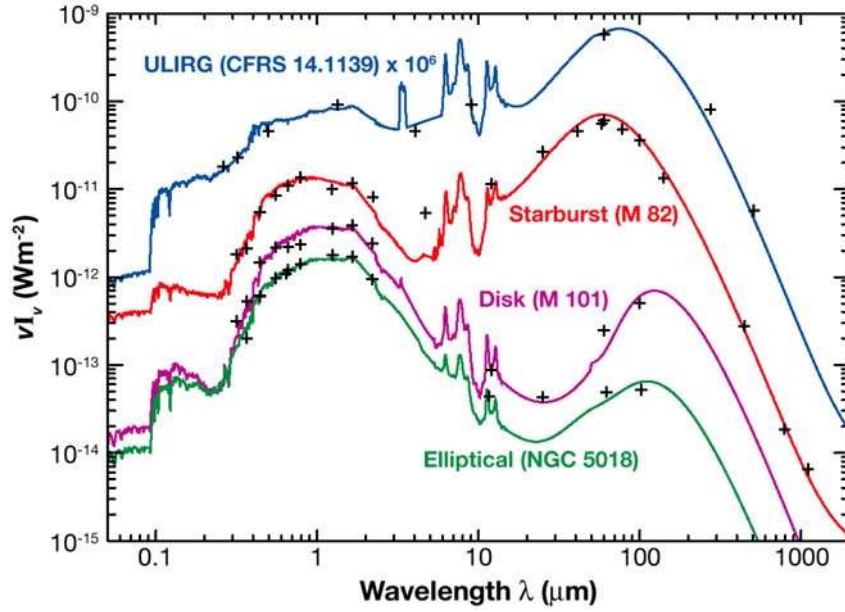
Figure 1.5 Spectral energy distribution of some typical galaxies. The area under the graph corresponds to the approximate luminosity in each regime. Depending on the morphology the infrared luminosity can contribute more than half of the total bolometric luminosity of a galaxy.

flux given as,

$$S_\nu = \frac{M_\mathrm{d}\,\kappa_\nu\,B_\nu(T)}{D^2}, \tag{1.3}$$

where M_d is the total mass of dust in kg, D is the distance between observer and source in metres and $B_\nu(T)/\,\mathrm{W\,m^{-2}}$ is the Planck function,

$$B_\nu(T) = \frac{2\mathrm{h}\nu^3}{\mathrm{c}^2}\frac{1}{\mathrm{e}^{[\mathrm{h}\nu/\mathrm{k_B T}]} - 1}. \tag{1.4}$$

Here, κ_ν is the frequency dependent mass emissivity of the dust grains,

$$\kappa_\nu = \kappa_0 \left(\frac{\nu}{\nu_0}\right)^\beta. \tag{1.5}$$

In this work κ_0, the assumed dust mass emissivity at $\lambda = 350\,\mu\mathrm{m}$ ($\nu_0 = 8.57\times10^{11}\,\mathrm{Hz}$) is taken to be $0.192\,\mathrm{m^2\,kg^{-1}}$ (Draine, 2003). Much of the analysis assumes β is fixed but it has been seen to vary from region to region, typically having values between 1 and 2. The value of this parameter is dependent on the properties of the dust grains with metals and crystalline substances having higher values within this range, whereas a β closer to unity suggests small amorphous carbon grains dominate. Related to this work, Smith et al. (2012a) finds a radial gradient in this parameter through the disk of M31 (see Chapter 3).

Typical dust in the ISM of nearby galaxies has a peak emission in the far-infrared (FIR) regime ($\sim 20\,\mu$m–1 mm) corresponding to temperatures of $\sim 20\,^{\circ}$K. This regime is also important for other tracers of the ISM and obtaining observations here is far from trivial. Infrared (IR) astronomy and some associated issues are outlined in 1.3.

1.2.4 THE STAR FORMATION LAW

The star formation law (although not a 'law' in the strictest sense) is an empirical relationship between the rate of formation of stars, and the amount of material from which they are made.

The first real attempt to devise a model of star formation on large scales was made by Maarten Schmidt in the mid-20th century. He derived a power law relationship between the number of stars being formed to the amount of hydrogen gas, in terms of the volume densities of star formation and gas mass (ρ_{SFR} and ρ_{Gas} respectively), for objects out of the plane of the Milky Way (Schmidt, 1959),

$$\rho_{\mathrm{SFR}} \sim \rho_{\mathrm{Gas}}^{N}.\qquad(1.6)$$

In studying these objects, he found the power index, $N \sim 2$.

The first extragalactic measurements of the Schmidt law were carried out by Sanduleak (1969), who compared the 21 cm emission to the density of Population I (young) stars in the Small Magellanic Cloud (SMC), and Hartwick (1971) who compared 21 cm emission from H I to ionised gas, H II in M31. They found indices of $N_{\mathrm{SMC}} = 1.84 \pm 0.14$ and $N_{\mathrm{M31}} = 3.50 \pm 0.12$, respectively.

Since then, similar studies have tended to relate surface density of star formation (Σ_{SFR}) to surface density of gas (Σ_{Gas}), which are the parameters we actually observe. However, the index probed using surface densities should be equivalent to that for volume densities as long as we are observing a constant thickness of material.

A later study of 16 nearby galaxies by Boissier et al. (2003) found $N = 2$. Wong & Blitz (2002) studied 6 nearby spirals and estimated N to be in the range 1.2–2.1. However Heyer et al. (2004) calculated an index of ~ 3.3 for M33 when considering total gas, but $N \sim 1.4$ when looking only at molecular hydrogen. A more recent work on the same object (Verley et al., 2010) found a wide range of indices ($1.0 < N < 2.6$) depending on gas tracer and fitting method. The SF law with total gas and H_2 only give $N > 1.6$.

In the comprehensive (and most often cited) work of Kennicutt (1998b), the

power index was estimated for 90 nearby galaxies using total gas (molecular gas only for starbursts) and found $N = 1.40 \pm 0.15$ (an updated plot, including revised data is shown in Figure 1.3). One immediate question is whether this slope only works when considering global measurements of galaxies, or is it a manifestation of a relationship on smaller scales.

One interpretation of the Kennicutt result is that star formation timescales are dictated by the free-fall time, SFR $\sim M / \tau_{\text{ff}}$ (e.g. Elmegreen, 1994; Krumholz & Thompson, 2007). Since $M \propto \rho$ and $\tau_{\text{ff}} \propto \rho^{-1/2}$ (e.g. Madore, 1977), $\rho_{\text{SFR}} \sim \rho^{3/2}$. Other work suggests that the super-linear slope is a result of variations in the fraction of dense gas between normal spiral galaxies and starbursts and that the star formation law is linear (constant star formation efficiency) given constant dense gas fraction (Lada et al. e.g. 2012).

Recently acquired data from the Galaxy Evolution Explorer (GALEX, Martin & GALEX Team 2005a) and The H I Nearby Galaxies Survey (THINGS, Walter et al. 2005) has allowed the star formation law to be probed on sub-kpc ($\sim 750\,\text{pc}$) scales. Many papers now suggest that star formation is more directly related to molecular rather than total gas and Bigiel et al. (2008) find that the molecular gas star formation law follows a relationship with index, $N = 1$ (a linear relationship), consistently lower than the values they find for total gas.

Despite being a relatively simple idea, probing the star formation law involves bringing together data from a variety of sources, each of which have their own difficulties as described earlier in this chapter. Much of the necessary information, especially probing the ISM, involves observation in the infrared, which has its own set of challenges.

1.3   INFRARED ASTRONOMY

The light we see with our eyes and optical telescopes is but a small portion of the electromagnetic (EM) radiation emitted in the universe. While it is true that stars
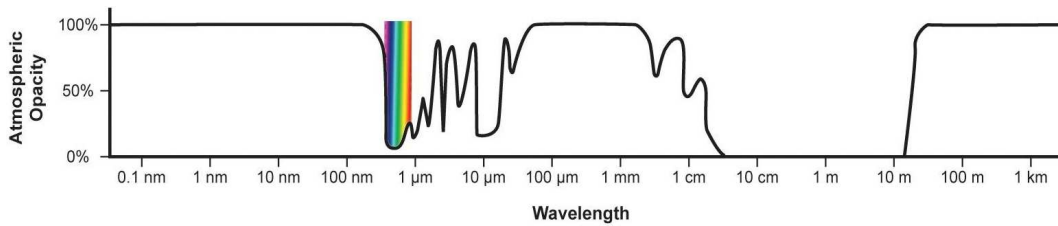
Figure 1.6 Transmission of electromagnetic waves through the atmosphere as a function of wavelength. Image credit: *NASA*.

predominantly emit in the optical, emission from other objects occurs over a much wider spectrum of wavelengths, from short-wavelength γ- and X-rays to the IR and radio.

The last century has seen astronomers gradually open up more and more windows on the universe. Every time we have come up with a way to view a new part of the spectrum, immense progress has been made in our understanding of the heavens, from the first radio telescopes in the 1930s to space based infrared telescopes developed first in the 1980s with *IRAS*, followed by *ISO* and *Spitzer* culminating most recently with the Herschel Space Telescope launched in 2009 covering the FIR.

About 1% of the mass in the ISM is made up of dust, which absorbs optical and UV light from stars, reradiating in the IR. Star forming regions tend to be especially dusty, so not accounting for this absorption can result in a significantly underestimated SFR. In fact, on average around half of the total bolometric luminosity of a galaxy is emitted at these wavelengths (Figure 1.5). Furthermore, spectral lines emitted by specific molecules at IR wavelengths can be detected using spectrometers, allowing astronomers to measure the chemical composition of interstellar clouds.

The ability of astronomers to observe certain parts of the spectrum is not just dependent on making detectors capable of receiving the required wavelength. Observers on the ground have the problem of the Earth's atmosphere. Molecules in the air absorb specific wavelengths of light meaning that much of the EM spectrum is difficult to observe from the ground (Figure 1.6). Because of this the most sensitive telescopes are placed in dry areas at high altitude, or in space.

This work uses data from a variety of IR telescopes. The catalyst for the studies conducted in this thesis were observations by the newest IR space telescope, *Herschel*.

1.3.1   THE HERSCHEL SPACE OBSERVATORY

The *Herschel Space Observatory* (Figure 1.7, left), built and operated by the *European Space Agency* (*ESA*) as one of its four 'cornerstone' missions, was the first space telescope to observe from the IR to the submillimetre (sub-mm, 55–672 μm). As such it was able to observe previously unseen dusty and cool regions of space.
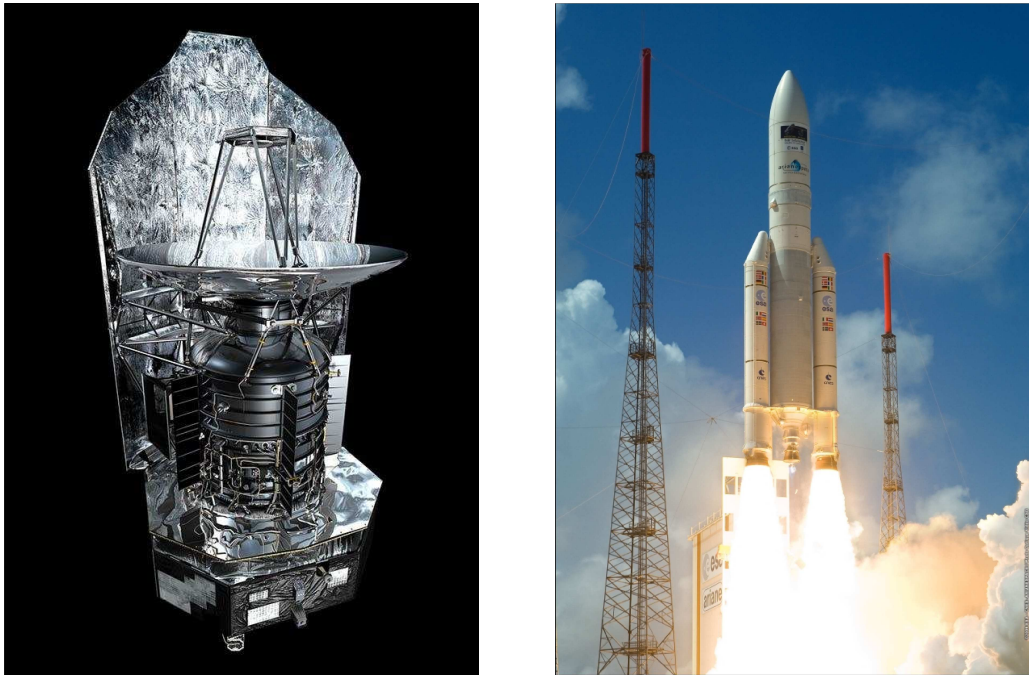
Figure 1.7 Left, The *Herschel Space Observatory*, image credit: *ESA*; right, launch of the *Ariane 5* rocket containing *Herschel* and *Planck*, image credit: *ESA*.

THE SATELLITE

The telescope is made up of four main parts: the telescope, payload (including instruments and cryostat), service module (communications and electronics) and sunshield. It has a 3.5 m primary mirror, the largest single dish ever launched into space (for civilian purposes at least). *Herschel* operates in the FIR regime. As such it is observing dust that has a temperature of tens of degrees kelvin ($^\circ$K). In order to be sensitive to such small amounts of energy, all of the onboard instruments must be cooled to a fraction of a degree above absolute zero, -273°C. This is done with a supply of liquid helium and is the limiting factor for the lifetime of *Herschel*.
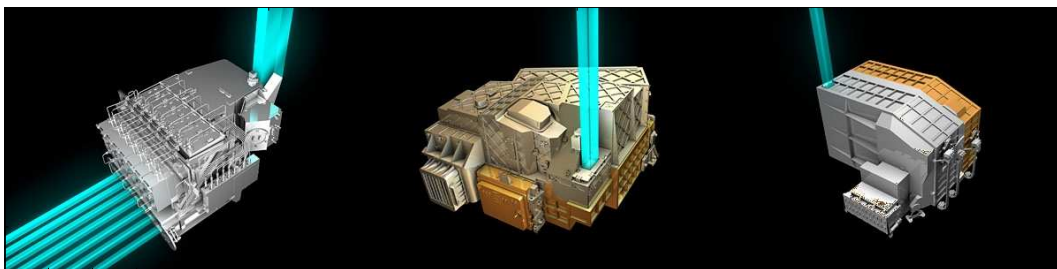
Figure 1.8 The three instruments onboard *Herschel*, from left they are the Heterodyne Instrument for the Far-Infrared (*HIFI*), Photodetector Array Camera and Spectrometer (*PACS*) and Spectral and Photometric Imaging Receiver (*SPIRE*). Image credit: *ESA*.

Unlike *Spitzer*, *Herschel* has no warm phase, so when the helium was depleted on 29th April 2013 the telescope ceased observations.

The three main instruments on *Herschel* are called the *Photodetecting Array Camera and Spectrometer* (*PACS*), *Spectral and Photometric Imaging REceiver* (*SPIRE*) and *Heterodyne Instrument for the Far-Infrared* (*HIFI*).

HIFI is a high resolution spectrometer and has the ability to observe FIR and sub-mm emission lines including water, covering the range 157–625 μm. An example spectrum can be seen in Figure 1.9. *PACS* and *SPIRE* are cameras covering the ranges 60–210 μm and 200–670 μm respectively. *PACS* observes in three bands, centred on 70, 100 and 160 μm, with two of the three able to be used at any one time. *SPIRE* observes in three bands also, centred on 250, 350 and 500 μm with the ability to observe all bands simultaneously. The two cameras can be used together in 'parallel' mode, allowing the full peak of the cold dust spectral energy distribution (SED) of nearby galaxies to be covered.

MISSION

Herschel was launched, along with the *Planck* satellite, on 14th May 2009 in an *Ariane 5* rocket from Guiana Space Centre in French Guiana (Figure 1.7, right) and took around two months to reach L2, the second Lagrangian point of the Sun-Earth system.
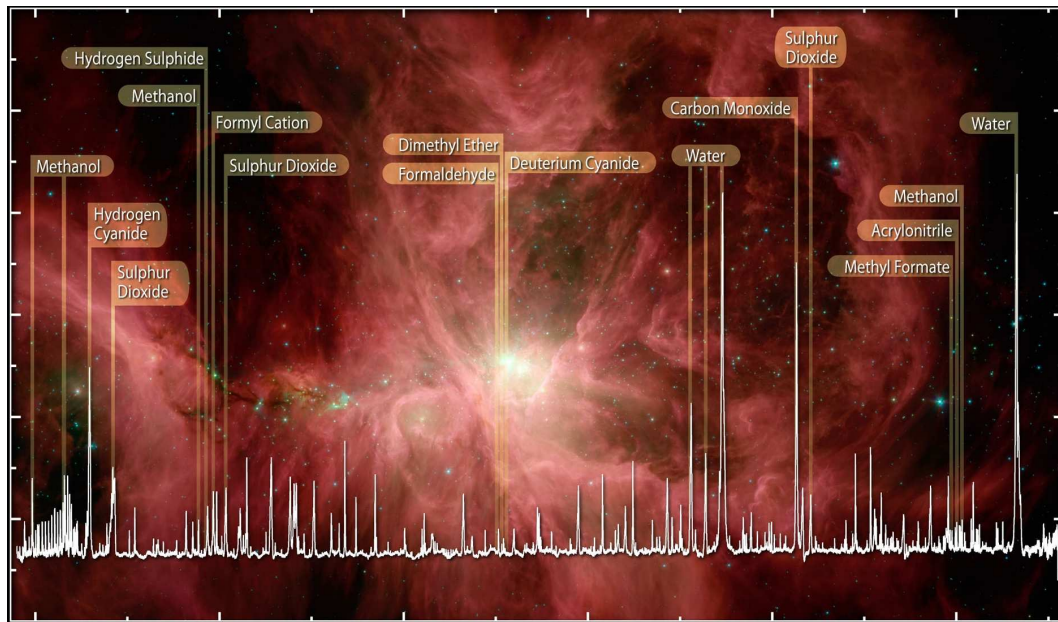
Figure 1.9 A spectrum of the Orion nebula taken by *Herschel*'s *HIFI* spectrometer overlayed on an infrared image of the same area of sky. Image credit: *ESA*.

This region of space is far from any sources of radiation that may interfere with observations, allowing for the highest possible sensitivity. It is not gravitationally stable, but the telescope requires only minor course corrections during its flight to orbit the L2 point on a Lissajous trajectory. Finally, because the Sun and Earth are in the same direction with respect to the telescope, a huge portion of the sky is available to be observed at any one time.

The telescope observed for 21 hours per day, with 3 hours for data download and communication regarding the following day's observations. *Herschel* operated for nearly four years, several months longer than estimated, running out of coolant on 29$^{\text{th}}$ April 2013.

Because of the many advantages of L2, this region of the solar system is extremely sought after. It is currently occupied by the *Planck* satellite and is the future home of *NASA*'s *James Webb Space Telescope* (*JWST*). Once *Herschel* had taken its final observations it had to vacate the region in order to keep it clear for other missions. Despite some interesting ideas, including crash landing the telescope into the moon and performing spectroscopy on the resulting debris, the telescope was pushed into a solar orbit where we are assured it will not collide with Earth for at least one hundred years.

1.4   THESIS OUTLINE

This thesis contains three major areas of study, two of which are very closely related.

The first work I present (Chapter 2) concerns the global star formation properties and dust masses of nearby spiral galaxies in the *Herschel Reference Survey* (HRS). I will look at how these properties vary between barred and unbarred spiral galaxies and between Virgo cluster and field galaxies. I will also explore trends with Hubble-type and stellar mass.

Chapters 3 and 4 focus on resolved observations of two of the largest galaxies in the local group, Andromeda (M31) and the Triangulum (M33). Here I present maps of the SFR created using two different methods and measure a global SFR for each source. I also present maps of three tracers of the ISM and test the SF law on sub-kpc scales using each. I then discuss how the SF law varies with gas tracer and which parts of the ISM appear more spatially correlated with star formation.

2 GLOBAL STAR FORMATION PROPERTIES AND DUST IN SPIRAL GALAXIES

A scientist! Call a scientist!

–PETER GRIFFIN, FAMILY GUY

2.1 INTRODUCTION

Clustering and merger events dominated galaxy evolution at early times (Kormendy & Kennicutt, 2004). As the universe expands and the distance between galaxies becomes greater, galaxy merger events are less common in all but the densest regions of the universe, as supported by observations made with the *Hubble Space Telescope* (HST, Le Fèvre et al. 2000). This means that environmental effects, which tend to be more rapid and violent (e.g Sandage, 2005) have less affect on galactic evolution and passive secular processes begin to dominate (Kormendy & Kennicutt, 2004). These processes are driven by the galactic structure (Kormendy, 2008), of which bars are a significant part, with their capacity to drive the motion of material in the centre of a galaxy.

Studying nearby galaxies in terms of size, morphology and environment gives us clues as to the major factors affecting their evolution. There are difficulties, however, as no two galaxies are the same and no two environments are the same so many studies in astronomy involve a statistical comparison of large samples. In this chapter I will attempt to ascertain any differences between barred and unbarred spiral galaxies in the *Herschel Reference Survey* (HRS, Boselli et al. 2010a). I will also look for differences between cluster and field galaxies, and trends with Hubble-type and stellar mass.

Probably the most well-known way to classify galaxies is the Hubble sequence (Hubble, 1926), visualised with the famous 'tuning-fork' diagram (Figure 1.2 in 1.1.2). It can be loosely split into early-type and late-type galaxies. Elliptical galaxies are early types and traditionally thought of as 'red and dead,' being old and large structures that have used up the majority of their fuel for star formation, making the convention 'early-type' rather misleading. The late-types (spirals) tend to be bluer, with more active star formation. A spiral's Hubble-type (Sa, Sb, Sc, etc) denotes how tightly wound the spiral arms are, and the dominance of the bulge compared to the disc, with later type spirals (Sc-d) having a less-dominant bulge component. Late-types are further split into barred and unbarred morphological classes (hence the 'fork').

Surveys suggest that around two-thirds of spiral galaxies in the local universe contain a bar (Eskridge & Frogel, 1999). Work by Sheth et al. (2008) with the *Cosmic Evolution Survey* (COSMOS) which studied over two thousand spiral galaxies found that over a period of seven billion years (out to redshift, $z = 0.84$), the number of barred spiral galaxies has tripled, with only around 20% of spirals in the distant past possessing a bar. This increase in bar fraction was found to be the case in low mass spirals only, suggesting low mass galaxies may form bars on longer timescales than more massive ones. This is supported by theoretical work on the topic, for a review see Athanassoula (2012). Provided bars are long-lived structures (e.g. Debattista et al., 2006; Athanassoula et al., 2013) the percentage of higher-mass spiral galaxies with bars should remain roughly constant, as their bars would have been constructed earlier. Other work opposes this view (e.g. Bournaud & Combes, 2002) suggesting that bars are repeatedly created and destroyed on timescales of approximately two billion years. There is some evidence from the Sloan Digital Sky Survey (SDSS, Abazajian et al. 2009) that bars are indeed ephemeral structures as non-barred and barred spirals were observed to have indistinguishable intrinsic colours (van den Bergh, 2011) hence they are at a variety of stages in their evolution. The mechanism for this is thought to be instabilities once a bar reaches a certain mass (e.g. Das et al., 2002).

Another finding in Sheth et al. (2008) is that redder galaxies and those with greater stellar mass and higher bulge to disc ratio have a larger bar fraction while work on the SDSS (Barazza et al., 2008) finds greater bar fraction in bluer low-mass galaxies. It is possible that this apparent contradiction is due to different selection effects in the two surveys. Sheth et al. (2008) is not sensitive to galaxies with stellar mass $M_* < 1.6 \times 10^{10}\,\mathrm{M_\odot}$ while Barazza et al. (2008) is insensitive to galaxies more massive than $3.2 \times 10^{10}\,\mathrm{M_\odot}$, so there is only a small overlap in stellar mass between

Figure 2.1 Hubble image of NGC 1300 displaying a strongly barred spiral structure. Its classification is (R')SB(s)bc. Image credit: *NASA/ESA*.

the two surveys. Therefore the discrepancy could be due to the different stellar masses being probed (Nair & Abraham, 2010).

Also contrary to Sheth et al. (2008), more recent work on the same survey suggests it is the high-mass spirals that drive evolution of the bar fraction out to $z = 1.0$ (Melvin et al., 2014), with a more modest evolution in low-mass spirals. However, both Sheth et al. (2008) and Melvin et al. (2014) agree that high mass galaxies dominate the barred population at high-z.

Bars are thought to funnel material into the centre of the galaxy. This is one possible reason why many barred spirals have active galactic nuclei (e.g. Oh et al., 2012), demonstrating the importance of understanding the origin and effects bars have on galaxy evolution. The funnelling of material is also thought to fuel star formation in the centre of the galaxy (e.g. Knapen et al., 2002). Conclusions from observations of CO in nearby galaxies by the Nobeyama Radio Observatory (NRO, Kuno et al. 2007) and BIMA Survey of Nearby Galaxies (SONG, Sheth et al. 2005) seem to support this as they found the central concentration of molecular gas is higher in barred galaxies. However, Masters et al. (2012) use the optical colours of barred galaxies to suggest these sources are much redder than an unbarred system, concluding that the presence of a bar in a late-type galaxy will ultimately quench star formation although this is based on studying the amount of atomic gas which recent work implies is less important for star formation than molecular (e.g. Bigiel

et al., 2008; Rahman et al., 2012). Also, using optical colours alone can result in large uncertainties, as differences in flux at each wavelength are likely to be small. It is possible that colour and presence of a bar are correlated as they are both signs of a galaxy's 'maturity' as stated earlier, but there may be no causal link.

In this study, I look at the global properties of dust emission in the largest nearby targeted sample of spiral galaxies with the *Herschel Space Observatory* (Pilbratt et al., 2010) taken from the *Herschel Reference Survey* (HRS, Boselli et al. 2010a), along with star formation, colour and stellar mass, for sources with and without bars. I also test for systematic variations between galaxies of difference Hubble-type and also whether they are in a cluster or the field.

2.2 DATA AND THE SAMPLE

The *Herschel Reference Survey* (HRS, Boselli et al. 2010a) is a volume limited sample of 322 galaxies observed with *Herschel* SPIRE (Griffin et al., 2010) at distances $15 < D / \mathrm{Mpc} < 25$. The galaxies were selected by their K-band magnitude with contamination from Galactic cirrus minimized (see Boselli et al. (2010a) for full details). The full sample includes 260 late-type galaxies (Sa-Sd-Im-BCD) and 62 early-types (E, S0, S0a), morphologically classified via the Virgo Cluster Catalogue or by eye (Boselli et al., 2010a; Ciesla et al., 2012). For more complete data on the HRS, see Table A.1 in Appendix A.

Uncertainties are assumed to be dominated by calibration. The *Herschel* SPIRE fluxes (along with detailed uncertainties accounting for calibration, confusion noise and background) are provided in Ciesla et al. (2012) and from the *Herschel* Virgo Cluster Survey (HeViCS) in Auld et al. (2013). For full details of the observing strategy, data reduction and flux extraction for the entire HRS, see Smith et al. (2012b), Ciesla et al. (2012) and Auld et al. (2013).

All galaxies have since been observed with the PACS instrument (Poglitsch et al., 2010). PACS fluxes for galaxies in HeViCS are taken from Auld et al. (2013), photometry for the rest of the sample can be found in Cortese et al. (2014). Previous work by Cortese et al. (2012b) determined dust masses from the SPIRE fluxes alone for these 211 sources using a scaling relationship between FIR flux and dust mass. The shorter-wavelength PACS data allows a more well constrained dust temperature as we cover the peak of the SED (see 1.2.3), although calculated dust mass should not be greatly affected by the additional datapoints. There is more data available in this wavelength range and at shorter wavelengths from *Spitzer* and *IRAS* but keeping to Herschel data alone allows full coverage of the SED peak in a consistent way
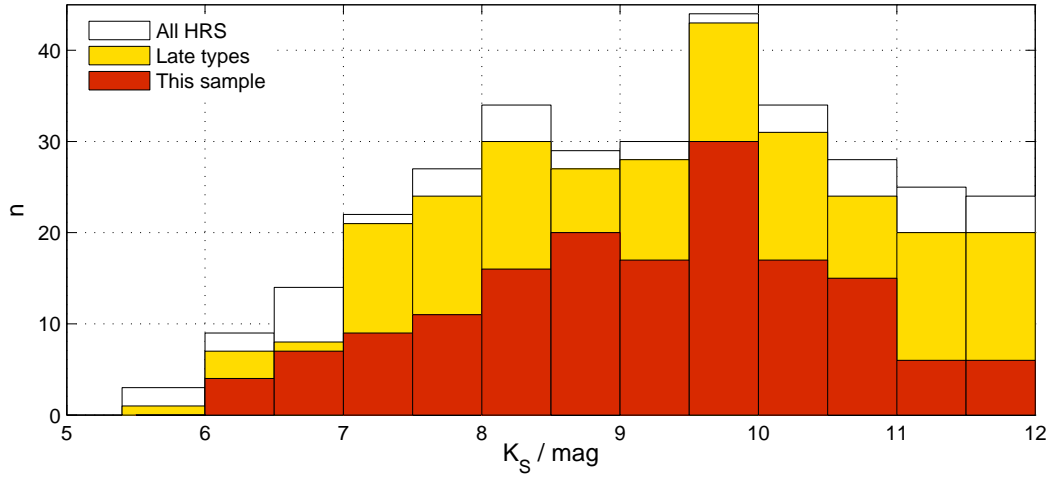
Figure 2.2 The K-band magnitude distribution for all the galaxies in the HRS (white), compared with the 234 late-types (yellow) and the sample of 153 galaxies with sufficient data used in this work (red).

for all galaxies, so I do not employ this data here. Also, warm dust contributes significantly to flux measurements at wavelengths $<70\,\mu m$ (Bendo et al., 2010), so would skew the SED and give spurious results for the cold component.

Ancillary optical and ultraviolet data for the HRS sources are provided by the SDSS Data Release 7 (SDSS DR7) and the GR6 data release from the *Galaxy Evolution Explorer* (*GALEX*, Martin & GALEX Team 2005b). These were used to estimate NUV-r colours and stellar masses for 211 galaxies from the HRS (taken from Cortese et al. 2012b), calculated from the i-band luminosities using the method detailed in Zibetti et al. (2009). *GALEX* FUV data is also used in conjunction with *Spitzer MIPS* 24 μm, (photometry from Bendo et al. 2012a) to determine a star formation rate for galaxies where data is available.

The final sample of spirals studied here (lenticular galaxies are removed) includes 153 galaxies of SA, SAB and SB types, with 104 and 49 morphologically classified as barred (including weakly barred, SAB) and unbarred respectively, according to the *NASA* Extragalactic Database (NED). The K-band luminosity distribution for all the galaxies in the HRS is shown in Figure 2.2 along with the distributions of the late-type subsample (234 sources) and the 153 galaxies used in this work. A KS-test indicates the sample selected here is representative of the late-type local galaxy population as a whole, as the samples cannot be separated to 90 % confidence.

2.3   MEASURED PROPERTIES OF THE GALAXIES

The IR-submillimetre fluxes from 100-500 μm are fit using a programme written by Matthew Smith of Cardiff University using the method described in Smith et al. (2012b) to a modified blackbody function,

$$S(\nu) = \frac{M_{\rm d}\,\kappa_\nu\,B(\nu, T_d)}{D^2} \tag{2.1}$$

where $M_{\rm d}$ is the dust mass and $B(\nu, T_{\rm d})$ is the Planck function at frequency ν and dust temperature, $T_{\rm d}$. D is the distance to the galaxy (assumed to be $D = 17$ Mpc for the Virgo Cluster, 23 Mpc for the Virgo B cloud or estimated from the recessional velocities (Heliocentric) in the NED database with a Hubble constant of $H_0 = 70\,{\rm km\,s^{-1}\,Mpc^{-1}}$). κ_ν is the dust mass opacity coefficient as a function of frequency ν, which varies as a power law with dust emissivity index β such that $\kappa_\nu \propto \nu^\beta$. We normalise this power law using $\kappa_\nu = 0.19\,{\rm m^2\,kg^{-1}}$ at 350 μm (e.g. Eales et al., 2012) and assume $\beta = 2$ (typical for interstellar grains). Changing β will change the dust masses Smith et al. e.g. 2012b, but in this work, we are interested in comparing populations of galaxies rather than the explicit dust masses themselves. We note that a source of uncertainty could be introduced here if barred and unbarred galaxies, or those of different hubble-type, have systematically different dust emissivity constants, κ_0, or indices, β. This can be tested for by treating β as a free parameter in our SED fit but there are difficulties due to β-$T_{\rm d}$ degeneracy and lack of data longward of 500 μm, so I elect to keep β fixed here.

Flux uncertainties are likely to be correlated for each instrument, but this is taken into account when computing χ^2 in the SED fitter by employing the full covariance matrix (see Smith, 2012, Section 3.4.5). The effect of any systematics introduced by the instruments on the calculated dust mass or temperature are the same for all galaxies in the sample, so for the purposes of comparison this should not be an issue.

I find that the vast majority of the galaxies are well described by this single temperature function, given a fixed emissivity index, $\beta = 2$. Figure 2.3 shows a histogram of the computed χ^2 values from the fit, with the limit for 90% confidence, along with an example SED where we have five *Herschel* fluxes with uncertainties. We determine the total luminosity $L_{\rm FIR}$ from a galaxy by summing over the emission between 60 and 500 μm using the greybody function with our best-fit parameters ($M_{\rm d}$, $T_{\rm d}$) for each galaxy. Data used for the fitting can be found in Table A.2 in Appendix A, with SED fitting results in Table A.3.
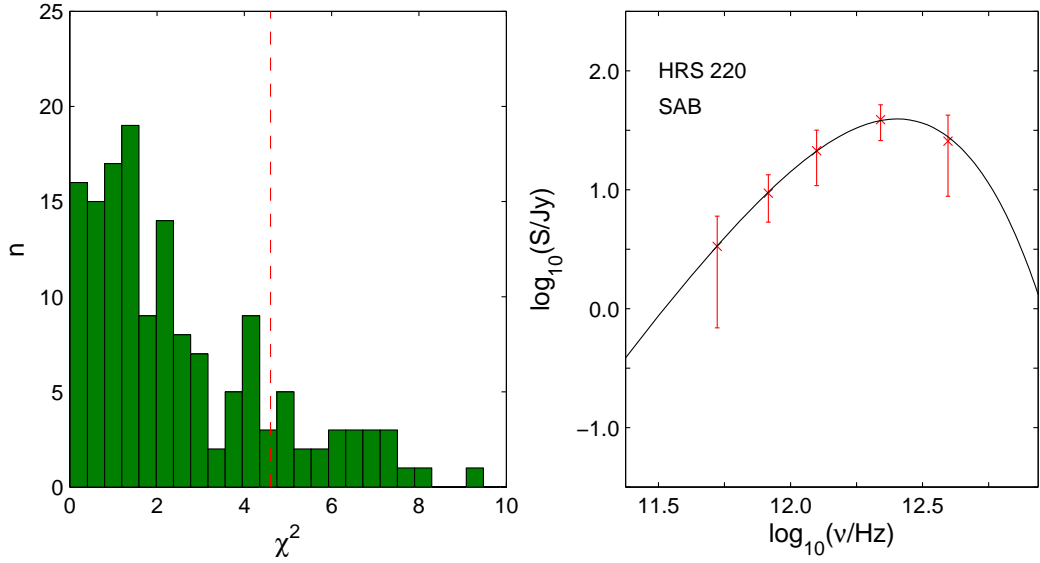
Figure 2.3 Left: histogram of reduced χ^2 values for the selected sample of the HRS assuming a one-temperature greybody function. The red dashed line represents the 90% confidence limit assuming two degrees of freedom (where we have 5 datapoints, $\chi^2 \sim 4.6$). Right: Fitted spectral energy distribution of HRS 220 (NGC4579), with datapoints used for fit. Red crosses represent *Herschel PACS* or *SPIRE* fluxes. χ^2 for this fit is 0.83.

I split our sample into subgroups of barred and unbarred galaxies using the morphology given in NED where available, as stated in Boselli et al. (2010b). 49 galaxies have no bar (morphologically classified as SA), 43 have a weak bar (SAB) and 61 are classified as having a strong bar (SB). We use these to test for any systematic differences between the populations. The average properties for each subset is listed in Table 2.1 along with those of different Hubble-type (split into three subsets) and environment (Virgo cluster or field galaxies).

A smaller sample of galaxies (N_{SF}, Table 2.1) is selected for which we have *GALEX* FUV (Cortese et al., 2012b) and *Spitzer MIPS* 24 μm photometry (Bendo et al., 2012a), which traces the unobscured and embedded star formation respectively. The prescription I use to determine total star formation rate surface density (Σ_{SFR} / $M_\odot$ yr^{-1} kpc^{-2}) is given in 3.3 in the following chapter.

In Figure 2.4 and 2.5, the dust temperature (T_d), dust-to-stellar mass ratio (M_d / M_*), Σ_{SFR}, NUV-r colour and FIR luminosity-to-stellar mass ratio (L_{FIR}/M_*) for the sample are presented. The average dust mass for the 153 late-types is $\langle \log_{10}(M_d / M_\odot) \rangle \sim 7.12 \pm 0.48$, with average dust temperature $\langle T_d \rangle \sim 19 \pm 3$ K (where the quoted uncertainty is the standard deviation, Table 2.1).

Variations in each property with bar morphology (Figures A.1 and A.2) and
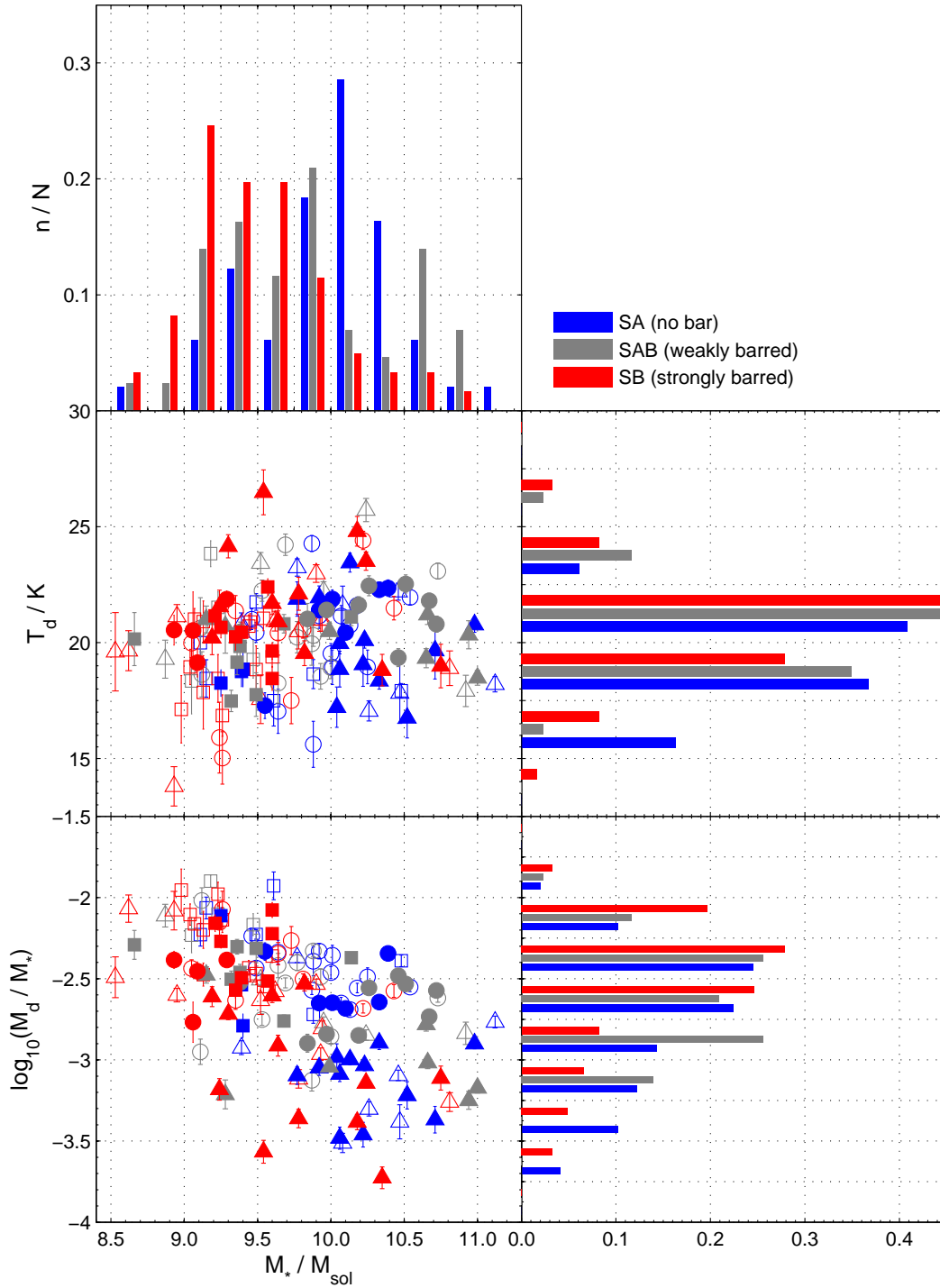
Figure 2.4 The dust temperatures, $T_{\rm d}$ and dust-to-stellar mass ratios, $M_{\rm d}/M_*$ for the 153 galaxies in the sample displayed as a function of stellar mass M_*. These are further split into morphology types with blue points representing SA galaxies, grey points SAB and red, SB galaxies; i.e. moving through unbarred sources to weakly barred to stongly barred. Marker shapes indicate Hubble-type, from a-ab-b (triangle) through bc-c (circle) to cd-d (square). Filled symbols denote galaxies in the Virgo cluster, open symbols are galaxies in the field.
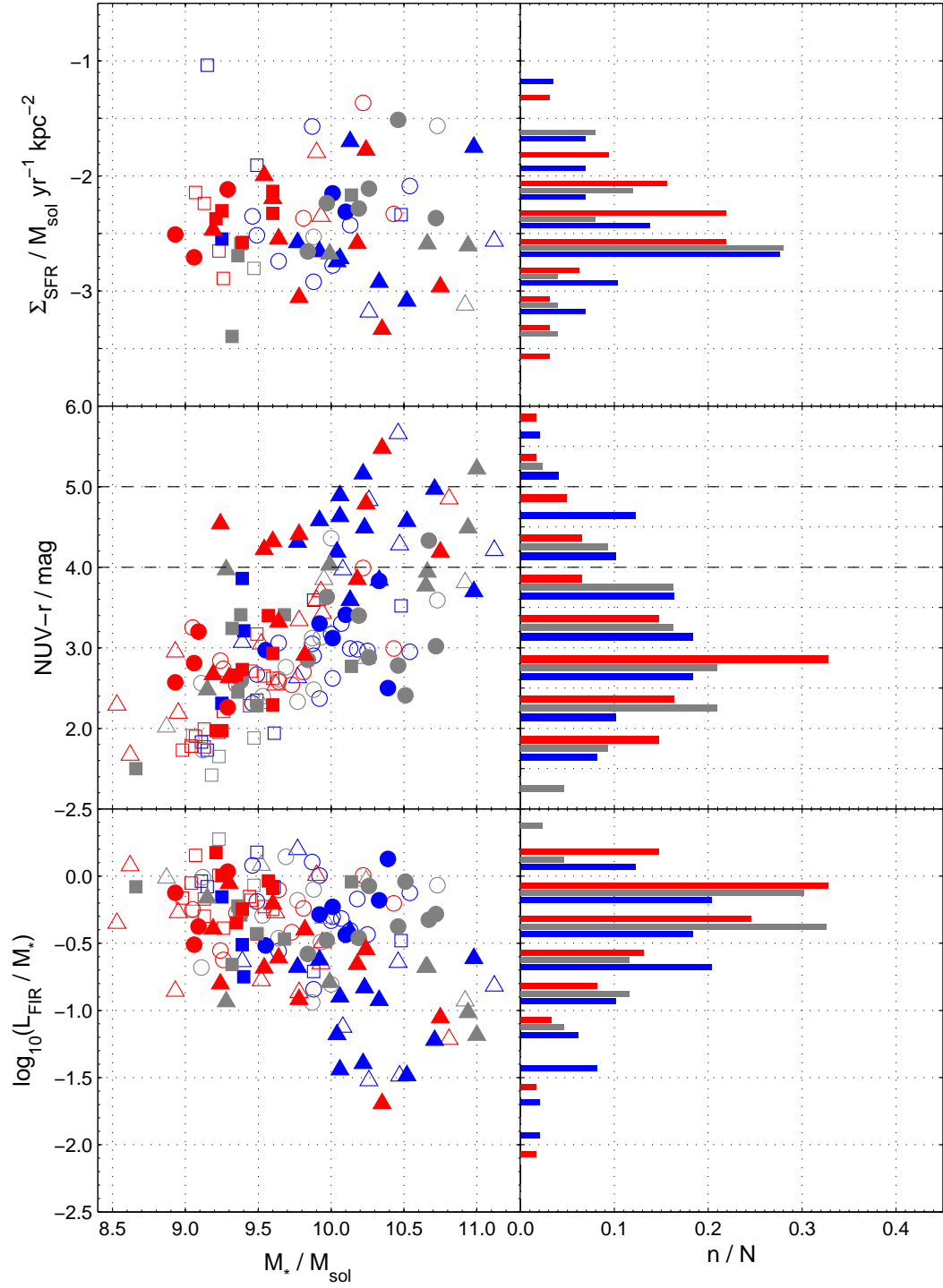
Figure 2.5 The star formation rate surface densities from *GALEX* FUV and *Spitzer MIPS* 24 μm, Σ_{SFR}; NUV-r colours and FIR luminosity to stellar mass ratios, L_{FIR}/M_* for the 153 galaxies in the sample displayed as a function of stellar mass M_*. These are further split into morphology types with blue points representing SA galaxies, grey points SAB and red, SB galaxies i.e. moving through unbarred sources to weakly barred to stongly barred. Marker shapes indicate Hubble-type, from a-ab-b (triangle) through bc-c (circle) to cd-d (square). Filled symbols denote galaxies in the Virgo cluster, open symbols are galaxies in the field.

Type	N_d	N_SF	$\log(M_*)$	T_d	Σ_SFR	$\log(M_\mathrm{d}/M_*)$	NUV-r	$\log(L_\mathrm{FIR}/M_*)$
			$M_\odot$	K	$M_\odot\,\mathrm{kpc}^{-2}\,\mathrm{yr}^{-1}$		mag	
Spirals		284						
Sample	153	69	10.11±1.57	19.1±3.1	-2.43±0.48	-2.63±0.43	3.19±1.02	-0.43±0.45
SA	49	24	10.22±1.35	19.0±3.3	-2.40±0.52	-2.72±0.42	3.53±1.03	-0.56±0.51
SAB	43	17	10.25±1.42	19.6±2.2	-2.47±0.48	-2.60±0.33	2.97±0.89	-0.35±0.38
SB	61	28	9.84±1.72	18.8±3.4	-2.44±0.47	-2.59±0.49	3.07±1.06	-0.38±0.41
a-b	54	24	10.32±1.39	19.6±3.1	-2.56±0.47	-2.94±0.38	3.88±0.98	-0.70±0.46
bc-c	52	24	10.08±1.08	19.6±3.0	-2.27±0.42	-2.53±0.22	2.93±0.51	-0.30±0.25
cd-d	39	18	9.54±1.41	18.1±2.2	-2.40±0.48	-2.31±0.23	2.43±0.66	-0.18±0.28
Virgo	70	43	10.19±1.36	19.4±3.1	-2.49±0.44	-2.79±0.46	3.60±1.03	-0.53±0.45
Field	83	26	10.02±1.82	18.7±3.1	-2.33±0.54	-2.51±0.36	2.82±0.86	-0.34±0.43

Table 2.1 Average properties for the HRS late types and the 158 galaxies in this study, split into strongly barred (SB), weakly barred (SAB) and unbarred (SA) types. Sample includes galaxies with available stellar mass information (Cortese et al., 2012a,b); Dust mass, M_d is found using modified-blackbody curves as described in Section 2.2. A smaller subsample (number of galaxies denoted by N_SFR) has sufficient data to measure both the unobscured and embedded star formation, Uncertainties are based on the standard deviation in log space.

Hubble-type (Figures A.3 and A.4) can be seen in Appendix A.2. Each plot contains subsets of Hubble-type (Figures A.1 and A.2) or morphology (Figures A.3 and A.4) and cluster/field galaxies to check for any biases.

2.4   DISCUSSION

It should be noted before discussing systematic differences between galaxies that the bar classification is an inexact science, very subjective and can depend largely on the view we have (i.e. the inclination of the galaxy and wavelength of light in which it is observed). Also, the three classes used here (SA, SAB and SB) are unlikely to fully describe the wide variety of bar structures that exist (Sellwood & Wilkinson, 1993).

The first noticeable thing in Figure 2.4 is the apparent dichotomy in stellar mass between the barred and unbarred galaxies, $\log_{10}(M_{*,\mathrm{SA}}/M_\odot) = 10.22\pm0.19$ and $\log_{10}(M_{*,\mathrm{SB}}/M_\odot) = 9.84\pm0.22$ (mean and error on mean calculated in log space). A two-sample Kolmogorov-Smirnov (KS) test suggests a difference in the samples to >99% confidence. Why barred galaxies in a K-band selected sample have systematically lower stellar masses is unclear. If the speed of bar formation depends on the mass of the host galaxy (Sheth et al., 2008) low-mass galaxies reach 'maturity' and form bars later than massive galaxies. If bars are ephemeral structures (e.g. Bournaud & Combes, 2002) the more massive galaxies in the nearby universe

may have created and destroyed their bars by this epoch resulting in these galaxies being unbarred. It would follow that the percentage of high-mass galaxies with bars should decrease, but the Sheth paper notes the percentage of high mass galaxies with bars remains roughly constant over cosmic time, suggesting that bars are in fact stable structures and are not destroyed. In any case, this dichotomy between low and high mass spirals throws up an immediate issue, as any difference between galaxies with and without bars could equally be attributed to mass effects.

When comparing the global properties of barred and unbarred galaxies it appears there is only minimal systematic difference in the parameters plotted with morphology (see Appendix A.2, Figures A.1 and A.2). Mean values are as follows: $\langle \log_{10} (M_{\rm d} / M_*) \rangle$ = -2.72$\pm$0.06 and $\langle$NUV-$r\rangle$ = 3.53$\pm$0.15 mag for unbarred galaxies, $\langle \log_{10} (M_{\rm d} / M_*) \rangle$ = -2.59$\pm$0.6 and $\langle$NUV-$r\rangle$ = 3.07$\pm$0.14 mag for barred spirals (uncertainties quoted are uncertainties on the mean, $\sigma / \sqrt{n}$). The mean of the log of SFR surface density ($\log_{10}(\Sigma_{\rm SFR})$) for unbarred galaxies is -2.40$\pm$0.11 and for barred spirals it is -2.44$\pm$0.09. This all suggests that the presence of a bar has little effect (difference $<2\,\sigma$) on the global star formation properties of a spiral galaxy. This is also the case when looking at galaxies of the same Hubble-type, consistent with van den Bergh (2011) who finds indistinguishable colours between barred and unbarred galaxies.

I calculate gas mass for each galaxy as traced by dust (Eales et al., 2012) assuming a constant gas-to-dust ratio of 100 (approximately the Milky Way value). Surface densities of gas $\Sigma_{\rm Gas}$ are compared to $\Sigma_{\rm SFR}$ in a plot analogous to the star formation law plots of Schmidt (1959), Kennicutt (1998b) and Bigiel et al. (2008) (Figure 2.6). Here it appears the selected HRS galaxies populate the sub-threshold ($\Sigma_{\rm Gas} < 10\,{\rm M}_\odot\,{\rm pc}^{-2}$) region of 'normal' galaxies studied in Kennicutt (1998b). In common with that work, there is no clear correlation between the surface densities of star formation and gas mass in this regime. It is likely that this is due to these galaxies being dominated by atomic gas, H I which is merely a gas reservoir and not directly linked to star formation (see the following chapters for a more detailed discussion of this relationship).

The mean gas depletion times ($\tau_{\rm dep} = \Sigma_{\rm Gas} / \Sigma_{\rm SFR}$, the inverse of star formation efficiency) are found to be $10^{9.09\pm0.52}$ yr ($\sim$1.2 Gyr) and $10^{9.14\pm0.44}$ yr ($\sim$1.4 Gyr) for unbarred and barred spirals respectively. Again a KS test cannot be rejected to 90 % confidence.

There is a tentative difference between galaxies in the Virgo cluster and those outside, with $\langle \log_{10}(M_{\rm d} / M_*) \rangle$ found to be -2.79$\pm$0.05 and -2.50$\pm$0.04 for cluster and field galaxies respectively. $\langle \log_{10}(\Sigma_{\rm SFR} / {\rm M}_\odot\,{\rm yr}^{-1}\,{\rm kpc}^{-2}) \rangle$ is -2.49$\pm$0.07 and
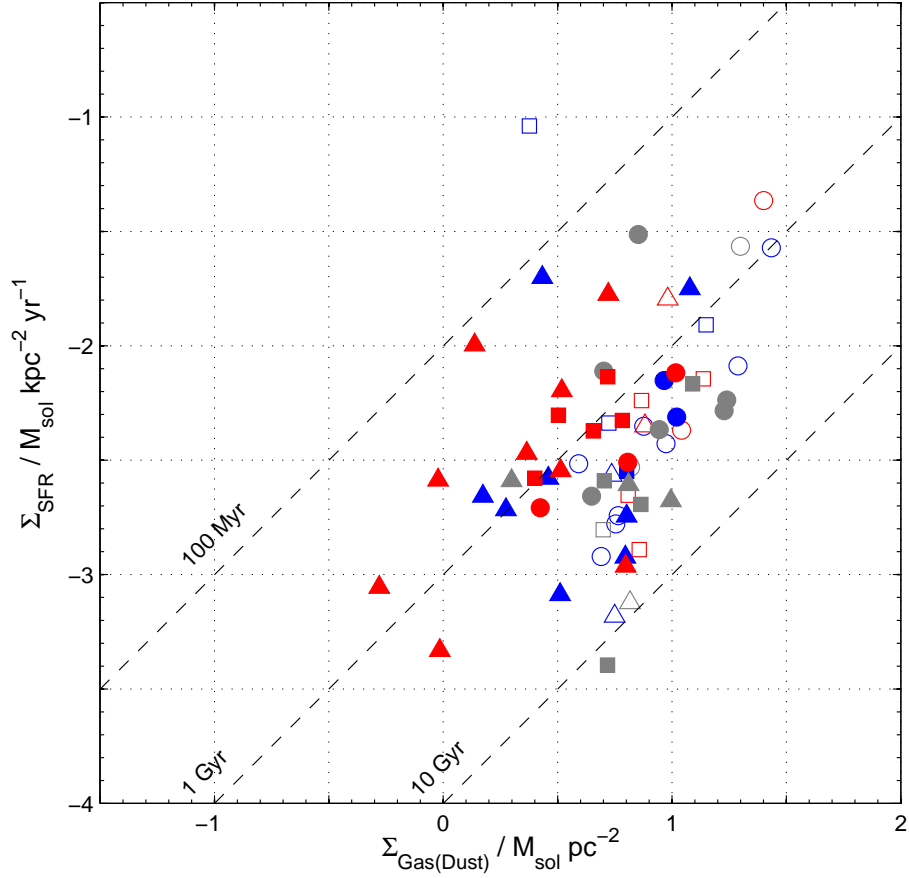
Figure 2.6 The star formation rate surface densities from *GALEX* FUV and *Spitzer MIPS* 24 μm, Σ_{SFR} versus gas surface density as traced by dust (Σ_{Gas}) assuming a gas to dust ratio of 100 ($\sim$ MW value). These galaxies are split into morphology types with blue points representing SA galaxies, grey points SAB and red, SB galaxies i.e. moving through unbarred sources to weakly barred to stongly barred. Marker shapes indicate Hubble-type, from a-ab-b (triangle) through bc-c (circle) to cd-d (square). Filled symbols denote galaxies in the Virgo cluster, open symbols are galaxies in the field. Dashed lines are of constant gas depletion time, τ_{dep}.

-2.33±0.11 for Virgo and the field. Previous work (e.g. Kennicutt, 1983; Gavazzi et al., 2002) observed lower SF activity and lower gas content in cluster galaxies (first noticed by Davies & Lewis 1973), often attributed to stripping of material due to tidal interactions in the cluster environment. However, the difference in star formation measured here is not significant ($<2\,\sigma$).

There is a clear trend in dust-to-stellar mass, NUV-r colour and to a lesser extent FIR luminosity normalised by stellar mass with Hubble-type with Pearson correlation coefficients of $R = 0.61$, -0.60 and 0.55 respectively. This agrees with known trends in the Hubble sequence (see Smith et al. (2012b) and Cortese et al. (2012b) for work on the HRS including ellipticals) that show later-type galaxies are more actively star forming (stars are generally bluer, hence younger) and contain more dust, which helps drive the collapse of gas clouds.

It appears there is a correlation between stellar mass and dust mass per unit stellar mass (Figure 2.4, bottom-left panel) with $R = -0.60$. Here, galaxies of higher stellar mass are measured to be less dusty. It follows that they should be less actively star forming which is supported by the measured correlation between stellar mass and NUV-r magnitude ($R = 0.65$) with larger galaxies being redder. This suggests that higher mass galaxies have consumed or expelled their dust after many generations of star formation with smaller galaxies that are more actively star forming still containing dust.

All of the above is also further evidence that dust and star formation are closely linked, with the dustier galaxies (higher $M_{\rm d}\,/\,M_*$) generally exhibiting a bluer NUV-r colour and higher SFR surface density, but that the presence of a bar has little effect on the global properties of a galaxy at a given epoch. If bars are indeed funneling material and fuelling star formation in the centre of spiral galaxies it is logical to assume star formation is quenched in the disc as interstellar material is removed. The result is little difference in the global star formation but a 'relocation' of actively star forming regions.

A logical follow-up piece of work would be to perform separate analyses on the inner and outer regions of the more resolved galaxies in the sample. By comparing results from barred and unbarred galaxies it would be possible to determine whether star formation rate and/or surface density of dust is enhanced in the galactic centre and diminished in the outskirts by the presence of a bar. However, preliminary work on the central concentration of $350\,\mu$m emission (which should be a good analogue to dust mass) also shows little enhancement in barred galaxies.

Utilisation of other *Herschel* surveys such as *H-Atlas* (Eales et al., 2010) could increase the sample significantly, but only with galaxies that have similarly robust

morphological classifications as those used here. It would also be useful to check for differences in the dust properties between galaxies of different morphology and environment by treating the mass emissivity index, β as a free parameter. Changes in observed β values have been attributed to dust composition and size, mantle growth, or different absorption mechanisms (Smith et al., 2012a); so any variations between different types of galaxy would be an intriguing result.

2.5   SUMMARY

Here a simple comparison was performed between the dust and star formation properties of spiral galaxies of different morphology, Hubble-type, environment and stellar mass. Dust temperature, dust to stellar mass ratio, SFR surface density, NUV-r colour and FIR luminosity to stellar mass are compared for 153 spiral galaxies in the HRS. There are clear trends in $M_{\mathrm{d}} \, / \, M_*$, NUV-$r$ magnitude and $L_{\mathrm{FIR}} \, / \, M_*$ along the Hubble-sequence and with stellar mass, in agreement with previous work. It also appears that the barred galaxies in this sample are generally lower stellar mass. Cluster galaxies appear less actively star forming and less dusty, again consistent with earlier studies.

However, the analysis performed here finds only tentative evidence for any difference between galaxies of different bar classification in terms of their dust-to-stellar masses, SFR or NUV-r colour suggesting that the presence of a bar has little effect on the global star formation properties of nearby galaxies.

ACKNOWLEDGMENTS

3 THE STAR FORMATION LAW IN M31

Look on my works ye mighty, and despair.

–PERCY BYSSHE SHELLEY, 'OZYMANDIAS'

As stated in 1.2.4, the star formation (SF) law on galactic scales is important in many areas of astrophysics, from star and galaxy formation simulations to cosmology. Observations of the nearby universe allow us to study relations on the smallest scales, but Galactic studies have problems with extinction hindering our view and introducing biases from region to region. Extragalactic sources, if looking at sufficiently high Galactic latitudes, do not have this problem, but resolved structures are often harder to discern.

The local group (Figure 3.1) gives us the opportunity to study scaling relations over whole galaxies to the smallest physical scales (comparable to the size of a giant molecular cloud). In this chapter I will aim to probe the SF law in the largest extragalactic object in the local group, Andromeda (M31, Figure 3.2). Its size and proximity makes M31 probably the best target to test our knowledge of the physical processes that govern the formation and evolution of massive spiral galaxies.

I present multi-wavelength data of M31 and measure the total unobscured and embedded star formation rates (SFR) separately using far-ultraviolet (FUV) and $24\,\mu m$ infrared (IR) data respectively. I determine the total gas, found by combining maps of neutral atomic hydrogen (H I) and carbon monoxide (CO, J=1-0) where available, which traces the molecular hydrogen (H_2).

The maps tracing SFR and gas mass are compared with those found using the far-infrared (FIR) emission from these galaxies, as observed with the *Herschel Space Observatory* (Pilbratt et al., 2010) as part of the *Herschel* Exploitation of Local Galaxy Andromeda (HELGA) project (Fritz et al., 2012). We compare our SFR from UV and $24\,\mu m$ emission with that found from FIR luminosity. The interstellar gas mass is also traced using the dust mass estimated from the FIR spectral
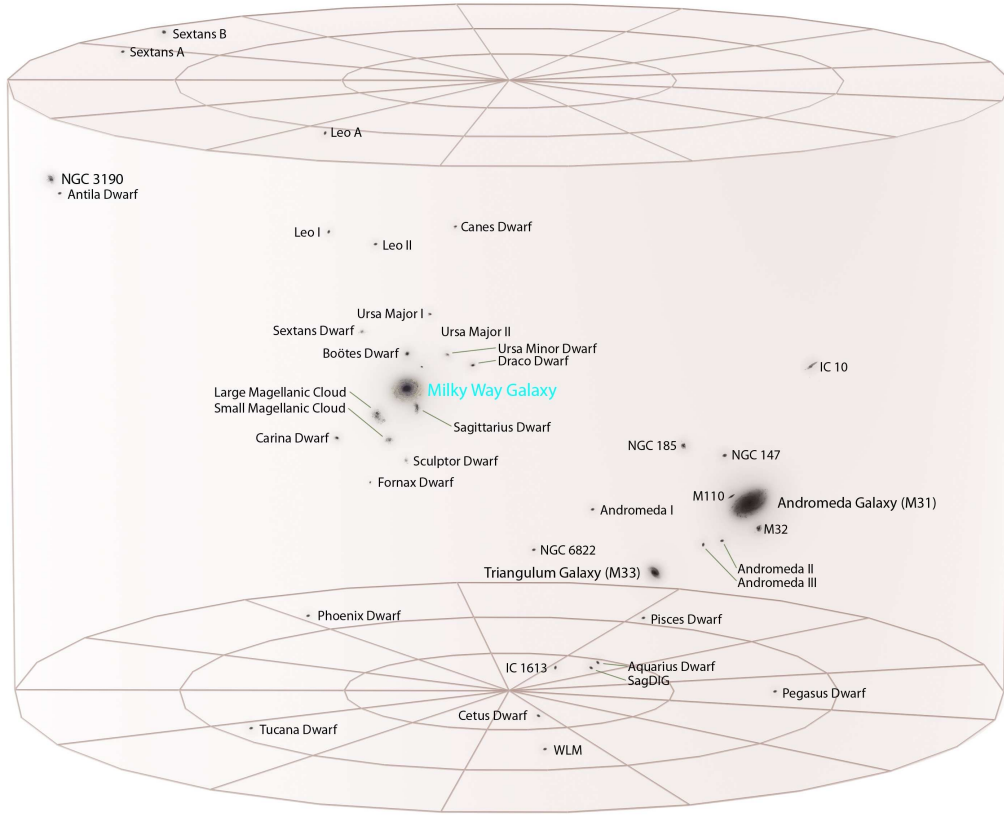
Figure 3.1 Schematic of the local group of galaxies. Image credit: Andrew Z. Colvin

energy distribution (SED), scaled using the observed gas to dust ratio. Here we aim to see how well this gas map correlates with SFR, hence whether dust mass traces star forming regions.

Finally, we use this collection of SFR and gas maps to probe the power law relationship between SFR surface density and the gas surface density, or Kennicutt-Schmidt (K-S) SF law. Our analysis is performed on individual pixels in M31 and investigates how the law varies with different gas tracers on sub-kpc scales.

Much of this work is published in Ford et al. (2013). However, all work herein is the author's unless otherwise stated (see 3.4.2).

3.1 ANDROMEDA

Andromeda (M31, Figure 3.2) is the largest galaxy in the local group, at a total mass of $\sim 10^{12}\,\mathrm{M_\odot}$ (Karachentsev & Kashibadze, 2006). It is classified as SA(s)b and has a prominent ring. The apparent angular size of M31 is $190\,'$ which, as previously stated, gives us the best view we have of any extragalactic object (as a comparison,

Figure 3.2 Messier 31, Andromeda. The image is approximately 30 kpc across, assuming a distance to M31 of 785 kpc. Image credit: *NASA/ESA*

the angular diameter of the moon is $\sim 30'$). It is approximately solar metallicity so is also a good analogue to the Milky Way. M31 shares some other characteristics of our galaxy including Hubble-type, luminosity and gas content within the disk. This makes it ideal for comparison with Galactic surveys.

There are significant differences between the two however. M31 contains approximately twice the baryonic mass of the Milky Way (~ 1 trillion stars compared to ~ 500 billion) and a disk more than twice as large (Yin et al., 2009).

M31 is currently at a distance of 785 kpc (McConnachie et al., 2005) but is approaching the Milky Way at $\sim 300\,\mathrm{km\,s^{-1}}$. It is thought that the two largest members of the local group will merge in ~ 4 billion years to form a giant elliptical galaxy (Sohn et al., 2012). M31 has many companion galaxies, including M32 and M110 (aka NGC 205) which are the two brightest and clearly visible in some of the images that follow. The warp that is visible in the disc of M31 is thought to be caused by one of these objects passing through it at some point in the past.

The SF law was determined previously for M31 (at a lower resolution than here) in Tabatabaei & Berkhuijsen (2010), who found a similar super-linear relationship between surface density of star formation from Hα and surface density of total gas to that found in Kennicutt (1998b) for whole galaxies. However, their result did not to take the clear SNR cut in SFR into account, with the majority of points appearing consistent with a steeper SF law. Other work (e.g. Bigiel et al., 2008) on the SF law uses a least squares bisector fit to avoid this problem but in this work I attempt to mitigate for this using another method (see 3.5.2 and Appendix B.3).

3.2 DATA

Our first method of tracing star formation uses *GALEX* (Martin & GALEX Team, 2005a) FUV and NUV observations of M31 (Thilker et al., 2005), along with warm dust emission seen in *Spitzer MIPS* 24 μm (Gordon et al., 2006) and stellar emission from *Spitzer IRAC* 3.6 μm (Barmby et al., 2006) (Figure 3.3).

Despite a plethora of observations of our nearest galactic neighbour, there was until recently a lack of data longward of ~ 170 μm apart from the low resolution ($\sim 40'$) *Diffuse Infrared Background Experiment* (*DIRBE*, Odenwald et al. 1998). The advent of the *Herschel Space Observatory* has allowed us to observe out to the cold dust dominated submillimetre (sub-mm) part of the spectrum to high resolution and sensitivity. The regime covered by *Herschel* is especially important as it probes the peak of the FIR SED allowing an accurate determination of both temperature and dust mass at small spatial scales throughout the galaxy.
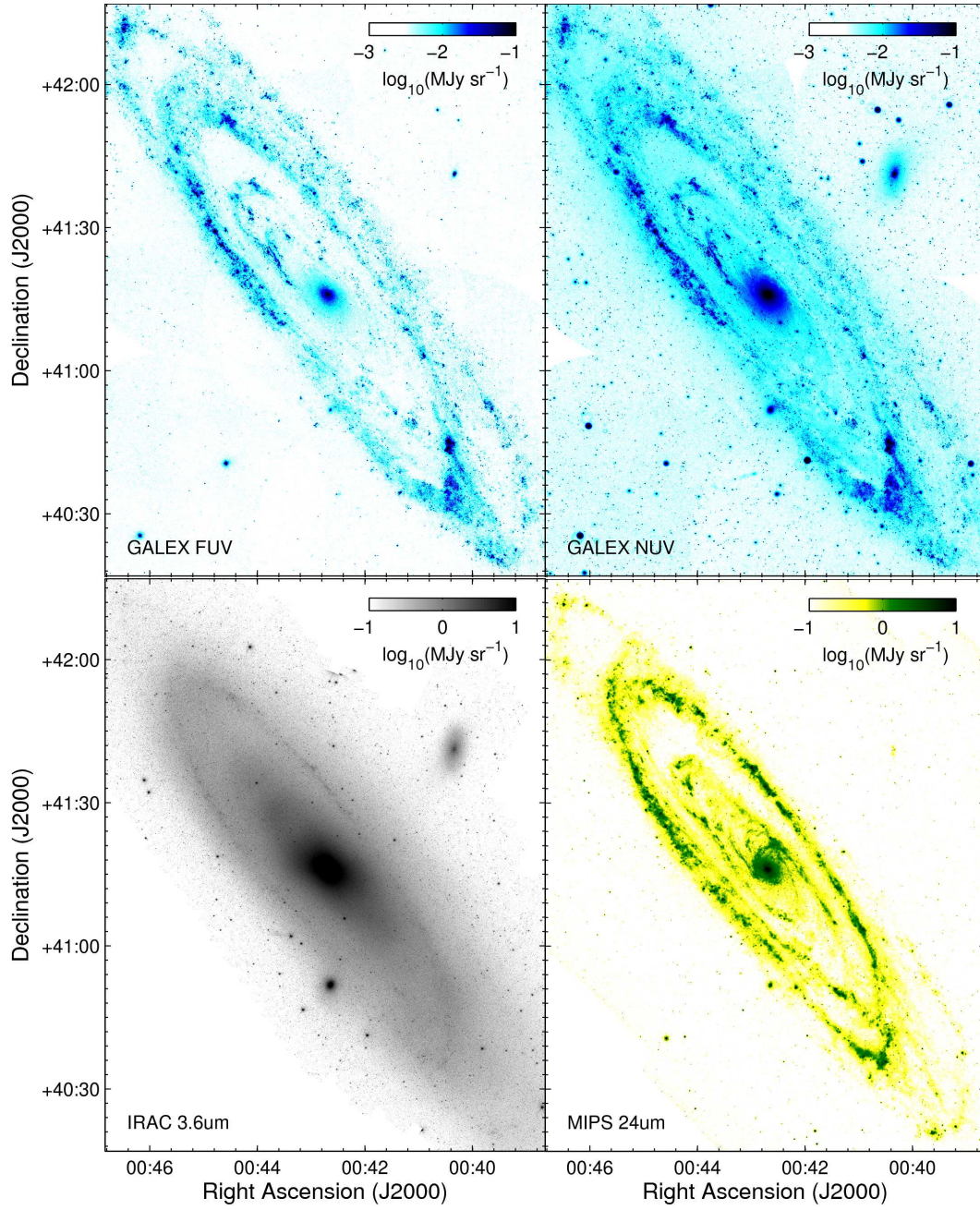
Figure 3.3 Images used in the creation of the FUV and 24 µm star formation maps of M31. From top left: *GALEX* FUV and NUV maps (Thilker et al., 2005); bottom, *Spitzer IRAC* 3.6 µm (Barmby et al., 2006) and *Spitzer MIPS* 24 µm (Gordon et al., 2006).

The HELGA collaboration obtained observations of M31 in five *Herschel* bands (Fritz et al., 2012). They are *PACS* (Poglitsch et al., 2010) 100 and 160 μm and *SPIRE* (Griffin et al., 2010) 250, 350 and 500 μm. Details of the data reduction for both *PACS* and *SPIRE* maps can be found in Fritz et al. (2012). The *Spitzer MIPS* 70 μm map (Gordon et al., 2006), is employed to extend the wavelength range for our calculation of the FIR spectral energy distribution (Figure 3.4).

We independently probe the interstellar medium using H I (Braun et al., 2009) and CO(J=1-0) maps (Nieten et al., 2006) (Figure 3.5). Note that the CO map covers a smaller area than the H I. The values for total gas surface density in the area not covered by the CO map will be the H I surface density only.

In this work, we also divide the maps into elliptical annuli of constant deprojected galactocentric radius. We do this to test the effect of radius on the star formation law, with the option to test this against the Toomre Q criterion, which relates to rotational velocity and shear. It also allows us to isolate the 10 kpc ring, where the majority of star formation in M31 is occurring; and the central regions which are dominated by an older stellar population. The colour coding of datapoints used in subsequent plots depends on their radial distance from the centre and is displayed in Appendix B.1 (Figure B.1). The ellipses are created assuming a position angle of M31 of 38° and an inclination of 77° (McConnachie et al., 2005). Distances are in units of the radius of M31, R_{M31} which we take to be 21.55 kpc (de Vaucouleurs et al., 1991) based on the apparent dimensions of the galaxy in visible light. We limit analysis to this radius to avoid any bright sources not associated with M31.

For analysis, the maps are individually smoothed and regridded to three pixel scales, based on the lowest resolution map used in the analysis. We modify the full-width half-maximum (FWHM) beamwidth to match the effective Point Spread Function (PSF) by Gaussian smoothing the image using the *IRAF* function *imgauss*. The maps are regridded using the IDL *astrolib* function, *FREBIN*. Any offsets in the coordinates of the pixels are corrected using *wcsmap* and *geotran* in *IRAF*.

The first scale used here is the highest resolution star formation map we can create using the FUV and 24 μm emission as a tracer. This corresponds to the lowest resolution (*MIPS* 24 μm) FWHM beamwidth of 6″ ($\sigma_{\mathrm{beam}} = 2.55$″) and a pixel size of 1.5″. This scale is applied to the 3.6 μm, 24 μm, NUV and FUV maps.

We aim to study the relationship between SFR and gas mass on the smallest scales attainable. To this end, we also use maps smoothed to the resolution and grid size of the neutral atomic hydrogen map, again the lowest resolution map used here. The effective FWHM beamwidth is 30″ ($\sigma_{\mathrm{beam}} = 12.7$″) with a 10″ pixel size. This scale is applied to the data mentioned above, with the addition of the
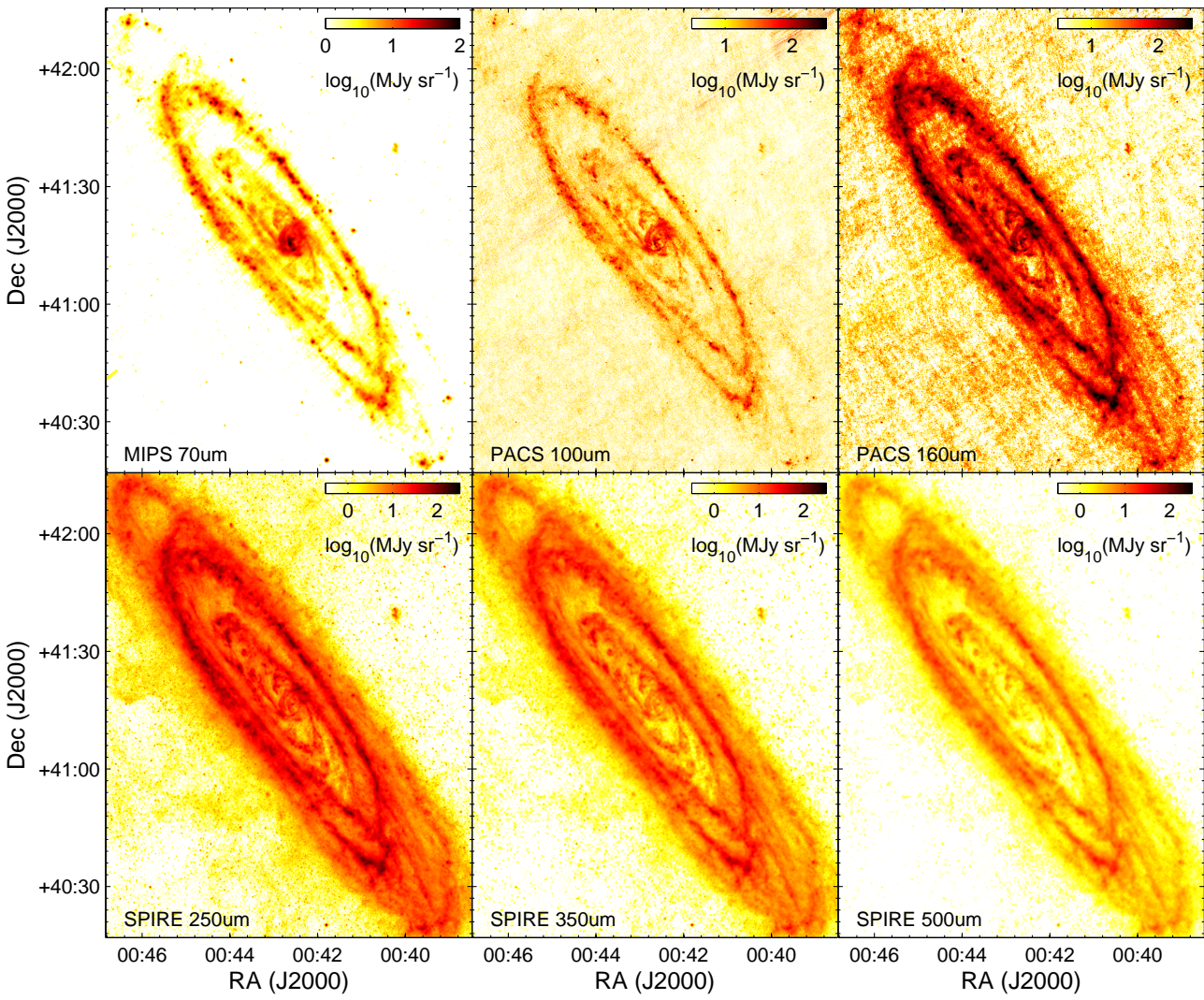
Figure 3.4 Top, from left (image orientation): *Spitzer MIPS* 70 μm (Gordon et al., 2006), *PACS* 100 and 160 μm (Fritz et al., 2012); bottom: *SPIRE* 250, 350 and 500 μm (Fritz et al., 2012). The *PACS* and *SPIRE* observations are from the HELGA collaboration.
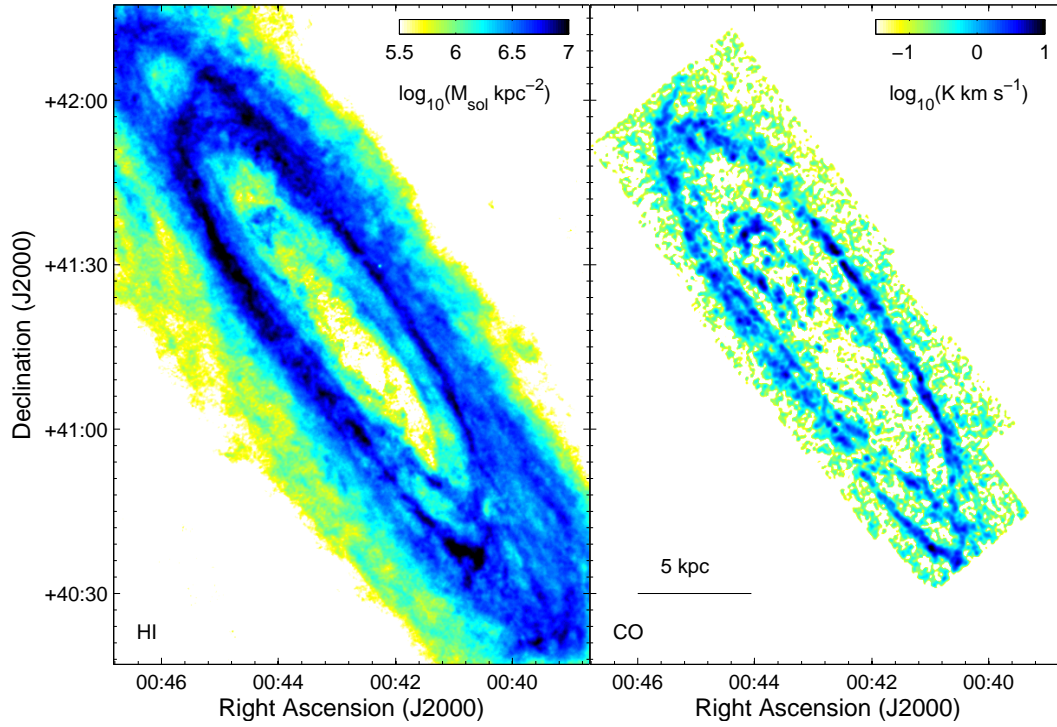
Figure 3.5 Left, integrated H I emission (Braun et al., 2009); right, CO(J=1-0) (Nieten et al., 2006).

CO(J=1-0) map.

In order to compare gas mass (from H I and CO(J=1-0)) and star formation in M31 (from FUV and 24 μm emission) with the *Herschel* observations, the majority of the analysis is performed on a scale corresponding to the beamsize of the lowest resolution SPIRE map (500 μm). These images have an effective FWHM beamwidth and are regridded to a grid size of $36''$ ($\sigma_{\mathrm{beam}} = 15.5''$), corresponding to a spatial scale at 785 kpc of $\sim$140 pc. This is done so that the beam area and pixel area are approximately equivalent, hence the pixels can be described as approximately 'independent,' as there is no correlation between them. Here, the *MIPS* maps (Figure 3.3, bottom left; Figure 3.4, top left) were smoothed using convolution kernels from Aniano et al. (2011) as used in Bendo et al. (2012b) and Smith et al. (2012a), due to the pronounced 'Airy rings' visible in the MIPS maps which these kernels take into account.

3.3   STAR FORMATION RATE

Whether looking at unobscured or embedded star formation, tracers invariably rely on the assumption that the emission used as a SF probe originates directly, or as a result of heating, from massive young stars (Calzetti, 2007). This is a reasonable

assumption in galaxies that have recently undergone a starburst, as massive young stars burn brightly and die young, with less massive stars living much longer and providing a minimal contribution to the UV luminosity. However, M31 has not undergone a starburst in at least 100 Myr (Olsen et al., 2006; Davidge et al., 2012) so contributions from older populations can have a significant effect on star formation estimates (Calzetti, 2013). This should, in principle, be possible to mitigate using tracers of the general stellar population.

3.3.1   FUV AND 24 μM

The star formation rate is first calculated from the *GALEX* FUV and *Spitzer* 24 μm maps, using the method prescribed in Leroy et al. (2008). However, to expand on this we also use *GALEX* NUV and *Spitzer IRAC* 3.6 μm maps to correct for foreground stars and emission from old stellar populations respectively.

FUV emission is dominated be emission from unobscured high-mass stars (O, B and A-type), so this tracer is sensitive to star formation on a timescale of ~ 100 Myr (e.g. Kennicutt, 1998a; Calzetti et al., 2005; Salim et al., 2007). 24 μm emission is predominantly due to dust-heating by UV photons from bright young stars, and is sensitive to a star formation timescale of <10 Myr (e.g. Calzetti et al., 2005; Pérez-González et al., 2006; Calzetti et al., 2007).

The SFR surface density is calculated using the formulation in Leroy et al. (2008) which uses a Chabrier (2003) initial mass function (IMF):

$$\Sigma_{\mathrm{SFR}} = 8.1 \times 10^{-2} \, I_{\mathrm{FUV}} + 3.2^{+1.2}_{-0.7} \times 10^{-3} \, I_{24}, \tag{3.1}$$

where Σ_{SFR} has units of $\mathrm{M_\odot \, yr^{-1} \, kpc^{-2}}$ and FUV and 24 μm intensity (I) are in $\mathrm{MJy \, sr^{-1}}$. The pixel size corresponds to a distance of ~ 140 pc. If comparing like for like with other galaxies, an inclination correction factor of $\cos i$ (where the inclination of M31, $i = 77°$) must be included in order to 'deproject' the image, effectively giving values as they would be for a face-on galaxy. This prescription assumes all the 24 μm emission in M31 is due to dust heating by newly formed stars, and that the FUV is emitted exclusively by young stars. There are, of course, other sources of these tracers which are unrelated to star formation which must be taken into account.

The first issue is foreground stars. These are selected and removed using the UV colour, as in Leroy et al. (2008) — if $I_{\mathrm{NUV}} / I_{\mathrm{FUV}} > 15$, the pixel is blanked in both the FUV and 24 μm map (some 24 μm emission will be stellar, e.g. Bendo et al. 2006). We assume this ratio will only be reached where a pixel is dominated by a

single star, which, given our resolution will never be associated with M31.

A second problem is that some of the emission could be from an older stellar population. This is a general problem and not specific to M31 (e.g. Kennicutt et al., 2009). We expect this to be a bigger issue near the centre of the galaxy as many galactic bulges have similar properties to elliptical galaxies, including dominance of old stars. This was indeed found to be the case for M31 in (Groves et al., 2012). Previous FIR work on M31 (Tabatabaei & Berkhuijsen, 2010) avoids this problem by measuring the SFR at radii greater than 6 kpc only, based on the assumption that the centre of the galaxy contains negligible star formation. Old stars are fainter but redder, so emit relatively stronger at 3.6 μm. This means we can mitigate for the old stars by determining $I_{\mathrm{FUV}} / I_{3.6}$ and $I_{24} / I_{3.6}$ in regions where we assume star formation has ceased (i.e. the bulge), and use this to remove the component of FUV and 24 μm emission coming from old stars. I define two new parameters,

$$\alpha_{\mathrm{FUV}} = I_{\mathrm{FUV}}^{\mathrm{B}}/I_{3.6}^{\mathrm{B}} \qquad \alpha_{24} = I_{24}^{\mathrm{B}}/I_{3.6}^{\mathrm{B}} \tag{3.2}$$

where the superscript B denotes the parameter as measured in the centre of the galaxy. So, the emission we associate with star formation is given by,

$$I_{\mathrm{FUV,SF}} = I_{\mathrm{FUV}} - \alpha_{\mathrm{FUV}} \, I_{3.6} \tag{3.3}$$

$$I_{24,\mathrm{SF}} = I_{24} - \alpha_{24} \, I_{3.6}. \tag{3.4}$$

Leroy et al. (2008) explored this by looking at the ratio of fluxes determined in elliptical galaxies. They found $\alpha_{\mathrm{FUV}} = 3 \times 10^{-3}$ and $\alpha_{24} = 0.1$. However, if we compare the 3.6 μm emission with the FUV and 24 μm in M31 (Figure 3.6), we see that these values are not necessarily appropriate here. The 24 μm emission in the bulge (shown by red points) follows the ratio found in ellipticals (black-dashed line, Figure 3.6, right panel), so we will use the same value for α_{24}. α_{FUV} is found to be much lower here (Figure 3.6, left panel). We speculate this is due to dust extinction in M31, which is not an issue in passive elliptical galaxies as they contain little dust (e.g. Smith et al., 2012b; Rowlands et al., 2012). It is also stated in Leroy et al. (2008) that there is a large scatter in this ratio so a discrepancy is not surprising. An independent correction is found by performing linear fits on the inner regions of M31 (see Appendix B.2). Ellipses within a radius 0.05, 0.1 and 0.2 R_{M31} give gradients (α_{FUV}) of 8.42×10^{-4}, 7.99×10^{-4} and 7.44×10^{-4} respectively. Here, the mean value, $\alpha_{\mathrm{FUV}} = 8.0 \times 10^{-4}$, will be employed to correct FUV emission for the old stellar population in M31. We performed this analysis on the high resolution maps to maximise the number of datapoints and checked that the slope was consistent with
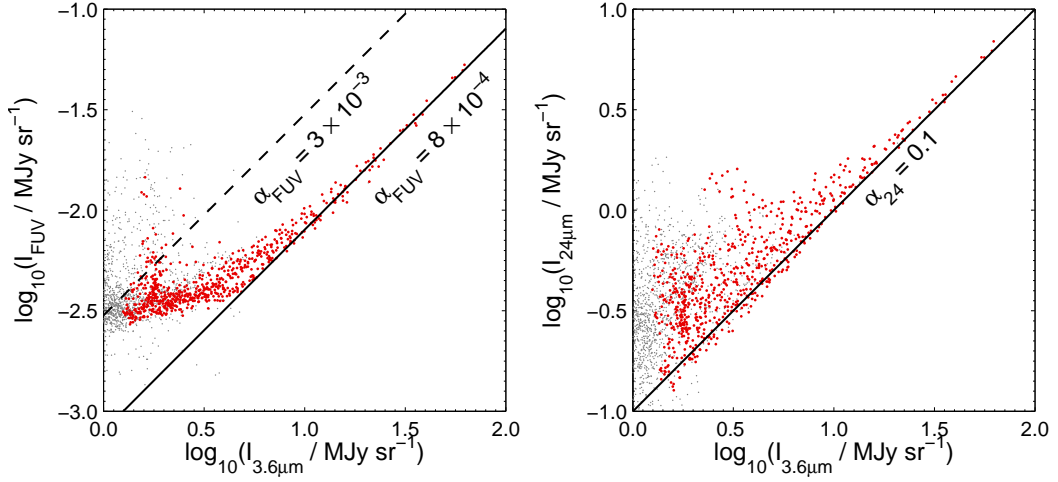
Figure 3.6 FUV (left) and 24 µm (right) vs 3.6 µm emission. The red points are those that within $0.2 \times R_{M31}$ (see Appendix B.1, Figure B.1). The black dashed trendline in the left plot indicates the correction for the old stellar population used in Leroy et al. (2008), based on $I_{FUV}/I_{3.6}$ found in ellipticals. The solid trendline is the best fit to FUV vs 3.6 µm in the inner regions of M31 ($r < 0.1\,R_{M31}$). The solid trendline in the right plot is the best fit to 24 µm vs 3.6 µm in the inner regions. This agrees with the Leroy et al. (2008) value.

that found using the lowest resolution ($36''$) maps.

Once this correction is applied, we have a map of surface density of star formation, Σ_{SFR} in units of $M_\odot\,yr^{-1}\,kpc^{-2}$ (Figure 3.7). The correction in this work has the effect of reducing the measured global SFR from $0.33^{+0.08}_{-0.05}\,M_\odot\,yr^{-1}$ to $0.25^{+0.06}_{-0.04}\,M_\odot\,yr^{-1}$ (a reduction of $\sim 25\%$). This is consistent with the lower limit of $\sim 0.27\,M_\odot\,yr^{-1}$ found in Tabatabaei & Berkhuijsen (2010) for M31.

It should be noted that when looking at the region immediately outside the 10 kpc ring only (see Appendix B.2), we see a tight correlation between the FUV and 3.6 µm emission. Unlike the centre, however, there are pixels in that region that do not follow this correlation. This indicates that despite a significant population of old stars in the ring, star formation is still occurring at significant rates compared to the rest of the galaxy ($\sim 0.2\,M_\odot\,yr^{-1}$).

For analysis of the star formation law (Section 3.5), this star formation map is masked such that all pixels satisfy $\Sigma_{SFR} > 5\,\sigma_{SFR}$, where σ_{SFR} is the standard deviation of the background, measured separately for each pixel scale.

3.3.2   STAR FORMATION FROM FAR-INFRARED LUMINOSITY

Star formation can also be calculated using the total FIR luminosity, often for more infrared-bright distant galaxies. This ideally probes the embedded SFR and is sen-

sitive to cooler dust temperatures. This can be an issue in determining total SFR in dust-deficient galaxies where significant starlight is not attenuated by dust but is not expected to be a problem here as the dust mass in M31 is comparable to that of other nearby spirals (see Chapter 2) with $M_{\mathrm{d}} \sim 10^{7.4}\,\mathrm{M_\odot}$ (Smith et al., 2012a). It also appears to have a significant presence in the ring where the majority of star formation is occurring. An issue that is relevant to M31 is that a significant component of the dust heating could be from an evolved stellar population (e.g. Bendo et al., 2010; Boquien et al., 2011; Bendo et al., 2012b; Smith et al., 2012a).

The total FIR flux was integrated in frequency space using a linear interpolation between the six datapoints (70–500 μm) for each pixel independently. Each value was converted from a flux to a luminosity in $\mathrm{L_\odot}$ assuming a distance to M31 of 785 kpc (McConnachie et al., 2005).

If we assume FIR luminosity is exclusively re-radiated emission from warm dust that is heated during a continuous starburst, the FIR luminosity is equal to the total luminosity of the starburst. The total SFR is then (taken from Telesco, 1988),

$$\mathrm{SFR} = \delta_{\mathrm{MF}}\ (L_{\mathrm{FIR}}/10^{10}\mathrm{L_\odot})\ \ \mathrm{M_\odot yr^{-1}}\ , \tag{3.5}$$

where δ_{MF} depends on the assumed IMF of the region being studied and the timescale of the starburst. Changing these assumptions gives significantly different conversion factors. For example, assuming a Kroupa (2001) IMF with a star formation timescale of 10 Gyr gives $\delta_{\mathrm{MF}} \sim\ 0.6$ whereas the same IMF with a timescale of 2 Myr gives $\delta_{\mathrm{MF}} \sim\ 3.2$ (Calzetti, 2013). L_{FIR} is defined here in the range 8-1000 μm, but in M31 I argue that L_{FIR} due to re-radiated emission from dust is dominated by emission longward of 70 μm (see Smith et al., 2012a), so integrating fluxes from 70 to 500 μm should be a reasonable estimate. There is also the problem of stellar emission starting to have an effect shortward of 70 μm which is mitigated here.

Here we employ the value for δ_{MF} of 1.1, equivalent to the value quoted in Kennicutt (1998b) of 1.7, reduced by a factor of 1.59 (equivalent to the difference quoted in Table 1.1, $\dot{M}_* / \dot{M}_{*,\mathrm{K98}}$) to approximate a Chabrier (2003) IMF with a low mass cut-off of 0.1 $\mathrm{M_\odot}$ and a SF timescale of $\sim$100 Myr, as assumed for the UV and 24 μm tracer. We should state here that this assumes a continuous starburst which keeps consistency with the previous method. This conversion factor gives a global star formation rate of 0.33 $\mathrm{M_\odot\ yr^{-1}}$, higher than the estimate for the FUV and 24 μm tracer but without a correction for old stars.

If, as before, the old stellar population has a significant effect on the dust heating at these wavelengths, we would naively expect to see a correlation between the FIR

luminosity and 3.6 μm emission. However, the total FIR luminosity is a function of dust mass and dust temperature, so if the distribution of dust is different to the distribution of stars (as it is in M31, Smith et al. 2012a) there will be no correlation, even if the old stars are the major heating source (Bendo et al., 2012b). This was tested by comparing our six FIR bands to 3.6 μm emission as in Figure 3.6 and no correlation is visible for any of the FIR bands used.

Without any kind of correction for the old stars, the star formation rate from the FIR emission is measured to be approximately 50 % greater than the estimate from the FUV and 24 μm tracers (Section 3.3.1). This significant discrepancy is due to M31 not having gone through a starburst in its recent history, so a significant portion of the heating is due to the interstellar radiation field (ISRF).

As discussed in the previous section, past work on M31 elected to omit the central region of the galaxy when determining the global SFR, due to the dominance of old stars in this region. If we omit the central region out to $0.2 \, R_{M31}$ the measured SFR reduces from $0.33 \, M_\odot \, yr^{-1}$ to $0.30 \, M_\odot \, yr^{-1}$. This minimal difference suggests that the over-estimate is not limited to heating from old stars in the bulge. This is consistent with the correlation observed between 3.6 μm emission and 24 μm in the ring (Section 3.3.1 and Figure B.3, Appendix B.2), indicating old stars have a significant heating effect here also.

3.3.3 COMPARISON OF STAR FORMATION TRACERS

The star formation maps made using FUV and 24 μm emission, and that from FIR luminosity can be seen in Figure 3.7. The FUV and 24 μm tracer has units of $M_\odot \, yr^{-1} \, kpc^{-2}$, but we have elected to display the FIR star formation tracer in terms of FIR luminosity as the conversion factor between luminosity and SFR is very uncertain and the central regions are likely to be dominated by heating from old stars.

Sub-mm wavelengths are more greatly affected by heating due to the ISRF than the 24 μm emission, as this regime is sensitive to cooler dust temperatures. This means the FIR emission is susceptible to heating from more distant stars (those that are not in the same pixel), making determination of a correction factor difficult (Section 3.3.2). In order to compare the two SFR tracers, we use the FUV and 24 μm tracer uncorrected for an old stellar population. This gives a global SFR of $0.32 \, M_\odot \, yr^{-1}$, consistent with the value from FIR luminosity.
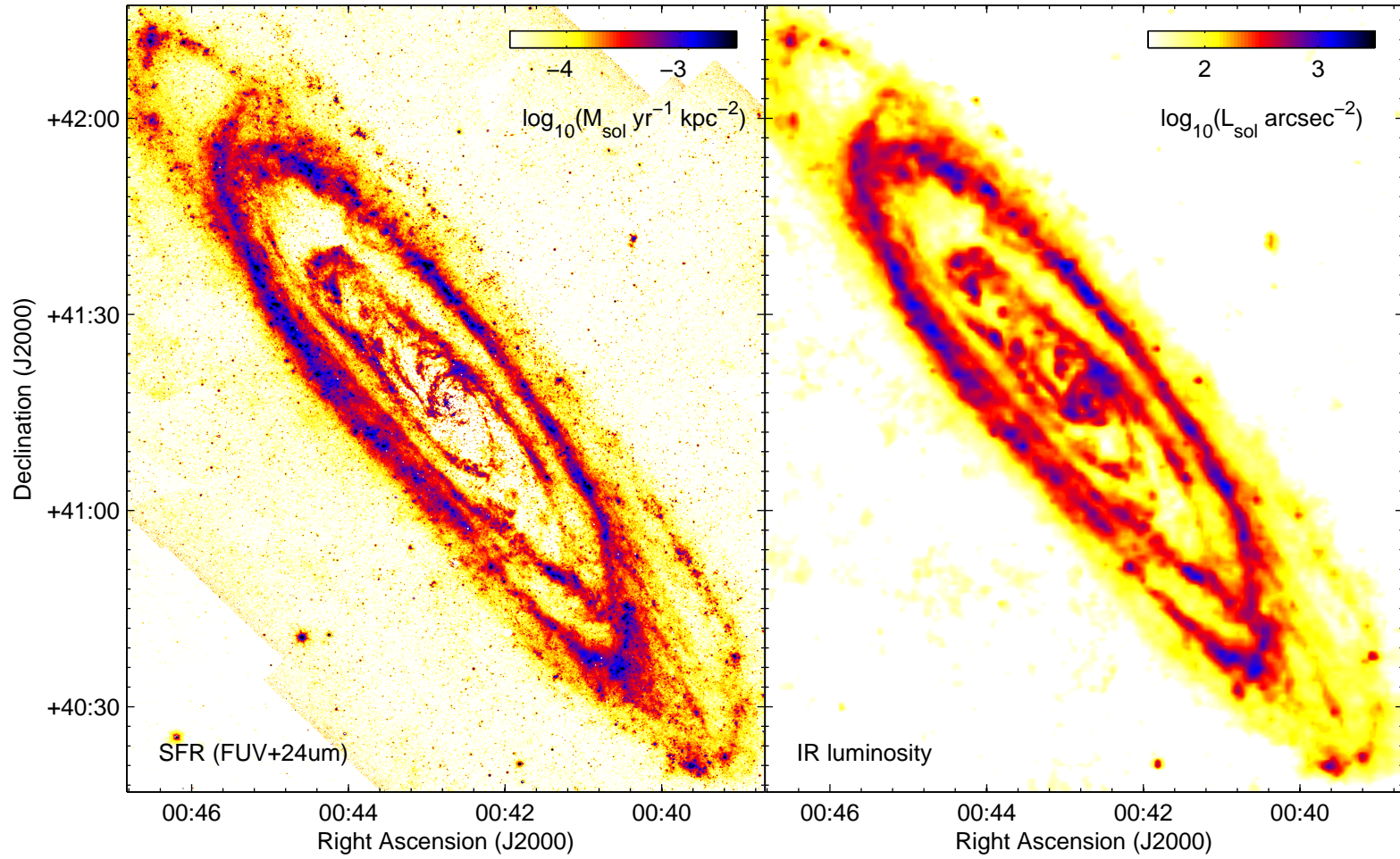
Figure 3.7 Left, star formation rate map obtained using the FUV and 24 μm emission (FWHM beamwidth = 6″, pixel size = 1.5″); right, total FIR luminosity at $\lambda > 70\,\mu\text{m}$ (FWHM beamwidth and pixel size = 36″), found by integrating the emission from *Herschel* and *Spitzer* observations shown in Figure 3.4. The SFR from infrared luminosity is found using a constant conversion factor based on the assumed IMF and assumed length of the continuous starburst.
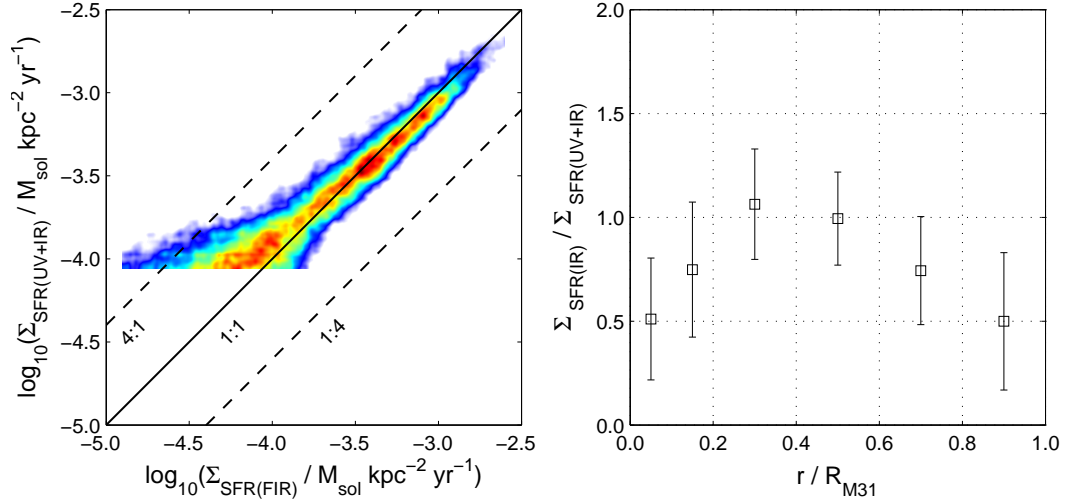
Figure 3.8 Left: Σ_{SFR} (star formation rate surface density) found from FIR luminosity (assuming a Salpeter (1955) IMF) vs Σ_{SFR} from FUV and $24\,\mu\mathrm{m}$ emission (scaled to match values assuming a Salpeter IMF and without a correction for the old stars). The colours indicate the density of datapoints. The solid black line indicates a 1:1 relationship, the dashed black lines are factors of 4 offset. Right: ratio of Σ_{SFR} from FIR luminosity to Σ_{SFR} from FUV + $24\,\mu\mathrm{m}$ star formation surface density with radius. The errorbars represent one standard deviation of the distribution of this value across each elliptical annulus.

It does appear that the SFR as measured from FIR luminosity is slightly lower relative to the FUV and $24\,\mu\mathrm{m}$ tracer in the very centre and outer regions of M31 (Figure 3.8, right). There is a possible issue with *PACS* observations not recovering all of the flux in low surface brightness regions (e.g. Aniano et al., 2012). If this was the case, it may contribute to the variations in $\Sigma_{\mathrm{SFR,IR}} / \Sigma_{\mathrm{SFR,UV+IR}}$ between annuli observed in Figure 3.8, but our global SFR will be minimally affected. We do not believe this discrepancy is a major issue here as this map is not used in any further resolved analyses of low surface brightness regions.

Despite the general consistency between SFR tracers, we should remain aware that since the conversion factor between tracer luminosity and star formation rate depends on the IMF, we are not necessarily recovering the correct value. It is possible that the IMF we assumed for M31 is not appropriate, or, because the star formation rate is low and the pixel area small, we are not sampling the whole IMF leading to fluctuations in the tracer luminosity for a fixed SFR. This can be an issue for a variety of tracers, including IR and UV emission (Kennicutt & Evans, 2012).

For the analysis that follows, we elected to use the combined FUV and $24\,\mu\mathrm{m}$ emission as our star formation tracer, as we are able to correct for the old stellar population. We argue that this gleans more reliable SFRs in low SFR regimes, like those in M31, than when using the FIR luminosity.

3.4   THE INTERSTELLAR MEDIUM IN M31

The interstellar medium (ISM) is made of predominantly neutral atomic and molecular hydrogen. A map of total gas can be produced by summing these two constituents and multiplying by a factor of 1.36 to account for heavier element abundances (mostly Helium), or alternatively by assuming the total gas is well traced by dust emission (e.g. Eales et al., 2012).

3.4.1   TOTAL GAS FROM H I AND CO OBSERVATIONS

The H I map is taken from Braun et al. (2009). In order to keep consistency with our maps of star formation, and to allow comparison of galaxies with different inclinations, i, I employ a factor of $\cos i$ to 'deproject' the galaxy.

H_2 is the most abundant molecule in the ISM, but lacks a dipole moment so is not easily observable. For this reason, the next most common molecule, CO (usually J=1-0) is employed as a tracer. For M31 we use the map from Nieten et al. (2006). The conversion between CO emission and quantity of H_2 is still a contentious topic and uses the so-called X_{CO}-factor (e.g. Wall, 2007; Glover & Mac Low, 2011; Narayanan et al., 2011; Feldmann et al., 2011; Bolatto et al., 2013), where:

$$N_{H_2}/\mathrm{cm}^{-2} = X \times I_{CO}/\mathrm{K\,km\,s}^{-1} \qquad (3.6)$$

The conversion factor specific to molecular clouds in the north eastern arm of M31 was argued to be $5.68 \times 10^{20}\,(\mathrm{K\,km\,s}^{-1})^{-1}\,\mathrm{cm}^{-2}$ in Sofue et al. (1994). This was found by estimating virial masses (from their size and velocity width) and comparing to the CO line intensity. This is larger than the value found by Bolatto et al. (2008) of $\sim 4 \times 10^{20}\,(\mathrm{K\,km\,s}^{-1})^{-1}\,\mathrm{cm}^{-2}$ using the same method. However, the ISM of M31 is dominated by neutral atomic hydrogen so it is likely the virial masses provide an overestimate of the mass of molecular hydrogen in these clouds. Here I will assume $X_{CO} = 2 \times 10^{20}\,(\mathrm{K\,km\,s}^{-1})^{-1}\,\mathrm{cm}^{-2}$ (e.g. Strong et al., 1988; Pineda et al., 2010), which agrees with the value derived in Smith et al. (2012a). Any constant discrepancy in the X_{CO}-factor will result in a horizontal translation in our $\log_{10}\Sigma_{H_2}$ versus $\log_{10}\Sigma_{SFR}$ plots and so will have no effect on the calculation of our K-S index for molecular gas. It may skew the calculation using total gas but the effect is likely to be small due to the dominance of H I in the ISM of M31. This will be explored later.

At this point we should note the suggestion that metallicity also has an effect on the X_{CO}-factor (e.g. Israel, 1997; Strong et al., 2004; Sandstrom et al., 2013).

Smith et al. (2012a) found a radial variation in the gas-to-dust ratio suggesting a metallicity gradient in M31 and hence a gradient in X_{CO}. Any variation should not be a big issue when looking at total gas, as the ISM in M31 is dominated by neutral atomic hydrogen, but may affect the star formation law with molecular gas only.

3.4.2 TOTAL GAS TRACED BY DUST

The interstellar gas can, in principle, also be traced by the distribution of dust in a galaxy (Eales et al., 2012). As dust drives the gravitational collapse of gas clouds and can act as a site for formation of molecular hydrogen (van de Hulst, 1948) it is arguably a better tracer of star forming regions than diffuse gas.

The dust map of M31 is taken from Smith et al. (2012a), where dust mass is found by fitting a modified blackbody function (Equation 1.3) in each pixel where there is a $5\,\sigma$ detection in all six bands (70-500 μm, Figure 3.4). This should mitigate against the low-surface brightness issues discussed in Section 3.3.3. In contrast to the previous chapter, here the emissivity index β is treated as a free parameter.

In Smith et al. (2012a) a fit was performed to gas-to-dust vs radius, to determine how the conversion factor between dust and total gas varies. It was found that the relationship is linear when plotting $\log_{10}\left(\Sigma_{\mathrm{Gas}}/\Sigma_{\mathrm{SFR}}\right)$ with radius varying between $\sim$30 near the centre and $\sim$100 in the 10 kpc ring, consistent with the value found in the Milky Way (Spitzer, 1978). This analysis is reproduced in Figure 3.9. We use the function found from a linear least squares fit to data in the right panel of Figure 3.9 to create a second total gas map as traced by dust. In the following
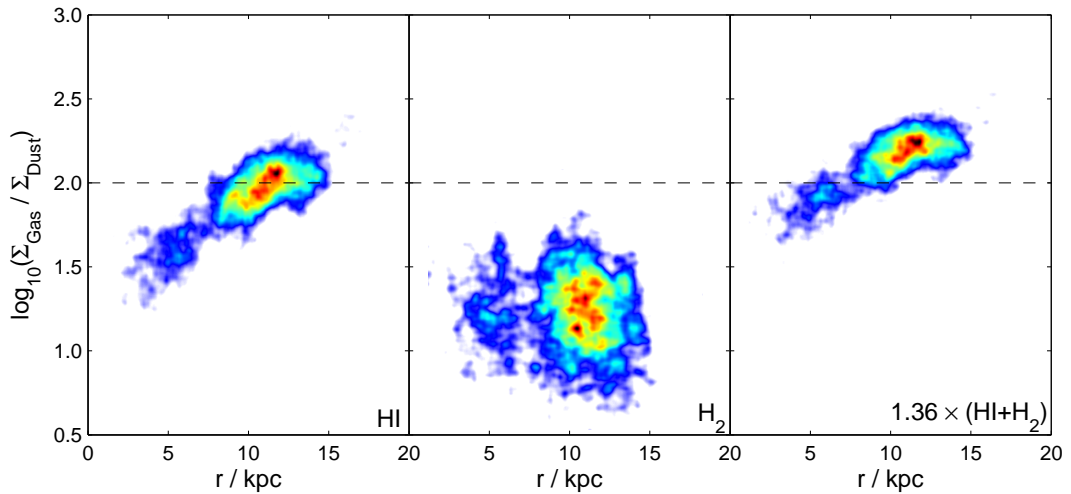
Figure 3.9 Gas to dust ratio with radius in M31 for monatomic hydrogen (H I), molecular hydrogen (H$_2$) and total gas (H I + H$_2$) with a factor of 1.36 for heavier element abundances. Colours indicate the density of datapoints.

section, as with the other ISM tracers, this will be used to observe how well dust mass correlates with star formation.

3.5 THE STAR FORMATION LAW

In this section, I probe the star formation or K-S law assuming the following relationship,

$$\Sigma_{\mathrm{SFR}} = A\,\Sigma_{\mathrm{Gas}}{}^{N}, \qquad (3.7)$$

where N is the power index and A is related to the star formation efficiency (SFE).

Many recent studies support a linear star formation law with molecular gas. This implies a constant gas depletion time, $\tau_{dep} = \Sigma_{\mathrm{Gas}} / \Sigma_{\mathrm{SFR}}$. Here I look at variation in this parameter with radius and gas tracer.

I separately look at how M31 compares to other local galaxies in terms of global SFR surface density (calculated from FUV and $24\,\mu\mathrm{m}$ emission) and gas surface density; and what relationship the star formation law follows on a pixel-by-pixel basis when considering various components of interstellar material.

3.5.1 GLOBAL STAR FORMATION LAW

Figure 3.10 compares the mean surface density of star formation rate with the mean surface density of gas for global measurements of galaxies from Kennicutt (1998b) and Leroy et al. (2008), with corresponding global values for M31 overplotted. The SFRs from this paper and Leroy et al. (2008) are scaled to match the assumptions made in Kennicutt (1998b) (i.e. a Salpeter (1955) IMF). The mean values for M31 are found over all pixels with sufficient signal-to-noise in both maps (SFR and gas). The difference in measured SFR is due to the different selection effects depending on the gas tracer, i.e. the regions with sufficient signal-to-noise in the dust and molecular gas mass maps have, on average, a higher SFR surface density than those with sufficient total gas, including H I.

The low gas surface density galaxies ($\Sigma_{\mathrm{Gas}} < 100\,\mathrm{M_\odot\,pc^2}$) studied by Kennicutt (1998b) generally appear to have higher star formation rates than M31, although we note that they estimate star formation using a different SF tracer. However, early-type spirals like M31 are expected to exhibit a low SFR per unit area, as stated in Kennicutt (1998a). Mean surface densities of both total and molecular gas are consistent with the same parameters for normal spirals studied in previous work.

When comparing the different gas tracers in M31 (Figure 3.10), we can immediately see that the mean SFR for regions containing sufficient H$_2$ ($I_{\mathrm{CO}} > 5\,\sigma_{\mathrm{CO}}$) or
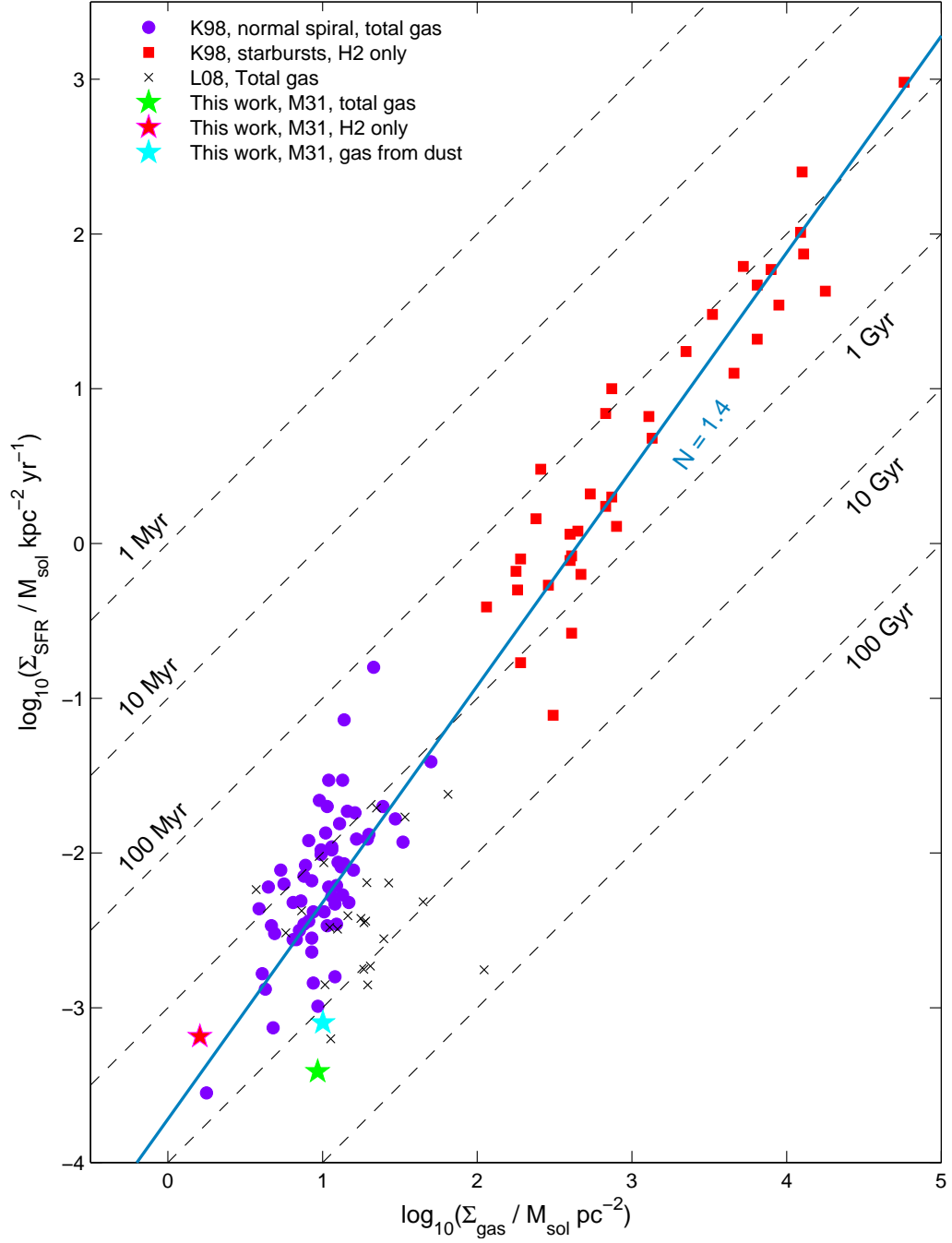
Figure 3.10 Global SFR vs gas mass, derived in M31 using three gas tracers, with Kennicutt (1998b) and Leroy et al. (2008) galaxies. Galaxies are plotted using total gas where possible or H_2 as traced by CO only, depending on availability of data. SFRs from this work and Leroy et al. (2008) are scaled to match the assumptions of Kennicutt (1998b). The dashed diagonal lines are of constant gas depletion time, τ_{dep}. The solid blue line is the gradient the galaxies should follow given a Schmidt law of the type found in Kennicutt (1998b) where $N = 1.4$.

dust ($I > 5\,\sigma$ in five *Herschel* bands) is higher, suggesting a better spatial correlation between SFR and both molecular hydrogen and dust than total gas. These regions are also more efficient, with gas depletion times measured to be $\langle \tau_{\mathrm{dep}}^{\mathrm{H_2}} \rangle \sim 4\,\mathrm{Gyr}$ and $\langle \tau_{\mathrm{dep}}^{\mathrm{Gas(Dust)}} \rangle \sim 20\,\mathrm{Gyr}$ compared to $\langle \tau_{\mathrm{dep}}^{\mathrm{Gas}} \rangle \sim 50\,\mathrm{Gyr}$.

3.5.2   RESOLVED STAR FORMATION LAW

From our gas and SFR maps, we should be able to investigate the Kennicutt-Schmidt star formation law, on a 'per pixel' basis across the galaxy. This section aims to test how calculation of this law changes with different gas tracers. It has been suggested that H_2 is a better tracer of star formation than total gas (e.g. Bigiel et al., 2011), although it is not clear if this is the case in M31 where H I dominates the ISM.

Here surface density of star formation as found from FUV and 24 μm emission is plotted against surface density of total gas, molecular hydrogen only and gas traced by dust. Selected pixels must satisfy $\Sigma_{\mathrm{SFR}} > 5\,\sigma_{\mathrm{SFR}}$ and $\Sigma_{\mathrm{Gas}} > 5\,\sigma_{\mathrm{Gas}}$, where σ_{SFR} is the standard deviation of the background of the star formation map and σ_{Gas} is a combination of the uncertainties of the constituent gas maps (e.g. for total gas this will be the scaled uncertainties in the integrated H I and CO(J=1-0) images).

I perform a linear fit in order to find the index, N from equation 3.7, assuming that

$$\log_{10} \Sigma_{\mathrm{SFR}} \propto N \log_{10} \Sigma_{\mathrm{Gas}}. \tag{3.8}$$

In Figure 3.11, the signal-to-noise (S/N) cuts are clearly manifest. In total gas, the major cut-off is horizontal (limited by σ_{SFR}); in molecular gas the cut is vertical (limited by $\sigma_{\mathrm{H_2}}$). Previous work appears to exhibit a similar cut-off (e.g. Tabatabaei & Berkhuijsen, 2010) but with no attempt to mitigate for this when performing a fit. After some exploration I conclude that the signal to noise cut does indeed bias the data and must be mitigated against. I test other methods of fitting and find that binning the data in order of increasing star formation gives the most reliable return gradient when testing the relationship to total gas (see Appendix B.3).

We therefore attempt to mitigate for the S/N cut in our data using the same method. When looking at the total gas from H I and CO measurements, we order in bins of increasing SFR, with an equal number of datapoints (500) in each. We then plot the mean surface density of gas (Σ_{Gas} / $M_\odot\,\mathrm{kpc}^{-2}$) in each bin, against the mean surface density of SFR (Σ_{SFR} / $M_\odot\,\mathrm{yr}^{-1}\,\mathrm{kpc}^{-2}$) and perform the fit on these points in the logarithmic domain using a least squares routine in *MATLAB*.

In the case of H_2 only, the S/N cut-off is more apparent in gas mass so I bin the
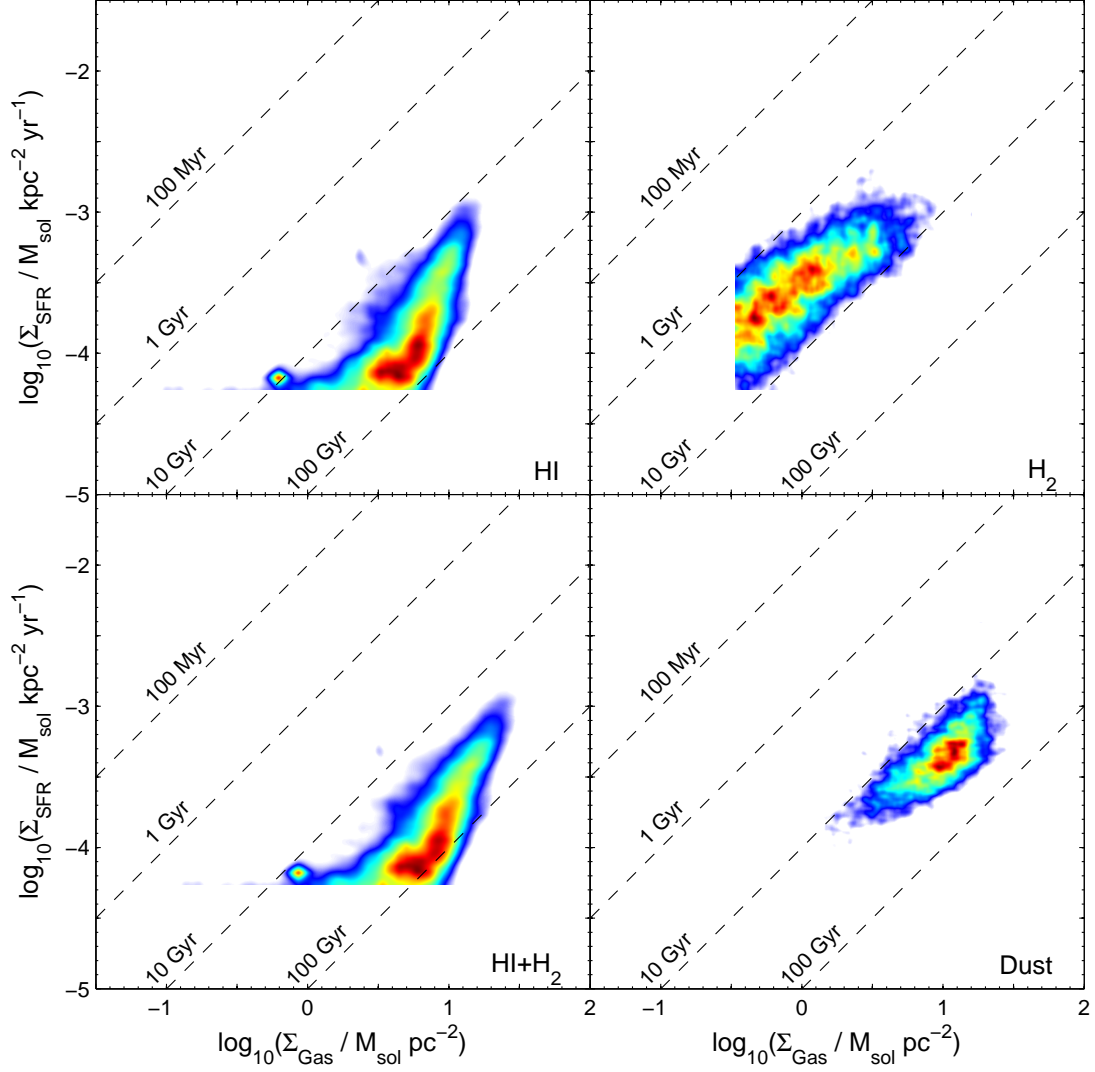
Figure 3.11 Star formation rate surface density against gas surface density in M31 for different gas tracers. From top left, they are H I only, molecular gas measured from H_2 as traced by CO(J=1-0), assuming a CO-H_2 conversion factor of $2 \times 10^{20} (K\,km\,s^{-1})^{-1}\,cm^{-2}$, with an additional factor of 1.36 for heavier element abundances; bottom, total gas from H I and H_2 and total gas traced by dust mass (see Smith et al., 2012a), assuming a radial gradient in the gas-to-dust ratio. The colour represents the density of datapoints. Dashed lines are of constant gas depletion time τ_{dep}.
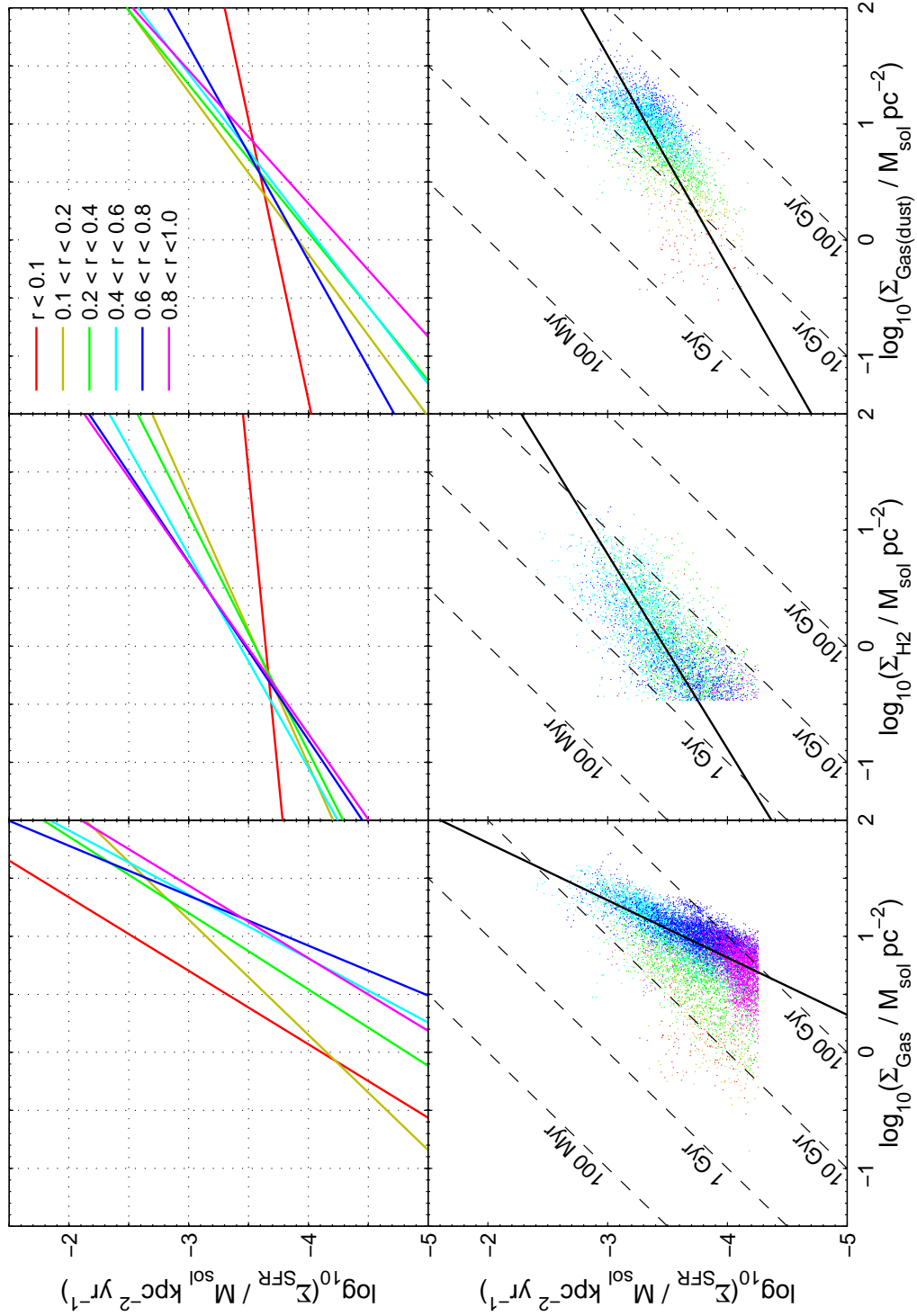
Figure 3.12 Star formation rate surface density against gas surface density split by galactocentric radius across M31. Each column covers one gas tracer. From left (image orientation), they are total gas from HI and CO(J=1-0), molecular gas from CO(J=1-0) only, and total gas traced by dust. The top row (image orientation) shows the fit to a power law for each radial annulus; the bottom row shows all pixels, colour coded by radius.
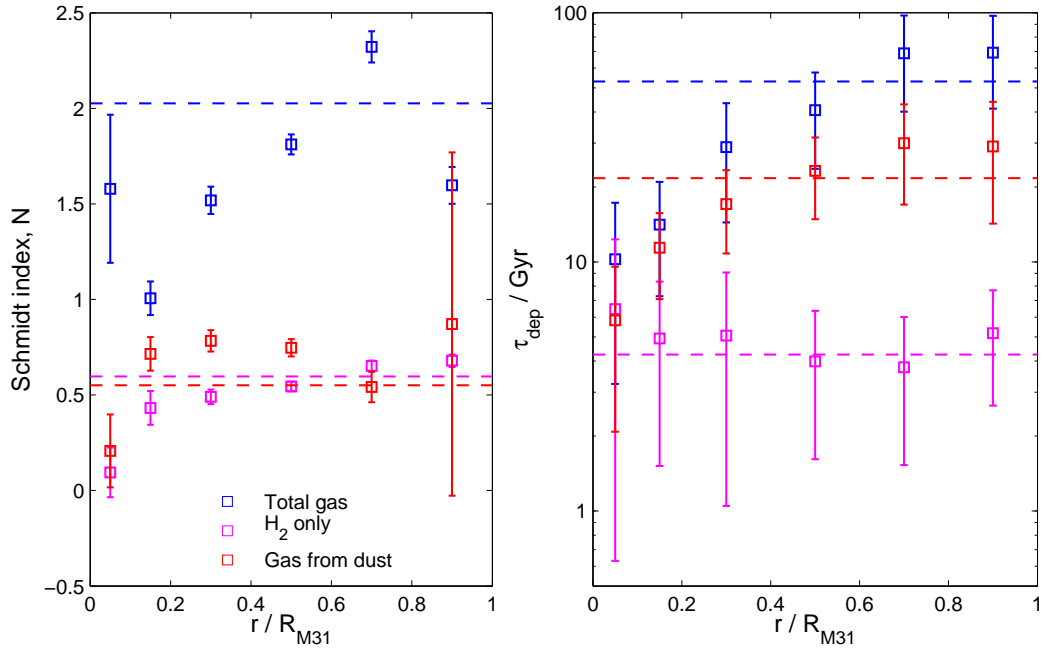
Figure 3.13 Kennicutt-Schmidt parameters with radius across M31. We compare the power law indices, N (left) and mean gas depletion time (τ_{dep}, right) using $H_I + H_2$, H_2 only and total gas mass traced by dust. The dashed lines indicate the global values for M31. Errorbars represent the $2\,\sigma$ uncertainty in N and the standard deviation in the distribution of τ_{dep}.

data in order of increasing gas mass, with 100 points in each bin.

Gas mass estimated from dust mass exhibits a more complex selection effect so binning is not attempted here. The majority of the points that are omitted correspond to points that appear towards the low-SFR regime of the bottom-left window in Figure 3.11. This will affect our calculation of the SF law but we believe the analysis is still valid as we are preferentially selecting regions that are more important for star formation.

Figure 3.11 shows plots of surface densities of SFR versus gas mass (the latter in units of $M_\odot\,\text{pc}^{-2}$, to keep consistency with previous work) for four tracers of the ISM (H_I only, $H_I + H_2$, H_2 only and total gas traced by dust mass), on a pixel-by-pixel basis. Fits to the star formation law across the whole galaxy can be seen in the bottom row of Figure 3.12, where Σ_{SFR} vs Σ_{Gas} is plotted for three ISM tracers (H_I only is omitted). Trendlines for each radial annulus (see Figure B.1 in Appendix B.1) are shown on the top row. Figure 3.13 shows K-S index and gas depletion time ($\tau_{\text{dep}} = \Sigma_{\text{Gas}}/\Sigma_{\text{SFR}}$) as a function of radius (using the same annuli) for the various gas tracers. In this plot, the global mean values are indicated by a dashed line of the same colour.

The K-S index for each annulus varies between 1.0 and 2.3 when considering
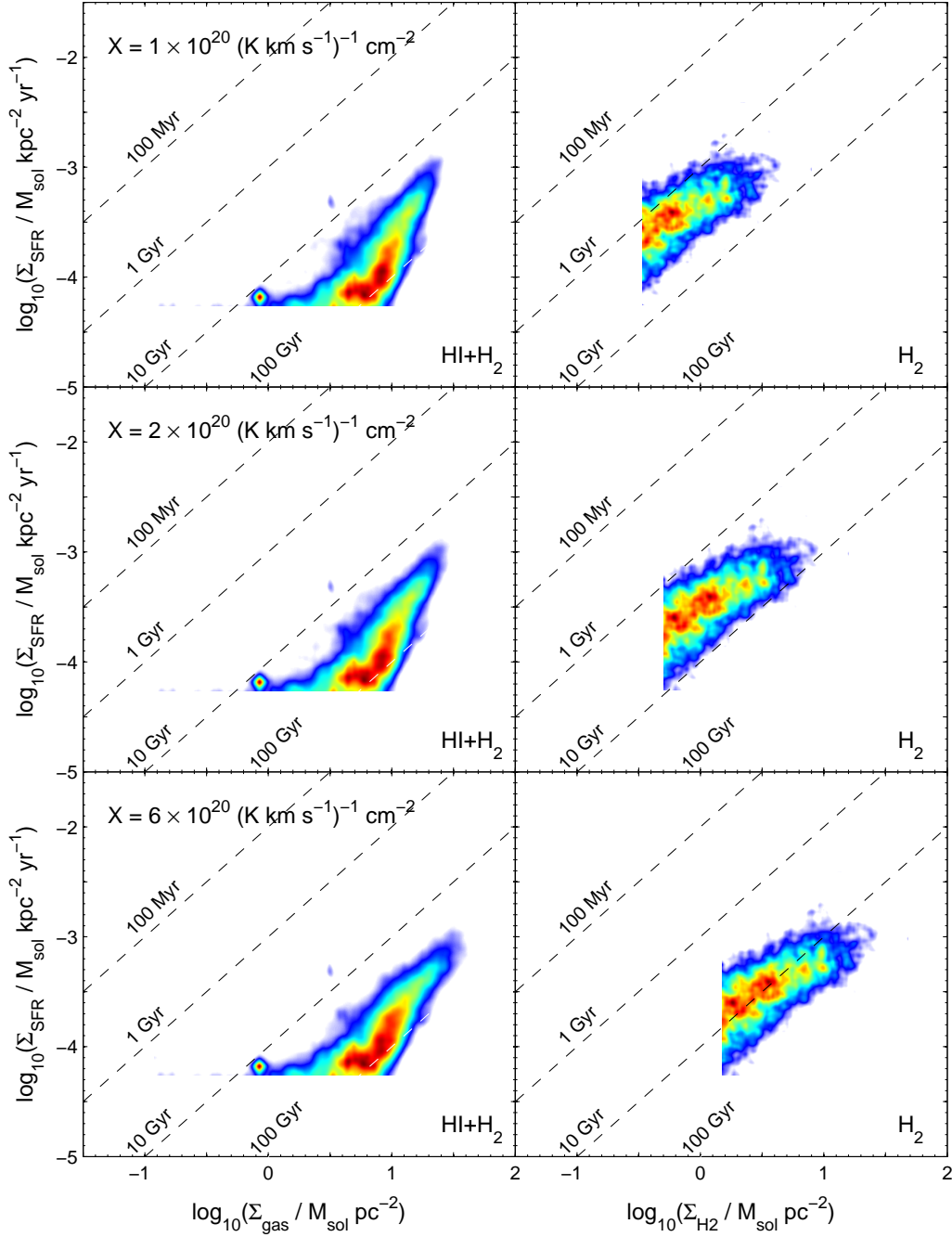
Figure 3.14 Star formation rate surface density against gas surface density in M31 for total gas and H_2 only assuming different CO-to-H_2 conversion factors. The left column shows total gas; the right, molecular hydrogen only. X-factor increases from top to bottom. The colour represents the density of datapoints. Dashed lines are of constant gas depletion time, τ_{dep}.
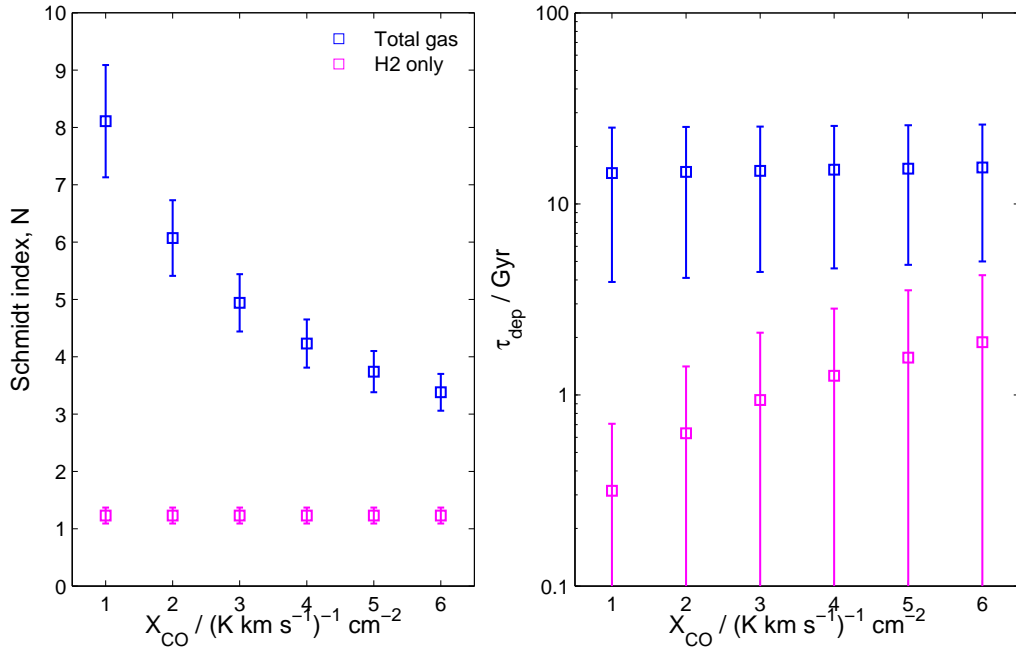
Figure 3.15 Kennicutt-Schmidt parameters with X_{CO} for M31. We compare the power law indices, N (left) and mean gas depletion time (τ_{dep}, right) using $H\,I + H_2$ and H_2 only. Errorbars represent the $2\,\sigma$ uncertainty in N and the standard deviation in the distribution of τ_{dep}.

total gas, with the higher values applying to the $10\,kpc$ ring. The global value for total gas is $N \sim 2.0$.

The star formation law with H_2 gives a shallower gradient ($N = 0.6$) but is more constant between annuli. Doing the same with gas traced by dust gives a similarly shallow slope.

CO-TO-H_2 CONVERSION FACTOR

The star formation law with total gas and H_2 assuming CO-to-H_2 conversion factors (X_{CO}) of 1, 2 (the nominal value) and $6 \times 10^{20}\,(K\,km\,s^{-1})^{-1}\,cm^{-2}$ can be seen in Figure 3.14. The indices, N with molecular gas are largely unchanged, but a higher X_{CO}-factor means a longer measured gas depletion time (Figure 3.15). Increasing X_{CO} gives a shallower fitted slope when looking at total gas, $N \sim 1.6$ for $X_{CO} = 6 \times 10^{20}\,(K\,km\,s^{-1})^{-1}\,cm^{-2}$.

SCALE

It has been suggested (e.g. Kruijssen & Longmore, 2014) that the scale on which the star formation law is studied can have an effect on the measured index and the scatter observed in the relation. Figure 3.16 shows the star formation law as measured
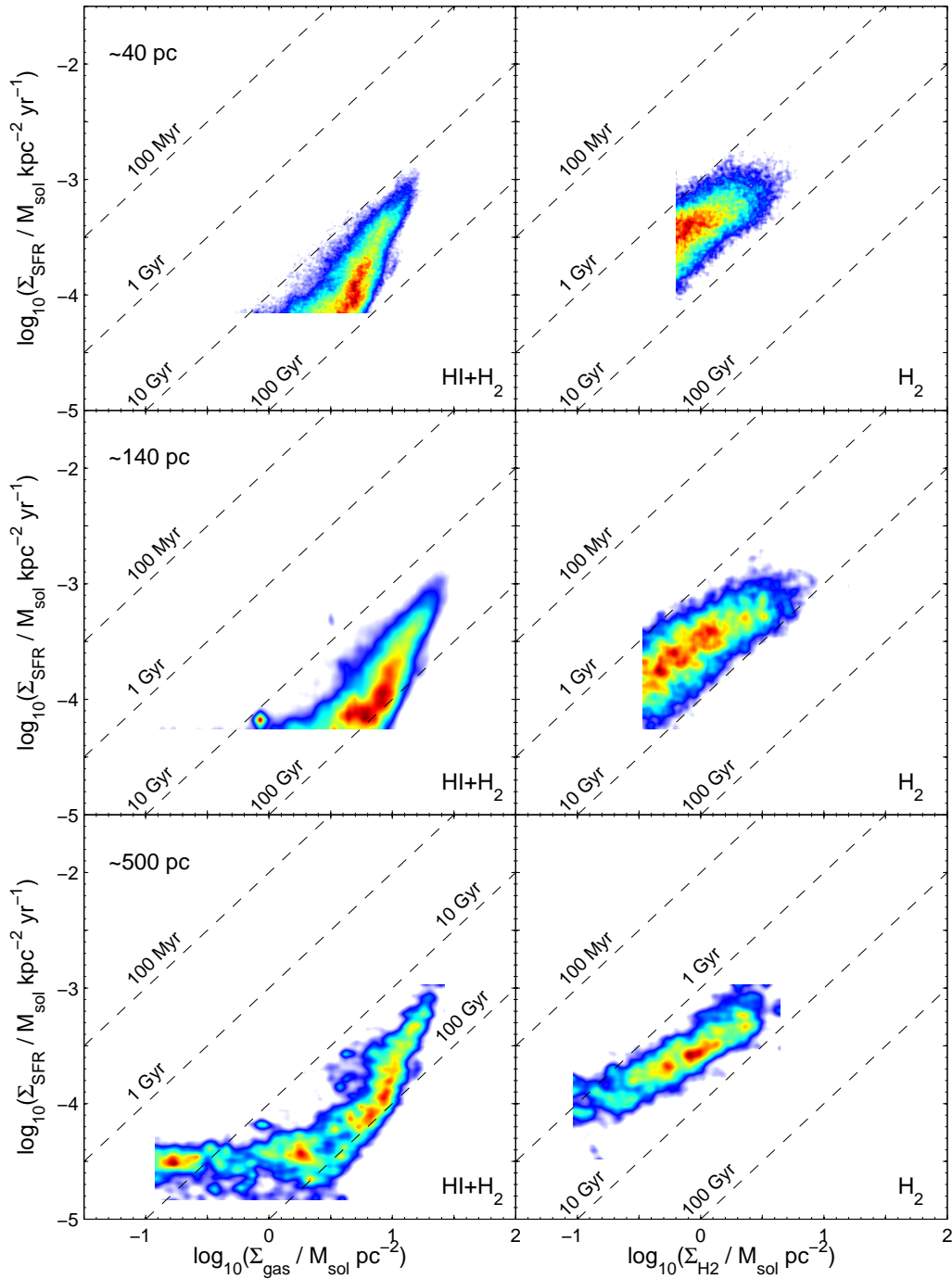
Figure 3.16 Star formation rate surface density against gas surface density in M31 for total gas and H_2 only on a range of pixel scales. From top they are ~ 40, ~ 140 and $500\,\mathrm{pc}$. The left column shows total gas; the right, molecular hydrogen only. The colour represents the density of datapoints. Dashed lines are of constant gas depletion time, τ_{dep}.
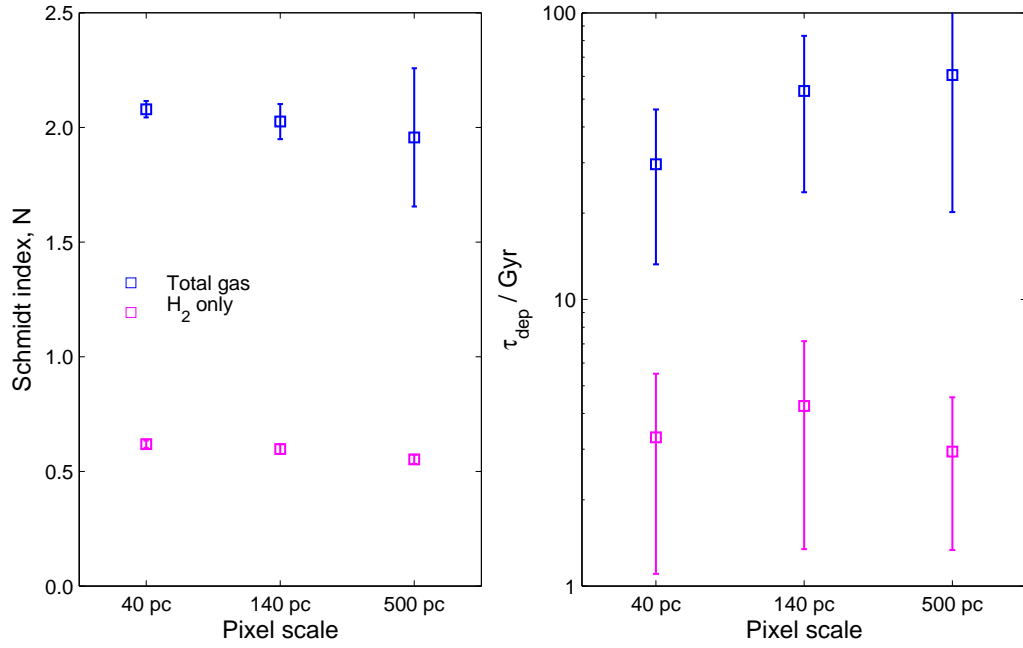
Figure 3.17 Kennicutt-Schmidt parameters with pixel scale. We compare the power law indices, N (left) and mean gas depletion time ($\tau_{\rm dep}$, right) using H I + H$_2$ and H$_2$ only. Errorbars represent the $2\,\sigma$ uncertainty in N and the standard deviation in the distribution of $\tau_{\rm dep}$.

on $\sim$40, $\sim$140 and $\sim$500 pc scales. The main difference appears to be a translation in the direction of constant gas depletion time. This is expected as we are averaging over larger regions so the higher surface densities will be smoothed over and sensitivity to the low-end is increased. The fitted indices are not greatly affected (Figure 3.17) although the scatter appears to be reduced, with the correlation coefficient for $\log_{10}\Sigma_{\rm SFR}$ versus $\log_{10}\Sigma_{\rm H_2}$ increasing from $R = 0.69$ to $R = 0.84$ (errorbars on N in Figure 3.17 suggest the opposite but are based on binned fitting, so are dominated by the number of datapoints, which is significantly fewer for the 500 pc maps).

MOLECULAR CLOUDS

Kirk et al. (2013) created a cloud catalogue and mask using *Herschel* data of M31. Jason Kirk (priv. comm) further determined mean star formation and gas surface densities for each cloud using the maps described previously but on a finer pixel scale of 8″. Despite the mask being created using the maps of dust mass, we can see clearly in Figure 3.18 that there is a significantly higher portion of molecular gas in the selected regions.

It is assumed that star formation is most concentrated in molecular clouds, so here I plot the star formation law using the four ISM tracers on a pixel by pixel basis,
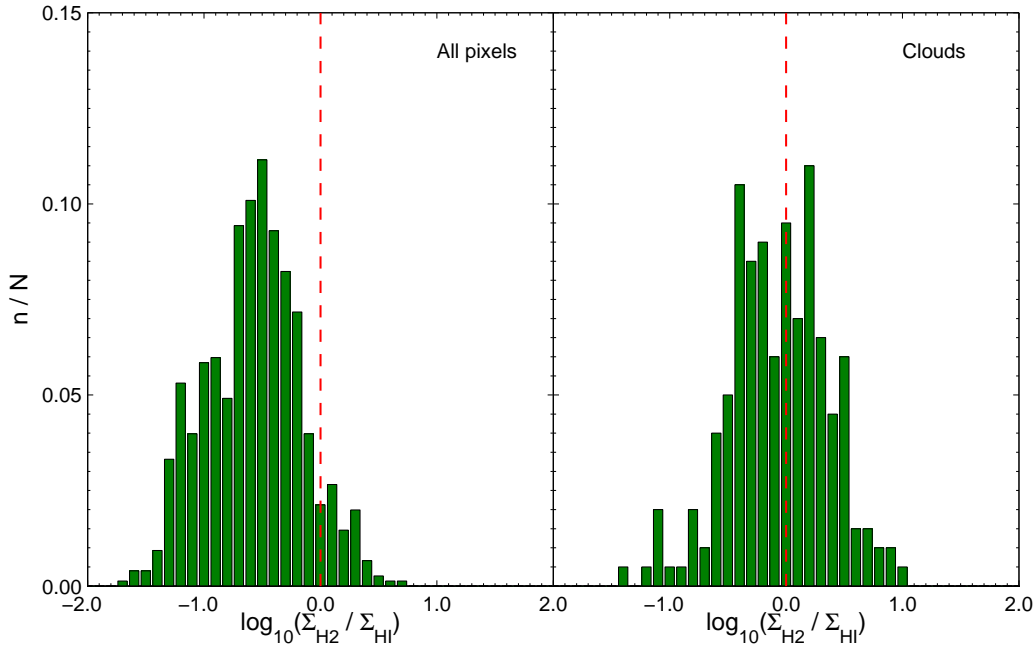
Figure 3.18 Histograms of ratio of molecular to monatomic gas in M31, over the whole galaxy, left; and selecting pixels only contained within clouds, right. The red dashed line indicates a 1:1 ratio.

selecting only those points that are part of the mask (Figure 3.19) and on a cloud by cloud basis (Figure 3.20). In the latter analysis, each cloud is treated equally, there is no weighting based on size or mass. It should be noted that the cloud by cloud analysis was performed on a finer pixel scale, corresponding to the resolution of the H I map (see Section 3.2). The scatter in the SF law appears larger in Figure 3.20, but we attribute this to the finer pixel scale used to retrieve data for each cloud (see aforementioned results on different pixel scales). The gas depletion times in clouds might be expected to be lower than the galaxy taken as a whole, indicating a higher star formation efficiency. The mean values for all clouds in M31 are $\tau_{\mathrm{dep}}^{\mathrm{Gas}} \sim 15\,\mathrm{Gyr}$, $\langle \tau_{\mathrm{dep}}^{\mathrm{Gas(Dust)}} \rangle \sim 14\,\mathrm{Gyr}$, $\langle \tau_{\mathrm{dep}}^{\mathrm{H2}} \rangle \sim 6.2\,\mathrm{Gyr}$ and $\langle \tau_{\mathrm{dep}}^{\mathrm{H\,I}} \rangle \sim 6.2\,\mathrm{Gyr}$.

3.5.3 DISCUSSION

I have found a lower mean star formation rate and a longer gas depletion time when looking at all regions of gas which suggests we are not isolating star forming regions as well as when using tracers of the denser ISM (Figure 3.10). This is consistent with previous work (e.g. Bigiel et al., 2008, 2011; Rahman et al., 2012) suggesting that molecular gas is more important for star formation than H I.

The star formation law in M31 using total gas gives a K-S index $N \sim 2.0$, significantly higher than the value found by Tabatabaei & Berkhuijsen (2010) but
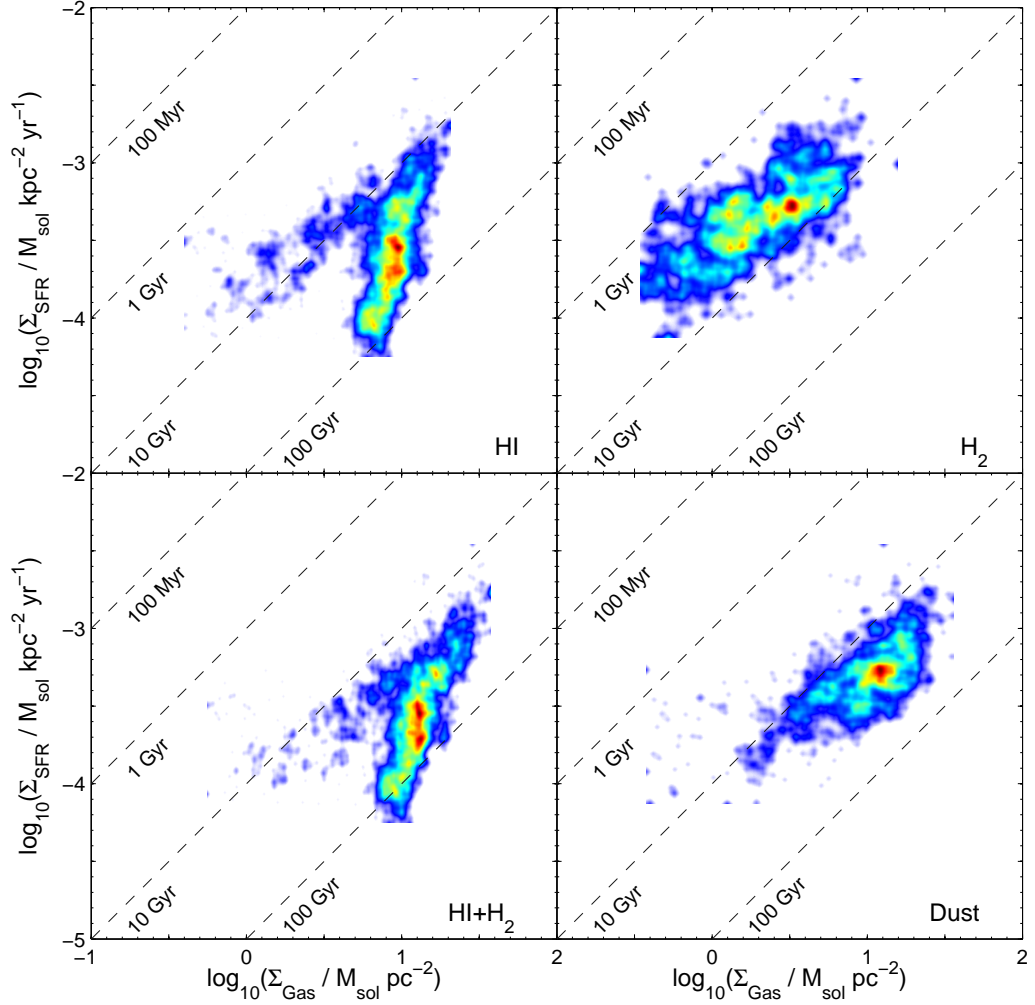
Figure 3.19 Star formation rate surface density against gas surface density in M31 for H I, H₂, total gas and gas traced by dust where selected pixels are part of a molecular cloud (as deteermined in Kirk et al. 2013). The colour represents the density of datapoints. Dashed lines are of constant gas depletion time, τ_{dep}.
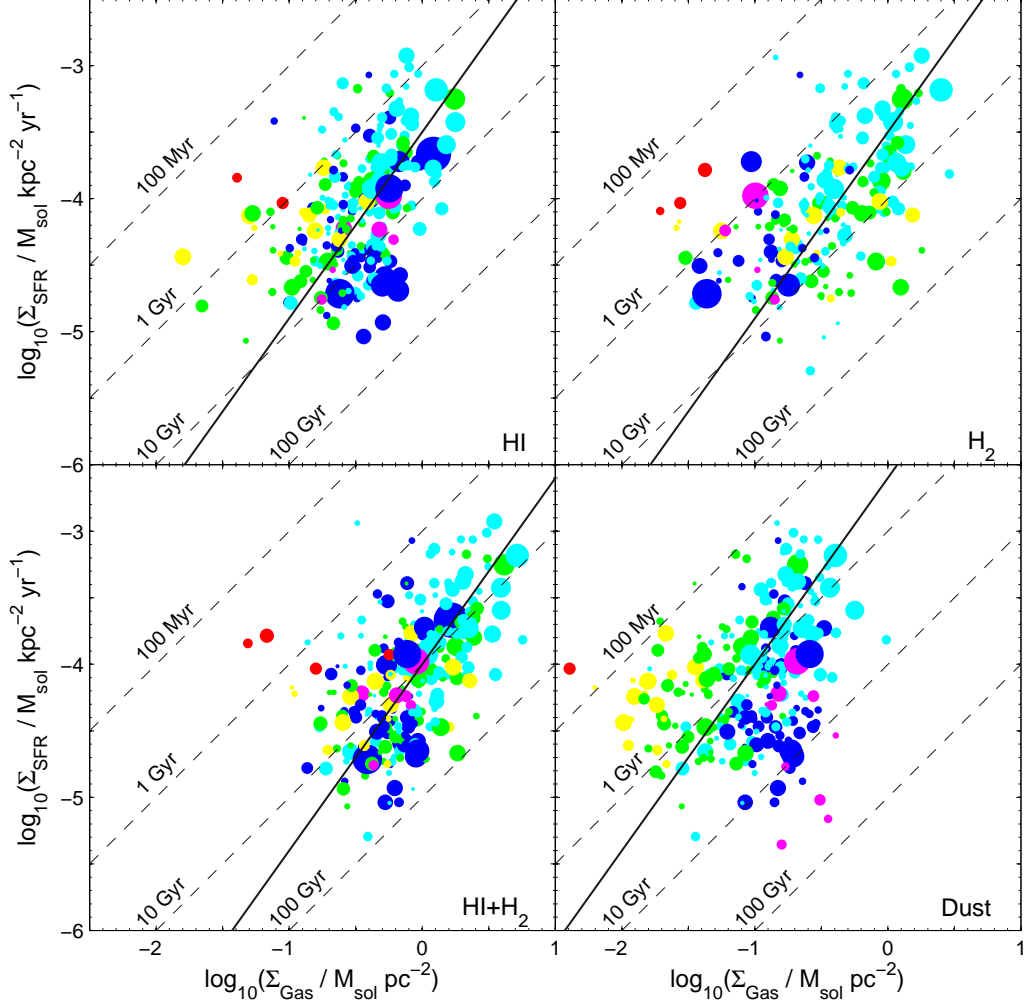
Figure 3.20 Star formation rate surface density against gas surface density in M31 for H I, H$_2$, total gas and gas traced by dust on a cloud basis. Size of datapoints are scaled by the square root of the surface area of each cloud, colours indicate galactocentric radius (see Figure B.1 in Appendix B.1). Dashed lines are of constant gas depletion time, τ_{dep}. The solid black line is a slope with gradient 1.4, representing a SF law of the type found in Kennicutt (1998b).

consistent with values found in previous work on other galaxies. The distribution of points in the bottom left panel of Figure 3.11 is clearly dominated by the monatomic hydrogen in M31 (top left panel), as the distributions appear very similar. One possible explanation for a steep slope is H I becoming optically thick at $\Sigma_{\mathrm{Gas}} \sim$ $10 \, \mathrm{M_{\odot} \, pc^{-2}}$. However, when performing the analysis on an opacity corrected map of H I taken from Braun et al. (2009), we see no real change in the calculated star formation law, with $N \sim 2$ in both cases. An alternative is that the hydrogen turns molecular but is not traced by our CO(J=1-0) map in these high SFR regimes. CO has a lower dissociation energy than H_2 (3.7 eV compared to 4.5 eV) so it is possible that stars in these regimes are formed by CO-free molecular hydrogen, hence the turnover apparent in previous work (e.g. Bigiel et al., 2008) is not visible here.

The index found here using molecular gas ($N \sim 0.6$) argues against a super-linear relationship on small scales. Some recent work has suggested that the star formation law is linear ($N = 1$) when looking at molecular clouds (e.g. Rahman et al., 2012) and that the superlinear relationship of Kennicutt (1998b) is not a manifestation of a relationship that applies on smaller scales, but may be the result of systematic differences between the galaxies that are related, but not limited to, gas mass alone. This linear law on small scales has also been found in atomic gas dominated regimes (Schruba et al., 2011) suggesting that the dominance of H I in M31 should not have a significant effect. The 'sub-linear' relationship ($N < 1$) we see here indicates that star formation is less efficient at high gas densities which would be an intriguing result and warrants further exploration.

The total gas surface densities in Figure 3.12 (bottom row) appear to depend on galactocentric radius. This is also indicated by the fits to each annulus showing a horizontal offset (top row), the inner regions of the galaxy appearing to the left of the plot (low gas surface density). This would suggest that the threshold for star formation and/or gas depletion time changes with radius (see also Figure 3.13). This makes sense as rings of constant galactocentric radius appear to dominate the structure of the galaxy. We should note that the inner regions contain relatively fewer datapoints so there is significant uncertainty here. Also, it is possible that despite our correction for the older stellar population, we still overestimate star formation in the centre.

Adjusting the CO-H_2 conversion factor does skew the slope when looking at total gas (Figures 3.14 and 3.15), with the highest value tested here of $X_{\mathrm{CO}} = 6 \times 10^{20}$ $\mathrm{(K \, km \, s^{-1})^{-1} \, cm^{-2}}$ resulting in a calculated slope of $N \sim 1.6$. Lower values of X_{CO} steepen the relationship ($X_{\mathrm{CO}} = 1 \times 10^{20} \, \mathrm{(K \, km \, s^{-1})^{-1} \, cm^{-2}}$, $N \sim 2.2$).

Varying the X_{CO}-factor as described previously has no significant effect on

the slope of the molecular star formation law (Figure 3.15) as it results in a horizontal translation only in the $\log_{10}\Sigma_{\mathrm{SFR}}$-$\log_{10}\Sigma_{\mathrm{H2}}$ plane. It does, however, alter the measured gas depletion time, given as $\tau_{\mathrm{dep}}^{\mathrm{H2}} = \Sigma_{\mathrm{SFR}}/\Sigma_{\mathrm{H2}}$. An X_{CO}-factor of $1\times10^{20}\,(\mathrm{K\,km\,s}^{-1})^{-1}\,\mathrm{cm}^{-2}$ gives $\langle\tau_{\mathrm{dep}}^{\mathrm{H2}}\rangle \sim 2.4\,\mathrm{Gyr}$ compared to $\sim 4.2\,\mathrm{Gyr}$ for the nominal value. Using $X_{\mathrm{CO}} = 6\times10^{20}\,(\mathrm{K\,km\,s}^{-1})^{-1}\,\mathrm{cm}^{-2}$ results in $\langle\tau_{\mathrm{dep}}^{\mathrm{H2}}\rangle \sim 11\,\mathrm{Gyr}$. Gas depletion time using total gas, $\tau_{\mathrm{dep}} \sim 50$–$60\,\mathrm{Gyr}$ depending on X_{CO}. This order of magnitude difference in τ_{dep} between the gas tracers emphasises the link between $\mathrm{H_2}$ and regions of star formation, implying molecular gas is more important than H I in forming stars, even in monatomic gas dominated regimes like those in M31. However, some argue that the key ingredient is dense gas rather than that which is specifically molecular, and that $\mathrm{H_2}$ is inevitably formed in regions that are dense enough to form stars.

Figure 3.18 shows that there is a significantly higher portion of molecular gas in the regions contained within the cloud mask of Kirk et al. (2013), made by selecting the regions of high dust surface density. This lends weight to the hypothesis that dust can be used to trace the dense gas in galaxies (Eales et al., 2012).

When testing the star formation law in molecular clouds only, the pixel by pixel analysis (Figure 3.19) shows a few interesting discrepancies from Figure 3.11 which looks at the whole galaxy. Firstly, the SF law with total gas shows evidence of the spur at high gas surface density seen in previous work (inc. Bigiel et al., 2008). It is interesting that a spur is also visible with H I, considering it is usually attributed to regions of high molecular gas density following a linear SF law. There are also two distinct populations on this plane. The first is a region at $\Sigma_{\mathrm{Gas}} \sim 10\,\mathrm{M_\odot\,pc}^{-2}$ which appears to follow a very steep relationship, possibly due to atomic hydrogen becoming saturated or turning molecular as discussed earlier. The second population follows a much shallower slope of roughly constant τ_{dep}, of the type seen when using molecular gas only, but again this is characteristic of the H I SF law also (Figure 3.19, top left panel), so cannot be attributed to molecular gas traced by CO.

The cloud by cloud analysis (Figure 3.20) shows considerable scatter, which we attribute to the smaller pixel scale used for analysis. Fitting a K-S index is troublesome due to the complexity of the selection effect. The measured K-S indices for total gas are $N \sim 0.7$ and $N \sim 2.9$ for minimising residuals in Σ_{SFR} and Σ_{Gas} respectively, with the general trend appearing consistent with a Kennicutt-Schmidt SF law of $N \sim 1.4$ as found in Kennicutt (1998b).

A significant issue we should keep in mind when interpreting all of the above, is that because the scales we are probing are small compared to other extragalactic sources, the surface density of star formation and surface density of gas may not

be directly relatable to the corresponding volume densities as our scale height is more likely to vary between regions. Also, due to the relatively small area covered by a single pixel, the IMF is not likely to be fully sampled, so conversion factors between surface brightness and star formation rate, which are calibrated on much larger scales, are not necessarily applicable. However, assuming the IMF is appropriate on larger scales in M31, this issue should manifest itself as a random scatter only, so the global SFR and overall trend in the star formation law should not be greatly affected. This is supported by Figure 3.16, where the measured Schmidt-indices and gas depletion times are largely unaffected and that larger pixel scales reduce scatter in the relationship with the correlation increasing from $R = 0.69$ for 140 pc scale to $R = 0.84$ for 500 pc pixels.

Future work should focus on utilising different tracers to measure the amount of dense gas in the ISM of M31, e.g. C II. This would allow further exploration of the high-density, low-SFE regions that give rise to the measured sub-linear SF law with molecular gas. It also has the potential to show regions of dense gas that are not traced by CO, i.e. CO-free molecular gas or 'dark-gas' as discussed in Planck Collaboration et al. (2011).

3.6   SUMMARY

In this paper I have determined the surface density of star formation in M31 using combined FUV and 24 μm emission and separately the far-infrared luminosity. I aim to correct the former for emission from both unobscured and embedded old stars and find a global star formation rate of $0.25^{+0.06}_{-0.04}\,\mathrm{M_\odot\,yr^{-1}}$. The FIR emission appears to be correlated with the SFR map made using FUV and 24 μm emission. However, we are unable to correct for the old stellar population as there is no correlation visible between FIR luminosity and 3.6 μm emission in the galactic centre.

I produce two maps of the total gas in M31. The first uses H I and CO, assuming a CO-H_2 conversion factor of $2\times10^{20}\,(\mathrm{K\,km\,s^{-1}})^{-1}\,\mathrm{cm^{-2}}$. We use the radially varying gas-to-dust ratio found in Smith et al. (2012a) to produce the second map of total gas from the dust emission.

When comparing with previous work by Kennicutt (1998b) and Leroy et al. (2008) on the global SFR and gas mass, I find the mean molecular gas surface density and SFR surface density for M31 sit on the low end of the relation determined in Kennicutt (1998b).

My measurement of the SF law on sub-kpc scales varies with gas tracer. I further explore the effect of CO-H_2 conversion factor, pixel scale and selection of molecular

clouds only on calculation of the Schmidt index and gas depletion time, τ_{dep}.

The most direct measurement, using H I and CO to trace total gas, gives power law index $N \sim 2.0$ when looking at the whole galaxy, consistent with the range of values found in previous work but I believe this slope is a result of H I saturation or atomic hydrogen turning molecular. The values measured in radial annuli vary between 1.0 and 2.3, with the highest values being measured in the 10 kpc ring, where the vast majority of star formation is occurring.

Using molecular gas only gives a much lower K-S index of $N \sim 0.6$, suggesting that a superlinear relationship with molecular gas is not applicable on sub-kpc scales in M31.

ACKNOWLEDGMENTS

4 THE STAR FORMATION LAW IN M33

When you have bacon in your mouth,
it doesn't matter who's president.

–LOUIS C. K.

As the second largest extragalactic source in the local group (Figure 3.1), M33 is a prime target for study of galactic scaling relations, hence the time granted on the *Herschel Space Observatory* to the *Herschel* M33 Extended Survey (HERM33ES) collaboration (Verley et al., 2007, 2009; Corbelli et al., 2009), data from whom I use here. Previous work on the star formation (SF) law in M33 (Heyer et al., 2004) found a Kennicutt-Schmidt (K-S) index of ∼3.3 with total gas but 1.4 for molecular (the same index found for whole galaxies in Kennicutt 1998b).

In this chapter, I will present multi-wavelength data of M33 and look at the relationship between star formation and the interstellar medium (ISM) in this galaxy as was done in the previous chapter on M31. I will further compare and contrast the measured properties of these two galaxies.

4.1 THE TRIANGULUM

The Triangulum (M33, figure 4.1) is the third largest galaxy in the local group but considerably smaller and less massive than the dominant two, containing ∼40 billion stars. It is a 'flocculent spiral', with morphological classification SA(s)cd so is 'later-type' than M31 and may be a companion to M31. Distance estimates range from 730 to 940 kpc (Magrini et al., 2009). Here I employ the value from McConnachie et al. (2004) of 794 kpc which places it at a similar distance to M31. The apparent angular size of M33 is 71′ corresponding to a radius, R_{M33} of 8.18 kpc. This combined with its inclination angle of 56° (inclination of M31 is 71°) gives a

Figure 4.1 Messier 33, The Triangulum Galaxy. The image is approximately 20 kpc across, assuming a distance to M33 of 794 kpc. Image credit: *NASA/ESA*

comparable number of pixels for study.

4.2   DATA

In this chapter I employ observations of M33 at the same wavelengths (and where possible, from the same telescopes) used to study M31 in the previous chapter.

GALEX (Martin & GALEX Team, 2005a) far- and near-ultraviolet (FUV and NUV) observations of M33 are taken from Thilker et al. (2005). I also use Spitzer (Rieke et al., 2004) maps of warm dust (*MIPS* 24 μm Verley et al. 2007) and stellar emission (*IRAC* 3.6 μm Fazio et al. 2004) to create the first map of SFR. These constituents can be seen in Figure 4.2.

The HERM33ES collaboration obtained observations of M33 in five *Herschel* bands (Kramer et al., 2010). They are *PACS* (Poglitsch et al., 2010) 100 and 160 μm and *SPIRE* (Griffin et al., 2010) 250, 350 and 500 μm. These public data were re-reduced in Cardiff by Matthew Smith to produce the maps used here. The *Spitzer MIPS* 70 μm map is employed to extend the wavelength range for our calculation of the far-infrared (FIR) spectral energy distribution (Figure 4.3).

My independent ISM tracers are the 21 cm emission line from monatomic hydrogen (H I Thilker et al. 2002) and the carbon monoxide (CO) J=1-0 transition (Tosaki et al., 2011) (Figure 4.4). The CO maps, provided by Erik Rosolowsky of the University of Alberta are masked to ensure use of only the highest fidelity data, here selecting $5\,\sigma$ peaks and including all surrounding data above $2\,\sigma$ signal-to-noise ratio (SNR). Note that this results in a significantly smaller coverage for the CO map than the H I. As with the M31 analysis, the area not covered by the CO will be used in the calculation of total gas, provided there is sufficient H I. It should be noted that the maps used for the majority of the analysis are significantly lower resolution than those presented in Figure 4.4, resulting in more regions of sufficient SNR, so greater coverage.

All maps are smoothed and regridded to three pixel scales, as in Chapter 3. The majority of the analysis is performed on a $36''$ grid, corresponding to a spatial scale at 794 kpc of ∼140 pc A colour-key for the elliptical annuli used in our analysis of radial variations in the SF law can be found in Appendix B.1, Figure B.1.
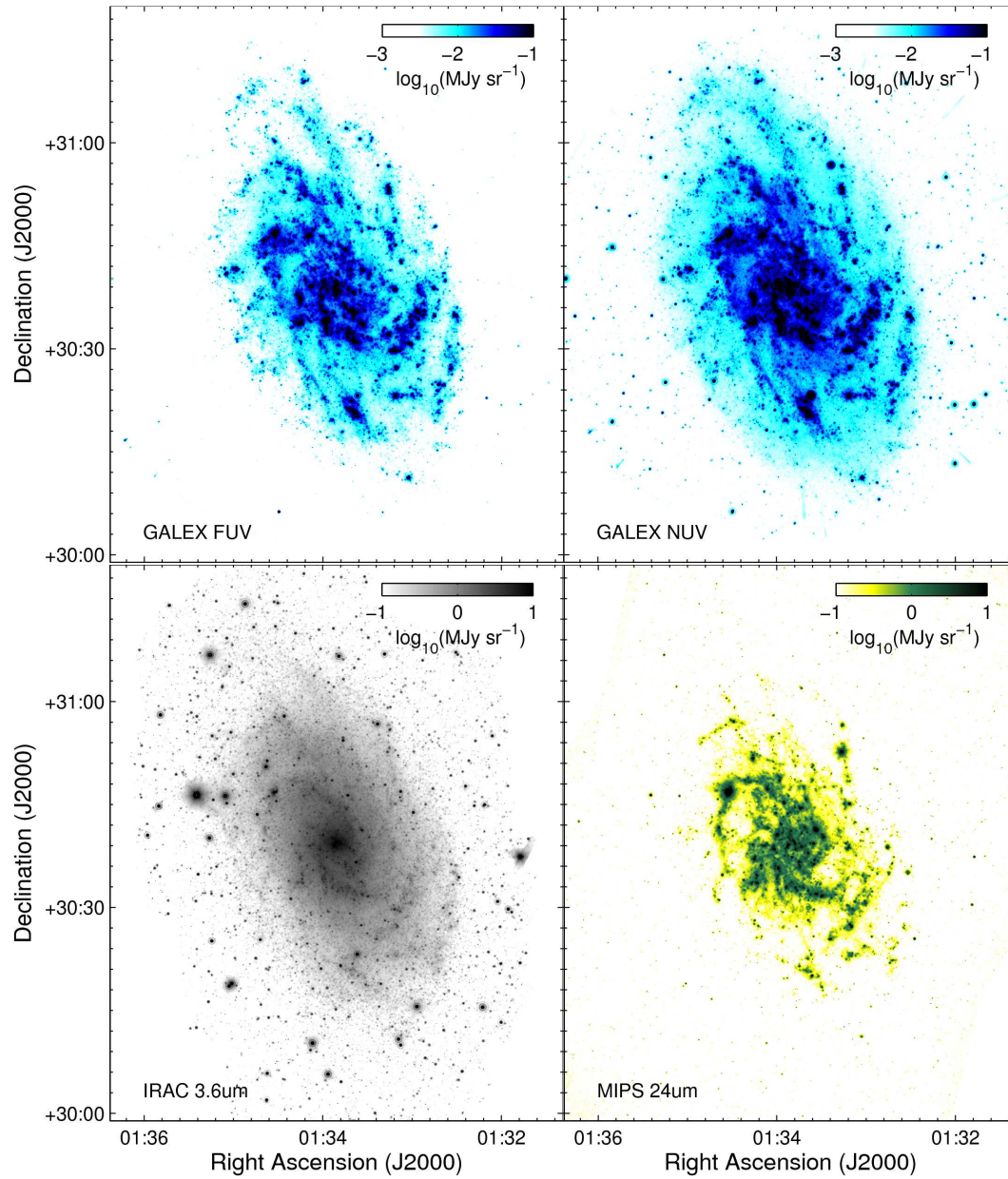
Figure 4.2 Images used in the creation of the FUV and 24µm star formation map of M33. From top left, *GALEX* FUV and NUV maps (Thilker et al., 2005); bottom, *Spitzer IRAC* 3.6 µm and *MIPS* 24 µm (Verley et al., 2007).
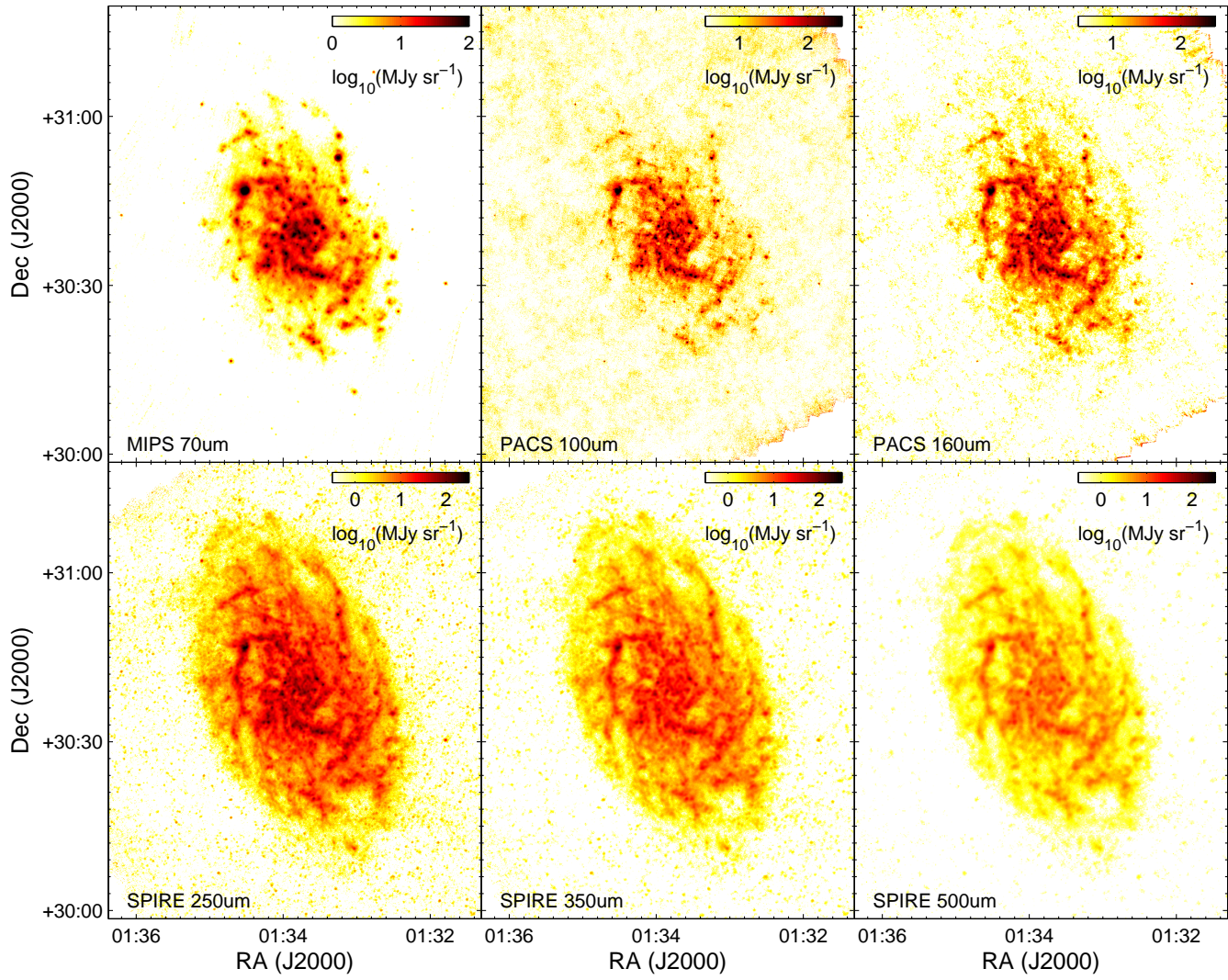
Figure 4.3 Top, from left: *Spitzer MIPS* 70 μm, *PACS* 100 and 160 μm; bottom: *SPIRE* 250, 350 and 500 μm. The *PACS* and *SPIRE* observations are from the HERM33ES collaboration (Kramer et al., 2010).
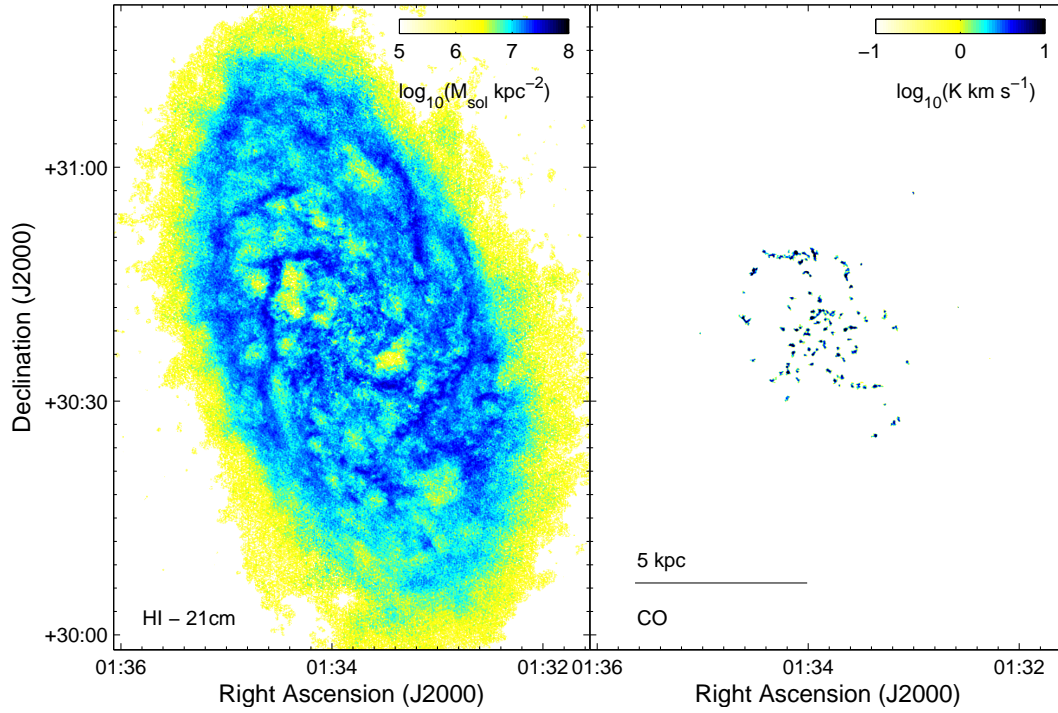
Figure 4.4 Left, integrated H I emission (Thilker et al., 2002); right, masked CO(J=1-0) map (Tosaki et al., 2011).

4.3   STAR FORMATION RATE

4.3.1   FUV AND 24 μM

The star formation rate is calculated from the *GALEX* FUV and *Spitzer* 24 μm maps, using the method described in 3.3.1 as prescribed in Leroy et al. (2008), assuming a Chabrier (2003) initial mass function (IMF). The prescription for Σ_{SFR} in units of $\mathrm{M_\odot\,yr^{-1}\,kpc^{-2}}$ given FUV and 24 μm intensity (I) in $\mathrm{MJy\,sr^{-1}}$ is given in Equation 3.1. The inclination of M33, $i = 56°$. As before, foreground stars are selected and removed in both the FUV and 24 μm map using the UV colour. For a more detailed description, see 3.3.1.

In Chapter 3 I was able to isolate the bulge of M31 where we assume star formation has ceased, in order to determine a correction factor for the contribution of old stars based on the 3.6 μm emission, which traces the general stellar population. The method of correction can be seen in 3.3.1, Equations 3.3 and 3.4.

In M33, a correlation between our star formation tracers and 3.6 μm emission is not clearly visible (see Figure B.4, Appendix B.2), so a bespoke correction factor is not attainable. In lieu of this, we employ the values quoted in 3 of $\alpha_{\mathrm{FUV}} = 8 \times 10^{-4}$ and $\alpha_{24} = 0.1$, based on the ratio of FUV and 24 μm emission to 3.6 μm in M31.

Any descrepancies in this value will be due to differences in the populations of stars and the effect of dust extinction on the respective wavelengths. As M33 is a later-type galaxy, I expect a slightly different value, but as it is less dominated by old stars the correction should be small. The correction in this work has the effect of reducing the measured global SFR by ~12%, a smaller effect than found for M31, as expected.

We can scale the star formation map to give the total star formation occurring within a pixel. This allows us to determine the global SFR for M33, which we find to be $0.16^{+0.03}_{-0.02} \, M_\odot \, yr^{-1}$. This is comparable to the value for M31, but as M33 is much smaller this suggests a greater star formation efficiency (SFE) which I will discuss more later.

For analysis of the star formation law (Section 4.5), I mask all points that do not satisfy $\Sigma_{SFR} > 5 \, \sigma_{SFR}$, where σ_{SFR} is the standard deviation of the background, measured separately for each pixel scale.

4.3.2   STAR FORMATION FROM FAR-INFRARED LUMINOSITY

Here I produce a second map of star formation from the FIR luminosity. For a more detailed discussion see 3.3.2. The total FIR luminosity is found assuming a distance to M33 of $D = 794 \, kpc$ (McConnachie et al., 2004).

The SFR from FIR luminosity is given in Equation 3.5 where the conversion δ_{MF} depends on the assumed IMF and the SF timescale. and changing these assumptions gives radically different conversion factors (Calzetti, 2013). Here we employ the value quoted in Kennicutt (1998b) which assumes a Salpeter IMF with a low mass cut-off of $0.1 \, M_\odot$ and a timescale of ~100 Myr, modified for a Chabrier (2003) IMF, of $\delta_{MF} = 1.1$ to keep consistency with the other method. This conversion factor gives a global star formation rate of $0.11 \, M_\odot \, yr^{-1}$, lower the value found for UV and $24 \, \mu m$ emission.

4.3.3   COMPARISON OF STAR FORMATION TRACERS

The star formation maps made using FUV and $24 \, \mu m$ emission, and FIR luminosity can be seen in Figure 4.5. The FUV and $24 \, \mu m$ tracer has units of $M_\odot \, yr^{-1} \, kpc^{-2}$, FIR luminosity is in solar units.

For consistency, we modify the FUV and $24 \, \mu m$ tracer to match the assumptions made in creating the map of Σ_{SFR} from FIR luminosity. As no correction for old stars was performed on the IR map, the correction is ignored in the FUV and $24 \, \mu m$ map.
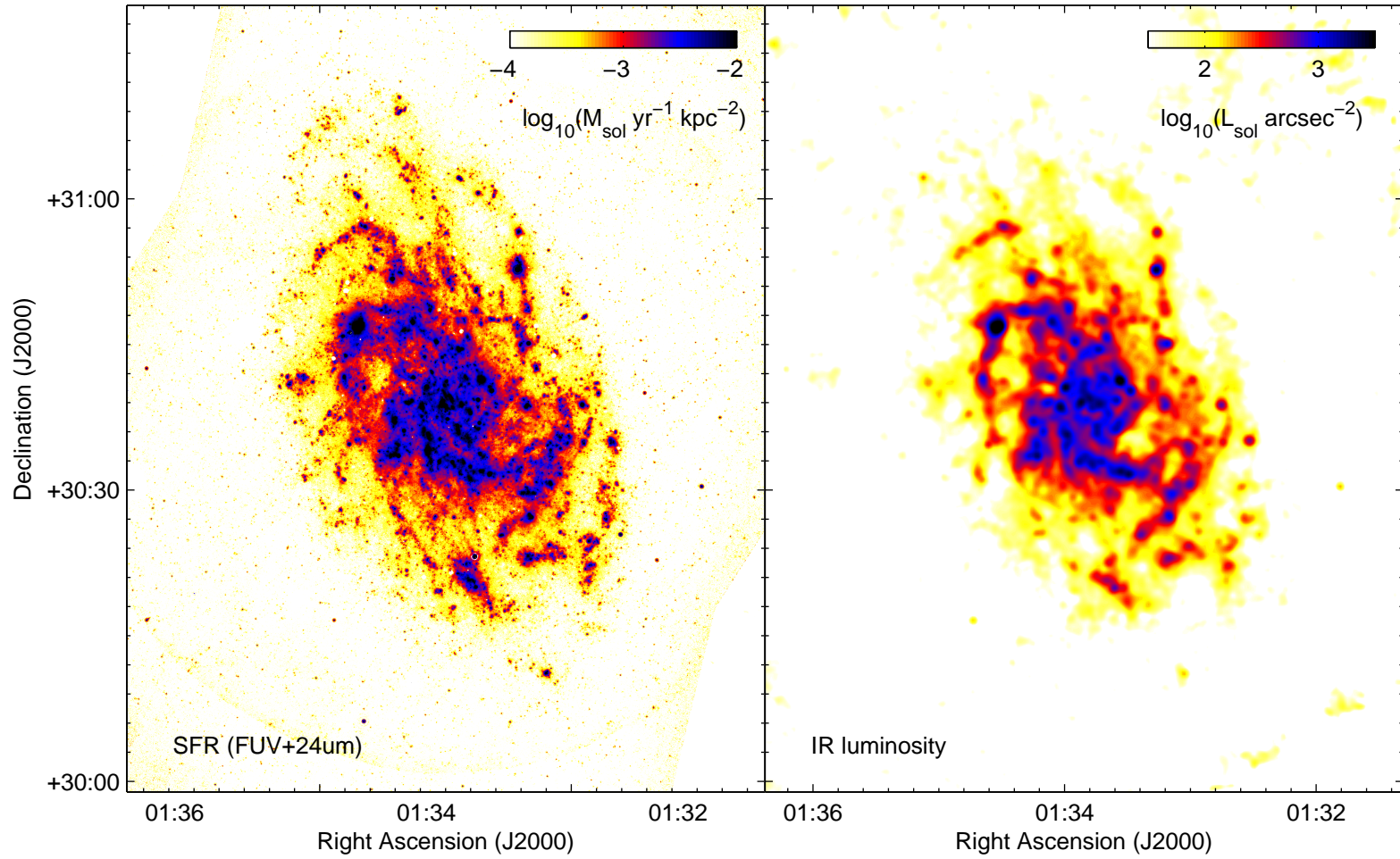
Figure 4.5 Left, star formation rate map obtained using the FUV and 24 μm emission (FWHM beamwidth $= 6''$, pixel size $= 1.5''$); right, total FIR luminosity at $\lambda > 70\,\mu m$ (FWHM beamwidth and pixel size $= 36''$), found by integrating the emission from *Herschel* and *Spitzer* observations shown in Figure 4.3. The SFR from IR luminosity is found using a constant conversion factor based on the assumed IMF and assumed length of the continuous starburst.
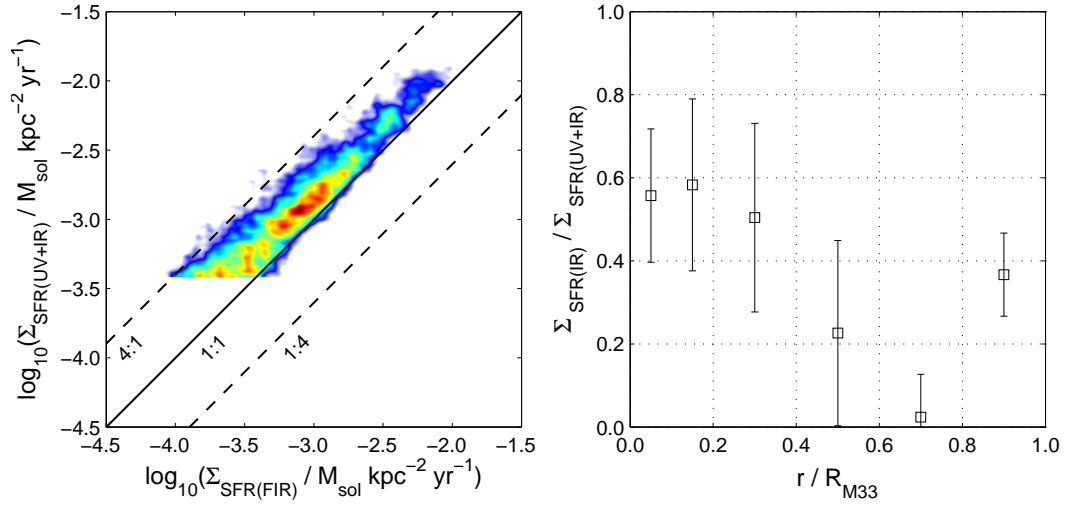
Figure 4.6 Left: Σ_{SFR} (SFR surface density) found from FIR luminosity vs Σ_{SFR} from FUV and $24\,\mu m$ emission (without a correction for the old stars). The colours represent the density of datapoints. The solid black line indicates a 1:1 relationship, the dashed black lines indicate factors of 4 offsets. Right: ratio of Σ_{SFR} from FIR luminosity to Σ_{SFR} from FUV + $24\,\mu m$ star formation surface density with radius. The errorbars represent one standard deviation of the scatter in this value across each elliptical annulus.

In Figure 4.6 we compare Σ_{SFR} from FIR luminosity (as described in Section 3.3.2) with the same from FUV and $24\,\mu m$ with the aforementioned caveats. This gives a global SFR of $0.19^{+0.04}_{-0.02}\,\mathrm{M_\odot\,yr^{-1}}$, higher than the value from FIR luminosity. This appears to be the case throughout the galaxy. One possibility is that there are many regions of unobscured star formation where dust is not present, so we are missing some star formation when looking at dust heating alone. When looking at Figures 4.5 and 4.6 however, it appears that the two maps are spatially very well correlated with a constant offset.

For the analyses that follow, as with the previous chapter on M31, I elected to use the combined FUV and $24\,\mu m$ emission as our star formation tracer as I have attempted to remove the contribution from the old stellar population and feel I can more reliably extract both the unobscured and embedded star formation.

4.4 THE INTERSTELLAR MEDIUM IN M33

4.4.1 TOTAL GAS FROM H I AND CO OBSERVATIONS

The H I map is taken from Thilker et al. (2002). The conversion from Jy to $M_\odot$ was performed using the following from Wild (1952),

$$M_{\mathrm{H\,I}}/M_\odot = 2.36 \times 10^5 \, (D/\mathrm{Mpc})^2 \int (F/\mathrm{Jy})\, \mathrm{d}v, \qquad (4.1)$$

where $D = 0.794\,\mathrm{Mpc}$. In order to keep consistency with our maps of star formation for analysis of the SF law, and to allow comparison of galaxies with different inclinations, i, when converting to a surface density ($\Sigma_{\mathrm{HI}} / M_\odot\,\mathrm{kpc}^{-2}$) I employ a factor of $\cos i$ to 'deproject' the galaxy.

I use CO maps from Rosolowsky et al. (2007) (BIMA+FCRAO) and Tosaki et al. (2011) (Nobeyama Radio Observatory, NRO) to trace molecular gas in M33. There is general consistency between the two maps but at the largest scale ($36''$) I employ the NRO CO map as it is believed to be better at recovering low surface brightness emission.

To ensure we use the most high fidelity data, the CO map (provided by Erik Rosolowsky of the University of Alberta) was masked to select only the brightest areas, with a $5\,\sigma$ peak selection, including all surrounding data down to $2\,\sigma$ SNR. This results in far less coverage at high resolutions (Figure 4.4, right panel) but this is not a significant issue if the mask is performed on smoothed data, as it is for our largest pixel scale.

Here we will assume a CO-H_2 conversion factor of $X_{\mathrm{CO}} = 2\times10^{20}\,(\mathrm{K\,km\,s}^{-1})^{-1}$ cm^{-2} (e.g. Strong et al., 1988; Pineda et al., 2010). I explore the effect of variations in this parameter on the SF law in 4.5.2.

4.4.2 TOTAL GAS TRACED BY DUST

The dust map of M33 was produced using Spitzer data and Herschel maps from the HERM33ES collaboration (Kramer et al., 2010). For a description of the method used to retrieve dust mass, see Section 3.4.2 and Smith et al. (2012a).

In M31 the FIR SED was well described by a greybody function with a single temperature component. In M33 this is not always the case. Here two fits were performed by Matthew Smith at Cardiff University assuming one or two dust temperature components. In both cases, many pixels do not satisfy the necessary χ^2 criteria (Figure 4.7). As there is no significant improvement when using two tem-
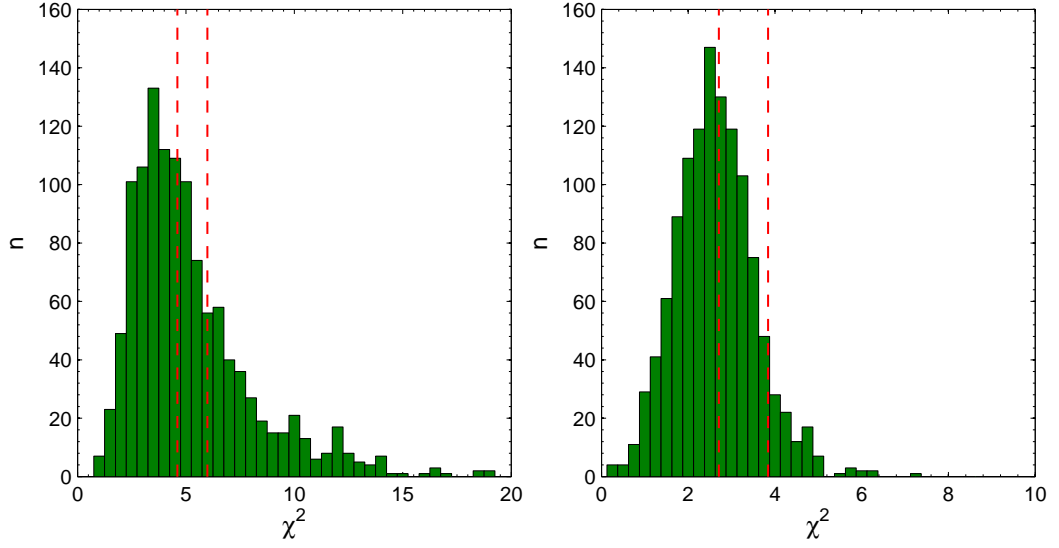
Figure 4.7 χ^2 of greybody fit for the one (left) and two (right) temperature component SED fits to FIR data of M33. The red dashed lines represent the point at which 10% and 5% of χ^2 values should be measured to be greater, given a good fit. Here we can see more than 10% of pixels have a larger χ^2, suggesting poor agreement for much of the map.
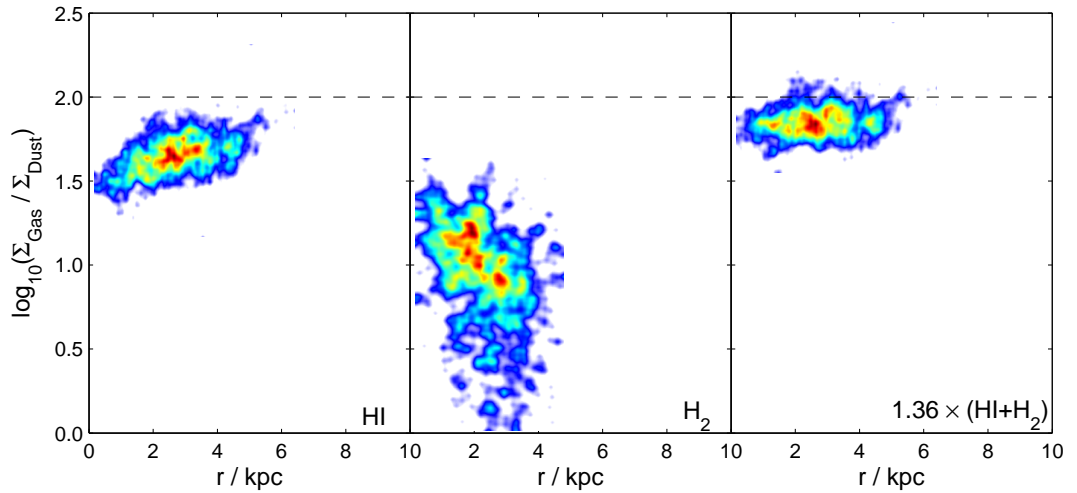
Figure 4.8 Gas to dust ratio with radius in M33 for monatomic hydrogen (H I), molecular hydrogen (H$_2$) and total gas (H I + H$_2$) with a factor of 1.36 for heavier element abundances.

perature components, I use the single temperature dust map to keep consistency with the analysis of M31, but omit pixels that do not satisfy the 5% rejection criteria.

The parameter we wish to test against SFR surface density is gas mass as traced by dust, so a fit was performed to gas-to-dust vs radius, to determine whether this factor varies across the galaxy (Figure 4.8). It appears that the ratio is approximately constant at $\sim$72, approximately the same as the Milky Way value (Spitzer, 1978). This value is used to uniformly convert dust mass to surface density of total gas for the analyses that follow.

4.5 THE STAR FORMATION LAW

In this section, we probe the star formation or Kennicutt-Schmidt law (Equation 3.7) in terms of the index, N and mean gas depletion times, τ_{dep}.

We separately look at how M33 compares to other local galaxies in terms of global SFR surface density (calculated from FUV and $24\,\mu\text{m}$ emission) and gas surface density; and what relationship the star formation law follows on a pixel-by-pixel basis when considering various components of interstellar material.

4.5.1 GLOBAL STAR FORMATION LAW

Figure 4.9 compares the mean surface density of SFR with the mean surface density of gas for global measurements of galaxies from Kennicutt (1998b) and Leroy et al. (2008), with corresponding global values for M33 overplotted. The SFRs from this work and Leroy et al. (2008) are scaled to match the assumptions made in Kennicutt (1998b) (see 4.3.3). The values for M33 are found by taking the mean over all pixels with sufficient signal-to-noise in both maps (SFR and gas surface density). The difference in measured SFR is due to the different selection effects depending on the gas tracer.

We can immediately see when looking at M33 alone, that the mean SFR for regions containing sufficient H_2 ($I_{\text{CO}} > 5\,\sigma_{\text{CO}}$) or dust ($I > 5\,\sigma$ in five *Herschel* bands) is higher than for total gas, suggesting a better spatial correlation between SFR and both molecular hydrogen and dust than more diffuse regions.

4.5.2 RESOLVED STAR FORMATION LAW

We test the K-S SF law, on a 'per pixel' basis across the galaxy. This section aims to test how calculation of this law changes with different gas tracers. In Chapter 3 I
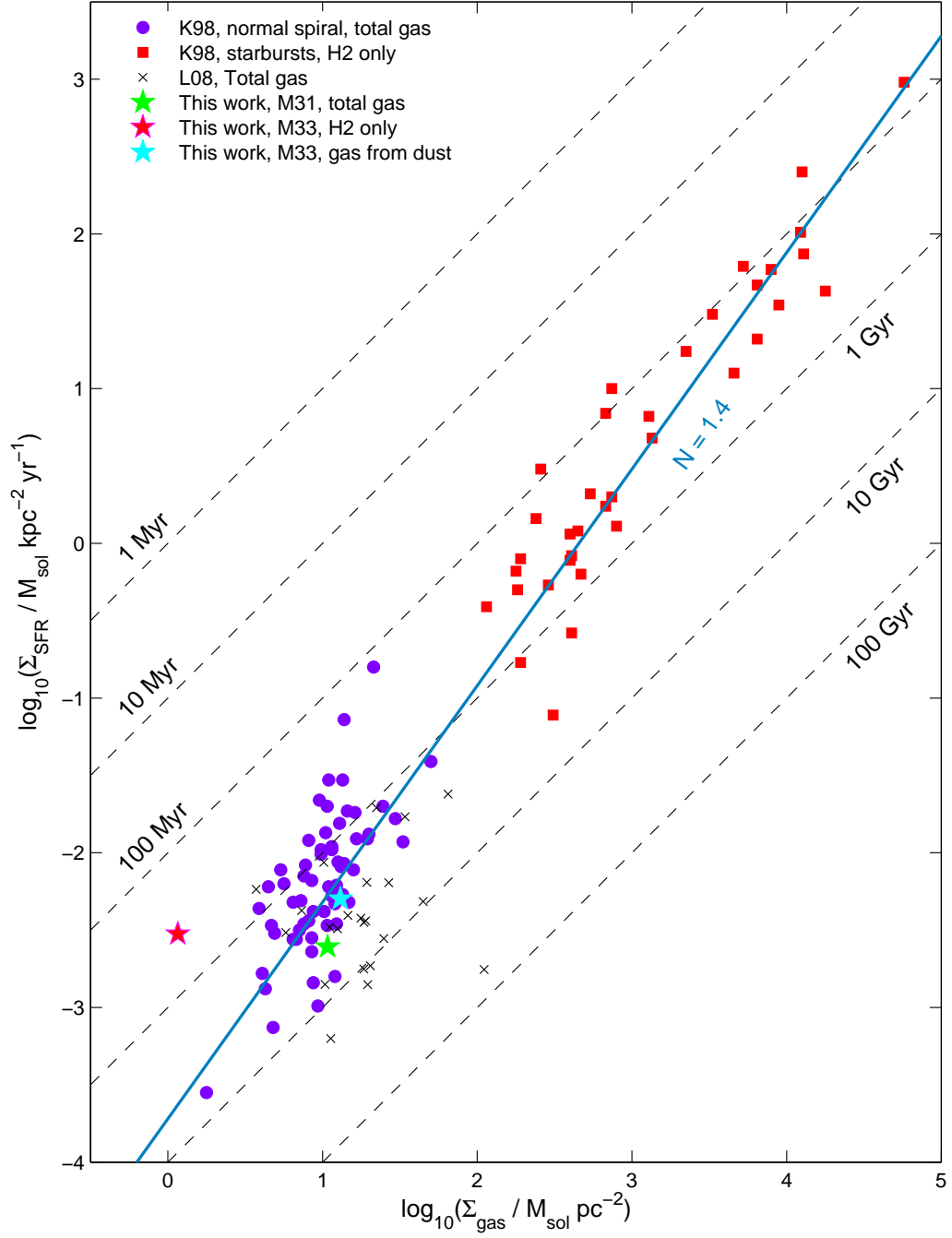
Figure 4.9 Global SFR vs gas mass, derived in M33 using three gas tracers, with Kennicutt (1998b) and Leroy et al. (2008) galaxies. Galaxies are plotted using total gas where possible or H_2 only, depending on availability of data. SFRs from this work and Leroy et al. (2008) are scaled to match the assumptions of Kennicutt (1998b). The dashed diagonal lines are of constant gas depletion time, τ_{dep}. The solid blue line is the gradient the galaxies should follow given a Schmidt law of the type found in Kennicutt (1998b) where $N = 1.4$.

find a sub-linear SF law with molecular gas in M31, suggesting lower SF efficiency at high gas surface density.

Here I use maps of surface density of star formation as found from FUV and 24 μm emission, against surface density of total gas, molecular hydrogen only and gas traced by dust. I select pixels that satisfy $\Sigma_{\mathrm{SFR}} > 5\,\sigma_{\mathrm{SFR}}$ and $\Sigma_{\mathrm{Gas}} > 5\,\sigma_{\mathrm{Gas}}$, where σ_{SFR} is the standard deviation of the background of the star formation map and σ_{Gas} is a combination of the uncertainties of the constituent gas maps (e.g. for total gas this will be the scaled uncertainties in the integrated H I and CO(J=1-0) images).

As before, I attempt to take clear SNR cuts into account. Here fits to all gas tracers minimise residuals in Σ_{Gas}, mitigating for the SNR cut in Σ_{SFR} (horizontal cut).

Figure 4.10 plots surface densities of SFR versus gas mass (in units of $\mathrm{M}_\odot\,\mathrm{pc}^{-2}$, to keep consistency with previous work) for each pixel individually and for four gas tracers. The colour represents the density of datapoints. Fits to the SF law across the whole galaxy can be seen in the bottom row of Figure 4.11, where $\log_{10}\Sigma_{\mathrm{SFR}}$ versus $\log_{10}\Sigma_{\mathrm{Gas}}$ is plotted for three ISM tracers (H I only is omitted). The SF law with total gas has an index of ∼6, but as in M31 this is thought to be dominated by saturation of H I or the gas turning molecular at $\Sigma_{\mathrm{Gas}} \sim 10\,\mathrm{M}_\odot\,\mathrm{pc}^{-2}$. A fit to the molecular SF law in M33 returns $N \sim$ 0.2 when minimising residuals in Σ_{SFR}, but this is severely skewed by points at low Σ_{H_2} with high measured SFRs. It appears that the highest density of datapoints in Figure 4.10 are consistent with a fit minimising residuals in Σ_{H_2} which gives $N \sim 1.2$.

Trendlines for each radial annulus (see Figure B.1 in Appendix B.1 for colour key) are shown on the top row of Figure 4.11 and the measured K-S index and gas depletion times ($\tau_{\mathrm{dep}} = \Sigma_{\mathrm{Gas}} / \Sigma_{\mathrm{SFR}}$) with radius are shown in Figure 4.12 with a dashed line of the same colour indicating the global value. Here it is clear that SFR surface density is generally higher in the inner regions (red points). When looking at the molecular gas SF law with radius (Figure 4.11, centre column), despite a constant measured K-S index of close to zero, the relationship is offset in Σ_{SFR} for each consecutive annulus. It is this offset with radius that appears to be the source of the global K-S index of ∼1.2.

CO-TO-H$_2$ CONVERSION FACTOR

The SF law with total gas and H$_2$ only assuming CO-to-H$_2$ conversion factors (X_{CO}) of 1, 2 (the nominal value) and $6 \times 10^{20}\,(\mathrm{K\,km\,s}^{-1})^{-1}\,\mathrm{cm}^{-2}$ can be seen in Figure 4.13. The K-S indices, N with molecular gas are largely unchanged, but a higher
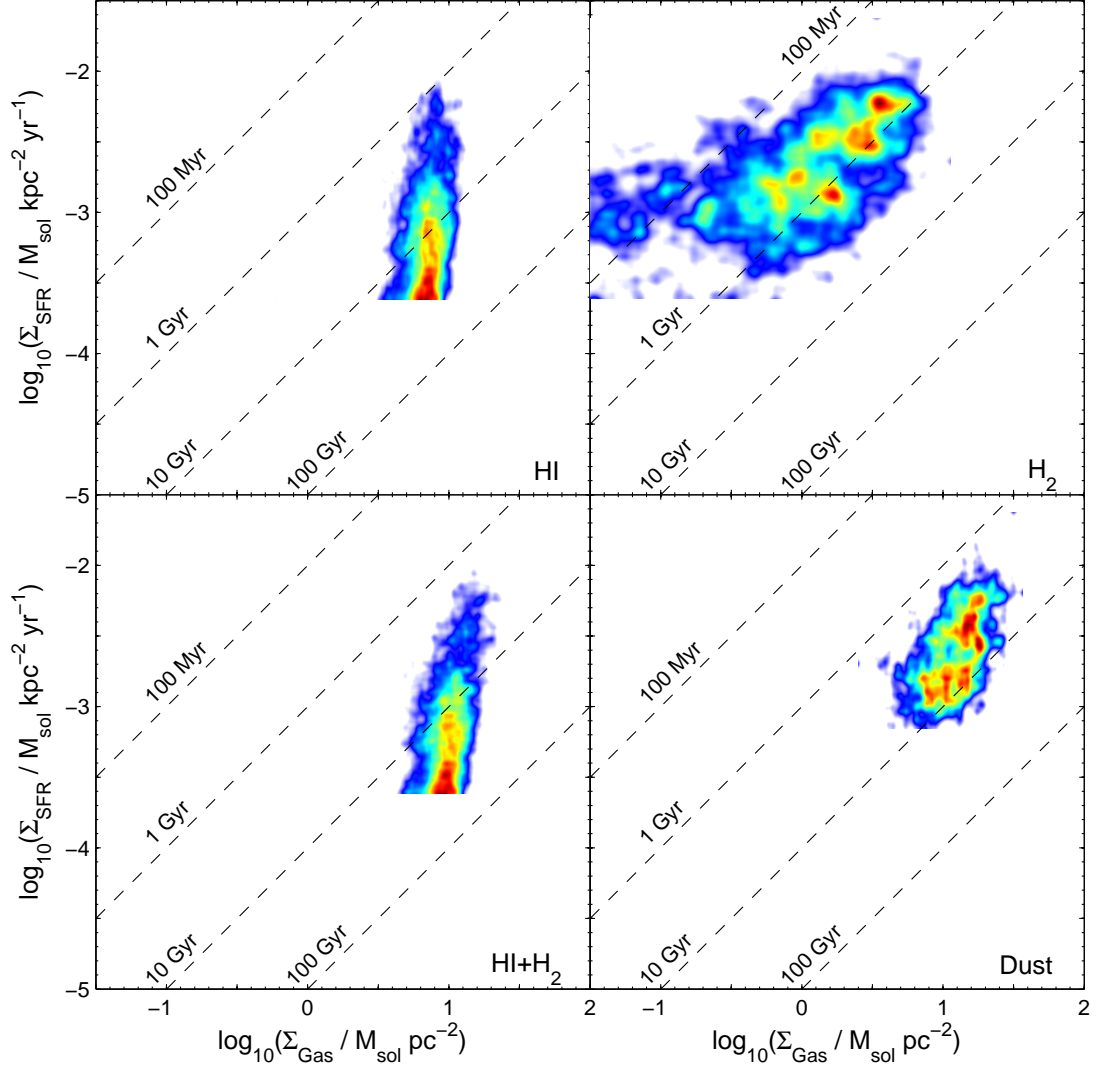
Figure 4.10 Star formation rate surface density against gas surface density in M33 for different gas tracers. From top left, they are H I only, molecular gas measured from H_2 as traced by CO(J=1-0), assuming a CO-H_2 conversion factor of $2\times10^{20}\,K\,km\,s^{-1})^{-1}\,cm^{-2}$, with an additional factor of 1.36 for heavier element abundances; bottom, total gas from H I and H_2 and total gas traced by dust mass (see Smith et al., 2012a), assuming a radial gradient in the gas-to-dust ratio. The colour represents the density of datapoints. Dashed lines are of constant gas depletion time.
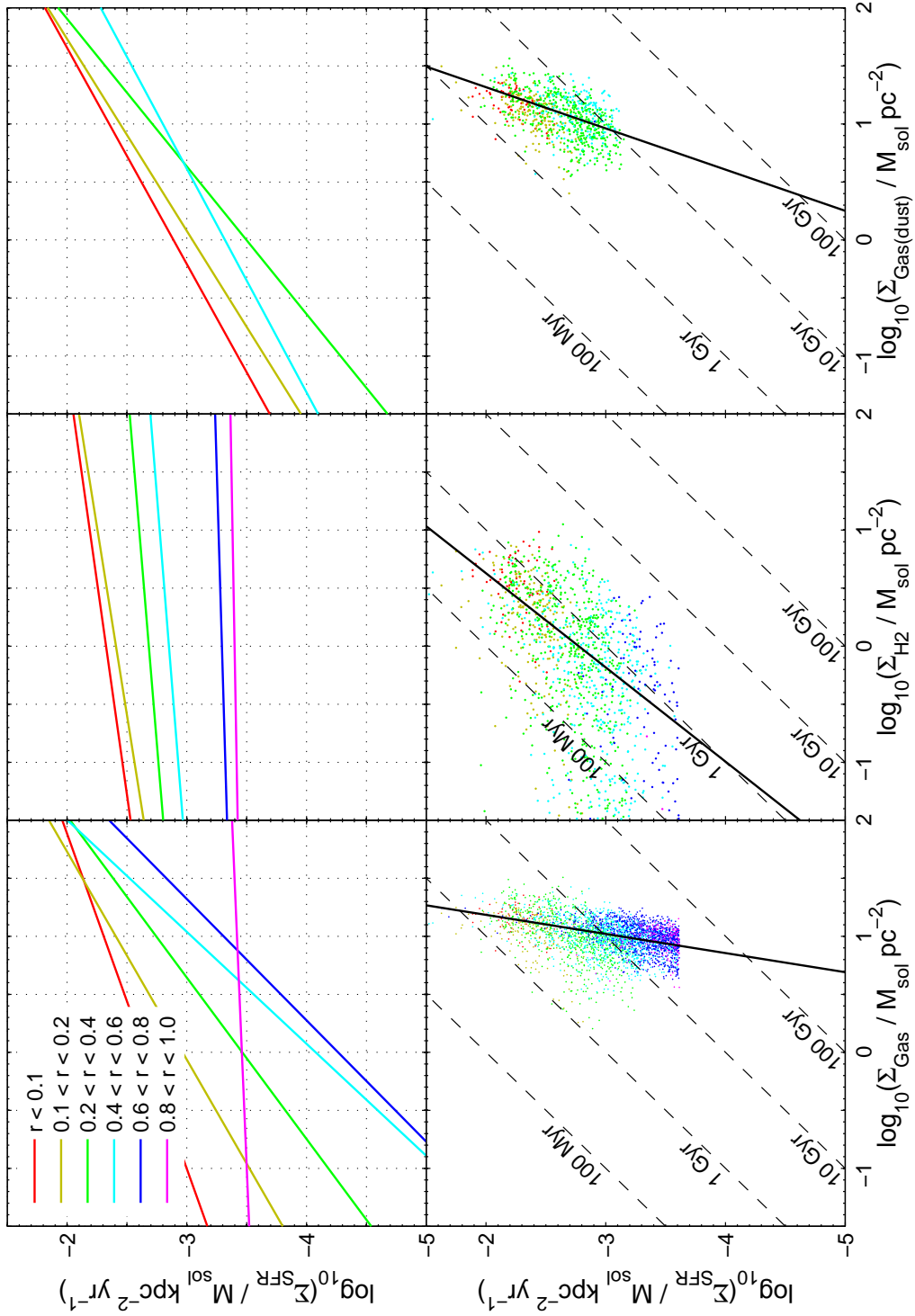
Figure 4.11 Star formation rate surface density against gas surface density split by galactocentric radius across M33. Each column covers one gas tracer. From left (image orientation), they are total gas from H I and CO(J=1-0), molecular gas from CO(J=1-0) only, and total gas traced by dust. The top row (image orientation) shows the fit to a power law for each radial annulus; the bottom row shows all pixels, colour coded by radius.
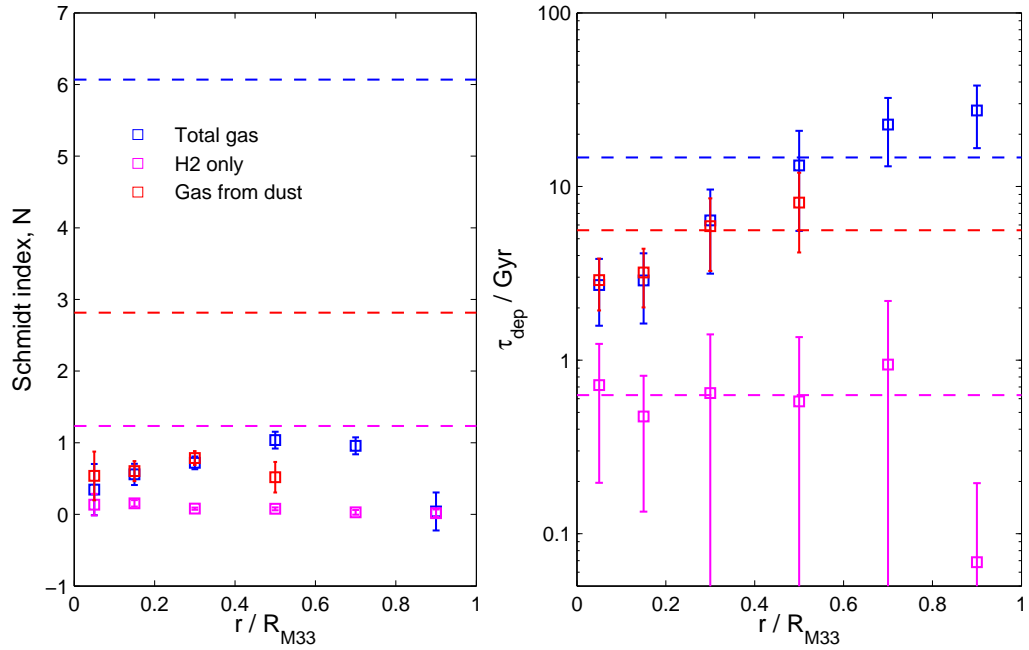
Figure 4.12 Kennicutt-Schmidt parameters with radius across M33. We compare the power law indices, N (left) and mean gas depletion time (τ_{dep}, right) using H I + H$_2$, H$_2$ only and total gas mass traced by dust. The dashed lines indicate the global values for M33. Errorbars represent the $2\,\sigma$ uncertainty in N and the standard deviation in the distribution of τ_{dep}.

X_{CO}-factor means a longer measured gas depletion time (Figure 4.14) varying from $\sim 300\,\mathrm{Myr}$ to $\sim 2\,\mathrm{Gyr}$. Increasing X_{CO} gives a shallower fitted slope when looking at total gas, $N \sim 3.5$ for $X_{\mathrm{CO}} = 6 \times 10^{20}\,(\mathrm{K\,km\,s^{-1}})^{-1}\,\mathrm{cm^{-2}}$.

4.5.3   DISCUSSION

The SF law in M33 using total gas (Figure 4.10, bottom left panel) appears to be dominated by either H I saturation at $\Sigma_{\mathrm{Gas}} = 10\,\mathrm{M_\odot\,pc^{-2}}$ (e.g Schruba et al., 2011) or gas turning molecular. However, as in Chapter 3 we do not see molecular gas above this density as would be expected. The same plot with molecular gas only (Figure 4.10, top right panel) appears consistent with a linear SF law and gas depletion time of $\sim 1\,\mathrm{Gyr}$. However, there are a significant number of datapoints exhibiting a low molecular gas surface density but high-SFR. This is indicative of the star formation law breaking down on small scales, due to single pixels picking out regions where gas has been depleted, but the young stars remain. A further explanation is that much of the molecular gas is missed by our CO tracer possibly due to the lower dissociation energy of CO compared to H$_2$.

We obtain a lower mean gas depletion time when looking at regions of molecular
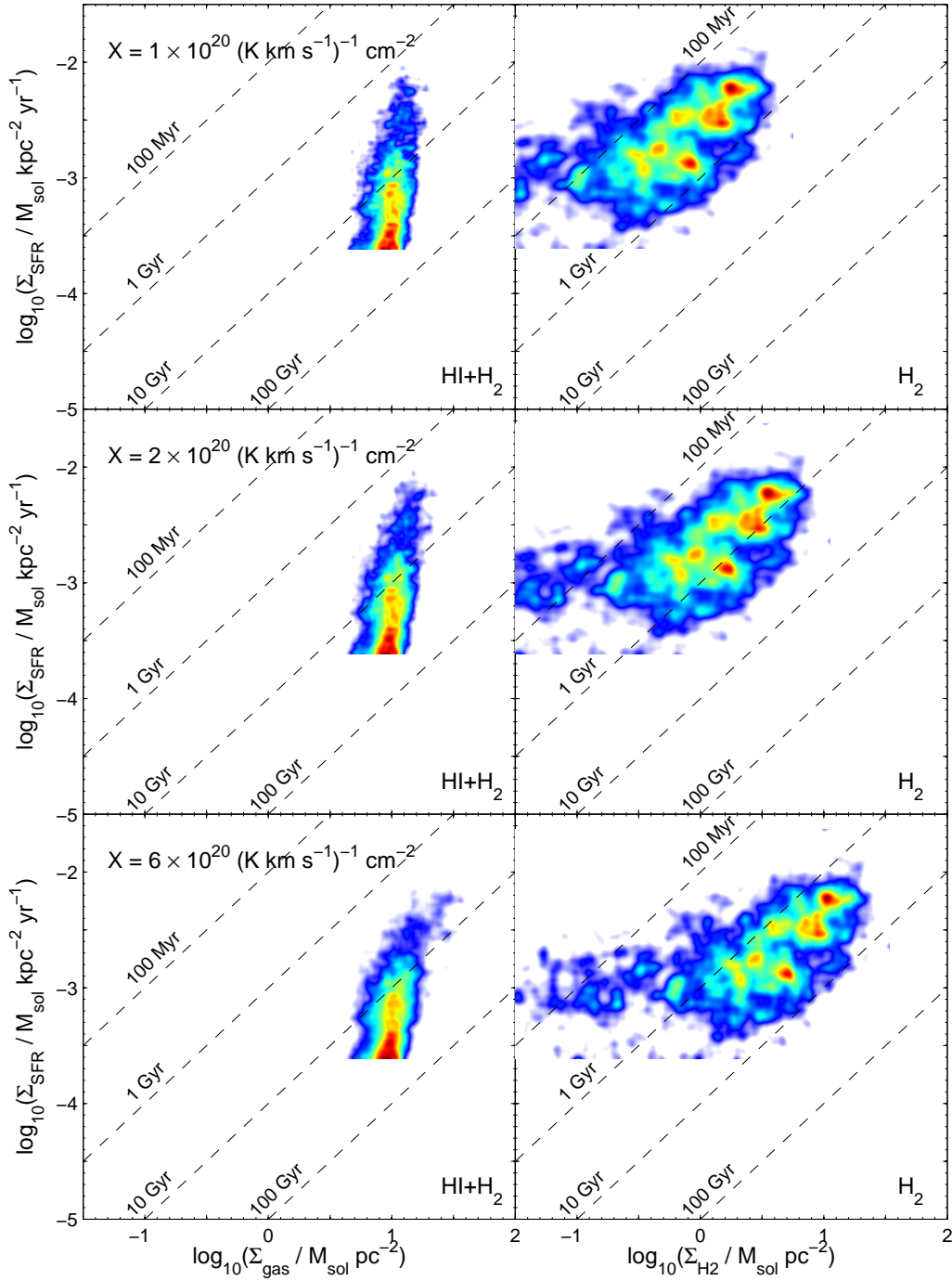
Figure 4.13 Star formation rate surface density against gas surface density in M31 for total gas and H_2 only assuming different CO-to-H_2 conversion factors. The left column shows total gas; the right, molecular hydrogen only. X-factor increases from top to bottom. The colour represents the density of datapoints. Dashed lines are of constant gas depletion time, τ_{dep}.
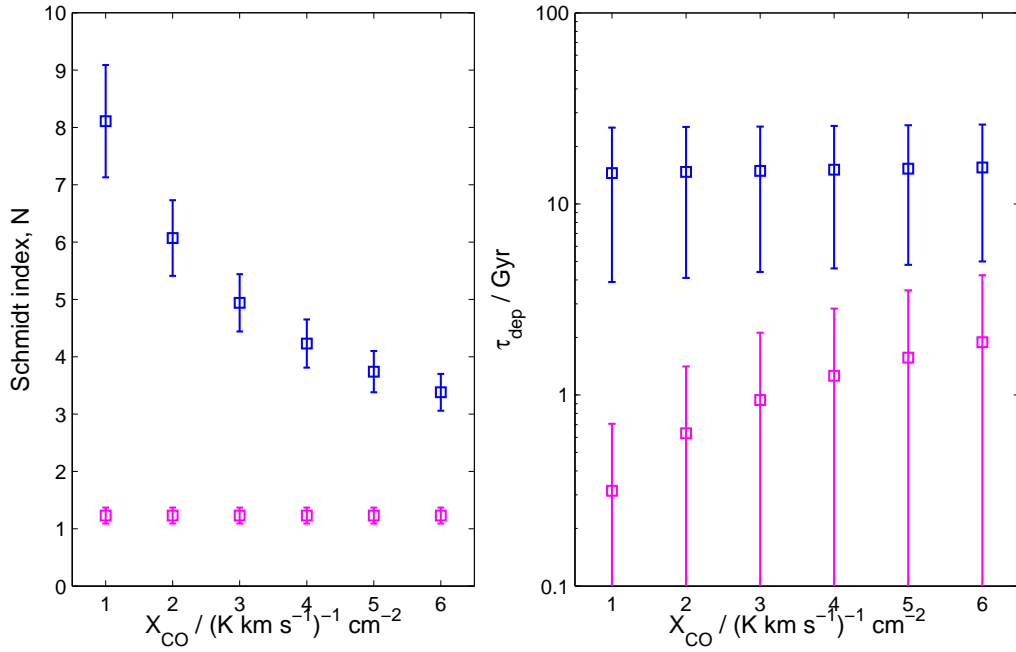
Figure 4.14 Kennicutt-Schmidt parameters with X_{CO} for M33. We compare the power law indices, N (left) and mean gas depletion time (τ_{dep}, right) using $H\,I + H_2$ and H_2 only. Errorbars represent the $2\,\sigma$ uncertainty in N and the standard deviation in the distribution of τ_{dep}.

gas ($\langle \tau_{dep}^{H2} \rangle \sim 600\,$Myr compared to $\langle \tau_{dep}^{Gas} \rangle \sim 15\,$Gyr) suggesting gas is converted to stars more efficiently here than in diffuse regions.

The star formation surface density is generally higher in the centre, with star formation efficiency with total gas decreasing with radius, as evidenced by the longer gas depletion times at high radii (Figure 4.12). The molecular gas depletion times appear roughly constant, consistently lower than those for total gas. This constant efficiency again suggests a linear relationship is representative of the SF law in M33.

As suggested in Chapter 3, observations of CII may help determine whether the regions of low gas surface density measured here do contain CO-free molecular gas, as discussed in Planck Collaboration et al. (2011). It would also be useful to fit the dust SED treating the mass emissivity index, β as a free parameter as was done for M31 (Smith et al., 2012a). This would hopefully improve the fit, but also give insights as to variations in the properties of the dust in different regions of M33.

4.6 M31 vs M33

Star formation is more centrally concentrated in M33, with M31 having largely depleted its gas (both monatomic and molecular) in the bulge. This conclusion as-

sumes an appropriate correction for the old stellar population, i.e. all of the contribution from old stars to our tracer emission has been removed. While the two methods of tracing star formation in M31 are consistent ($\Sigma_{\mathrm{SFR,UV+24}} = 0.32\,\mathrm{M_\odot\,yr^{-1}}$ and $\Sigma_{\mathrm{SFR,FIR}} = 0.33\,\mathrm{M_\odot\,yr^{-1}}$) when using the same assumptions, there is a discrepancy between the two in M33 ($\Sigma_{\mathrm{SFR,UV+24}} = 0.19\,\mathrm{M_\odot\,yr^{-1}}$ and $\Sigma_{\mathrm{SFR,FIR}} = 0.11\,\mathrm{M_\odot\,yr^{-1}}$). The underestimate from the FIR emission in M33 could be due to dust and star formation not being spatially correlated, so much of the emission from young stars is not absorbed by dust. However, the similarity between the two maps in Figure 4.5 suggests otherwise. It is possible that as many pixels are not well fit by a one- or two- temperature greybody (Figure 4.7), the conversion between FIR luminosity and SFR is not well calibrated for this galaxy.

M33 appears consistent with other nearby galaxies both in terms of SFR and gas surface density (Figure 4.9). When comparing to M31 however (Figure 3.10), it is clear that the mean SFR surface density is higher in M33 despite a lower global SFR. This is expected as M33 is a later-type galaxy, but significantly smaller. The gas surface densities appear approximately equivalent, suggesting a higher star formation efficiency (SFE) or lower gas depletion time ($\tau_{\mathrm{dep}} = \Sigma_{\mathrm{Gas}} / \Sigma_{\mathrm{SFR}}$). Indeed, the measured gas depletion times in M33 when considering each gas tracer separately are all shorter than the corresponding values for M31 (Table 4.1).

The higher K-S index with total gas in M33 appears to be the result of significantly less diffuse hydrogen, with all datapoints studied here having $\Sigma_{\mathrm{HI}} > 3\,\mathrm{M_\odot\,pc^{-2}}$, close to the threshold for gas turning molecular at $\sim 10\,\mathrm{M_\odot\,pc^{-2}}$. The molecular gas SF law suggests a roughly constant gas depletion time in M33 (for the majority of datapoints) while M31 exhibits lower SFE at high H_2 surface densities, suggesting star formation is being quenched in these regions. This may be an indication of M31 being at a later stage in its evolution than M33, expected as it is an earlier-type galaxy.

Table 4.1 Comparison of M31 and M33 in terms of SF law parameters.

Galaxy	SFR / $\mathrm{M_\odot\,yr^{-1}}$	N_{Gas}	$\tau_{\mathrm{dep}}^{\mathrm{Gas}}$ / Gyr	N_{H2}	$\tau_{\mathrm{dep}}^{\mathrm{H2}}$ / Gyr	N_{Dust}	$\tau_{\mathrm{dep}}^{\mathrm{Dust}}$ / Gyr
M31	0.25	2.0	50	0.6	4	0.6	20
M33	0.16	6.1	15	1.2	0.63	2.8	5.6

4.7   SUMMARY

In this chapter I have determined the surface density of star formation in M33 using combined FUV and 24 μm emission and separately the FIR luminosity. I aim to correct the former for emission from both unobscured and embedded old stars and find a global SFR of $0.16^{+0.03}_{-0.02}\,\mathrm{M_\odot\,yr^{-1}}$. The FIR emission appears to be spatially correlated with the SFR map made using FUV and 24 μm emission, but gives a consistently lower SFR than the FUV and 24 μm map given the same assumptions.

I produce two maps of the total gas in M33. The first uses H I and CO, assuming a CO-H_2 conversion factor of $2\times10^{20}\,(\mathrm{K\,km\,s^{-1}})^{-1}\,\mathrm{cm^{-2}}$. I produce the second map of total gas from the dust emission.

When comparing with previous work by Kennicutt (1998b) and Leroy et al. (2008) on the global SFR and gas mass, I find the mean molecular gas surface density and SFR surface density for M33 sit on the low end of the relation determined in Kennicutt (1998b).

Our measurement of the star formation law on sub-kpc scales varies with gas tracer. The most direct measurement, using H I and CO to trace total gas, shows little correlation and is dominated by H I saturation at approximately $\Sigma_{\mathrm{Gas}} = 10\,\mathrm{M_\odot\,pc^{-2}}$.

Using molecular gas only gives a much lower K-S index of $N \sim 0.2$, but this is severely skewed by high SFR at low gas masses, when the majority of points appear to be consistent with a linear SF law. We suggest that the spurious low molecular gas mass could be due to CO-free molecular hydrogen forming stars at a significant rate.

When compared to M31, M33 has a significantly higher surface density of star formation, as expected for a later type spiral. However, their global SFRs are roughly equivalent as M31 is a much larger galaxy.

ACKNOWLEDGMENTS

5 CONCLUSIONS

Take the risk of thinking for yourself. Much more happiness,
truth, beauty and wisdom will come to you that way.

–CHRISTOPHER HITCHENS

In this thesis I have explored the star formation and the interstellar medium (ISM) properties of a number of nearby galaxies including the two largest extra-galactic sources in the local group. I have used multiwavelength datasets that are publicly available as well as some of the most recent and high fidelity observations made by the *Herschel Space Observatory*.

5.1 THE HERSCHEL REFERENCE SURVEY

Here I compared the dust and star formation properties of 153 spiral galaxies in the *Herschel* Reference Survey (HRS). The sample was divided into galaxies of different morphology (barred or unbarred), environment (cluster or field), Hubble-type and stellar mass.

The far-infrared (FIR) spectral energy distribution (SED) was fitted to *Herschel SPIRE* and *PACS* data (over a range 100–500 μm) in order to determine the dust mass, luminosity and dust temperature of each galaxy. Stellar masses, surface densities of star formation and NUV-r colour were also compared.

It appears that the HRS galaxies occupy the sub-threshold regime of the Kennicutt-Schmidt star formation law plot, when using dust to trace total gas mass, with little correlation visible between Σ_{SFR} and Σ_{Gas}. Any follow-up could make use of recently obtained carbon monoxide (CO) observations of the HRS (Matthew Smith, priv. comm) enabling study of a molecular gas star formation law (see Bigiel et al., 2011; Rahman et al., 2012) for these galaxies.

It appears that the barred galaxies in this sample are generally lower stellar mass than their unbarred counterparts. It is possible that this is related to the speed at which bars are formed in galaxies of different mass, i.e. low mass spirals take longer

to form bars whereas higher mass galaxies have already created and destroyed their bar by the current epoch, assuming bar creation is a cyclic process. This is counter to some previous work which finds a constant bar fraction in high-mass galaxies with redshift.

There is little difference in the other properties between barred and unbarred galaxies. However, there is a trend in dust-to-stellar mass ratio, NUV-r colour and FIR luminosity normalised by stellar mass with Hubble-type, consistent with previous work. I also find that cluster galaxies are less dusty than those in the field.

Galaxies of high stellar mass have a lower dust-to-stellar mass ratio. They are also generally redder in terms of NUV-r colour, so less actively star forming. This suggests larger galaxies have destroyed their dust and become more passive. The correlation between these parameters is expected if we assume interstellar dust is a primary driver of star formation.

Morphological classification is very subjective, so an immediate follow-up piece of work would be to check the classifications used here against those used in other large surveys. Here, I focus on global galaxy properties only. Other studies have suggested that bars funnel material, fuelling star formation in the centre. This suggests that it would be useful to isolate the central regions to determine whether barred galaxies have more centrally concentrated star formation and/or dust mass than unbarred spirals. Future work could also explore the dust properties of the galaxies by setting the mass emissivity index, β, to be a free parameter in the SED fitting routine.

5.2   THE STAR FORMATION LAW IN M31

The star formation (SF) law in both M31 and M33 has been explored down to $140\,\mathrm{pc}$ scales. To that end, this work uses a variety of tracers of star formation and the ISM.

Star formation is traced using far-ultraviolet (FUV) and $24\,\mu\mathrm{m}$ (infrared) emission to probe unobscured and embedded star formation respectively. Foreground stars are removed using the UV-colour in each pixel and old stars are corrected for by assuming $3.6\,\mu\mathrm{m}$ emission traces the general stellar population.

After correcting for foreground stars and the old stellar population we find a global star formation rate (SFR) in M31 of $0.25\,\mathrm{M_\odot\,yr^{-1}}$. This is compared with star formation traced using the FIR luminosity (L_{IR}), as calculated using *Herschel SPIRE* and *PACS* observations made by the *Herschel* Exploitation of Local Galaxy Andromeda (HELGA) collaboration, and assuming the same initial mass function and starburst timescale. There is general agreement between the two SFR tracers,

however, we are unable to correct the old stars when using FIR emission as there is no visible correlation between L_{IR} and our tracer of the old stellar population (3.6 μm emission) as was the case with UV and 24 μm emission.

H I and CO(J=1-0) are combined to produce a map of total gas in M31 which is dominated by monatomic hydrogen. The SF law using total gas yields an index of $N \sim$ 2.0. I attribute this large index to saturation of monatomic hydrogen, or gas turning molecular and not being traced by CO. The same with molecular gas from CO shows a good correlation with $N \sim$ 0.6. This is consistent with work by Schruba et al. (2011) that found a molecular gas star formation law in a regime dominated by monatomic gas. An index lower than unity suggests that star formation becomes less efficient in M31 at high gas densities. Gas traced by dust mass, calculated from *Herschel* observations on a pixel-by-pixel basis, results in a similarly small index.

Radial variations in the SF law are probed by dividing the galaxy into elliptical annuli. Mean gas depletion time appears to increase with radius in M31. This is consistent with a sub-linear SF law and the inner regions of the galaxy containing a low density of gas.

Employing a larger conversion factor between CO(J=1-0) emission and molecular hydrogen surface density obviously results in a longer depletion time with molecular gas, but it also has the effect of shallowing the slope of the SF law with total gas. The difference is minimal however, due to the dominance of H I in M31.

Effects due to the scale on which the SF law is probed, are tested using pixel sizes of 40, 140 and 500 pc. It has been suggested that the SF law varies depending on the scale being probed (e.g. Kruijssen & Longmore, 2014). Here however, no difference in the SF law slope with pixel size is observed. Gas depletion times also appear consistent. Studying the SF law with total gas while selecting pixels in molecular clouds only does show some interesting characteristics. A spur beyond the region at which H I saturates, which follows a line of approximately constant gas depletion time, mimics similar plots in previous work (e.g. Bigiel et al., 2008).

The most obvious piece of follow-up is to employ different tracers to measure the amount of dense gas, e.g. C II. This would allow further exploration of the high gas density, low star formation efficiency (SFE) regions that give rise to the measured sub-linear SF law. It also has the potential to show regions of dense gas that are not traced by CO, i.e. CO-free molecular gas.

5.3 THE STAR FORMATION LAW IN M33

The same prescriptions are applied to the third local group member, M33. Here the correction for the older stellar population is found from the ratio of SFR tracer to $3.6\,\mu$m emission found in M31. This is done because a clear correlation, from which we derive our correction factor, is not visible. This is possibly due to the flocculent nature of M33 and lacking a prominent bulge.

Using FUV and $24\,\mu$m emission gives a global SFR of $0.16\,M_\odot\,\mathrm{yr}^{-1}$. This is a lower rate than the much larger M31 but the mean surface density of star formation for M33 is higher, as expected for a later type spiral. SFR from FIR luminosity is spatially correlated with the FUV and $24\,\mu$m tracer, but is consistently lower, assuming the same initial mass function.

In common with M31, molecular gas is sparse in M33. The SF law using total gas is again dominated by monatomic hydrogen, the steep slope indicating that SFR cannot be predicted from the gas mass in these regimes (e.g. Schruba, 2013). Using molecular gas in M33 gives an even shallower slope than that found for M31 while minimising residuals in Σ_{SFR}. However, it appears most pixels follow an approximately linear SF law ($N = 1.2$ when minimising residuals in Σ_{H_2}), with the shallower measured slope due to some areas of low molecular gas mass (as measured from CO(J=1-0) showing high SFR. This may be evidence for molecular gas in M33 that is not traced by CO or the SF law breaking down on GMC scales due to regions with a young stellar population where gas is fully depleted.

More vigorous exploration of the dust SED in M33 would be beneficial due to the relatively poor fits to the FIR data when compared to M31. The first task would be to test for variations in β across the galaxy as was done in M31. C II observations would also be useful to explore the regions that appear to deviate from the linear molecular gas SF law followed by the majority of datapoints, particularly those areas with a high-SFR surface density, but little molecular gas.

5.4 THE FUTURE

The work contained within this thesis, and significant studies undertaken by the THINGS and KINGFISH collaborations, among others, have shown that the 'star formation law' is approximately linear on sub-galactic scales. The super-linear index of Kennicutt (1998b) was often attributed to free-fall time being the main driver of this relation, which becomes more significant on the smallest scales. Since studies conducted on sub-kpc scales have shown a different form of the star formation

law, it appears this assertion was incorrect. We in fact have a much simpler picture of star formation in a galaxy as it appears that in nearby galaxies the star formation efficiency is constant between GMCs and GMC complexes. The result is that when averaging over larger regions, we are simply counting regions of constant SFE, hence building up a linear 'star formation law.'

If the majority of galaxies in the local universe adhere to this one-to-one relationship between molecular gas surface density and star formation rate surface density, the focus should shift from this relationship to an earlier stage in the process. If molecular gas appears to form stars at a constant efficiency, how efficiently is the more diffuse interstellar medium converted to molecular gas, and what are the key processes that regulate this transition?

The 'if' still needs to be looked at however. New observations of dense gas, including those taken by the *Atacama Large Millimetre Array* (*ALMA*) and recent observations of CO in the HRS, could help discover more regions that deviate from this simple relationship. As the work in this thesis shows, there are some exceptions where efficiency is enhanced or decreased, making them prime candidates for future studies. Current and future observations of M31, will help immeasurably in this endeavour. Most notably the Panchromatic Hubble Andromeda Treasury (PHAT) will allow kinematic decomposition of the galactic structure and study of the star formation history of small regions ($\sim 50\,\mathrm{pc}$). It will also allow more reliable calibration of SFR indicators, allowing for more reliable exploration of the coupling between star formation and the ISM.

AFTERWORD

At the beginning of my PhD, I remember getting the obligatory talk about what is expected of you during your studies, in my case by Professor Peter Coles, now of the University of Sussex. He made it clear that research that makes it into a thesis must be put into context. Your work must include how it relates to the state of the art. I hope I have managed to do that throughout this work but I did want to add a further level, namely putting astronomy into context.

There are of course the practical advances that have come as a byproduct of astronomy and space travel, which are now part of everyday life in the western world. There is the educational side too, undoubtedly astronomy is one of the most inspiring topics when trying to attract young people to science. But more than this, studying the universe helps put ourselves as human beings into context. There is no better illustration of this than the Voyager photograph "The Pale Blue Dot," and some words from Carl Sagan.
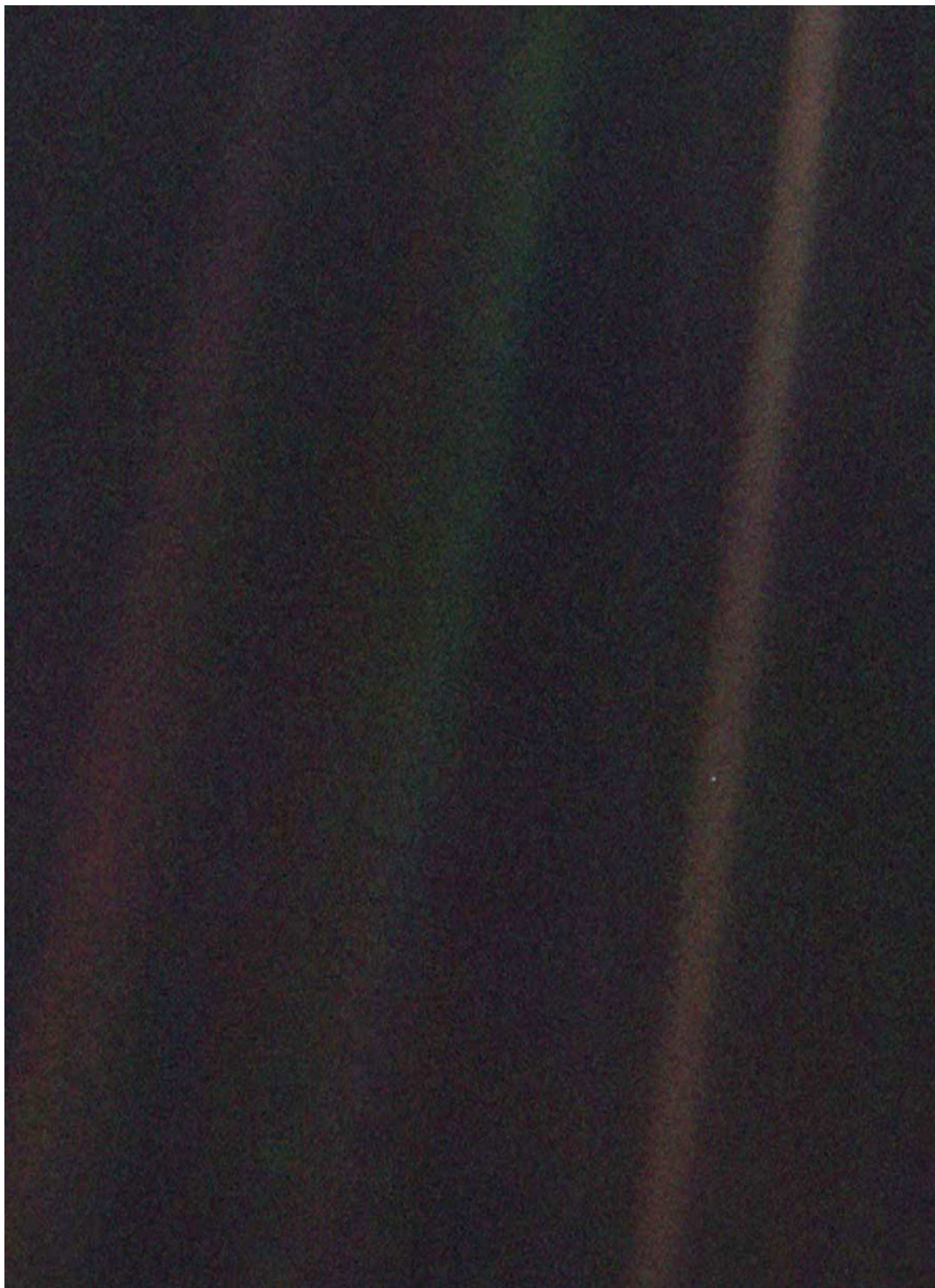
From this distant vantage point, the Earth might not seem of any particular interest. But for us, it's different... That's here. That's home. That's us. On it everyone you love, everyone you know, everyone you ever heard of, every human being who ever was, lived out their lives. The aggregate of our joy and suffering, thousands of confident religions, ideologies, and economic doctrines, every hunter and forager, every hero and coward, every creator and destroyer of civilization, every king and peasant, every young couple in love, every mother and father, hopeful child, inventor and explorer, every teacher of morals, every corrupt politician, every "superstar," every "supreme leader," every saint and sinner in the history of our species lived there on a mote of dust suspended in a sunbeam.

The Earth is a very small stage in a vast cosmic arena. Think of the rivers of blood spilled by all those generals and emperors so that in glory and triumph they could become the momentary masters of a fraction of a dot. Think of the endless cruelties visited by the inhabitants of one corner of this pixel on the scarcely distinguishable inhabitants of some other corner. How frequent their misunderstandings, how eager they are to kill one another, how fervent their hatreds. Our posturings, our imagined self-importance, the delusion that we have some privileged position in the universe, are challenged by this point of pale light. Our planet is a lonely speck in the great enveloping cosmic dark. In our obscurity in all this vastness there is no hint that help will come from elsewhere to save us from ourselves.

The Earth is the only world known, so far, to harbor life. There is nowhere else, at least in the near future, to which our species could migrate. Visit, yes. Settle, not yet. Like it or not, for the moment, the Earth is where we make our stand. It has been said that astronomy is a humbling and character-building experience. There is perhaps no better demonstration of the folly of human conceits than this distant image of our tiny world. To me, it underscores our responsibility to deal more kindly with one another and to preserve and cherish the pale blue dot, the only home we've ever known.

Bibliography

Abazajian, K. N., et al. 2009, ApJS, 182, 543

Aniano, G., Draine, B. T., Gordon, K. D., & Sandstrom, K. 2011, PASP, 123, 1218

Aniano, G., et al. 2012, ApJ, 756, 138

Athanassoula, E. 2012, ArXiv e-prints

Athanassoula, E., Machado, R. E. G., & Rodionov, S. A. 2013, MNRAS, 429, 1949

Auld, R., et al. 2013, MNRAS, 428, 1880

Barazza, F. D., Jogee, S., & Marinova, I. 2008, ApJ, 675, 1194

Barmby, P., et al. 2006, ApJ, 650, L45

Bendo, G. J., Galliano, F., & Madden, S. C. 2012a, MNRAS, 423, 197

Bendo, G. J., et al. 2006, ApJ, 645, 134

—. 2010, A&A, 518, L65

—. 2012b, MNRAS, 419, 1833

Bessel, F. W. 1838, MNRAS, 4, 152

Bigiel, F., Leroy, A., & Walter, F. 2011, in IAU Symposium, Vol. 270, Computational Star Formation, ed. J. Alves, B. G. Elmegreen, J. M. Girart, & V. Trimble, 327–334

Bigiel, F., Leroy, A., Walter, F., Brinks, E., de Blok, W. J. G., Madore, B., & Thornley, M. D. 2008, AJ, 136, 2846

Boissier, S., Prantzos, N., Boselli, A., & Gavazzi, G. 2003, MNRAS, 346, 1215

Bolatto, A. D., Leroy, A. K., Rosolowsky, E., Walter, F., & Blitz, L. 2008, ApJ, 686, 948

Bolatto, A. D., Wolfire, M., & Leroy, A. K. 2013, ARA&A, 51, 207

Boquien, M., et al. 2011, AJ, 142, 111

Boselli, A., et al. 2010a, PASP, 122, 261

—. 2010b, PASP, 122, 261

Bournaud, F., & Combes, F. 2002, A&A, 392, 83

Braun, R., Thilker, D. A., Walterbos, R. A. M., & Corbelli, E. 2009, ApJ, 695, 937

Calzetti, D. 2007, Nuovo Cimento B Serie, 122, 971

—. 2013, Star Formation Rate Indicators, ed. J. Falcón-Barroso & J. H. Knapen, 419

Calzetti, D., et al. 2005, ApJ, 633, 871

—. 2007, ApJ, 666, 870

—. 2010, ApJ, 714, 1256

Chabrier, G. 2003, PASP, 115, 763

Ciesla, L., et al. 2012, A&A, 543, A161

Corbelli, E., Verley, S., Elmegreen, B. G., & Giovanardi, C. 2009, A&A, 495, 479

Cortese, L., et al. 2012a, A&A, 540, A52

—. 2012b, A&A, 544, A101

—. 2014, MNRAS, 440, 942

Das, M., Teuben, P. J., Vogel, S. N., Harris, A., Regan, M. W., & Sheth, K. 2002, in Astronomical Society of the Pacific Conference Series, Vol. 275, Disks of Galaxies: Kinematics, Dynamics and Peturbations, ed. E. Athanassoula, A. Bosma, & R. Mujica, 157–160

Davidge, T. J., McConnachie, A. W., Fardal, M. A., Fliri, J., Valls-Gabaud, D., Chapman, S. C., Lewis, G. F., & Rich, R. M. 2012, ApJ, 751, 74

Davies, J. I., et al. 2010, A&A, 518, L48

Davies, R. D., & Lewis, B. M. 1973, MNRAS, 165, 231

de Vaucouleurs, G., de Vaucouleurs, A., Corwin, Jr., H. G., Buta, R. J., Paturel, G., & Fouqué, P. 1991, Third Reference Catalogue of Bright Galaxies. Volume I: Explanations and references. Volume II: Data for galaxies between 0^h and 12^h. Volume III: Data for galaxies between 12^h and 24^h.

Debattista, V. P., Mayer, L., Carollo, C. M., Moore, B., Wadsley, J., & Quinn, T. 2006, ApJ, 645, 209

Draine, B. T. 2003, ARA&A, 41, 241

Dreyer, J. L. E. 1888, MmRAS, 49, 1

—. 1895, MmRAS, 51, 185

Eales, S., et al. 2010, PASP, 122, 499

—. 2012, ApJ, 761, 168

Elbaz, D., et al. 2011, A&A, 533, A119

Elmegreen, B. G. 1994, ApJ, 425, L73

Eskridge, P. B., & Frogel, J. A. 1999, Ap&SS, 269, 427

Ewen, H. I., & Purcell, E. M. 1951, Nature, 168, 356

Fazio, G. G., et al. 2004, ApJS, 154, 10

Feldmann, R., Gnedin, N. Y., & Kravtsov, A. V. 2011, ApJ, 732, 115

Ford, G. P., et al. 2013, ApJ, 769, 55

Fritz, J., et al. 2012, A&A, 546, A34

Gavazzi, G., Boselli, A., Pedotti, P., Gallazzi, A., & Carrasco, L. 2002, A&A, 396, 449

Glover, S. C. O., & Mac Low, M.-M. 2011, in EAS Publications Series, Vol. 52, EAS Publications Series, ed. M. Röllig, R. Simon, V. Ossenkopf, & J. Stutzki, 147–150

Gordon, K. D., et al. 2006, ApJ, 638, L87

Griffin, M. J., et al. 2010, A&A, 518, L3

Groves, B., et al. 2012, MNRAS, 426, 892

Hao, C.-N., Kennicutt, R. C., Johnson, B. D., Calzetti, D., Dale, D. A., & Moustakas, J. 2011, ApJ, 741, 124

Hartwick, F. D. A. 1971, ApJ, 163, 431

Heyer, M. H., Corbelli, E., Schneider, S. E., & Young, J. S. 2004, ApJ, 602, 723

Hubble, E. 1926, Contributions from the Mount Wilson Observatory / Carnegie Institution of Washington, 324, 1

Hubble, E. P. 1925, The Observatory, 48, 139

Israel, F. P. 1997, A&A, 328, 471

Karachentsev, I. D., & Kashibadze, O. G. 2006, Astrophysics, 49, 3

Kennicutt, R. C., & Evans, N. J. 2012, ARA&A, 50, 531

Kennicutt, Jr., R. C. 1983, AJ, 88, 483

—. 1998a, ARA&A, 36, 189

—. 1998b, ApJ, 498, 541

Kennicutt, Jr., R. C., et al. 2009, ApJ, 703, 1672

Kirk, J. M., et al. 2013, ArXiv e-prints

Knapen, J. H., Pérez-Ramírez, D., & Laine, S. 2002, MNRAS, 337, 808

Kormendy, J. 2008, in IAU Symposium, Vol. 245, IAU Symposium, ed. M. Bureau, E. Athanassoula, & B. Barbuy, 107–112

Kormendy, J., & Kennicutt, Jr., R. C. 2004, ARA&A, 42, 603

Kramer, C., et al. 2010, A&A, 518, L67

Kroupa, P. 2001, MNRAS, 322, 231

Kruijssen, J. M. D., & Longmore, S. N. 2014, ArXiv e-prints

Krumholz, M. R., & Thompson, T. A. 2007, ApJ, 669, 289

Kuno, N., et al. 2007, PASJ, 59, 117

Lada, C. J., Forbrich, J., Lombardi, M., & Alves, J. F. 2012, ApJ, 745, 190

Le Fèvre, O., et al. 2000, MNRAS, 311, 565

Le Floc'h, E., et al. 2005, ApJ, 632, 169

Leavitt, H. S. 1908, Annals of Harvard College Observatory, 60, 87

Leroy, A. K., Walter, F., Brinks, E., Bigiel, F., de Blok, W. J. G., Madore, B., & Thornley, M. D. 2008, AJ, 136, 2782

Madore, B. F. 1977, MNRAS, 178, 1

Magrini, L., Stanghellini, L., & Villaver, E. 2009, ApJ, 696, 729

Martin, C., & GALEX Team. 2005a, in IAU Symposium, Vol. 216, Maps of the Cosmos, ed. M. Colless, L. Staveley-Smith, & R. A. Stathakis, 221

Martin, C., & GALEX Team. 2005b, in IAU Symposium, Vol. 216, Maps of the Cosmos, ed. M. Colless, L. Staveley-Smith, & R. A. Stathakis, 221

Masters, K. L., et al. 2012, MNRAS, 424, 2180

McConnachie, A. W., Irwin, M. J., Ferguson, A. M. N., Ibata, R. A., Lewis, G. F., & Tanvir, N. 2004, MNRAS, 350, 243

—. 2005, MNRAS, 356, 979

McKee, C. F., & Ostriker, E. C. 2007, ARA&A, 45, 565

Melvin, T., et al. 2014, MNRAS

Morgan, H. L., & Edmunds, M. G. 2003, MNRAS, 343, 427

Murphy, E. J., et al. 2011, ApJ, 737, 67

Nair, P. B., & Abraham, R. G. 2010, ApJ, 714, L260

Narayanan, D., Krumholz, M., Ostriker, E. C., & Hernquist, L. 2011, MNRAS, 418, 664

Nieten, C., Neininger, N., Guélin, M., Ungerechts, H., Lucas, R., Berkhuijsen, E. M., Beck, R., & Wielebinski, R. 2006, A&A, 453, 459

Odenwald, S., Newmark, J., & Smoot, G. 1998, ApJ, 500, 554

Oh, S., Oh, K., & Yi, S. K. 2012, ApJS, 198, 4

Olsen, K. A. G., Blum, R. D., Stephens, A. W., Davidge, T. J., Massey, P., Strom, S. E., & Rigaut, F. 2006, AJ, 132, 271

Pérez-González, P. G., et al. 2006, ApJ, 648, 987

Pilbratt, G. L., et al. 2010, A&A, 518, L1

Pineda, J. L., Goldsmith, P. F., Chapman, N., Snell, R. L., Li, D., Cambrésy, L., & Brunt, C. 2010, ApJ, 721, 686

Planck, M. 1901, Annalen der Physik, 309, 553

Planck Collaboration et al. 2011, A&A, 536, A19

Poglitsch, A., et al. 2010, A&A, 518, L2

Proctor, R. A. 1869, MNRAS, 29, 337

Rahman, N., et al. 2012, ApJ, 745, 183

Ranalli, P., Comastri, A., & Setti, G. 2003, A&A, 399, 39

Rieke, G. H., Alonso-Herrero, A., Weiner, B. J., Pérez-González, P. G., Blaylock, M., Donley, J. L., & Marcillac, D. 2009, ApJ, 692, 556

Rieke, G. H., et al. 2004, ApJS, 154, 25

Rosolowsky, E., Keto, E., Matsushita, S., & Willner, S. P. 2007, ApJ, 661, 830

Rowlands, K., et al. 2012, MNRAS, 419, 2545

Salim, S., et al. 2007, ApJS, 173, 267

Salpeter, E. E. 1955, ApJ, 121, 161

Sandage, A. 2005, ARA&A, 43, 581

Sandstrom, K. M., et al. 2013, ApJ, 777, 5

Sanduleak, N. 1969, AJ, 74, 47

Schmidt, M. 1959, ApJ, 129, 243

Schruba, A. 2013, in IAU Symposium, Vol. 292, IAU Symposium, ed. T. Wong & J. Ott, 311–318

Schruba, A., et al. 2011, AJ, 142, 37

Sellwood, J. A., & Wilkinson, A. 1993, Reports on Progress in Physics, 56, 173

Sheth, K., Vogel, S. N., Regan, M. W., Thornley, M. D., & Teuben, P. J. 2005, ApJ, 632, 217

Sheth, K., et al. 2008, ApJ, 675, 1141

Smith, M. W. L. 2012, PhD thesis, Cardiff University

Smith, M. W. L., et al. 2012a, ApJ, 756, 40

—. 2012b, ApJ, 748, 123

Sofue, Y., Takabayashi, M., & Murata, Y. 1994, in Astronomical Society of the Pacific Conference Series, Vol. 59, IAU Colloq. 140: Astronomy with Millimeter and Submillimeter Wave Interferometry, ed. M. Ishiguro & J. Welch, 366–+

Sohn, S. T., Anderson, J., & van der Marel, R. P. 2012, ApJ, 753, 7

Spitzer, L. 1978, Physical processes in the interstellar medium (New York Wiley)

Strong, A. W., Moskalenko, I. V., Reimer, O., Digel, S., & Diehl, R. 2004, A&A, 422, L47

Strong, A. W., et al. 1988, A&A, 207, 1

Tabatabaei, F. S., & Berkhuijsen, E. M. 2010, A&A, 517, A77

Telesco, C. M. 1988, ARA&A, 26, 343

Thilker, D. A., Braun, R., & Walterbos, R. A. M. 2002, in Astronomical Society of the Pacific Conference Series, Vol. 276, Seeing Through the Dust: The Detection of HI and the Exploration of the ISM in Galaxies, ed. A. R. Taylor, T. L. Landecker, & A. G. Willis, 370

Thilker, D. A., et al. 2005, ApJ, 619, L67

Tosaki, T., et al. 2011, PASJ, 63, 1171

van de Hulst, H. C. 1945, Nederlands Tijdschrift voor Natuurkunde, 11, 201

—. 1948, Harvard Observatory Monographs, 7, 73

van den Bergh, S. 2011, AJ, 141, 188

Verley, S., Corbelli, E., Giovanardi, C., & Hunt, L. K. 2009, A&A, 493, 453

—. 2010, A&A, 510, A64

Verley, S., Hunt, L. K., Corbelli, E., & Giovanardi, C. 2007, A&A, 476, 1161

Wall, W. F. 2007, MNRAS, 379, 674

Walter, F., Brinks, E., de Blok, W. J. G., Thornley, M. D., & Kennicutt, R. C. 2005, in Astronomical Society of the Pacific Conference Series, Vol. 331, Extra-Planar Gas, ed. R. Braun, 269

Wild, J. P. 1952, ApJ, 115, 206

Wong, T., & Blitz, L. 2002, ApJ, 569, 157

Wright, T. 1750

Yin, J., Hou, J. L., Prantzos, N., Boissier, S., Chang, R. X., Shen, S. Y., & Zhang, B. 2009, A&A, 505, 497

Zibetti, S., Charlot, S., & Rix, H.-W. 2009, MNRAS, 400, 1181

A THE HERSCHEL REFERENCE SURVEY

A.1 THE SAMPLE

Here I present information on the galaxies of the *Herschel* Reference Survey (HRS) used in chapter 2. Table A.1 shows the HRS sample, reproduced and modified from Boselli et al. (2010a) with stellar masses taken from Cortese et al. (2012b). This thesis analyses spirals only, that have sufficient data to constrain the temperature peak of the SED.

All galaxies have been observed with the *Herschel SPIRE* instrument (Griffin et al., 2010), photometry taken from Ciesla et al. (2012). Table A.2 shows the available FIR photometry for each galaxy. In order to sufficiently constrain the SED, galaxies must have *Herschel PACS* (Poglitsch et al., 2010) photometry at $100\,\mu\mathrm{m}$ and $160\,\mu\mathrm{m}$ from Auld et al. (2013), taken as part of the *Herschel* Virgo Cluster Survey (HeViCS, Davies et al. 2010) with which the HRS has an overlap; or subsequent data from the same instrument from Cortese et al. (2014).

Table A.1: The Herschel Reference Survey, reproduced and modified from Boselli et al. (2010a).

HRS	CGCG	VCC	NGC	IC	RA (J2000) h m s	Dec (J2000) ° ′ ″	type	K_S mag	$D(25)$ ′	v km s^{-1}	d Mpc
1	123035	-	-	-	10:17:39.66	+22:48:35.9	Pec	11.59	1.00	1175	16.79
2	124004	-	-	-	10:20:57.13	+25:21:53.4	S?	11.03	0.52	1291	18.44
3	94026	-	3226	-	10:23:27.01	+19:53:54.7	E2:pec;LINER;Sy3	8.57	3.16	1169	16.70
4	94028	-	3227	-	10:23:30.58	+19:51:54.2	SAB(s)pec;Sy1.5	7.64	5.37	1148	16.40
5	94052	-	-	610	10:26:28.37	+20:13:41.5	Sc	9.94	1.86	1170	16.71
6	154016	-	3245A	-	10:27:01.16	+28:38:21.9	SB(s)b	11.83	3.31	1322	18.89
7	154017	-	3245	-	10:27:18.39	+28:30:26.6	SA(r)0:?;HII;LINER	7.86	3.24	1314	18.77
8	154020	-	3254	-	10:29:19.92	+29:29:29.2	SA(s)bc;Sy2	8.80	5.01	1356	19.37
9	154026	-	3277	-	10:32:55.45	+28:30:42.2	SA(r)ab;HII	8.93	1.95	1415	20.21
10	183028	-	-	-	10:34:29.82	+35:15:24.4	S?	11.31	0.91	1516	21.66
11	124038	-	3287	-	10:34:47.31	+21:38:54.0	SB(s)d	9.78	2.09	1325	18.93
12	124041	-	-	-	10:35:42.07	+26:07:33.7	cI	11.98	0.59	1392	19.89
13	183030	-	3294	-	10:36:16.25	+37:19:28.9	SA(s)c	8.38	3.55	1573	22.47
14	124045	-	3301	-	10:36:56.04	+21:52:55.7	(R')SB(rs)0/a	8.52	3.55	1341	19.16
15	65087	-	3338	-	10:42:07.54	+13:44:49.2	SA(s)c	8.13	5.89	1300	18.57
16	94116	-	3346	-	10:43:38.91	+14:52:18.7	SB(rs)cd	9.59	2.69	1260	18.00
17	95019	-	3370	-	10:47:04.05	+17:16:25.3	SA(s)c	9.43	3.16	1281	18.30
18	155015	-	3380	-	10:48:12.17	+28:36:06.5	(R')SBa?	9.92	1.70	1604	22.91
19	184016	-	3381	-	10:48:24.82	+34:42:41.1	SB pec	10.32	2.04	1630	23.29
20	184018	-	3395	2613	10:49:50.11	+32:58:58.3	SAB(rs)cd pec:	9.95	2.09	1617	23.10
21	155028	-	-	-	10:51:15.81	+27:50:54.9	Sbc	11.56	1.45	1182	16.89
22	155029	-	3414	-	10:51:16.23	+27:58:30.0	S0 pec;LINER	7.98	3.55	1414	20.20
23	184028	-	3424	-	10:51:46.33	+32:54:02.7	SB(s)b:?;HII	9.04	2.82	1501	21.44
24	184029	-	3430	-	10:52:11.41	+32:57:01.5	SAB(rs)c	8.90	3.98	1585	22.64
25	125013	-	3437	-	10:52:35.75	+22:56:02.9	SAB(rs)c:	8.88	2.51	1277	18.24
26	184031	-	-	-	10:52:38.34	+34:28:59.3	Sab	11.71	1.35	1569	22.41
27	184034	-	3442	-	10:53:08.11	+33:54:37.3	Sa?	10.90	0.62	1734	24.77
28	155035	-	3451	-	10:54:20.86	+27:14:22.9	Sd	10.23	1.70	1332	19.03
29	95060	-	3454	-	10:54:29.45	+17:20:38.3	SB(s)c? sp;HII	10.67	2.09	1101	15.73
30	95062	-	3455	-	10:54:31.07	+17:17:04.7	(R')SAB(rs)b	10.39	2.38	1105	15.79
31	267027	-	3448	-	10:54:39.24	+54:18:18.8	I0	9.47	5.62	1374	19.63
32	95065	-	3457	-	10:54:48.63	+17:37:16.3	S?	9.64	0.91	1158	16.54
33	95085	-	3485	-	11:00:02.38	+14:50:29.7	SB(r)b:	9.46	2.10	1432	20.46
34	95097	-	3501	-	11:02:47.32	+17:59:22.2	Scd	9.41	3.89	1130	16.14
35	267037	-	3499	-	11:03:11.03	+56:13:18.2	I0	10.23	0.81	1522	21.74
36	155049	-	3504	-	11:03:11.21	+27:58:21.0	(R)SAB(s)ab;HII	8.27	2.69	1536	21.94
37	155051	-	3512	-	11:04:02.98	+28:02:12.5	SAB(rs)c	9.65	1.62	1373	19.61
38	38129	-	3526	-	11:06:56.63	+07:10:26.1	SAc pec sp	10.69	1.91	1419	20.27
39	66115	-	-	-	11:07:03.35	+12:03:36.2	Sb:	11.13	1.86	1557	22.24
40	67019	-	3547	-	11:09:55.94	+10:43:15.0	Sb:	10.44	1.91	1584	22.63
41	96011	-	3592	-	11:14:27.25	+17:15:36.5	Sc? sp	10.78	1.78	1303	18.61
42	96013	-	3596	-	11:15:06.21	+14:47:13.5	SAB(rs)c	8.70	4.06	1193	17.04
43	96022	-	3608	-	11:16:58.96	+18:08:54.9	E2;LINER:	8.10	3.16	1108	15.83
44	96026	-	-	-	11:18:17.24	+18:50:49.0	S?	10.99	0.89	1121	16.01
45	291054	-	3619	-	11:19:21.60	+57:45:27.8	(R)SA(s)0+:	8.58	2.69	1544	22.06
46	96029	-	3626	-	11:20:03.80	+18:21:24.5	(R)SA(rs)0+	8.16	2.69	1494	21.34
47	156064	-	3629	-	11:20:31.82	+26:57:48.2	SA(s)cd:	10.50	2.29	1507	21.53
48	268021	-	3631	-	11:21:02.85	+53:10:11.0	SA(s)c	7.99	5.01	1155	16.50
49	39130	-	3640	-	11:21:06.85	+03:14:05.4	E3	7.52	3.98	1251	17.87
50	96037	-	3655	-	11:22:54.62	+16:35:24.5	SA(s)c:;HII	8.83	1.55	1500	21.43
51	96038	-	3659	-	11:23:45.49	+17:49:06.8	SB(s)m?	10.28	2.09	1299	18.56
52	268030	-	3657	-	11:23:55.57	+52:55:15.5	SAB(rs)c pec	10.29	1.45	1204	17.20
53	67071	-	3666	-	11:24:26.07	+11:20:32.0	SA(rs)c:	9.23	4.37	1060	15.14
54	96045	-	3681	-	11:26:29.80	+16:51:47.5	SAB(r)bc;LINER	9.79	2.25	1244	17.77
55	96047	-	3684	-	11:27:11.18	+17:01:49.0	SA(rs)bc;HII	9.28	2.89	1158	16.54
56	291072	-	3683	-	11:27:31.85	+56:52:37.4	SB(s)c?;HII	8.67	1.86	1708	24.40
57	96049	-	3686	-	11:27:43.95	+17:13:26.8	SB(s)bc	8.49	3.19	1156	16.51
58	96050	-	3691	-	11:28:09.41	+16:55:13.7	SBb?	10.51	1.35	1067	15.24
59	67084	-	3692	-	11:28:24.01	+09:24:27.5	Sb;LINER;HII	9.52	3.16	1717	24.53
60	268051	-	3729	-	11:33:49.34	+53:07:31.8	SB(r)a pec	8.73	2.82	991	15.14
61	292009	-	-	-	11:36:26.47	+58:11:29.0	Scd:;HII	11.40	1.95	1217	17.39
62	186012	-	3755	-	11:36:33.37	+36:24:37.2	SAB(rs)c pec	10.60	3.16	1571	22.44
63	268063	-	3756	-	11:36:48.02	+54:17:36.8	SAB(rs)bc	8.78	4.17	1289	18.41
64	292017	-	3795	-	11:40:06.84	+58:36:47.2	Sc;HII	10.64	2.14	1213	17.33
65	292019	-	3794	-	11:40:53.42	+56:12:07.3	SAB(s)d	11.60	2.24	1383	19.76
66	186024	-	3813	-	11:41:18.65	+36:32:48.3	SA(rs)b:	8.86	2.24	1468	20.97
67	268076	-	-	-	11:44:14.83	+55:02:05.9	SB(s)m:	11.28	1.91	1436	20.51
68	186045	-	-	-	11:46:25.96	+34:51:09.2	S?	11.44	0.32	1412	20.17
69	268088	-	3898	-	11:49:15.37	+56:05:03.7	SA(s)ab;LINE;HII	7.66	4.37	1171	16.73
70	-	-	-	2969	11:52:31.27	-03:52:20.1	SB(r)bc?;HII	11.15	1.23	1617	23.10
71	292042	-	3945	-	11:53:13.73	+60:40:32.0	SB(rs)0+;LINER	7.53	5.25	1259	17.99
72	-	-	3952	2972	11:53:40.63	-03:59:47.5	IBm: sp;HII	11.01	1.58	1577	22.53

Table A.1 – CONTINUED FROM PREVIOUS PAGE

HRS	CGCG	VCC	NGC	IC	RA (J2000) h m s	Dec (J2000) ° ′ ″	type	K_S mag	D(25) ′	v km s^{-1}	d Mpc
73	269013	-	3953	-	11:53:48.92	+52:19:36.4	SB(r)bc;HII/LINER	7.05	6.92	1050	15.00
74	269019	-	3982	-	11:56:28.10	+55:07:30.6	SAB(r)b:;HII;Sy2	8.85	2.34	1108	15.83
75	269020	-	-	-	11:56:37.51	+55:37:59.5	Sdm:	11.56	1.45	1283	18.33
76	269022	-	-	-	11:56:49.43	+53:09:37.3	Im:	11.32	2.00	1069	15.27
77	13033	-	4030	-	12:00:23.64	-01:06:00.0	SA(s)bc;HII	7.33	4.17	1458	20.83
78	98019	-	4032	-	12:00:32.82	+20:04:26.0	Im:	10.45	1.86	1269	18.13
79	69024	-	4019	755	12:01:10.39	+14:06:16.2	SBb? sp	11.33	2.40	1508	21.54
80	69027	-	4037	-	12:01:23.67	+13:24:03.7	SB(rs)b:	10.11	2.51	932	17.00
81	13046	-	4045	-	12:02:42.26	+01:58:36.4	SAB(r)a;HII	8.75	3.00	2011	17.00
82	98037	-	-	-	12:03:35.94	+16:03:20.0	Sab	11.19	0.60	931	17.00
83	41031	-	-	-	12:03:40.14	+02:38:28.4	SB(r)a::;HII	11.82	1.10	1232	17.60
84	69036	-	4067	-	12:04:11.55	+10:51:15.8	SA(s)b:	9.90	1.20	2424	17.00
85	243044	-	4100	-	12:06:08.60	+49:34:56.3	(R')SA(rs)bc;HII	8.03	5.37	1072	15.31
86	41041	-	4116	-	12:07:36.82	+02:41:32.0	SB(rs)dm	10.27	3.80	1309	17.00
87	69058	-	4124	-	12:08:09.64	+10:22:43.4	SA(r)0+	8.49	4.10	1652	17.00
88	41042	-	4123	-	12:08:11.11	+02:52:41.8	SB(r)c;Sbrst;HII	8.79	5.00	1326	17.00
89	69088	66	4178	-	12:12:46.45	+10:51:57.5	SB(rs)dm;HII	9.58	5.35	369	17.00
90	13104	-	4179	-	12:12:52.11	+01:17:58.9	Sb(f)	7.92	3.80	1279	17.00
91	98108	92	4192	-	12:13:48.29	+14:54:01.2	SAB(s)ab;HII;Sy	6.89	9.78	-135	17.00
92	69101	131	-	3061	12:15:04.44	+14:01:44.3	SBc? sp	10.64	2.60	2317	17.00
93	187029	-	4203	-	12:15:05.06	+33:11:50.4	SAB0-:;LINER;Sy3	7.41	3.39	1091	15.59
94	69104	145	4206	-	12:15:16.81	+13:01:26.3	SA(s)bc:	9.39	5.10	702	17.00
95	69107	152	4207	-	12:15:30.50	+09:35:05.6	Scd	9.44	1.96	592	17.00
96	69110	157	4212	-	12:15:39.36	+13:54:05.4	SAc:;HII	8.38	3.60	-83	17.00
97	69112	167	4216	-	12:15:54.44	+13:08:57.8	SAB(s)b:;HII/LINER	6.52	9.12	140	17.00
98	69119	187	4222	-	12:16:22.52	+13:18:25.5	Sc	10.33	3.52	226	17.00
99	69123	213	-	3094	12:16:56.00	+13:37:31.0	S;BCD	11.25	0.93	-162	17.00
100	98130	226	4237	-	12:17:11.42	+15:19:26.3	SAB(rs)bc;HII	10.03	2.01	864	17.00
101	158060	-	4251	-	12:18:08.31	+28:10:31.1	SB0? sp	7.73	3.63	1014	15.30
102	98144	307	4254	-	12:18:49.63	+14:24:59.4	SA(s)c	6.93	6.15	2405	17.00
103	42015	341	4260	-	12:19:22.24	+06:05:55.2	SB(s)a	8.54	3.52	1935	23.00
104	99015	-	-	-	12:19:28.66	+17:13:49.4	Spiral	11.99	1.20	925	17.00
105	99014	355	4262	-	12:19:30.58	+14:52:39.8	SB(s)0-?	8.36	1.87	1369	17.00
106	42032	393	4276	-	12:20:07.50	+07:41:31.2	S(s)c II	10.69	2.10	2617	23.00
107	42033	404	-	-	12:20:17.35	+04:12:05.1	Sd(f)	10.74	1.89	1733	17.00
108	42037	434	4287	-	12:20:48.49	+05:38:23.5	Sc(f)	11.02	1.76	2155	23.00
109	42038	449	4289	-	12:21:02.25	+03:43:19.7	SA(s)cd: sp	9.89	4.33	2541	17.00
110	70024	465	4294	-	12:21:17.79	+11:30:40.0	SB(s)cd	9.70	3.95	357	17.00
111	99024	483	4298	-	12:21:32.76	+14:36:22.2	SA(rs)c	8.47	3.60	1136	17.00
112	42044	492	4300	-	12:21:41.47	+05:23:05.4	Sa	9.53	2.16	2310	23.00
113	99027	497	4302	-	12:21:42.48	+14:35:53.9	Sc: sp	7.83	6.74	1150	17.00
114	42045	508	4303	-	12:21:54.90	+04:28:25.1	SAB(rs)bc;HII;Sy2	6.84	6.59	1568	17.00
115	42047	517	-	-	12:22:01.30	+05:06:00.2	SBab(s)	10.79	1.41	1864	17.00
116	70031	522	4305	-	12:22:03.60	+12:44:27.3	SA(r)a	9.83	2.60	1888	17.00
117	70029	524	4307	-	12:22:05.63	+09:02:36.8	Sb	8.72	3.95	1035	23.00
118	42053	552	-	-	12:22:27.25	+04:33:58.7	SAB(s)cd	11.20	1.89	1296	17.00
119	99029	559	4312	-	12:22:31.36	+15:32:16.5	SA(rs)ab: sp	8.79	5.10	153	17.00
120	70034	570	4313	-	12:22:38.55	+11:48:03.4	SA(rs)ab: sp	8.47	5.10	1443	17.00
121	70035	576	4316	-	12:22:42.24	+09:19:56.9	Sbc	9.25	2.48	1254	23.00
122	99030	596	4321	-	12:22:54.90	+15:49:20.6	SAB(s)bc;LINER;HII	6.59	9.12	1575	17.00
123	42063	613	4324	-	12:23:06.18	+05:15:01.5	SA(r)0+	8.48	3.52	1670	17.00
124	70039	630	4330	-	12:23:17.25	+11:22:04.7	Scd	9.51	5.86	1564	17.00
125	42068	648	4339	-	12:23:34.94	+06:04:54.2	E0;Sy2	8.54	2.31	1298	23.00
126	99036	654	4340	-	12:23:35.31	+16:43:19.9	SB(r)0+	8.32	3.60	930	17.00
127	42070	656	4343	-	12:23:38.70	+06:57:14.7	SA(rs)b:	8.97	2.48	1014	23.00
128	42072	667	-	3259	12:23:48.52	+07:11:12.6	SAB(s)dm?	11.06	1.89	1420	23.00
129	99038	685	4350	-	12:23:57.81	+16:41:36.1	SA0;LINER	7.82	3.20	1241	17.00
130	70045	692	4351	-	12:24:01.56	+12:12:18.1	SB(rs)ab pec:	10.24	2.92	2324	17.00
131	42079	697	-	3267	12:24:05.53	+07:02:28.6	SA(s)cd	10.95	1.55	1231	23.00
132	42080	699	-	3268	12:24:07.44	+06:36:26.9	Sm/Im	11.49	1.95	727	23.00
133	158099	-	4359	-	12:24:11.06	+31:31:17.8	SB(rs)c? sp	10.81	3.60	1253	17.90
134	70048	713	4356	-	12:24:14.53	+08:32:08.9	Sc	9.69	3.20	1137	23.00
135	42083	731	4365	-	12:24:28.23	+07:19:03.1	E3	6.64	8.73	1240	23.00
136	42089	758	4370	-	12:24:54.93	+07:26:40.4	Sa	9.31	1.76	784	23.00
137	70057	759	4371	-	12:24:55.43	+11:42:15.4	SB(r)0+	7.72	5.10	943	17.00
138	70058	763	4374	-	12:25:03.78	+12:53:13.1	E1;LERG;LINER;Sy2	6.22	10.07	910	17.00
139	42093	787	4376	-	12:25:18.06	+05:44:28.3	Im	11.23	1.84	1136	23.00
140	42092	785	4378	-	12:25:18.09	+04:55:30.2	(R)SA(s)a;Sy2	8.51	3.06	2557	17.00
141	70061	792	4380	-	12:25:22.17	+10:01:00.5	SA(rs)b:?	8.33	3.52	971	23.00
142	99044	801	4383	-	12:25:25.50	+16:28:12.0	Sa? pec;HII	9.49	2.60	1710	17.00
143	42095	827	-	-	12:25:42.63	+07:13:00.1	SB(s)cd: sp	9.79	3.60	992	23.00
144	70068	836	4388	-	12:25:46.82	+12:39:43.5	SA(s)b: sp;Sy2	8.00	5.10	2515	17.00
145	70067	849	4390	-	12:25:50.67	+10:27:32.6	Sbc(s) II	10.33	2.18	1103	23.00
146	42098	851	-	3322	12:25:54.12	+07:33:17.4	SAB(s)cd: sp	10.47	2.16	1195	23.00

Table A.1 – CONTINUED FROM PREVIOUS PAGE

HRS	CGCG	VCC	NGC	IC	RA (J2000) h m s	Dec (J2000) ° ′ ″	type	K_S mag	D(25) ′	v km s^{-1}	d Mpc
147	42099	859	-	-	12:25:58.30	+03:25:47.3	Sd(f)	10.18	2.92	1428	17.00
148	99049	865	4396	-	12:25:58.80	+15:40:17.3	SAd: sp	10.34	3.36	-124	17.00
149	70071	873	4402	-	12:26:07.56	+13:06:46.0	Sb	8.49	3.95	234	17.00
150	70072	881	4406	-	12:26:11.74	+12:56:46.4	S0(3)/E3	6.10	11.37	-221	17.00
151	70076	912	4413	-	12:26:32.25	+12:36:39.5	(R')SB(rs)ab:	9.80	2.92	105	17.00
152	42104	921	4412	-	12:26:36.10	+03:57:52.7	SB(r)b? pec;LINER	9.65	1.89	2289	17.00
153	42105	938	4416	-	12:26:46.72	+07:55:08.4	SB(rs)cd:;Sbrst	10.97	2.18	1395	17.00
154	70082	939	-	-	12:26:47.23	+08:53:04.6	SAB(s)cd	10.71	3.45	1271	23.00
155	70080	944	4417	-	12:26:50.62	+09:35:03.0	SB0: s	8.17	3.60	832	23.00
156	99054	958	4419	-	12:26:56.43	+15:02:50.7	SB(s)a;LINER;HII	7.74	3.52	-273	17.00
157	42106	957	4420	-	12:26:58.48	+02:29:39.7	SB(r)bc	9.66	2.01	1695	17.00
158	42107	971	4423	-	12:27:08.97	+05:52:48.6	Sdm:	11.05	3.06	1120	23.00
159	70090	979	4424	-	12:27:11.59	+09:25:14.0	SB(s)a:;HII	9.09	4.33	438	23.00
160	42111	1002	4430	-	12:27:26.41	+06:15:46.0	SB(rs)b:	9.35	3.02	1450	23.00
161	70093	1003	4429	-	12:27:26.56	+11:06:27.1	SA(r)0+;LINER;HII	6.78	8.12	1130	17.00
162	70098	1030	4435	-	12:27:40.49	+13:04:44.2	SB(s)0;LINER;HII	7.30	2.92	775	17.00
163	70097	1043	4438	-	12:27:45.59	+13:00:31.8	SA(s)0/a pec:;LINER	7.27	8.12	70	17.00
164	70099	1047	4440	-	12:27:53.57	+12:17:35.6	SB(rs)a	8.91	2.01	724	17.00
165	42117	1048	-	-	12:27:55.39	+05:43:16.4	Sdm:	11.58	1.89	2252	23.00
166	70100	1062	4442	-	12:28:03.89	+09:48:13.0	SB(s)0	7.29	5.05	517	23.00
167	70104	1086	4445	-	12:28:15.94	+09:26:10.7	Sab: sp	9.83	3.20	328	23.00
168	70108	1091	-	-	12:28:18.77	+08:43:46.1	Sbc	11.77	1.76	1119	23.00
169	99063	-	-	3391	12:28:27.28	+18:24:55.1	Scd:	10.45	1.10	1701	24.30
170	99062	1110	4450	-	12:28:29.63	+17:05:05.8	SA(s)ab;LINER;Sy3	7.05	6.15	1954	17.00
171	70111	1118	4451	-	12:28:40.55	+09:15:32.2	Sbc:	9.99	1.96	865	23.00
172	99065	1126	-	3392	12:28:43.26	+14:59:58.2	SAb:	9.26	2.92	1687	17.00
173	42124	1145	4457	-	12:28:59.01	+03:34:14.2	(R)SAB(s)0/a;LINER	7.78	2.92	884	17.00
174	70116	1154	4459	-	12:29:00.03	+13:58:42.9	SA(r)0+;HII;LINER	7.15	3.36	1210	17.00
175	70115	1158	4461	-	12:29:03.01	+13:11:01.5	SB(s)0+:	8.01	3.52	1919	17.00
176	70121	1190	4469	-	12:29:28.03	+08:44:59.7	SB(s)0/a? sp	8.04	4.33	508	23.00
177	42132	1205	4470	-	12:29:37.78	+07:49:27.1	Sa?;HII	10.12	1.84	2339	17.00
178	42134	1226	4472	-	12:29:46.76	+08:00:01.7	E2/S0;Sy2;LINER	5.40	10.25	868	17.00
179	70125	1231	4473	-	12:29:48.87	+13:25:45.7	E5	7.16	4.04	2236	17.00
180	70129	1253	4477	-	12:30:02.17	+13:38:11.2	SB(s)0:?;Sy2	7.35	3.60	1353	17.00
181	70133	1279	4478	-	12:30:17.42	+12:19:42.8	E2	8.36	1.89	1370	17.00
182	42139	1290	4480	-	12:30:26.78	+04:14:47.3	SAB(s)c	9.75	2.01	2438	17.00
183	70139	1316	4486	-	12:30:49.42	+12:23:28.0	E+0-1 pec;NLRG;Sy	5.81	11.00	1292	17.00
184	70140	1326	4491	-	12:30:57.13	+11:29:00.8	SB(s)a:	9.88	1.89	497	17.00
185	42141	1330	4492	-	12:30:59.74	+08:04:40.6	SA(s)a?	9.08	1.96	1777	17.00
186	129005	-	4494	-	12:31:24.03	+25:46:29.9	E1-2;LINER	7.00	4.79	1310	18.71
187	42144	1375	4505	-	12:31:39.21	+03:56:22.1	SB(rs)m	9.56	4.76	1732	17.00
188	99075	1379	4498	-	12:31:39.57	+16:51:10.1	SAB(s)d	9.66	2.85	1505	17.00
189	99077	1393	-	797	12:31:54.76	+15:07:26.2	SB(s)c II.5	10.80	1.69	2100	17.00
190	99076	1401	4501	-	12:31:59.22	+14:25:13.5	SA(rs)b;HII;Sy2	6.27	7.23	2284	17.00
191	99078	1410	4502	-	12:32:03.35	+16:41:15.8	Scd:	11.90	1.48	1629	17.00
192	70152	1419	4506	-	12:32:10.53	+13:25:10.6	Sa pec?	10.26	2.16	737	17.00
193	70157	1450	-	3476	12:32:41.88	+14:03:01.8	IB(s)m:	10.91	2.60	-173	17.00
194	14063	-	4517	-	12:32:45.59	+00:06:54.1	SA(s)cd: sp	7.33	11.00	1129	17.00
195	99087	1479	4516	-	12:33:07.56	+14:34:29.8	SB(rs)ab?	9.99	2.16	958	17.00
196	70167	1508	4519	-	12:33:30.25	+08:39:17.1	SB(rs)d	9.56	3.60	1212	17.00
197	70168	1516	4522	-	12:33:39.66	+09:10:29.5	SB(s)cd: sp	10.35	4.04	2330	17.00
198	159016	-	4525	-	12:33:51.19	+30:16:39.1	Scd:	9.99	3.00	1174	16.77
199	99090	1532	-	800	12:33:56.66	+15:21:17.4	SB(rs)c pec?	10.58	1.96	2335	17.00
200	42155	1535	4526	-	12:34:03.03	+07:41:56.9	SAB(s)0:	6.47	7.00	448	17.00
201	42156	1540	4527	-	12:34:08.50	+02:39:13.7	SAB(s)bc;HII;LINER	6.93	5.86	1736	17.00
202	70173	1549	-	3510	12:34:14.79	+11:04:17.7	S?	11.42	1.10	1357	17.00
203	42158	1554	4532	-	12:34:19.33	+06:28:03.7	IBm;HII	9.48	2.60	2021	17.00
204	42159	1555	4535	-	12:34:20.31	+08:11:51.9	SAB(s)c;HII	7.38	8.33	1962	17.00
205	14068	1562	4536	-	12:34:27.13	+02:11:16.4	SAB(rs)bc;HII;Sbrst	7.52	7.23	1807	17.00
206	42162	1575	-	3521	12:34:39.42	+07:09:36.0	SBm pec;BCD	11.01	2.00	597	17.00
207	99093	1588	4540	-	12:34:50.87	+15:33:05.2	SAB(rs)cd;LINER;Sy1	9.24	2.60	1288	17.00
208	99096	1615	4548	-	12:35:26.43	+14:29:46.8	SBb(rs);LINER;Sy	7.12	6.00	484	17.00
209	-	-	4546	-	12:35:29.51	-03:47:35.5	SB(s)0-:	7.39	3.31	1050	15.00
210	70182	1619	4550	-	12:35:30.61	+12:13:15.4	SB0: sp;LINER	8.69	3.95	381	17.00
211	70184	1632	4552	-	12:35:39.88	+12:33:21.7	E;LINER;HII;Sy2	6.73	7.23	322	17.00
212	99098	-	4561	-	12:36:08.14	+19:19:21.4	SB(rs)dm	10.63	1.51	1410	20.14
213	129010	-	4565	-	12:36:20.78	+25:59:15.6	SA(s)b? sp;Sy3;Sy1.9	6.06	14.18	1233	17.61
214	70186	1664	4564	-	12:36:26.99	+11:26:21.5	E6	7.94	4.33	1165	17.00
215	70189	1673	4567	-	12:36:32.71	+11:15:28.8	SA(rs)bc	8.30	2.92	2277	17.00
216	70188	1676	4568	-	12:36:34.26	+11:14:20.0	SA(rs)bc	7.52	5.10	2255	17.00
217	70192	1690	4569	-	12:36:49.80	+13:09:46.3	SAB(rs)ab;LINER;Sy	6.58	10.73	-216	17.00
218	42178	1692	4570	-	12:36:53.40	+07:14:48.0	S0(7)/E7	7.69	3.52	1730	17.00
219	70195	1720	4578	-	12:37:30.55	+09:33:18.4	SA(r)0:	8.40	3.77	2284	17.00
220	70197	1727	4579	-	12:37:43.52	+11:49:05.5	SAB(rs)b;LINER;Sy1.9	6.49	6.29	1520	17.00

Table A.1 – CONTINUED FROM PREVIOUS PAGE

HRS	CGCG	VCC	NGC	IC	RA (J2000) h m s	Dec (J2000) ° ′ ″	type	K_S mag	D(25) ′	v km s^{-1}	d Mpc
221	42183	1730	4580	-	12:37:48.40	+05:22:06.4	SAB(rs)a pec	8.77	2.16	1032	17.00
222	70199	1757	4584	-	12:38:17.89	+13:06:35.5	SAB(s)a?	10.46	1.96	1783	17.00
223	42186	1758	-	-	12:38:20.82	+07:53:28.7	Sdm	11.76	1.89	1788	17.00
224	42187	1760	4586	-	12:38:28.44	+04:19:08.8	SA(s)a: sp	8.47	4.33	792	17.00
225	70202	1778	-	3611	12:39:04.14	+13:21:48.7	S?	11.42	1.76	2750	17.00
226	42191	1780	4591	-	12:39:12.44	+06:00:44.3	Sb	10.24	1.96	2424	17.00
227	14091	-	4592	-	12:39:18.74	-00:31:55.2	SA(s)dm:	10.22	5.75	1069	15.27
228	-	-	-	-	12:39:22.26	-05:39:53.3	Pec	11.95	0.43	1199	17.13
229	70204	1809	-	3631	12:39:48.02	+12:58:26.1	S?	11.11	1.10	2839	17.00
230	99106	1811	4595	-	12:39:51.91	+15:17:52.1	SAB(rs)b?	10.03	2.16	632	17.00
231	70206	1813	4596	-	12:39:55.94	+10:10:33.9	SB(r)0+;LINER:	7.46	4.76	1834	17.00
232	70213	1859	4606	-	12:40:57.56	+11:54:43.6	SB(s)a:	9.17	5.10	1645	17.00
233	70216	1868	4607	-	12:41:12.41	+11:53:11.9	SBb? sp	9.58	3.95	2255	17.00
234	70214	1869	4608	-	12:41:13.29	+10:09:20.9	SB(r)0	8.16	4.30	1864	17.00
235	42205	1883	4612	-	12:41:32.76	+07:18:53.2	(R)SAB0	8.56	2.16	1875	17.00
236	70223	1903	4621	-	12:42:02.32	+11:38:48.9	E5	6.75	7.67	444	17.00
237	42208	1923	4630	-	12:42:31.15	+03:57:37.3	IB(s)m?	9.89	2.31	742	17.00
238	14109	-	4629	-	12:42:32.67	-01:21:02.4	SAB(s)m pec	11.84	1.38	1116	15.94
239	99112	1932	4634	-	12:42:40.96	+14:17:45.0	SBcd: sp	9.25	2.92	116	17.00
240	70229	1938	4638	-	12:42:47.43	+11:26:32.9	S0-	8.21	2.01	1147	17.00
241	43002	1939	4636	-	12:42:49.87	+02:41:16.0	E/S0/1;LINER;Sy3	6.42	9.63	1094	17.00
242	70230	1943	4639	-	12:42:52.37	+13:15:26.9	SAB(rs)bc;Sy1.8	8.81	3.20	1048	17.00
243	15008	-	4643	-	12:43:20.14	+01:58:42.1	SB(rs)0/a;LINER	7.41	3.00	1346	17.00
244	71015	1972	4647	-	12:43:32.45	+11:34:57.4	SAB(rs)c	8.05	2.60	1422	17.00
245	71016	1978	4649	-	12:43:40.01	+11:33:09.4	E2	5.74	5.10	1095	17.00
246	100004	-	4651	-	12:43:42.63	+16:23:36.2	SA(rs)c;LINER	8.03	3.90	797	17.00
247	71019	1987	4654	-	12:43:56.58	+13:07:36.0	SAB(rs)cd;HII	7.74	4.99	1039	17.00
248	71023	2000	4660	-	12:44:31.97	+11:11:25.9	E5	8.21	1.89	1115	17.00
249	71026	2006	-	3718	12:44:45.99	+12:21:05.2	S	11.91	2.60	844	17.00
250	43018	-	4665	-	12:45:05.96	+03:03:20.5	SB(s)0/a	7.43	4.50	785	17.00
251	15015	-	4666	-	12:45:08.59	-00:27:42.8	SABc:;HII;LINER	7.06	4.57	1513	21.61
252	15016	-	4668	-	12:45:32.14	-00:32:05.0	SB(s)d:;NLAGN	10.58	1.38	1619	23.13
253	15019	-	4684	-	12:47:17.52	-02:43:38.6	SB(r)0+;HII	8.39	2.88	1490	21.29
254	71043	2058	4689	-	12:47:45.56	+13:45:46.1	SA(rs)bc	7.96	5.86	1620	17.00
255	43028	-	4688	-	12:47:46.46	+04:20:09.9	SB(s)cd	11.16	4.40	984	17.00
256	15023	-	4691	-	12:48:13.63	-03:19:57.8	(R)SB(s)0/a pec;HII	8.54	2.82	1119	15.99
257	71045	2070	4698	-	12:48:22.92	+08:29:14.3	SA(s)ab;Sy2	7.56	5.67	1008	17.00
258	-	-	4697	-	12:48:35.91	-05:48:03.1	E6;AGN	6.37	7.24	1241	17.73
259	43034	-	4701	-	12:49:11.56	+03:23:19.4	SA(s)cd	9.77	3.60	727	17.00
260	100011	-	4710	-	12:49:38.96	+15:09:55.8	SA(r)0+? sp;HII	7.57	4.30	1129	17.00
261	43040	-	-	-	12:49:50.19	+02:51:10.4	Sd(f)	10.17	3.39	1158	16.54
262	43041	-	4713	-	12:49:57.87	+05:18:41.1	SAB(rs)d;LINER	9.75	3.20	652	17.00
263	129027	-	4725	-	12:50:26.61	+25:30:02.7	SAB(r)ab pec;Sy2	6.17	9.66	1209	17.27
264	15027	-	-	-	12:50:38.96	+01:27:52.3	Sd(f)	11.61	1.70	1272	18.17
265	-	-	4720	-	12:50:42.78	-04:09:21.0	Pec	10.77	0.65	1504	21.49
266	-	-	4731	-	12:51:01.09	-06:23:35.0	SB(s)cd	9.79	6.61	1491	21.30
267	129028	-	4747	-	12:51:45.96	+25:46:38.3	SBcd? pec sp	10.29	3.95	1179	16.84
268	71060	-	4746	-	12:51:55.37	+12:04:58.9	Sb: sp	9.50	2.20	1779	17.00
269	71062	2092	4754	-	12:52:17.56	+11:18:49.2	SB(r)0-:	7.41	5.03	1377	17.00
270	15029	-	4753	-	12:52:22.11	-01:11:58.9	I0	6.72	6.03	1239	17.70
271	100015	-	4758	-	12:52:44.04	+15:50:55.9	Im:;HII	10.93	3.00	1240	17.00
272	71065	2095	4762	-	12:52:56.05	+11:13:50.9	SB(r)0 sp;LINER	7.30	8.70	985	17.00
273	15031	-	4771	-	12:53:21.27	+01:16:09.0	SAd? sp;NLAGN	9.01	4.00	1119	17.00
274	15032	-	4772	-	12:53:29.17	+02:10:06.0	SA(s)a;LINER;Sy3	8.36	2.90	1038	17.00
275	-	-	4775	-	12:53:45.70	-06:37:19.8	SA(s)d	9.22	2.14	1566	22.37
276	71068	-	4779	-	12:53:50.86	+09:42:35.7	SB(rs)bc;Sbrst	9.87	2.10	2832	17.00
277	43060	-	4791	-	12:54:43.97	+08:03:10.7	cI	11.35	1.20	2529	17.00
278	71071	-	-	-	12:54:44.19	+13:14:14.2	S	10.39	2.75	1121	16.01
279	15037	-	-	-	12:55:12.68	+00:07:00.0	SB(s)d	11.98	3.10	1321	17.00
280	43066	-	4799	-	12:55:15.53	+02:53:47.9	S?	9.89	1.60	2802	17.00
281	43068	-	-	-	12:55:23.62	+07:54:34.0	IBm:	11.82	0.91	2801	17.00
282	43069	-	4803	-	12:55:33.67	+08:14:25.8	Comp	10.71	0.50	2664	17.00
283	43071	-	4808	-	12:55:48.94	+04:18:14.7	SA(s)cd:;HII	9.04	2.60	760	17.00
284	-	-	-	3908	12:56:40.62	-07:33:46.1	SB(s)d?;HII	9.10	1.82	1296	18.51
285	15049	-	4845	-	12:58:01.19	+01:34:33.0	SA(s)ab sp;HII	7.79	5.20	1097	17.00
286	71092	-	4866	-	12:59:27.14	+14:10:15.8	SA(r)0+: sp;LINER	7.92	6.00	1986	17.00
287	15055	-	4904	-	13:00:58.67	-00:01:38.8	SB(s)cd;Sbrst	9.50	2.40	1174	17.00
288	-	-	4941	-	13:04:13.14	-05:33:05.8	(R)SAB(r)ab:;Sy2	8.22	3.63	1114	15.91
289	-	-	4981	-	13:08:48.74	-06:46:39.1	SAB(r)bc;LINER	8.49	2.75	1678	23.97
290	189037	-	5014	-	13:11:31.16	+36:16:54.9	Sa? sp	10.11	1.70	1136	16.23
291	217031	-	5103	-	13:20:30.08	+43:05:02.3	Sab	9.49	1.45	1297	18.53
292	218010	-	5145	-	13:25:13.92	+43:16:02.2	S?;HII;Sbrst	9.33	2.00	1225	17.50
293	16069	-	5147	-	13:26:19.71	+02:06:02.7	SB(s)dm	9.73	1.91	1092	15.60
294	246017	-	-	902	13:36:01.22	+49:57:39.0	Sb	10.42	2.19	1608	22.97

Table A.1 – CONTINUED FROM PREVIOUS PAGE

HRS	CGCG	VCC	NGC	IC	RA (J2000)	Dec (J2000)	type	K_S	$D(25)$	v	d
					h m s	° ′ ″		mag	′	km s^{-1}	Mpc
295	73054	-	5248	-	13:37:32.07	+08:53:06.2	(R)SB(rs)bc;Sy2;HII	7.25	1.79	1152	16.46
296	190041	-	5273	-	13:42:08.34	+35:39:15.2	SA(s)0;Sy1.9	8.67	2.75	1064	15.20
297	246023	-	5301	-	13:46:24.61	+46:06:26.7	SA(s)bc: sp	9.11	4.17	1508	21.54
298	218047	-	5303	-	13:47:44.97	+38:18:16.4	Pec	10.23	0.91	1419	20.27
299	45108	-	5300	-	13:48:16.04	+03:57:03.1	SAB(r)c	9.50	3.89	1171	16.73
300	218058	-	-	-	13:50:35.89	+42:32:29.5	Sab	10.34	1.70	1354	19.34
301	17088	-	5334	4338	13:52:54.46	-01:06:52.7	SB(rs)c:	9.94	4.17	1380	19.71
302	45137	-	5348	-	13:54:11.27	+05:13:38.8	SBbc: sp	10.87	3.55	1443	20.61
303	295024	-	5372	-	13:54:46.01	+58:39:59.4	S?	10.65	0.65	1717	24.53
304	46001	-	5356	-	13:54:58.46	+05:20:01.4	SABbc: sp;HII	9.64	3.09	1370	19.57
305	46003	-	5360	958	13:55:38.75	+04:59:06.2	I0	11.15	2.19	1171	16.73
306	46007	-	5363	-	13:56:07.21	+05:15:17.2	I0?	6.93	4.07	1136	16.23
307	46009	-	5364	-	13:56:12.00	+05:00:52.1	SA(rs)bc pec;HII	7.80	6.76	1242	17.74
308	46011	-	-	-	13:56:26.61	+04:23:48.0	Sb(f)	11.93	0.91	1091	15.59
309	272031	-	5486	-	14:07:24.97	+55:06:11.1	SA(s)m:	11.95	1.86	1383	19.76
310	47010	-	5560	-	14:20:05.42	+03:59:28.4	SB(s)b pec	9.98	3.72	1718	24.54
311	47012	-	5566	-	14:20:19.95	+03:56:00.9	SB(r)ab;LINER	7.39	6.61	1492	21.31
312	47020	-	5576	-	14:21:03.68	+03:16:15.6	E3	7.83	3.55	1482	21.17
313	47022	-	5577	-	14:21:13.11	+03:26:08.8	SA(rs)bc:	9.75	3.39	1490	21.29
314	19012	-	-	-	14:23:27.12	+01:43:34.7	SB(s)d	10.54	2.19	1389	19.84
315	220015	-	-	-	14:25:21.02	+39:32:22.7	Sc	11.73	5.01	1440	20.57
316	47063	-	5638	-	14:29:40.39	+03:14:00.2	E1	8.25	2.69	1845	23.94
317	47066	-	-	1022	14:30:01.85	+03:46:22.3	S?	11.70	1.10	1716	24.51
318	47070	-	5645	-	14:30:39.35	+07:16:30.3	SB(s)d	9.69	2.40	1370	19.57
319	75064	-	5669	-	14:32:43.88	+09:53:30.5	SAB(rs)cd	10.35	3.98	1368	19.54
320	47090	-	5668	-	14:33:24.34	+04:27:01.6	SA(s)d	11.71	3.31	1583	22.61
321	47123	-	5692	-	14:38:18.12	+03:24:37.2	S?	10.54	0.89	1581	22.59
322	47127	-	5701	-	14:39:11.06	+05:21:48.8	(R)SB(rs)0/a;LINER	8.14	4.27	1505	21.50
323	48004	-	-	1048	14:42:57.88	+04:53:24.5	S	9.55	2.24	1640	23.43

Table A.2: Fluxes used in determination of dust properties in the HRS. *PACS* fluxes taken from Cortese et al. (2014), *SPIRE* fluxes are from Ciesla et al. (2012) and Auld et al. (2013).

	PACS		SPIRE		
HRS	S_{100} / Jy	S_{160} / Jy	S_{250} / Jy	S_{350} / Jy	S_{500} / Jy
1	0.748 ± 0.169	0.932 ± 0.079	0.5 ± 0.04	0.21 ± 0.03	0.08 ± 0.02
2	2.439 ± 0.227	2.808 ± 0.179	1.16 ± 0.06	0.48 ± 0.04	0.15 ± 0.02
3	-	0.846 ± 0.087	0.58 ± 0.03	0.24 ± 0.02	0.08 ± 0.01
4	17.589 ± 1.104	22.675 ± 1.165	12.67 ± 0.21	5.24 ± 0.14	1.82 ± 0.07
5	4.502 ± 0.331	5.563 ± 0.528	2.74 ± 0.06	1.14 ± 0.05	0.36 ± 0.03
6	0.275 ± 0.14	0.483 ± 0.085	0.62 ± 0.07	0.39 ± 0.06	0.18 ± 0.04
7	3.472 ± 0.206	2.843 ± 0.151	1.24 ± 0.01	0.48 ± 0.01	0.15 ± 0.01
8	2.878 ± 1.092	4.641 ± 1.041	3.98 ± 0.3	2.25 ± 0.15	1.02 ± 0.06
9	1.948 ± 0.397	3.037 ± 0.523	1.43 ± 0.08	0.58 ± 0.06	0.18 ± 0.03
10	1.168 ± 0.238	0.788 ± 0.094	0.68 ± 0.04	0.3 ± 0.03	0.1 ± 0.02
11	5.192 ± 0.3	6.148 ± 0.409	3.44 ± 0.07	1.61 ± 0.05	0.61 ± 0.03
12	0.613 ± 0.054	0.492 ± 0.05	0.27 ± 0.02	0.12 ± 0.01	0.05 ± 0.01
13	19.809 ± 1.322	25.224 ± 1.717	12.33 ± 0.13	5.27 ± 0.11	1.89 ± 0.05
14	0.477 ± 0.078	0.372 ± 0.106	0.22 ± 0.02	0.1 ± 0.02	0.03 ± 0.02
15	13.12 ± 2.907	20.386 ± 2.277	12.9 ± 0.77	6.27 ± 0.46	2.44 ± 0.29
16	5.688 ± 0.695	10.294 ± 0.785	5.6 ± 0.19	2.6 ± 0.18	0.99 ± 0.07
17	10.209 ± 0.872	12.793 ± 0.832	6.69 ± 0.19	2.97 ± 0.12	1.17 ± 0.06
18	1.465 ± 0.248	2.015 ± 0.241	1.12 ± 0.05	0.51 ± 0.05	0.18 ± 0.02
19	4.335 ± 0.525	4.371 ± 0.375	2.61 ± 0.12	1.23 ± 0.07	0.47 ± 0.04
20	16.137 ± 1.402	16.068 ± 0.871	6.72 ± 0.11	2.84 ± 0.07	1.02 ± 0.04
21	0.625 ± 0.255	1.084 ± 0.148	0.55 ± 0.06	0.33 ± 0.05	0.16 ± 0.02
22	0.618 ± 0.072	0.685 ± 0.118	0.49 ± 0.09	0.22 ± 0.06	0.1 ± 0.03
23	18.098 ± 0.981	19.636 ± 1.076	8.87 ± 0.12	3.74 ± 0.07	1.28 ± 0.04
24	10.909 ± 1.182	16.037 ± 1.577	8.48 ± 0.29	3.81 ± 0.17	1.47 ± 0.09
25	21.647 ± 1.187	21.174 ± 1.142	8.68 ± 0.1	3.55 ± 0.07	1.27 ± 0.05
26	0.744 ± 0.098	0.864 ± 0.106	0.48 ± 0.03	0.27 ± 0.03	0.12 ± 0.02
27	3.148 ± 0.286	3.173 ± 0.253	1.37 ± 0.05	0.55 ± 0.03	0.17 ± 0.02
28	3.569 ± 0.232	5.184 ± 0.321	2.45 ± 0.07	1.1 ± 0.04	0.39 ± 0.03
29	2.403 ± 0.292	3.422 ± 0.326	1.81 ± 0.13	0.94 ± 0.07	0.37 ± 0.05
30	2.87 ± 0.545	3.859 ± 0.37	2.31 ± 0.17	1.16 ± 0.09	0.5 ± 0.06
31	12.17 ± 1.183	10.63 ± 1.579	5.48 ± 0.33	2.49 ± 0.2	1 ± 0.1
32	0.042 ± 0.024	0.182 ± 0.034	0.13 ± 0.03	-	-
33	5.138 ± 0.368	6.83 ± 0.532	3.46 ± 0.1	1.58 ± 0.08	0.6 ± 0.05
34	5.002 ± 0.64	8.619 ± 0.832	4.92 ± 0.15	2.46 ± 0.13	1.01 ± 0.07
35	0.24 ± 0.057	0.273 ± 0.081	0.18 ± 0.02	0.07 ± 0.02	-
36	35.557 ± 1.977	31.358 ± 1.651	12.2 ± 0.22	4.75 ± 0.12	1.57 ± 0.06
37	4.532 ± 0.346	5.328 ± 0.513	2.53 ± 0.09	1.09 ± 0.06	0.37 ± 0.03
38	1.818 ± 0.291	1.886 ± 0.286	1.27 ± 0.05	0.68 ± 0.03	0.28 ± 0.02
39	0.915 ± 0.21	1.199 ± 0.333	0.84 ± 0.06	0.44 ± 0.04	0.2 ± 0.03
40	4.478 ± 0.305	4.51 ± 0.363	2.04 ± 0.05	0.88 ± 0.04	0.31 ± 0.03
41	1.418 ± 0.278	1.584 ± 0.144	1.08 ± 0.05	0.55 ± 0.04	0.22 ± 0.02
42	12.111 ± 2.072	18.583 ± 1.787	9.35 ± 0.53	4.35 ± 0.4	1.75 ± 0.15
43	-	-	-	-	-
44	2.521 ± 0.197	1.982 ± 0.208	1.11 ± 0.06	0.51 ± 0.04	0.2 ± 0.02
45	1.782 ± 0.393	2.72 ± 0.439	1.79 ± 0.11	0.82 ± 0.07	0.3 ± 0.04
46	4.995 ± 0.272	4.9 ± 0.284	2.11 ± 0.05	0.86 ± 0.04	0.28 ± 0.02
47	2.652 ± 0.465	3.163 ± 0.509	1.82 ± 0.13	0.92 ± 0.08	0.37 ± 0.04
48	29.87 ± 3.057	38.272 ± 3.115	19.91 ± 0.75	8.73 ± 0.7	3.24 ± 0.36
49	-	-	-	-	-
50	20.97 ± 1.076	22.078 ± 1.141	9.18 ± 0.09	3.56 ± 0.05	1.12 ± 0.04
51	4.542 ± 0.423	4.996 ± 0.582	2.81 ± 0.11	1.36 ± 0.1	0.55 ± 0.03

Table A.2 – CONTINUED FROM PREVIOUS PAGE

	PACS		SPIRE		
HRS	S_{100} / Jy	S_{160} / Jy	S_{250} / Jy	S_{350} / Jy	S_{500} / Jy
52	0.783 ± 0.274	1.305 ± 0.237	0.62 ± 0.05	0.28 ± 0.04	0.11 ± 0.02
53	8.762 ± 0.75	10.815 ± 0.829	5.97 ± 0.18	2.85 ± 0.13	1.13 ± 0.05
54	2.819 ± 0.577	3.076 ± 0.537	2.13 ± 0.13	0.96 ± 0.07	0.36 ± 0.04
55	7.742 ± 0.768	11.416 ± 0.769	5.89 ± 0.16	2.66 ± 0.15	0.98 ± 0.07
56	28.93 ± 1.498	30.107 ± 1.604	12.59 ± 0.11	4.74 ± 0.08	1.54 ± 0.04
57	12.431 ± 1.106	17.983 ± 1.255	9.84 ± 0.25	4.22 ± 0.15	1.52 ± 0.07
58	2.098 ± 0.194	2.449 ± 0.155	1.33 ± 0.03	0.61 ± 0.03	0.23 ± 0.02
59	3.801 ± 0.395	5.622 ± 0.431	3.31 ± 0.17	1.67 ± 0.13	0.67 ± 0.05
60	7.738 ± 0.915	10.477 ± 0.772	5.64 ± 0.12	2.43 ± 0.09	0.86 ± 0.04
61	0.70 ± 0.121	0.937 ± 0.15	0.59 ± 0.04	0.32 ± 0.03	0.13 ± 0.02
62	2.73 ± 0.498	3.527 ± 0.528	2.17 ± 0.12	1.19 ± 0.08	0.54 ± 0.05
63	6.471 ± 1.15	12.252 ± 1.339	7.39 ± 0.25	3.6 ± 0.21	1.42 ± 0.09
64	1.333 ± 0.326	1.682 ± 0.29	1.21 ± 0.1	0.68 ± 0.06	0.27 ± 0.03
65	1.909 ± 0.476	2.082 ± 0.426	1.4 ± 0.11	0.76 ± 0.07	0.34 ± 0.04
66	21.54 ± 1.151	23.821 ± 1.255	10.59 ± 0.06	4.24 ± 0.04	1.44 ± 0.03
67	0.841 ± 0.181	1.209 ± 0.279	0.89 ± 0.08	0.51 ± 0.07	0.22 ± 0.03
68	1.518 ± 0.1	1.531 ± 0.092	0.51 ± 0.01	0.22 ± 0.01	0.07 ± 0.01
69	3.46 ± 1.115	4.318 ± 1.203	3.48 ± 0.42	1.83 ± 0.26	0.72 ± 0.1
70	1.605 ± 0.2	2.018 ± 0.161	1.14 ± 0.04	0.55 ± 0.03	0.2 ± 0.02
71	1.567 ± 0.957	4.253 ± 0.685	2.43 ± 0.88	1.21 ± 0.57	0.42 ± 0.32
72	2.403 ± 0.261	1.972 ± 0.308	0.92 ± 0.08	0.42 ± 0.06	0.15 ± 0.04
73	28.168 ± 2.638	49.52 ± 4.004	31.44 ± 1.54	14.04 ± 0.83	5.09 ± 0.34
74	16.493 ± 1.023	17.392 ± 0.978	7.49 ± 0.23	3.1 ± 0.21	1.11 ± 0.09
75	0.148 ± 0.071	0.37 ± 0.062	0.35 ± 0.04	0.2 ± 0.03	0.09 ± 0.02
76	0.886 ± 0.176	0.909 ± 0.172	0.67 ± 0.05	0.38 ± 0.04	0.15 ± 0.02
77	58.47 ± 3.251	73.761 ± 4.064	36.01 ± 0.5	14.72 ± 0.31	5.02 ± 0.17
78	2.04 ± 0.223	2.802 ± 0.442	1.6 ± 0.17	0.83 ± 0.09	0.35 ± 0.04
79	0.986 ± 0.192	1.583 ± 0.428	0.79 ± 0.11	0.41 ± 0.07	0.18 ± 0.04
80	1.479 ± 0.57	2.875 ± 0.68	2.03 ± 0.23	1.05 ± 0.11	0.43 ± 0.08
81	15.308 ± 0.97	17.08 ± 1.267	8.56 ± 0.21	3.69 ± 0.1	1.25 ± 0.04
82	1.89 ± 0.293	1.683 ± 0.158	0.86 ± 0.06	0.37 ± 0.04	0.13 ± 0.02
83	0.674 ± 0.137	0.48 ± 0.109	0.39 ± 0.03	0.21 ± 0.03	0.09 ± 0.02
84	1.791 ± 0.191	2.595 ± 0.179	1.33 ± 0.03	0.59 ± 0.03	0.21 ± 0.02
85	23.375 ± 2.26	30.458 ± 1.966	15.29 ± 0.35	6.77 ± 0.23	2.58 ± 0.13
86	6.575 ± 1.5	9.40 ± 1.357	5.14 ± 0.27	2.62 ± 0.16	1.16 ± 0.05
87	1.703 ± 0.293	1.831 ± 0.266	0.92 ± 0.09	0.38 ± 0.07	0.13 ± 0.03
88	12.906 ± 2.2	14.472 ± 2.443	8.14 ± 0.49	3.91 ± 0.29	1.64 ± 0.15
89	10.83 ± 1.126	15.005 ± 1.774	9.63 ± 0.24	5.16 ± 0.18	2.29 ± 0.07
90	-	-	-	-	-
91	28.035 ± 2.497	45.141 ± 2.893	27.17 ± 1.16	12.56 ± 0.6	4.74 ± 0.32
92	1.686 ± 0.23	2.382 ± 0.199	1.51 ± 0.1	0.74 ± 0.06	0.3 ± 0.03
93	2.028 ± 0.348	2.87 ± 0.42	1.49 ± 0.16	0.67 ± 0.09	0.25 ± 0.05
94	3.312 ± 0.404	5.238 ± 0.536	3.86 ± 0.14	2.21 ± 0.1	1.03 ± 0.06
95	7.801 ± 0.45	8.137 ± 0.444	3.5 ± 0.06	1.37 ± 0.03	0.44 ± 0.02
96	20.43 ± 1.226	25.125 ± 1.338	12.66 ± 0.23	5.21 ± 0.16	1.79 ± 0.08
97	18.247 ± 1.559	33.198 ± 2.559	21.49 ± 0.49	10.25 ± 0.31	3.92 ± 0.15
98	3.222 ± 0.323	5.373 ± 0.362	3.22 ± 0.12	1.72 ± 0.07	0.74 ± 0.04
99	1.077 ± 0.067	1.304 ± 0.079	0.64 ± 0.02	0.26 ± 0.02	0.08 ± 0.01
100	10.131 ± 0.529	14.106 ± 0.736	7.1 ± 0.08	2.91 ± 0.05	0.94 ± 0.04
101	-	-	-	-	-
102	111.145 ± 6.099	141.58 ± 7.52	64.03 ± 2.33	25.75 ± 0.6	8.69 ± 0.41
103	0.859 ± 0.125	1.039 ± 0.113	0.85 ± 0.05	0.39 ± 0.03	0.14 ± 0.02
104	-	-	-	-	-

CONTINUED ON NEXT PAGE

Table A.2 – CONTINUED FROM PREVIOUS PAGE

	PACS		SPIRE		
HRS	S_{100} / Jy	S_{160} / Jy	S_{250} / Jy	S_{350} / Jy	S_{500} / Jy
105	-	-	-	-	-
106	2.069 ± 0.504	2.238 ± 0.466	1.48 ± 0.14	0.65 ± 0.1	0.25 ± 0.04
107	1.021 ± 0.143	1.499 ± 0.115	0.96 ± 0.06	0.49 ± 0.04	0.2 ± 0.03
108	1.011 ± 0.167	1.313 ± 0.132	0.6 ± 0.04	0.26 ± 0.03	0.09 ± 0.02
109	2.676 ± 0.347	3.376 ± 0.391	2.24 ± 0.08	1.17 ± 0.06	0.5 ± 0.03
110	6.137 ± 0.495	7.821 ± 0.501	4.02 ± 0.13	1.97 ± 0.11	0.83 ± 0.06
111	14.297 ± 0.758	22.151 ± 1.142	11.96 ± 0.12	5.01 ± 0.07	1.72 ± 0.04
112	1.059 ± 0.149	1.002 ± 0.139	0.65 ± 0.05	0.29 ± 0.03	0.11 ± 0.02
113	17.551 ± 1.098	30.598 ± 1.62	18.64 ± 0.25	8.3 ± 0.14	2.97 ± 0.07
114	102.907 ± 5.799	118.6 ± 6.85	54.64 ± 0.91	22.72 ± 0.69	8.1 ± 0.42
115	1.012 ± 0.095	1.014 ± 0.086	0.64 ± 0.04	0.28 ± 0.03	0.09 ± 0.02
116	-	-	-	-	-
117	4.524 ± 0.534	7.711 ± 0.477	4.43 ± 0.11	1.94 ± 0.08	0.67 ± 0.05
118	1.385 ± 0.287	1.611 ± 0.269	0.92 ± 0.09	0.49 ± 0.07	0.2 ± 0.04
119	6.626 ± 0.487	8.675 ± 0.606	4.09 ± 0.24	1.63 ± 0.16	0.52 ± 0.09
120	4.293 ± 0.454	7.038 ± 0.533	3.93 ± 0.18	1.69 ± 0.16	0.58 ± 0.07
121	5.544 ± 0.322	8.633 ± 0.506	4.7 ± 0.07	2.09 ± 0.05	0.75 ± 0.03
122	87.905 ± 6.335	123.549 ± 7.21	66.01 ± 2.21	27.95 ± 1.79	9.74 ± 0.82
123	1.473 ± 0.397	2.938 ± 0.336	1.78 ± 0.09	0.85 ± 0.06	0.32 ± 0.03
124	3.122 ± 0.66	6.081 ± 0.82	3.5 ± 0.23	1.72 ± 0.14	0.68 ± 0.08
125	-	-	-	-	-
126	-	-	-	-	-
127	4.339 ± 0.267	6.305 ± 0.35	3.57 ± 0.1	1.6 ± 0.06	0.59 ± 0.03
128	0.595 ± 0.115	1.331 ± 0.109	0.95 ± 0.05	0.47 ± 0.03	0.19 ± 0.02
129	0.853 ± 0.114	0.502 ± 0.123	0.32 ± 0.01	0.1 ± 0.01	-
130	2.01 ± 0.309	2.918 ± 0.29	1.53 ± 0.08	0.75 ± 0.07	0.29 ± 0.04
131	0.552 ± 0.19	1.263 ± 0.136	0.78 ± 0.06	0.34 ± 0.04	0.13 ± 0.03
132	1.695 ± 0.259	1.396 ± 0.158	0.84 ± 0.08	0.44 ± 0.04	0.19 ± 0.03
133	1.661 ± 0.504	2.545 ± 0.371	1.89 ± 0.08	1.25 ± 0.09	0.61 ± 0.05
134	1.602 ± 0.289	2.763 ± 0.274	1.36 ± 0.09	0.6 ± 0.06	0.21 ± 0.03
135	-	-	-	-	-
136	3.107 ± 0.198	3.891 ± 0.22	1.95 ± 0.05	0.77 ± 0.04	0.25 ± 0.02
137	-	-	-	-	-
138	1.014 ± 0.074	0.896 ± 0.067	0.21 ± 0.01	0.13 ± 0.01	0.11 ± 0.01
139	1.801 ± 0.195	2.078 ± 0.25	1.07 ± 0.07	0.54 ± 0.04	0.21 ± 0.03
140	1.92 ± 0.534	3.115 ± 0.833	3.03 ± 0.23	1.47 ± 0.19	0.55 ± 0.09
141	3.723 ± 0.391	7.037 ± 0.498	4.87 ± 0.16	2.23 ± 0.13	0.79 ± 0.09
142	12.722 ± 0.736	11.722 ± 0.674	4.82 ± 0.11	1.96 ± 0.06	0.66 ± 0.04
143	5.804 ± 0.429	8.478 ± 0.449	4.68 ± 0.13	2.32 ± 0.08	0.95 ± 0.04
144	18.998 ± 1.033	19.916 ± 1.193	8.57 ± 0.31	3.54 ± 0.11	1.29 ± 0.08
145	2.168 ± 0.348	3.319 ± 0.346	1.82 ± 0.1	0.94 ± 0.08	0.41 ± 0.04
146	2.383 ± 0.221	2.886 ± 0.191	1.75 ± 0.07	0.87 ± 0.05	0.35 ± 0.02
147	2.257 ± 0.363	3.973 ± 0.552	2.56 ± 0.08	1.31 ± 0.06	0.54 ± 0.03
148	3.96 ± 0.53	6.539 ± 0.826	3.78 ± 0.15	2.03 ± 0.11	0.9 ± 0.04
149	18.263 ± 0.974	26.98 ± 1.385	14.01 ± 0.12	5.93 ± 0.07	2.02 ± 0.05
150	-	0.579 ± 0.356	0.74 ± 0.26	0.46 ± 0.16	0.18 ± 0.08
151	3.781 ± 0.552	4.395 ± 0.543	2.5 ± 0.17	1.13 ± 0.11	0.43 ± 0.06
152	6.307 ± 0.405	6.358 ± 0.416	2.79 ± 0.07	1.08 ± 0.07	0.34 ± 0.03
153	3.24 ± 0.376	4.547 ± 0.465	2.54 ± 0.11	1.16 ± 0.1	0.43 ± 0.04
154	2.224 ± 0.417	2.702 ± 0.448	2.21 ± 0.18	1.22 ± 0.13	0.54 ± 0.08
155	-	-	-	-	-
156	17.548 ± 1.121	18.421 ± 0.992	8.49 ± 0.17	3.37 ± 0.12	1.1 ± 0.05
157	7.145 ± 0.436	9.352 ± 0.608	4.1 ± 0.08	1.79 ± 0.06	0.65 ± 0.03

CONTINUED ON NEXT PAGE

Table A.2 – CONTINUED FROM PREVIOUS PAGE

	PACS		SPIRE		
HRS	S_{100} / Jy	S_{160} / Jy	S_{250} / Jy	S_{350} / Jy	S_{500} / Jy
158	0.928 ± 0.178	1.4 ± 0.347	1.08 ± 0.11	0.63 ± 0.09	0.31 ± 0.05
159	6.7 ± 0.438	6.132 ± 0.381	2.64 ± 0.08	1.02 ± 0.08	0.33 ± 0.05
160	4.205 ± 0.583	7.142 ± 0.79	4.15 ± 0.16	1.86 ± 0.1	0.68 ± 0.05
161	4.848 ± 1.025	5.509 ± 0.593	-	-	0.22 ± 0.01
162	4.72 ± 0.304	4.484 ± 0.302	1.84 ± 0.28	0.69 ± 0.11	0.19 ± 0.05
163	11.949 ± 0.863	15.454 ± 1.09	8.13 ± 0.69	3.66 ± 0.27	1.26 ± 0.12
164	-	-	-	-	-
165	0.905 ± 0.208	1.342 ± 0.223	0.69 ± 0.04	0.33 ± 0.04	0.13 ± 0.02
166	-	-	-	-	-
167	1.215 ± 0.139	2.378 ± 0.181	1.38 ± 0.06	0.58 ± 0.05	0.19 ± 0.02
168	0.935 ± 0.088	0.916 ± 0.12	0.61 ± 0.05	0.3 ± 0.03	0.12 ± 0.02
169	1.39 ± 0.212	2.187 ± 0.32	1.17 ± 0.06	0.56 ± 0.06	0.21 ± 0.03
170	9.713 ± 3.046	14.263 ± 3.336	8.52 ± 1.16	3.88 ± 0.69	1.47 ± 0.2
171	4.509 ± 0.257	4.894 ± 0.269	2.24 ± 0.06	0.9 ± 0.06	0.29 ± 0.03
172	4.083 ± 0.632	5.039 ± 0.426	2.67 ± 0.15	1.11 ± 0.1	0.35 ± 0.04
173	10.527 ± 0.664	10.627 ± 0.834	5.02 ± 0.19	1.99 ± 0.08	0.63 ± 0.05
174	4.355 ± 0.25	4.049 ± 0.226	1.45 ± 0.01	0.57 ± 0.01	0.19 ± 0.01
175	-	-	-	-	-
176	3.158 ± 0.282	4.171 ± 0.323	2.13 ± 0.07	0.89 ± 0.04	0.28 ± 0.03
177	4.592 ± 0.246	4.981 ± 0.308	2.43 ± 0.07	1.03 ± 0.03	0.37 ± 0.03
178	-	-	-	-	-
179	-	-	-	-	-
180	1.221 ± 0.101	1.285 ± 0.127	0.44 ± 0.05	0.16 ± 0.04	0.04 ± 0.02
181	-	-	-	-	-
182	4.369 ± 0.319	5.391 ± 0.353	3.11 ± 0.08	1.48 ± 0.04	0.55 ± 0.03
183	0.693 ± 0.182	0.82 ± 0.156	0.76 ± 0.06	1.01 ± 0.04	1.27 ± 0.02
184	2.644 ± 0.217	2.265 ± 0.196	0.82 ± 0.09	0.31 ± 0.06	0.1 ± 0.03
185	1.181 ± 0.276	1.979 ± 0.283	1.35 ± 0.1	0.61 ± 0.07	0.22 ± 0.04
186	0.37 ± 0.037	0.313 ± 0.046	0.09 ± 0.02	0.04 ± 0.02	-
187	12.509 ± 2.008	15.141 ± 3.227	8.47 ± 0.4	4.21 ± 0.29	1.74 ± 0.16
188	4.308 ± 0.549	6.629 ± 0.617	3.93 ± 0.13	1.89 ± 0.08	0.77 ± 0.04
189	2.238 ± 0.304	2.67 ± 0.262	1.57 ± 0.05	0.72 ± 0.04	0.27 ± 0.03
190	74.118 ± 5.57	104.85 ± 5.821	57.34 ± 1.38	24.22 ± 0.65	8.46 ± 0.37
191	0.633 ± 0.163	0.854 ± 0.212	0.38 ± 0.04	0.2 ± 0.04	0.08 ± 0.02
192	0.403 ± 0.049	0.583 ± 0.062	0.32 ± 0.03	0.14 ± 0.02	0.04 ± 0.01
193	3.138 ± 0.314	3.928 ± 0.363	2.24 ± 0.13	1.1 ± 0.08	0.45 ± 0.04
194	28.254 ± 1.875	48.955 ± 2.661	33.39 ± 1.11	17.56 ± 0.45	7.6 ± 0.22
195	-	-	-	-	-
196	8.617 ± 0.893	10.184 ± 0.763	5.09 ± 0.28	2.5 ± 0.19	1.03 ± 0.1
197	4.664 ± 0.381	6.095 ± 0.44	3.39 ± 0.08	1.57 ± 0.07	0.6 ± 0.04
198	1.015 ± 0.487	2.011 ± 0.377	1.78 ± 0.07	0.94 ± 0.06	0.41 ± 0.04
199	1.256 ± 0.546	1.533 ± 0.226	0.87 ± 0.12	0.39 ± 0.08	0.15 ± 0.04
200	15.632 ± 0.827	17.282 ± 0.88	7.78 ± 0.09	3.04 ± 0.06	1.0 ± 0.03
201	75.281 ± 3.999	93.527 ± 4.864	45.59 ± 0.43	19.24 ± 0.2	6.78 ± 0.11
202	-	-	-	-	-
203	15.489 ± 0.835	15.638 ± 0.953	6.90 ± 0.12	3.09 ± 0.07	1.18 ± 0.05
204	34.851 ± 3.113	61.656 ± 3.907	34.62 ± 1.15	15.61 ± 1.02	5.89 ± 0.45
205	56.393 ± 3.262	58.539 ± 3.082	27.62 ± 0.62	12.28 ± 0.43	4.88 ± 0.16
206	2.733 ± 0.481	3.017 ± 0.367	1.52 ± 0.07	0.67 ± 0.06	0.24 ± 0.03
207	5.468 ± 0.398	6.779 ± 0.528	4.03 ± 0.11	1.74 ± 0.07	0.61 ± 0.04
208	13.601 ± 5.576	24.022 ± 3.148	15.63 ± 1.68	7.15 ± 0.74	2.66 ± 0.28
209	0.513 ± 0.132	0.632 ± 0.121	0.58 ± 0.10	0.29 ± 0.09	0.13 ± 0.05
210	0.516 ± 0.096	0.486 ± 0.125	-	-	-

Table A.2 – CONTINUED FROM PREVIOUS PAGE

	PACS		SPIRE		
HRS	S_{100} / Jy	S_{160} / Jy	S_{250} / Jy	S_{350} / Jy	S_{500} / Jy
211	-	-	-	-	-
212	2.505 ± 0.299	2.426 ± 0.293	1.45 ± 0.08	0.76 ± 0.07	0.31 ± 0.04
213	55.365 ± 4.659	90.833 ± 5.143	62.06 ± 1.18	31.07 ± 0.69	12.87 ± 0.29
214	-	-	-	-	-
215	14.15 ± 0.743	19.184 ± 0.976	9.68 ± 0.11	3.99 ± 0.05	1.36 ± 0.03
216	47.991 ± 2.419	59.217 ± 2.974	28.83 ± 0.16	11.51 ± 0.07	3.81 ± 0.03
217	31.332 ± 2.268	42.761 ± 2.608	22.02 ± 0.89	9.22 ± 0.58	3.11 ± 0.27
218	-	-	-	-	-
219	-	-	-	-	-
220	25.583 ± 3.355	38.766 ± 2.589	21.26 ± 2.09	9.34 ± 0.8	3.34 ± 0.53
221	5.049 ± 0.335	7.3 ± 0.501	3.99 ± 0.1	1.74 ± 0.06	0.61 ± 0.03
222	0.523 ± 0.228	1.259 ± 0.201	0.51 ± 0.06	0.22 ± 0.04	0.09 ± 0.02
223	0.346 ± 0.139	0.612 ± 0.145	0.48 ± 0.08	0.28 ± 0.04	0.12 ± 0.03
224	2.206 ± 0.53	2.806 ± 0.514	2.16 ± 0.2	0.99 ± 0.11	0.34 ± 0.06
225	0.044 ± 0.025	0.194 ± 0.038	0.09 ± 0.02	-	-
226	1.717 ± 0.217	2.468 ± 0.226	1.33 ± 0.05	0.63 ± 0.04	0.24 ± 0.02
227	5.65 ± 0.713	6.237 ± 0.875	4.23 ± 0.23	2.46 ± 0.13	1.17 ± 0.07
228	-	-	-	-	-
229	-	-	-	-	-
230	3.515 ± 0.327	3.768 ± 0.323	2.3 ± 0.11	1.05 ± 0.07	0.37 ± 0.03
231	1.102 ± 0.113	0.897 ± 0.125	0.36 ± 0.01	0.13 ± 0.01	0.05 ± 0.02
232	2.524 ± 0.289	2.9 ± 0.28	1.52 ± 0.09	0.61 ± 0.05	0.21 ± 0.04
233	8.108 ± 0.768	10.674 ± 0.752	5.22 ± 0.21	2.2 ± 0.11	0.75 ± 0.07
234	-	-	-	-	-
235	-	-	-	-	-
236	-	-	-	-	-
237	5.408 ± 0.703	6.54 ± 0.611	3.45 ± 0.16	1.47 ± 0.12	0.51 ± 0.05
238	0.695 ± 0.179	0.581 ± 0.234	0.35 ± 0.06	0.19 ± 0.04	0.09 ± 0.02
239	11.903 ± 0.702	13.602 ± 0.771	6.68 ± 0.13	2.74 ± 0.09	0.94 ± 0.03
240	-	-	-	-	-
241	0.31 ± 0.07	0.32 ± 0.066	0.10 ± 0.03	0.04 ± 0.02	-
242	6.587 ± 0.759	7.273 ± 0.849	4.01 ± 0.22	1.92 ± 0.16	0.77 ± 0.08
243	0.673 ± 1.005	3.354 ± 0.916	3.28 ± 0.24	1.64 ± 0.18	0.62 ± 0.09
244	17.159 ± 1.265	24.35 ± 1.408	11.63 ± 0.19	4.83 ± 0.09	1.61 ± 0.05
245	-	-	-	-	-
246	17.873 ± 1.553	22.95 ± 1.833	12.46 ± 0.41	5.56 ± 0.21	2.13 ± 0.12
247	41.7 ± 2.59	55.404 ± 3.425	27.79 ± 0.42	12.09 ± 0.27	4.53 ± 0.14
248	-	-	-	-	-
249	0.208 ± 0.045	0.088 ± 0.025	0.15 ± 0.03	0.08 ± 0.02	0.03 ± 0.01
250	-	-	-	-	-
251	99.531 ± 5.076	113.011 ± 5.791	50.62 ± 0.23	20.09 ± 0.2	6.82 ± 0.07
252	1.662 ± 0.424	1.726 ± 0.400	1.22 ± 0.08	0.65 ± 0.09	0.3 ± 0.03
253	2.112 ± 0.176	1.58 ± 0.125	0.48 ± 0.04	0.15 ± 0.01	0.06 ± 0.01
254	12.633 ± 3.503	18.399 ± 3.807	11.19 ± 0.78	4.93 ± 0.54	1.74 ± 0.25
255	3.409 ± 1.426	3.476 ± 0.613	2.2 ± 0.39	1.31 ± 0.19	0.62 ± 0.08
256	23.132 ± 1.206	20.28 ± 1.095	7.38 ± 0.08	2.79 ± 0.06	0.91 ± 0.03
257	3.278 ± 0.908	4.883 ± 0.894	4.79 ± 0.44	2.47 ± 0.31	0.95 ± 0.13
258	1.376 ± 0.131	0.849 ± 0.132	0.27 ± 0.01	0.1 ± 0.01	0.03 ± 0.01
259	6.584 ± 1.499	7.759 ± 1.956	4.07 ± 0.26	2.12 ± 0.14	0.95 ± 0.09
260	13.653 ± 0.771	15.533 ± 0.920	7.12 ± 0.16	2.99 ± 0.1	1.04 ± 0.04
261	1.179 ± 0.335	2.729 ± 0.355	1.99 ± 0.12	1.04 ± 0.12	0.42 ± 0.06
262	11.675 ± 1.373	12.858 ± 1.079	6.73 ± 0.19	3.06 ± 0.18	1.16 ± 0.1
263	25.625 ± 5.416	49.023 ± 5.139	32.49 ± 2.55	16.66 ± 2.24	7.14 ± 1.12

Table A.2 – CONTINUED FROM PREVIOUS PAGE

	PACS		SPIRE		
HRS	S_{100} / Jy	S_{160} / Jy	S_{250} / Jy	S_{350} / Jy	S_{500} / Jy
264	0.326 ± 0.136	1.059 ± 0.099	0.72 ± 0.05	0.41 ± 0.03	0.18 ± 0.02
265	2.061 ± 0.243	2.044 ± 0.148	1.02 ± 0.04	0.44 ± 0.03	0.14 ± 0.02
266	8.201 ± 2.776	12.794 ± 2.873	7.62 ± 0.74	4.06 ± 0.43	1.85 ± 0.17
267	3.826 ± 1.103	6.215 ± 0.992	3.43 ± 0.18	1.72 ± 0.1	0.7 ± 0.05
268	11.969 ± 0.675	13.585 ± 0.765	6.29 ± 0.09	2.69 ± 0.06	0.99 ± 0.03
269	-	-	-	-	-
270	8.061 ± 1.914	11.83 ± 1.406	6.24 ± 0.58	2.69 ± 0.26	0.97 ± 0.11
271	3.233 ± 0.449	4.223 ± 0.449	2.74 ± 0.14	1.45 ± 0.1	0.61 ± 0.05
272	-	-	-	-	-
273	4.318 ± 0.802	7.264 ± 0.829	4.7 ± 0.19	2.28 ± 0.16	0.89 ± 0.09
274	1.197 ± 0.235	3.001 ± 0.295	2.24 ± 0.1	1.12 ± 0.07	0.44 ± 0.03
275	10.521 ± 0.813	10.513 ± 0.865	5.16 ± 0.15	2.38 ± 0.1	0.9 ± 0.05
276	4.501 ± 0.433	4.355 ± 0.403	2.68 ± 0.11	1.23 ± 0.09	0.45 ± 0.05
277	0.376 ± 0.095	0.69 ± 0.134	0.24 ± 0.04	0.1 ± 0.03	0.04 ± 0.02
278	1.098 ± 0.472	1.506 ± 0.275	1.0 ± 0.11	0.45 ± 0.05	0.16 ± 0.03
279	1.769 ± 0.755	4.518 ± 0.564	2.76 ± 0.19	1.6 ± 0.13	0.73 ± 0.07
280	3.51 ± 0.251	3.967 ± 0.239	1.99 ± 0.05	0.86 ± 0.03	0.31 ± 0.02
281	0.446 ± 0.094	0.632 ± 0.093	0.41 ± 0.03	0.18 ± 0.02	0.06 ± 0.01
282	-	-	-	-	-
283	15.894 ± 0.959	19.757 ± 1.077	9.26 ± 0.14	4.01 ± 0.08	1.5 ± 0.05
284	16.823 ± 0.883	17.731 ± 0.908	7.55 ± 0.07	2.9 ± 0.05	0.96 ± 0.03
285	22.761 ± 1.473	27.136 ± 1.842	13.01 ± 0.26	5.51 ± 0.17	1.87 ± 0.08
286	0.961 ± 0.31	1.54 ± 0.27	1.28 ± 0.28	0.82 ± 0.2	0.39 ± 0.12
287	6.998 ± 0.774	9.004 ± 0.949	4.59 ± 0.13	2.07 ± 0.07	0.78 ± 0.05
288	5.335 ± 0.983	9.141 ± 0.965	5.84 ± 0.25	2.7 ± 0.15	1 ± 0.06
289	12.715 ± 0.947	16.561 ± 1.065	8.04 ± 0.15	3.53 ± 0.11	1.3 ± 0.06
290	4.237 ± 0.276	3.989 ± 0.321	1.65 ± 0.05	0.65 ± 0.05	0.22 ± 0.03
291	-	-	-	-	-
292	12.76 ± 0.763	12.629 ± 0.731	5.55 ± 0.08	2.24 ± 0.07	0.72 ± 0.05
293	6.929 ± 0.585	8.435 ± 0.571	4.39 ± 0.11	2.02 ± 0.07	0.79 ± 0.04
294	2.84 ± 0.302	3.614 ± 0.288	2.1 ± 0.06	1.05 ± 0.05	0.4 ± 0.03
295	59.271 ± 6.469	76.825 ± 5.363	38.87 ± 1.16	16.6 ± 0.67	5.92 ± 0.29
296	1.02 ± 0.342	0.913 ± 0.103	0.42 ± 0.04	0.21 ± 0.04	0.1 ± 0.02
297	9.13 ± 0.952	13.649 ± 0.834	7.83 ± 0.17	3.75 ± 0.11	1.52 ± 0.08
298	5.863 ± 0.378	6.448 ± 0.385	2.63 ± 0.07	1.05 ± 0.03	0.35 ± 0.02
299	5.027 ± 1.139	7.654 ± 1.211	5.05 ± 0.26	2.61 ± 0.25	1.14 ± 0.14
300	0.628 ± 0.104	0.853 ± 0.169	0.57 ± 0.06	0.29 ± 0.04	0.11 ± 0.02
301	5.009 ± 1.236	8.024 ± 1.589	5.18 ± 0.46	2.87 ± 0.28	1.32 ± 0.12
302	1.507 ± 0.52	1.961 ± 0.535	1.46 ± 0.11	0.85 ± 0.05	0.39 ± 0.03
303	4.719 ± 0.292	3.354 ± 0.374	1.5 ± 0.06	0.57 ± 0.04	0.17 ± 0.02
304	3.403 ± 0.489	5.721 ± 0.553	3.68 ± 0.1	1.73 ± 0.07	0.64 ± 0.04
305	0.236 ± 0.105	0.489 ± 0.114	0.33 ± 0.06	0.16 ± 0.05	0.06 ± 0.02
306	5.30 ± 1.69	7.018 ± 1.311	3.2 ± 0.29	1.28 ± 0.19	0.37 ± 0.1
307	18.365 ± 3.444	30.263 ± 4.249	17.76 ± 0.8	8.65 ± 0.64	3.5 ± 0.31
308	0.087 ± 0.019	0.158 ± 0.026	0.09 ± 0.01	0.03 ± 0.01	-
309	1.185 ± 0.135	1.071 ± 0.135	0.79 ± 0.03	0.42 ± 0.03	0.18 ± 0.02
310	4.257 ± 0.395	6.346 ± 0.518	3.07 ± 0.15	1.29 ± 0.12	0.47 ± 0.06
311	7.067 ± 1.771	12.277 ± 1.435	7.82 ± 0.38	3.67 ± 0.3	1.38 ± 0.14
312	-	-	-	-	-
313	2.55 ± 0.802	3.803 ± 0.819	3.05 ± 0.15	1.6 ± 0.08	0.67 ± 0.05
314	2.772 ± 0.417	3.316 ± 0.23	2.05 ± 0.08	1.12 ± 0.05	0.49 ± 0.05
315	1.056 ± 0.409	0.863 ± 0.327	0.52 ± 0.13	0.28 ± 0.08	0.15 ± 0.05
316	-	-	-	-	-

Table A.2 – CONTINUED FROM PREVIOUS PAGE

	PACS		SPIRE		
HRS	S_{100} / Jy	S_{160} / Jy	S_{250} / Jy	S_{350} / Jy	S_{500} / Jy
317	0.222 ± 0.1	0.475 ± 0.062	0.33 ± 0.06	0.19 ± 0.03	0.07 ± 0.02
318	4.998 ± 0.406	6.331 ± 0.483	3.27 ± 0.12	1.61 ± 0.11	0.65 ± 0.05
319	6.923 ± 0.996	8.145 ± 1.192	5.1 ± 0.33	2.67 ± 0.22	1.16 ± 0.09
320	7.735 ± 2.205	10.256 ± 1.478	6.7 ± 0.36	3.58 ± 0.21	1.58 ± 0.1
321	2.942 ± 0.17	3.164 ± 0.179	1.39 ± 0.03	0.6 ± 0.03	0.21 ± 0.02
322	1.453 ± 1.035	1.859 ± 1.201	2.97 ± 0.38	1.7 ± 0.31	0.77 ± 0.14
323	5.689 ± 0.391	7.547 ± 0.575	4.05 ± 0.06	1.86 ± 0.05	0.71 ± 0.02

A.2 RESULTS

Here I display results of the SED fitting routine described in Smith et al. (2012b) and other parameters used for comparison in Chapter 2, including star formation rate from *GALEX* FUV and *Spitzer MIPS* 24 μm data, and NUV-*r* colours from Cortese et al. (2012b) (Table A.3). I also show variations in each parameter with morphology (Figures A.1 and A.2) and Hubble-type (Figures A.3 and A.4).

Table A.3: Results of SED fitting applied to fluxes in Table A.2. Stellar masses and NUV-*r* magnitude taken from Cortese et al. (2012b).

HRS	χ^2	$\log M_*$	$T_{\rm d}$	$\log M_{\rm d}$	$\log L_{\rm IR}$	NUV-*r*	$\log(\Sigma_{\rm SFR})$
		$M_\odot$	K	$M_\odot$	$L_\odot$	mag	$M_\odot\,{\rm yr}^{-1}\,{\rm kpc}^{-2}$
1	0.18	8.68	21.32±0.99	5.984±0.078	8.34	3.26	-
2	2.74	8.77	23.52±0.59	6.328±0.043	8.93	2.27	-
3	2.21	-	20.05±1.00	6.084±0.072	8.28	-	-
4	1.46	-	21.15±0.36	7.360±0.031	9.69	-	-
5	1.66	-	22.08±0.47	6.664±0.038	9.11	-	-
6	1.33	8.93	13.80±0.85	6.849±0.119	8.07	2.95	-
7	0.50	10.29	25.68±0.53	6.242±0.035	9.05	5.39	-
8	2.60	9.88	15.61±0.99	7.487±0.089	9.04	2.9	-2.92
9	2.22	10.08	21.61±0.82	6.568±0.059	8.96	3.97	-
10	10.41	-	18.97±1.09	6.448±0.095	8.50	-	-
11	2.88	9.45	20.88±0.37	6.969±0.035	9.27	2.71	-
12	4.83	8.47	23.39±0.77	5.745±0.059	8.33	2.14	-
13	1.26	10.18	21.60±0.36	7.623±0.029	10.01	2.98	-
14	0.94	10.12	23.19±1.28	5.639±0.091	8.20	5.12	-
15	0.31	10.01	18.93±0.74	7.655±0.061	9.71	2.62	-2.78
16	2.29	9.60	19.39±0.45	7.240±0.041	9.35	2.62	-
17	2.34	9.46	21.01±0.45	7.223±0.037	9.54	2.31	-2.35
18	0.03	9.78	20.47±0.75	6.663±0.057	8.91	3.34	-
19	4.06	9.40	20.79±0.70	7.028±0.053	9.32	2.2	-
20	2.39	9.18	23.83±0.56	7.282±0.036	9.91	1.42	-
21	6.81	8.82	18.15±1.27	6.335±0.111	8.28	3.78	-
22	1.96	10.50	20.29±0.93	6.180±0.114	8.41	5.39	-
23	0.70	9.90	22.98±0.38	7.367±0.031	9.91	3.59	-1.80
24	1.35	9.88	20.31±0.47	7.551±0.037	9.78	2.48	-2.53
25	2.34	9.69	24.22±0.46	7.164±0.031	9.83	2.76	-
26	5.78	8.93	20.45±0.90	6.308±0.080	8.56	3.04	-
27	0.79	8.94	24.19±0.65	6.605±0.045	9.27	1.71	-
28	3.19	9.16	20.95±0.32	6.831±0.031	9.14	2.34	-
29	1.95	9.05	19.97±0.62	6.614±0.053	8.80	3.25	-
30	2.43	8.87	19.28±0.82	6.759±0.070	8.86	2.02	-
31	4.21	9.28	22.87±0.81	7.100±0.057	9.63	2.2	-2.39
32	1.12	9.46	15.62±1.23	5.887±0.161	7.44	4.97	-
33	1.25	9.62	20.92±0.43	7.042±0.039	9.35	2.54	-
34	2.74	9.59	18.85±0.53	7.140±0.044	9.18	3.2	-
35	0.49	-	20.67±1.37	5.789±0.116	8.06		-
36	1.13	10.24	25.71±0.50	7.393±0.032	10.21	2.87	-
37	0.26	9.53	22.24±0.46	6.778±0.036	9.24	2.4	-
38	8.15	-	18.91±0.98	6.750±0.073	8.80		-
39	2.64	9.09	18.49±1.18	6.675±0.090	8.66	2.82	-
40	0.55	9.18	23.34±0.53	6.759±0.041	9.34	2.17	-

Table A.3 – CONTINUED FROM PREVIOUS PAGE

HRS	χ^2	$\log M_*$	T_D	$\log M_D$	$\log L_{IR}$	NUV-r	$\log(\Sigma_{SFR})$
		$M_\odot$	K	$M_\odot$	$L_\odot$	mag	$M_\odot\,yr^{-1}\,kpc^{-2}$
41	3.84	9.24	18.63±0.79	6.605±0.071	8.62	3.75	-
42	2.19	9.77	20.23±0.68	7.369±0.049	9.59	2.33	-
43	-	10.29	-	-	-	5.67	-3.77
44	8.11	8.69	23.15±0.73	6.196±0.057	8.75	1.99	-
45	0.15	10.23	19.22±0.82	6.907±0.062	9.00	4.84	-
46	0.43	10.29	24.12±0.46	6.675±0.036	9.33	4.52	-
47	2.55	9.11	19.99±0.94	6.881±0.070	9.07	1.83	-
48	0.36	9.92	21.15±0.54	7.590±0.045	9.92	2.37	-
49	-	10.69	-	-	-	5.48	-3.99
50	5.01	9.87	24.27±0.34	7.300±0.027	9.97	3.05	-1.57
51	6.18	9.21	20.74±0.59	6.891±0.048	9.18	2.27	-
52	0.91	9.11	20.63±1.31	6.160±0.078	8.43	2.56	-
53	4.25	9.49	20.43±0.43	7.056±0.041	9.30	2.67	-2.52
54	1.29	9.87	19.95±0.93	6.745±0.067	8.93	3.12	-
55	1.34	-	20.51±0.46	7.111±0.041	9.37	2.41	-
56	5.11	10.22	24.41±0.40	7.537±0.028	10.23	3.99	-1.37
57	1.25	9.81	20.56±0.38	7.308±0.033	9.57	2.7	-2.37
58	1.32	8.95	21.12±0.51	6.349±0.042	8.68	2.19	-
59	2.23	9.96	19.28±0.48	7.301±0.048	9.40	3.27	-
60	0.55	9.93	20.99±0.50	6.965±0.038	9.28	3.7	-2.35
61	2.41	-	19.09±0.85	6.267±0.076	8.34		-
62	7.31	9.12	18.63±0.98	7.102±0.078	9.11	1.73	-
63	1.04	9.93	18.54±0.55	7.441±0.050	9.44	3.13	-
64	2.75	-	17.84±1.12	6.677±0.098	8.57		-
65	4.88	9.05	18.34±1.42	6.818±0.108	8.79	1.91	-
66	2.28	9.77	23.24±0.37	7.401±0.031	9.97	2.63	-
67	2.86	8.99	17.73±0.99	6.703±0.090	8.58	2.18	-
68	6.68	8.94	25.45±0.59	5.987±0.037	8.78	3.23	-
69	1.08	10.47	17.82±1.31	7.088±0.105	8.98	4.28	-
70	0.84	-	20.39±0.57	6.695±0.051	8.94		-
71	0.84	10.56	18.20±1.34	6.993±0.153	8.94	5.48	-
72	1.04	-	24.39±1.05	6.358±0.071	9.04		-
73	1.27	-	19.00±0.38	7.825±0.039	9.89		-
74	1.27	9.52	23.42±0.46	7.014±0.038	9.60	2.31	-
75	0.21	8.99	15.40±0.98	6.392±0.113	7.91	4.02	-
76	5.03	-	18.61±1.15	6.244±0.089	8.25		-
77	2.76	10.54	21.95±0.31	7.988±0.028	10.41	2.95	-2.09
78	2.50	9.20	19.61±0.60	6.715±0.064	8.86	2.14	-
79	1.29	8.62	19.65±0.86	6.552±0.084	8.70	1.67	-
80	0.18	9.52	17.55±1.05	6.887±0.087	8.74	3.05	-
81	0.01	9.95	22.22±0.41	7.181±0.034	9.64	3.85	-
82	0.95	8.69	22.95±1.05	6.139±0.070	8.68	2.51	-2.20
83	7.23	8.53	19.60±1.69	6.039±0.126	8.18	2.29	-
84	1.17	9.39	20.79±0.49	6.465±0.043	8.76	3.07	-
85	1.85	10.07	21.15±0.45	7.420±0.035	9.75	3.3	-
86	7.70	9.23	18.45±1.03	7.251±0.073	9.24	1.95	-2.65
87	0.04	10.01	22.52±1.10	6.189±0.082	8.68	4.69	-
88	3.58	9.64	20.41±0.95	7.295±0.069	9.54	2.58	-
89	13.72	9.60	18.45±0.52	7.523±0.046	9.51	2.29	-2.33
90	-	10.25	-	-	-	5.37	-
91	0.49	10.65	19.33±0.41	7.868±0.041	9.97	3.77	-
92	1.47	9.09	19.13±0.62	6.636±0.057	8.71	3.2	-
93	0.25	10.43	20.67±0.81	6.447±0.075	8.72	5.42	-3.39

Table A.3 – CONTINUED FROM PREVIOUS PAGE

HRS	χ^2	$\log M_*$	T_D	$\log M_D$	$\log L_{IR}$	NUV-r	$\log(\Sigma_{SFR})$
		$M_\odot$	K	$M_\odot$	$L_\odot$	mag	$M_\odot\,yr^{-1}\,kpc^{-2}$
94	11.17	9.55	17.28±0.56	7.217±0.054	9.03	2.97	-
95	2.70	9.66	24.04±0.41	6.691±0.030	9.34	4.08	-2.03
96	1.47	10.01	21.88±0.40	7.362±0.032	9.78	3.12	-2.15
97	0.56	11.00	18.47±0.32	7.827±0.031	9.82	5.22	-
98	6.40	9.29	18.45±0.44	7.047±0.043	9.03	3.44	-
99	2.33	8.82	22.17±0.44	6.047±0.040	8.50	2.92	-
100	7.00	9.97	21.41±0.28	7.129±0.026	9.49	3.63	-2.24
101	-	10.21	-	-	-	5.22	-
102	5.42	10.39	22.35±0.36	8.046±0.031	10.52	2.5	-
103	3.97	10.35	18.81±0.68	6.624±0.067	8.66	5.48	-3.33
104	-	8.80	-	-	-	4.17	-
105	-	9.88	-	-	-	4.72	-
106	0.78	9.35	20.26±1.23	6.792±0.090	9.02	2.68	-
107	1.29	8.98	18.92±0.63	6.456±0.062	8.51	3.78	-
108	0.79	9.26	22.12±0.86	6.306±0.067	8.75	3.81	-
109	7.44	9.39	18.75±0.66	6.853±0.057	8.88	3.86	-
110	6.03	9.25	20.65±0.45	6.980±0.041	9.25	1.97	-2.30
111	6.46	10.10	20.43±0.26	7.417±0.025	9.66	3.41	-2.31
112	2.52	10.05	21.15±0.85	6.373±0.072	8.71	5.15	-
113	3.35	10.44	19.21±0.26	7.696±0.027	9.79	4.5	-2.35
114	1.40	10.51	22.53±0.39	7.977±0.030	10.47	2.41	-
115	3.03	9.24	21.55±0.71	6.058±0.066	8.44	4.54	-
116	-	9.62	-	-	-	5.18	-3.98
117	2.86	10.35	19.86±0.42	7.292±0.035	9.47	5.09	-
118	2.00	8.66	20.15±1.14	6.369±0.089	8.58	1.5	-
119	3.08	9.92	21.94±0.50	6.872±0.047	9.30	4.58	-2.66
120	2.17	10.06	19.97±0.46	6.973±0.046	9.16	4.89	-2.72
121	2.12	10.08	20.04±0.29	7.319±0.030	9.52	4.22	-
122	1.56	10.72	20.79±0.35	8.148±0.035	10.44	3.02	-2.37
123	0.63	10.14	18.78±0.70	6.726±0.057	8.76	4.44	-
124	0.94	9.52	18.69±0.67	7.038±0.062	9.06	3.15	-2.76
125	-	10.29	-	-	-	5.52	-
126	-	10.23	-	-	-	5.59	-
127	0.58	10.23	20.09±0.33	7.196±0.033	9.40	4.49	-
128	0.64	9.32	17.48±0.46	6.817±0.050	8.66	3.24	-3.40
129	6.88	10.27	25.85±1.05	5.524±0.064	8.35	5.27	-
130	1.19	9.19	20.20±0.73	6.579±0.061	8.80	2.67	-2.47
131	1.70	9.40	18.85±0.77	6.610±0.074	8.65	3.21	-
132	8.15	9.10	20.81±1.29	6.543±0.096	8.84	2.01	-
133	10.68	9.26	15.02±1.13	7.188±0.111	8.64	2.74	-
134	2.22	9.96	20.52±0.68	6.753±0.056	9.01	5.01	-2.51
135	-	11.49	-	-	-	5.65	-3.86
136	3.69	10.14	22.05±0.39	6.791±0.034	9.23	5.53	-2.62
137	-	10.57	-	-	-	5.71	-3.77
138	72.14	11.19	29.45±1.07	5.319±0.058	8.45	5.49	-3.58
139	2.43	9.00	21.18±0.70	6.633±0.058	8.97	2.01	-2.69
140	1.06	10.04	17.21±0.87	7.056±0.082	8.86	4.19	-2.74
141	1.46	10.33	18.35±0.36	7.435±0.042	9.41	3.84	-2.92
142	0.54	9.42	24.78±0.46	6.812±0.033	9.54	2.27	-1.54
143	5.24	9.60	19.64±0.36	7.378±0.036	9.52	2.93	-2.14
144	1.81	10.13	23.45±0.41	7.132±0.033	9.72	3.59	-1.70
145	4.22	9.28	19.25±0.73	6.997±0.060	9.09	2.34	-2.54
146	5.85	9.38	19.84±0.53	6.919±0.049	9.09	3.41	-2.59

Table A.3 – CONTINUED FROM PREVIOUS PAGE

HRS	χ^2	$\log M_*$	T_D	$\log M_D$	$\log L_{IR}$	NUV-r	$\log(\Sigma_{SFR})$
		$M_\odot$	K	$M_\odot$	$L_\odot$	mag	$M_\odot$ yr^{-1} kpc^{-2}
147	2.08	9.45	18.05±0.60	6.958±0.052	8.89	4.3	-
148	9.14	9.25	18.25±0.59	7.138±0.051	9.09	2.31	-2.55
149	5.15	10.03	20.77±0.29	7.471±0.027	9.76	4.2	-2.13
150	0.07	11.23	14.08±2.20	6.784±0.010	8.06	5.63	-3.87
151	0.60	9.64	20.90±0.80	6.728±0.064	9.03	3.32	-2.55
152	1.64	9.30	24.15±0.50	6.583±0.036	9.25	2.63	-
153	0.22	9.35	20.24±0.57	6.780±0.048	9.00	2.66	-
154	4.73	9.49	17.75±0.94	7.177±0.088	9.06	2.28	-
155	-	10.60	-	-	-	5.56	-3.60
156	1.28	10.24	23.51±0.39	7.098±0.032	9.69	4.79	-1.77
157	3.63	9.29	21.87±0.35	6.906±0.029	9.32	2.26	-2.12
158	3.93	9.03	17.48±0.94	6.911±0.091	8.76	2.29	-
159	0.40	10.18	24.80±0.64	6.797±0.047	9.52	3.85	-2.59
160	0.86	9.82	19.54±0.54	7.289±0.044	9.42	2.91	-
161	3.60	10.79	26.75±0.98	6.291±0.035	9.20	5.61	-
162	1.75	10.30	24.98±0.74	6.368±0.060	9.11	5.39	-2.94
163	0.11	10.66	21.04±0.46	7.233±0.044	9.55	4.45	-2.98
164	-	9.90	-	-	-	5.49	-
165	0.90	8.85	20.22±1.04	6.489±0.077	8.71	2.91	-
166	-	10.67	-	-	-	5.54	-3.51
167	6.81	9.96	19.41±0.42	6.802±0.040	8.92	4.27	-2.78
168	4.88	8.64	20.85±0.68	6.378±0.065	8.68	1.71	-2.19
169	0.53	9.30	19.85±0.63	6.786±0.058	8.96	2.52	-
170	0.08	10.71	19.65±1.23	7.342±0.082	9.49	4.97	-
171	1.29	9.70	23.15±0.44	6.808±0.036	9.37	3.16	-2.25
172	0.94	9.77	21.88±0.74	6.674±0.054	9.09	4.31	-2.58
173	0.84	10.44	23.63±0.50	6.856±0.039	9.46	4.42	-
174	3.63	10.77	25.85±0.50	6.253±0.032	9.08	5.63	-3.12
175	-	10.39	-	-	-	5.66	-3.62
176	2.07	10.64	21.59±0.46	6.861±0.039	9.25	5.55	-3.03
177	0.42	9.20	22.52±0.40	6.620±0.033	9.11	2.25	-2.02
178	-	11.58	-	-	-	5.43	-
179	-	10.72	-	-	-	5.55	-3.69
180	3.94	10.58	25.33±0.89	5.754±0.065	8.53	5.79	-3.66
181	-	10.09	-	-	-	5.21	-3.31
182	1.98	9.38	20.45±0.43	6.857±0.038	9.11	2.59	-
183	51.59	11.36	6.95±0.32	8.529±0.105	7.85	5.05	-
184	0.78	9.54	26.48±0.97	5.974±0.070	8.86	4.22	-2.00
185	0.33	10.06	18.85±0.77	6.578±0.068	8.62	4.63	-
186	1.18	-	27.75±1.78	5.093±0.128	8.08		-
187	3.67	9.40	20.12±0.87	7.333±0.060	9.54	2.07	-2.54
188	2.33	9.36	19.15±0.54	7.057±0.045	9.14	2.45	-2.69
189	0.78	8.93	20.54±0.65	6.546±0.053	8.81	2.57	-2.51
190	1.93	10.98	20.77±0.33	8.080±0.031	10.37	3.7	-1.75
191	1.52	8.57	21.15±1.51	5.925±0.105	8.26	2.23	-
192	1.22	9.39	20.63±0.66	5.834±0.068	8.10	4.43	-3.38
193	3.19	9.03	20.19±0.52	6.746±0.047	8.96	2	-
194	6.52	10.48	17.92±0.31	8.090±0.036	10.00	3.52	-2.34
195	-	9.66	-			5.26	-
196	4.12	9.21	21.15±0.59	7.052±0.051	9.39	1.97	-2.37
197	1.16	9.39	20.45±0.43	6.896±0.039	9.14	2.73	-2.58
198	0.70	9.29	16.17±0.95	6.934±0.087	8.58	2.79	-
199	0.12	9.06	20.52±1.67	6.292±0.124	8.55	2.81	-2.71

CONTINUED ON NEXT PAGE

Table A.3 – CONTINUED FROM PREVIOUS PAGE

HRS	χ^2	$\log M_*$	T_D	$\log M_D$	$\log L_{IR}$	NUV-r	$\log(\Sigma_{SFR})$
		$M_\odot$	K	$M_\odot$	$L_\odot$	mag	$M_\odot\,yr^{-1}\,kpc^{-2}$
200	3.51	10.96	23.38±0.38	7.066±0.029	9.65	5.63	-3.04
201	1.51	10.67	21.80±0.32	7.936±0.028	10.35	4.33	-
202	-	9.01	-	-	-	5.4	-3.41
203	5.57	9.21	23.10±0.41	7.071±0.032	9.62	1.71	-1.89
204	2.60	10.46	19.35±0.39	7.978±0.039	10.08	2.78	-1.51
205	6.95	10.26	22.45±0.43	7.703±0.035	10.19	2.88	-2.11
206	0.22	9.25	21.99±0.84	6.449±0.056	8.88	3.18	-
207	0.59	9.68	20.81±0.40	6.919±0.037	9.21	3.41	-
208	0.16	10.75	18.99±0.94	7.638±0.074	9.70	4.19	-2.96
209	2.25	-	17.75±1.56	6.176±0.176	8.06		-3.23
210	-	9.97	-	-	-	4.89	-3.27
211	-	10.80	-	-	-	5.23	-
212	6.65	9.13	20.90±0.89	6.655±0.071	8.96	1.77	-2.24
213	3.76	11.12	18.20±0.33	8.353±0.036	10.30	4.21	-2.57
214	-	10.24	-	-	-	5.38	-3.69
215	4.27	9.92	21.41±0.31	7.270±0.028	9.63	3.3	-
216	4.69	10.33	22.28±0.32	7.686±0.028	10.15	3.83	-
217	1.99	10.66	21.20±0.43	7.643±0.037	9.98	3.94	-2.59
218	-	10.48	-	-	-	5.59	-3.47
219	-	10.19	-	-	-	5.22	-3.84
220	0.83	10.94	20.34±0.61	7.691±0.055	9.92	4.49	-2.61
221	1.13	9.99	20.48±0.35	6.947±0.032	9.20	4.03	-2.68
222	3.56	9.28	20.70±1.16	6.067±0.089	8.35	3.97	-
223	0.62	8.61	16.71±1.33	6.356±0.128	8.08	2.81	-
224	1.05	10.22	19.05±0.94	6.759±0.076	8.83	5.16	-
225	3.48	8.73	17.24±1.28	5.609±0.153	7.42	2.95	-
226	0.99	9.31	20.14±0.57	6.517±0.050	8.73	3.07	-
227	19.73	9.15	18.45±0.81	7.086±0.067	9.07	1.73	-1.04
228	-	-	-	-	-		-
229	-	8.89	-	-	-	3.06	-
230	2.18	9.15	21.00±0.58	6.673±0.050	8.99	2.48	-
231	0.82	10.62	26.51±0.88	5.588±0.051	8.47	5.66	-3.60
232	0.49	9.78	22.10±0.71	6.419±0.057	8.86	4.41	-3.06
233	1.42	9.60	21.70±0.49	6.995±0.042	9.39	4.32	-2.20
234	-	-	-	-	-		-
235	-	9.95	-	-	-	5.35	-
236	-	10.98	-	-	-	5.56	-3.47
237	0.12	9.51	21.58±0.64	6.816±0.046	9.20	2.78	-2.15
238	3.39	-	20.97±1.73	5.867±0.137	8.18	-	-
239	0.74	9.57	22.40±0.35	7.056±0.031	9.53	3.4	-
240	-	10.12	-	-	-	5.4	-3.60
241	0.81	10.96	25.85±2.14	5.117±0.157	7.94	5.33	-
242	2.89	9.84	21.02±0.68	6.943±0.055	9.26	2.85	-2.66
243	1.49	10.59	16.19±0.88	7.180±0.078	8.83	5.49	-
244	5.68	10.19	21.62±0.35	7.341±0.028	9.73	3.4	-2.28
245	-	11.34	-	-	-	5.7	-3.55
246	1.18	10.13	20.75±0.45	7.440±0.037	9.72	2.99	-2.43
247	2.00	10.14	21.10±0.37	7.770±0.032	10.10	2.77	-2.17
248	-	10.05	-	-	-	4.97	-3.54
249	16.88	9.00	15.25±7.67	5.884±0.294	7.37	3.55	-3.58
250	-	10.59	-	-	-	5.56	-
251	3.24	10.73	23.08±0.34	8.111±0.026	10.66	3.59	-1.56
252	5.99	9.13	17.85±1.58	6.931±0.114	8.83	1.99	-

Table A.3 – CONTINUED FROM PREVIOUS PAGE

HRS	χ^2	$\log M_*$	T_D	$\log M_D$	$\log L_{IR}$	NUV-r	$\log(\Sigma_{SFR})$
		M$_\odot$	K	M$_\odot$	L$_\odot$	mag	M$_\odot$ yr^{-1} kpc^{-2}
253	6.71	10.26	30.84±1.03	5.748±0.048	8.98	4.23	-
254	0.20	-	20.03±0.95	7.418±0.070	9.61		-
255	4.01	8.98	17.12±1.46	7.026±0.130	8.82	1.73	-
256	2.88	9.94	26.42±0.47	6.871±0.028	9.75	2.55	-
257	1.70	10.52	16.75±0.87	7.301±0.084	9.04	4.57	-3.09
258	0.07	11.09	31.40±1.33	5.343±0.061	8.61	5.4	-3.84
259	6.58	-	19.53±1.45	7.069±0.093	9.20		-
260	0.98	10.46	22.62±0.37	7.088±0.031	9.59	5.21	-
261	0.22	9.43	17.09±0.74	6.893±0.074	8.68	3.9	-
262	1.57	9.23	21.52±0.67	7.128±0.049	9.51	1.65	-
263	0.71	10.92	17.91±0.68	8.084±0.069	9.99	3.81	-3.12
264	2.94	9.06	16.62±0.58	6.607±0.061	8.32	3.67	-
265	0.27	-	22.88±0.71	6.419±0.052	8.95		-
266	3.49	-	17.69±1.40	7.680±0.108	9.56		-
267	2.26	9.49	18.84±1.02	7.021±0.067	9.06	3.17	-
268	2.06	9.41	22.37±0.37	7.056±0.030	9.53	2.92	-
269	-	10.62	-	-	-	5.72	-3.70
270	0.44	10.93	20.87±0.86	7.155±0.062	9.45	5.29	-
271	5.14	9.33	18.81±0.68	6.936±0.061	8.97	3.46	-
272	-	10.58	-	-	-	5.19	-3.75
273	0.26	9.88	18.64±0.63	7.160±0.054	9.17	3.59	-
274	0.83	10.26	17.05±0.44	6.958±0.044	8.74	4.83	-3.18
275	4.38	-	22.35±0.51	7.217±0.040	9.69		-
276	3.99	9.35	21.37±0.66	6.717±0.056	9.08	2.54	-
277	2.67	8.90	21.75±1.31	5.682±0.108	8.09	3.56	-
278	0.18	9.31	19.50±1.20	6.349±0.094	8.48	4.7	-
279	4.65	9.26	16.85±0.89	7.123±0.078	8.87	2.21	-2.89
280	0.46	9.48	22.03±0.48	6.563±0.038	9.00	3.57	-
281	0.56	8.78	19.85±0.81	5.984±0.070	8.16	2.92	-
282	-	9.29	-	-	-	5.41	-
283	2.87	9.49	21.75±0.36	7.263±0.030	9.67	2.35	-1.91
284	3.83	-	24.04±0.40	7.099±0.027	9.75		-
285	0.68	10.46	22.19±0.37	7.365±0.032	9.82	5.66	-
286	1.79	10.45	16.38±1.43	6.820±0.170	8.50	5.24	-
287	1.14	9.54	21.05±0.54	6.992±0.040	9.31	2.65	-
288	0.29	-	19.00±0.54	7.157±0.044	9.22		-
289	1.67	-	21.39±0.43	7.516±0.034	9.88		-
290	0.45	9.22	24.75±0.57	6.301±0.042	9.02	3.26	-
291	-	9.86	-	-	-	5.47	-
292	0.57	9.79	24.05±0.44	6.921±0.034	9.57	3.65	-
293	3.00	9.07	21.01±0.45	6.907±0.036	9.22	1.9	-2.14
294	2.68	9.54	19.98±0.50	6.990±0.045	9.18	3.6	-
295	0.75	10.43	21.48±0.51	7.854±0.039	10.23	2.99	-2.33
296	3.71	9.95	22.15±1.82	5.815±0.124	8.26	5.05	-3.11
297	2.76	10.00	19.52±0.43	7.538±0.037	9.67	3.17	-
298	3.32	9.11	23.85±0.43	6.743±0.030	9.37	2.2	-1.32
299	2.07	9.64	18.25±0.87	7.221±0.075	9.18	2.61	-
300	0.62	9.48	19.18±0.86	6.323±0.077	8.41	4.82	-
301	4.28	9.73	17.50±1.00	7.465±0.087	9.31	2.54	-
302	4.75	9.24	15.90±1.53	7.088±0.123	8.69	2.84	-
303	1.04	9.22	26.72±0.72	6.510±0.046	9.41	2.34	-
304	0.17	10.00	18.92±0.48	7.144±0.043	9.19	4.36	-
305	0.08	9.07	18.01±1.35	6.034±0.138	7.96	3.7	-

CONTINUED ON NEXT PAGE

Table A.3 – CONTINUED FROM PREVIOUS PAGE

HRS	χ^2	$\log M_*$	T_D	$\log M_D$	$\log L_{IR}$	NUV-r	$\log(\Sigma_{SFR})$
		$M_\odot$	K	$M_\odot$	$L_\odot$	mag	$M_\odot\,yr^{-1}\,kpc^{-2}$
306	1.04	10.78	22.92±1.38	6.659±0.086	9.19	5.48	-3.17
307	1.18	10.25	18.95±0.73	7.761±0.056	9.82	2.96	-
308	1.81	8.60	19.59±0.99	5.272±0.105	7.41	3.52	-
309	13.04	8.71	19.80±0.86	6.434±0.071	8.60	1.84	-
310	2.48	9.94	20.97±0.49	7.134±0.045	9.45	3.43	-
311	0.15	10.81	18.89±0.75	7.550±0.058	9.60	4.85	-
312	-	10.62	-	-	-	5.26	-3.68
313	1.49	9.64	17.04±0.96	7.304±0.072	9.08	3.06	-2.74
314	8.12	9.04	18.95±0.76	6.935±0.065	8.99	1.78	-
315	2.27	8.76	20.45±2.74	6.287±0.160	8.54	1.97	-
316	-	10.52	-	-	-	5.53	-
317	0.19	8.94	17.28±1.03	6.460±0.109	8.28	2.49	-
318	4.31	9.44	20.71±0.49	7.007±0.045	9.29	2.28	-
319	6.76	9.47	19.27±0.82	7.303±0.068	9.40	1.88	-2.80
320	5.08	9.61	17.49±1.09	7.682±0.085	9.53	1.94	-
321	0.98	9.12	23.09±0.43	6.609±0.036	9.16	2.13	-1.84
322	1.03	10.46	14.40±1.48	7.557±0.142	8.89	4.12	-
323	2.01	9.87	20.52±0.36	7.254±0.031	9.51	3.83	-2.27
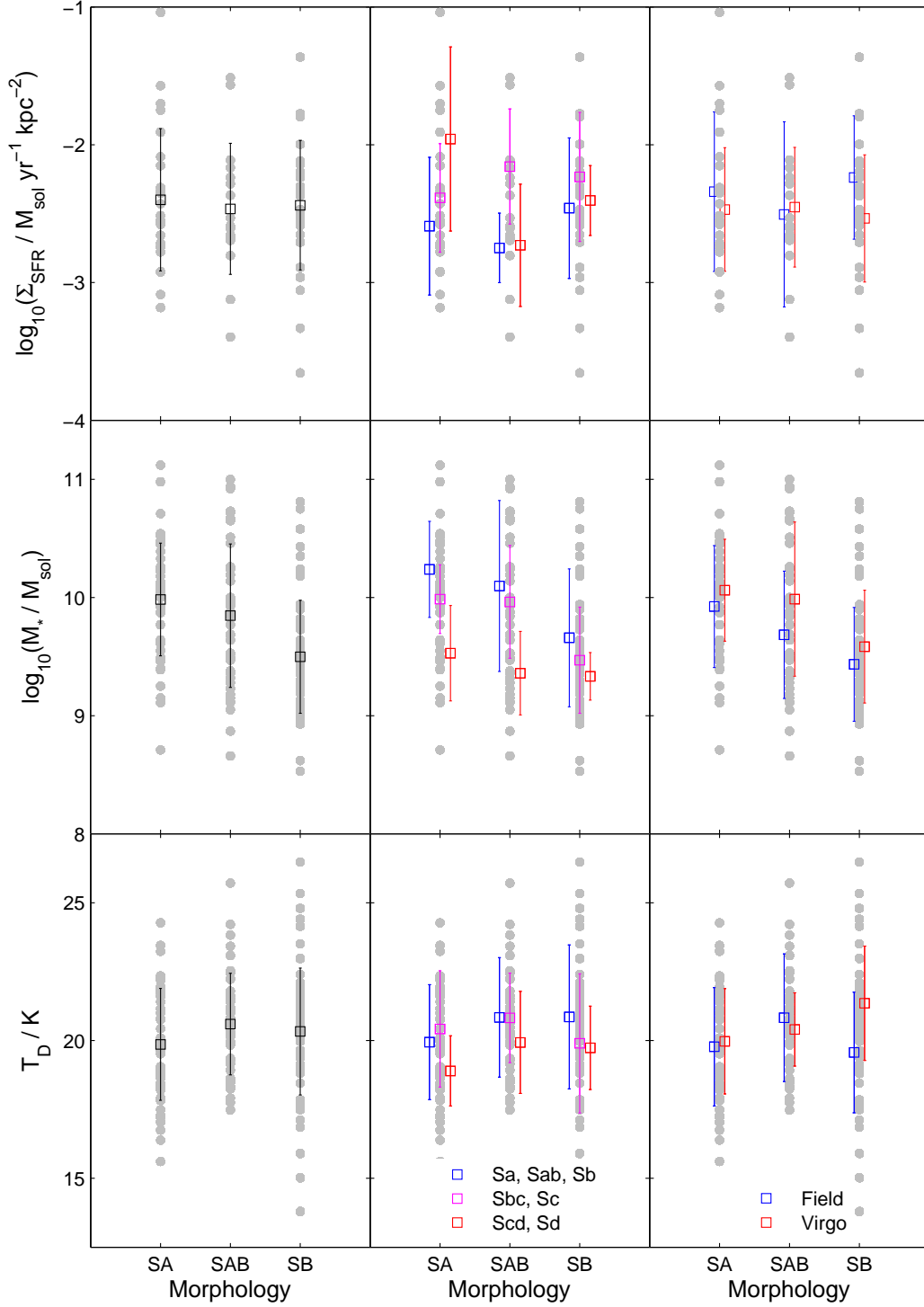
Figure A.1 Properties of HRS galaxies vs bar classification. Far left column shows the mean and standard deviation of each property for all galaxies in each bin. Subsequent columns split sample into Hubble-type and environment. The grey circles are raw data for all galaxies in the sample.
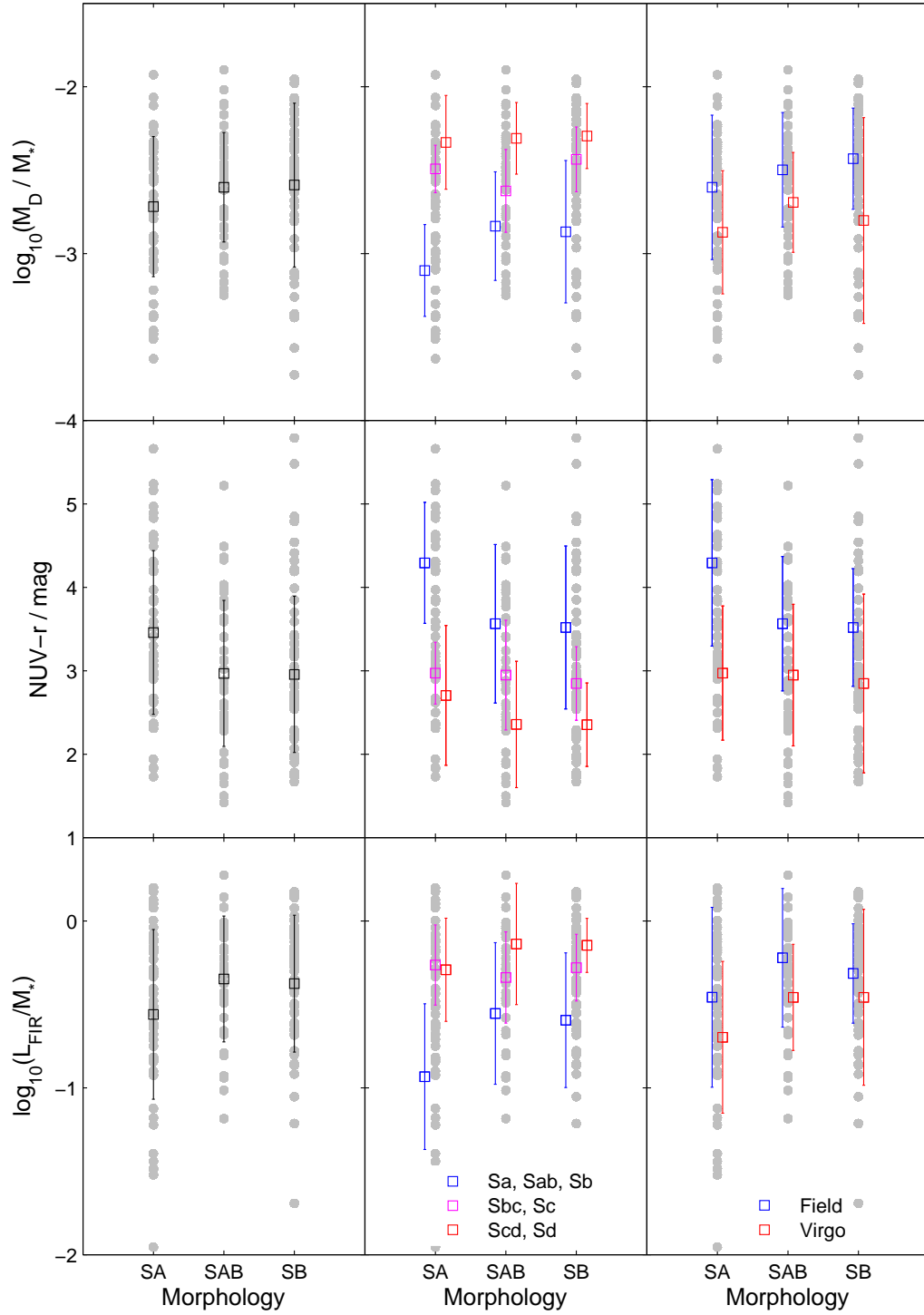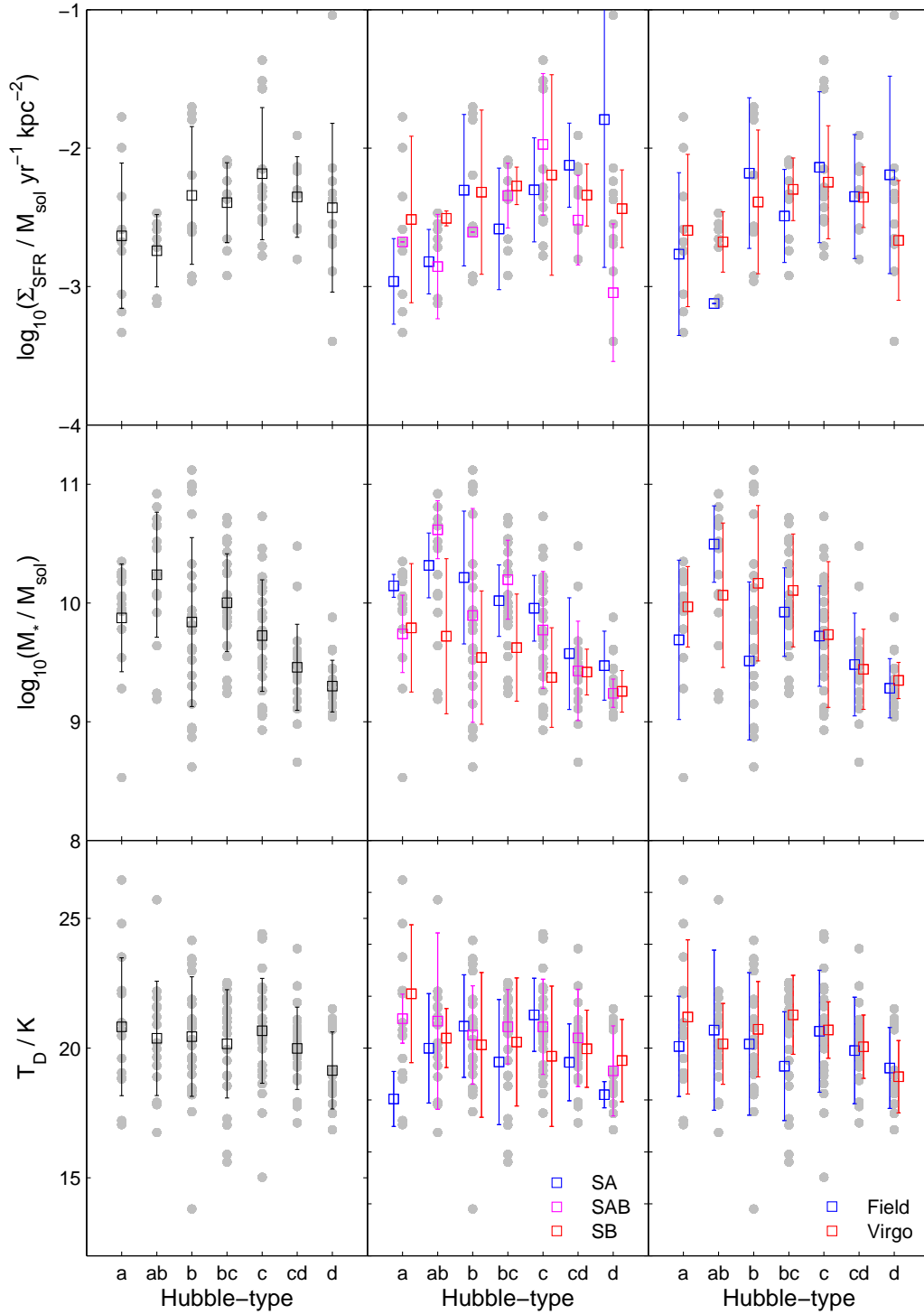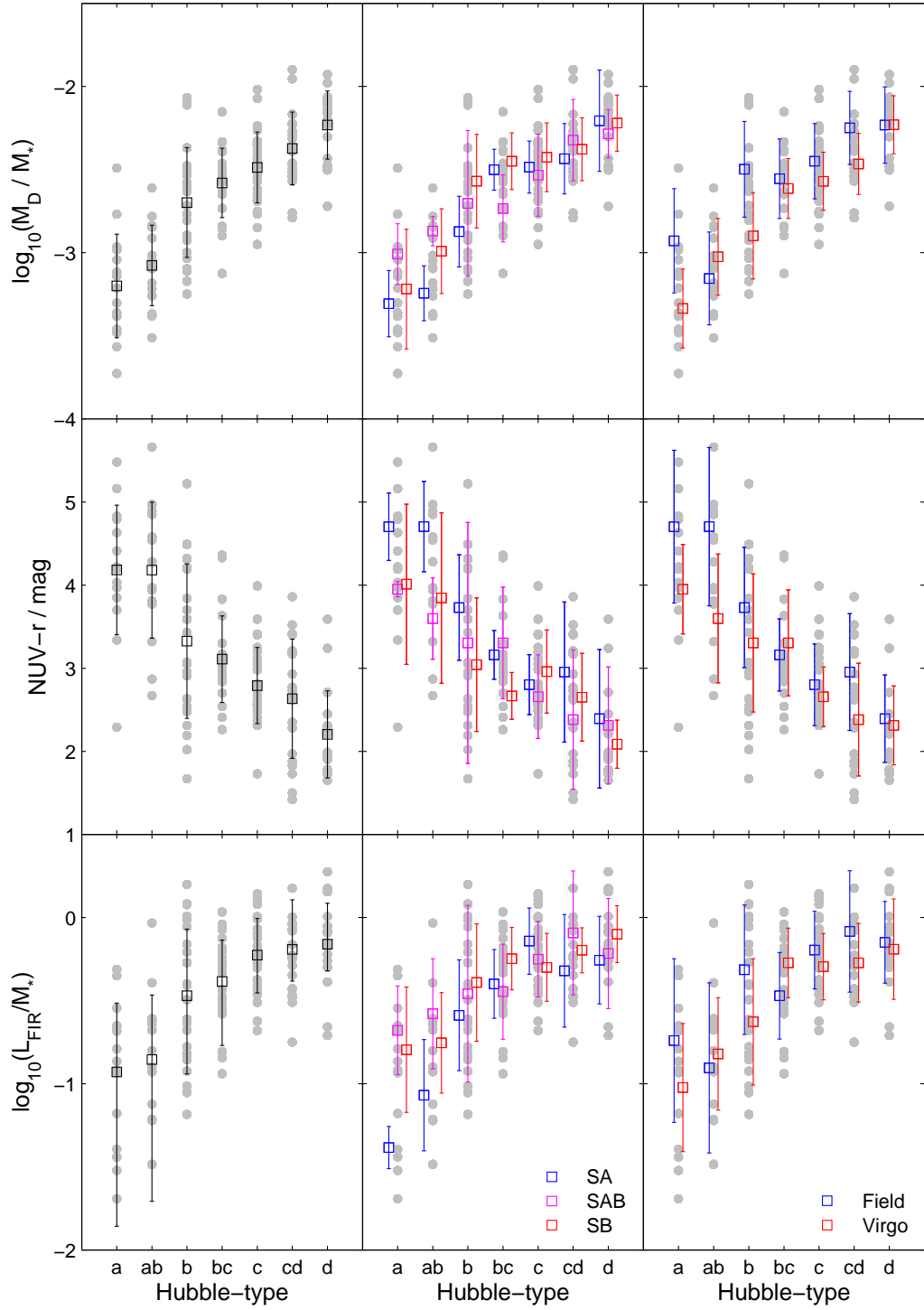
Figure A.2 Properties of HRS galaxies vs bar classification. Far left column shows the mean and standard deviation of each property for all galaxies in each bin. Subsequent columns split sample into Hubble-type and environment. The grey circles are raw data for all galaxies in the sample.

Figure A.3 Properties of HRS galaxies vs Hubble-type. Far left column shows the mean and standard deviation of each property for all galaxies in each bin. Subsequent columns split sample into Hubble-type and environment. The grey circles are raw data for all galaxies in the sample.

Figure A.4 Properties of HRS galaxies vs Hubble-type. Far left column shows the mean and standard deviation of each property for all galaxies in each bin. Subsequent columns split sample into Hubble-type and environment. The grey circles are raw data for all galaxies in the sample.

B THE LOCAL GROUP

B.1 GALACTOCENTRIC RADIUS

Much of the work on the star formation law studies variations with radius. Both M31 and M33 are divided into six elliptical annuli (Figure B.1) that are scaled based on the radius of the galaxy where $R_{M31} = 95'$ (21.55 kpc) and $R_{M33} = 70.8'$ (8.18 kpc). M31 has an inclination, $i = 77°$ and position angle of $38°$, with the corresponding values for M33 being $56°$ and $22.5°$ respectively.

B.2 STAR FORMATION RATE

Here I display the far-ultraviolet and $24\,\mu m$ emission (the two components of the maps of star formation rate) against $3.6\,\mu m$ emission (a tracer of the general stellar population) with radius in M31 and M33. As described in Section 3.3, I use this information to remove the component of the star formation tracers that is likely to originate from an old stellar population. To do this, I determine the following parameters in regions where star formation is ceased,

$$\alpha_{\text{FUV}} = I_{\text{FUV}}/I_{3.6}, \tag{B.1}$$

$$\alpha_{24} = I_{24}/I_{3.6}. \tag{B.2}$$

In the case of M31 it is central bulge of the galaxy that is likely to be dominated by old stars. For this reason the galaxy is divided into six radial annuli (Figure B.1). Where a linear correlation is observed, we assume the general stellar population dominates the emission and not the newly formed stars.

In Figure B.2 it is clear that there is a correlation in the inner regions of the galaxy ($r < 0.1\,R_{M31}$) as expected. The ratios found are $\alpha_{\text{FUV}} = 8.0 \times 10^{-4}$ and $\alpha_{24} = 0.1$.
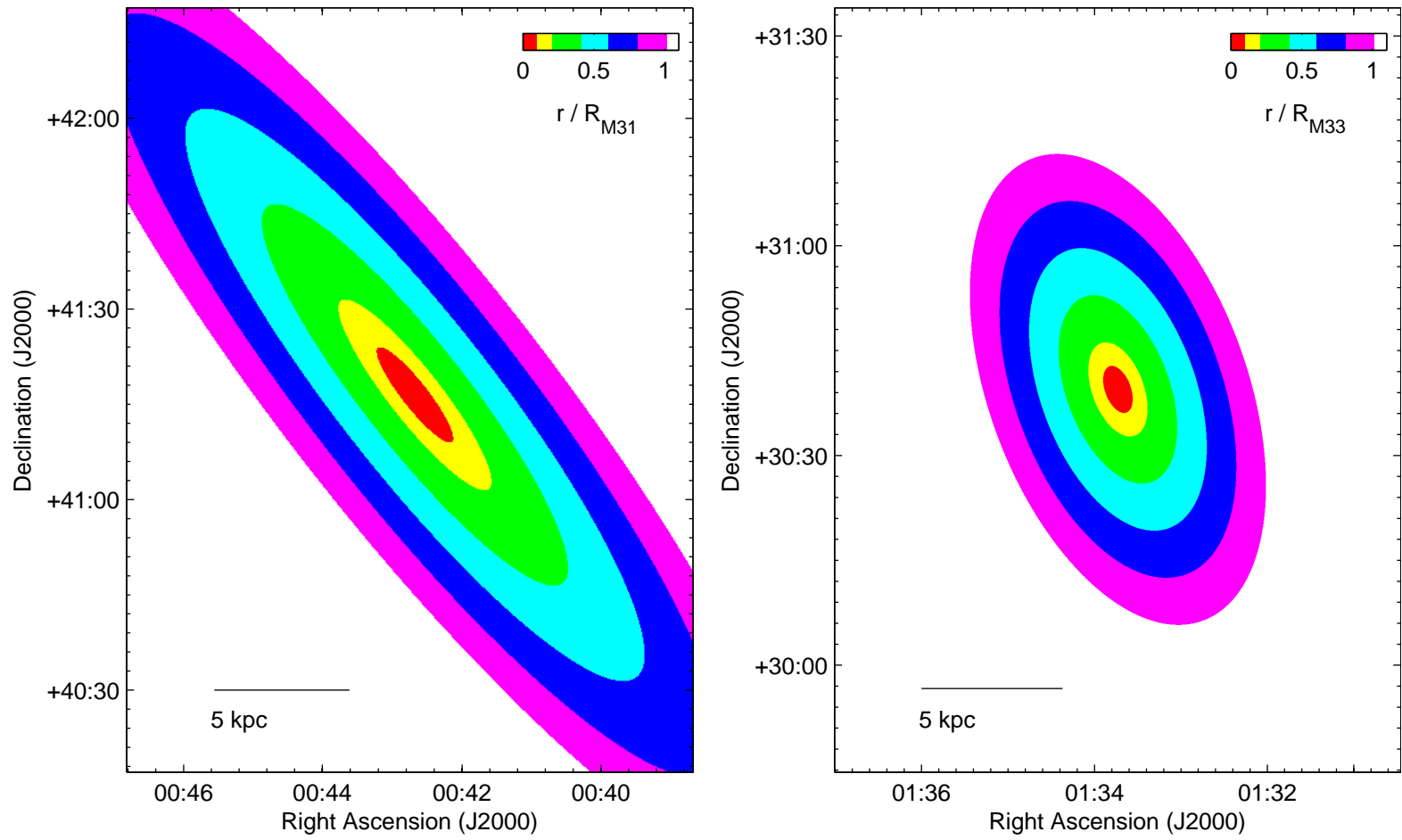
Figure B.1 Colour key of datapoints based on galactocentric radius in M31 (left) and M33 (right).

It also appears that there is a (albeit weaker) correlation between the SFR and old population tracers at approximately the radius of the ring (Figure B.3), a region where significant star formation is occurring. The correction should remove this component here also, such that we recover a valid star formation rate.

As M33 is a flocculent spiral, it lacks a dominant bulge where we can assume star formation has ceased. There is tentative evidence in Figures B.4 and B.5 of correlations between SFR indicators and $3.6\,\mu$m emission in each annulus but here I elect to use the correction factor found in M31 to estimate the contribution from the old stellar population.

B.3 STAR FORMATION LAW

Our Σ_{Gas} against Σ_{SFR} plots for both M31 and M33 exhibit clear signal-to-noise (S/N) cut offs which it is imperative we address. The first task was to test whether the cuts result in a bias when performing the fit.

We created two arrays, x and y where x contains all integers between -1000 and +1000 and $y = mx$ where $-1 < m < +3$. Gaussian noise is applied to both the x and y values to simulate the observed spread in points. We then apply a cut at a specified y value, again mimicking the data (Figure B.6).

The *polyfit* algorithm in *MATLAB* is used to perform the fit on the data above the cut. *Polyfit* is a least-squares routine that minimises residuals in the y-axis parameter. When $m \neq 0$ the calculated gradient is consistently shallower than the input, indicating a bias. We attempt to mitigate for this by ordering the data in bins of increasing y with an equal number of points in each bin. We replace this data with a single point based on the the mean or median of the binned data. The fit is then performed using the same algorithm on these averaged points. In both cases we get slightly steeper gradients when -1 $\lesssim$ m $\lesssim$ +1 converging to near perfect agreement in the region where 1.5 $\lesssim$ m $\lesssim$ 2.0. In all cases studied, the unmitigated fit is more deviant.

We therefore attempt to mitigate for the S/N cut in our data using the same method. When looking at the total gas from HI and CO measurements, we order in bins of increasing SFR, with an equal number of datapoints (500 for M31) in each. We then plot the mean gas mass in each bin, against the mean SFR and perform the fit on these points, using the logarithmic units.

In the case of H_2 only, the SNR cut-off is more apparent in gas mass in M31 so we bin the data in order of increasing gas mass, with 100 points in each bin. Gas mass as estimated from dust mass exhibits a more complex selection effect so
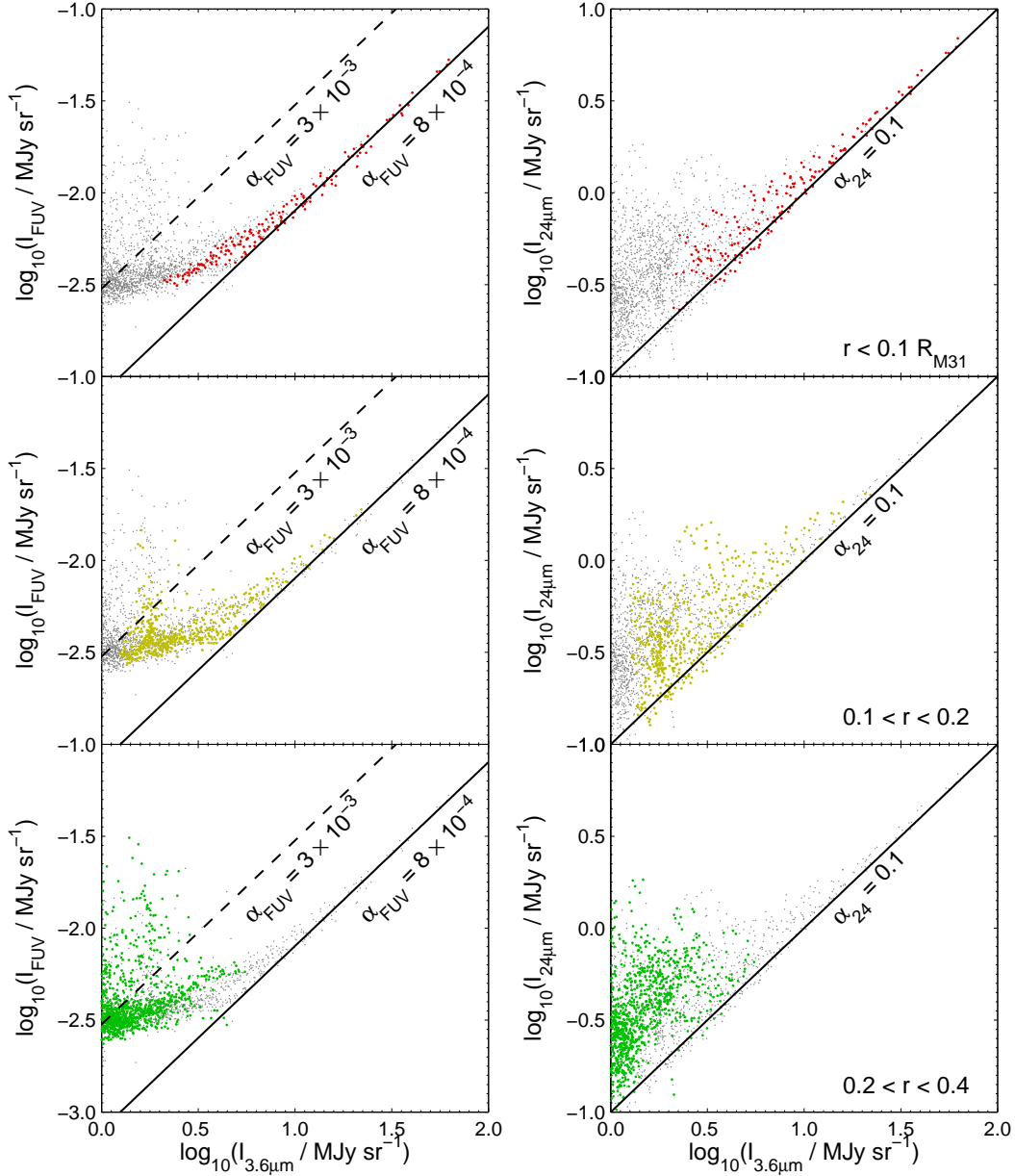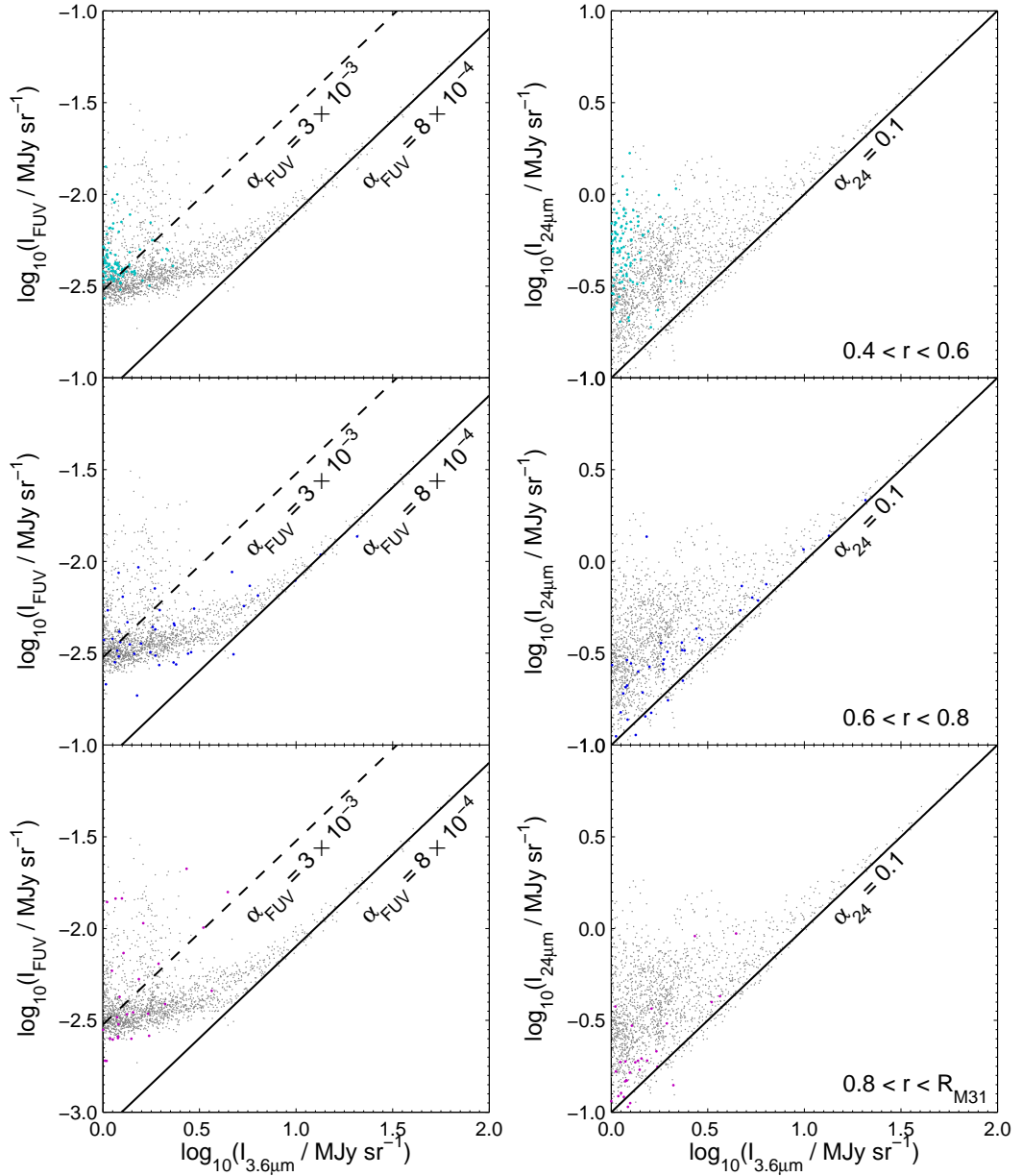
Figure B.2 FUV (left) and 24 μm (right) vs 3.6 μm emission for the central three annuli in M31 (see Figure B.1). The black dashed trendlines in the left column indicate the correction for the old stellar population used in Leroy et al. (2008), based on $I_{\rm FUV}/I_{3.6}$ found in ellipticals. The solid trendlines are the best fit to FUV vs 3.6 μm in the inner regions of M31 ($r < 0.1\,{\rm R_{M31}}$). The solid trendlines in the right column are the best fit to 24 μm vs 3.6 μm in the inner regions. This agrees with the Leroy et al. (2008) value.
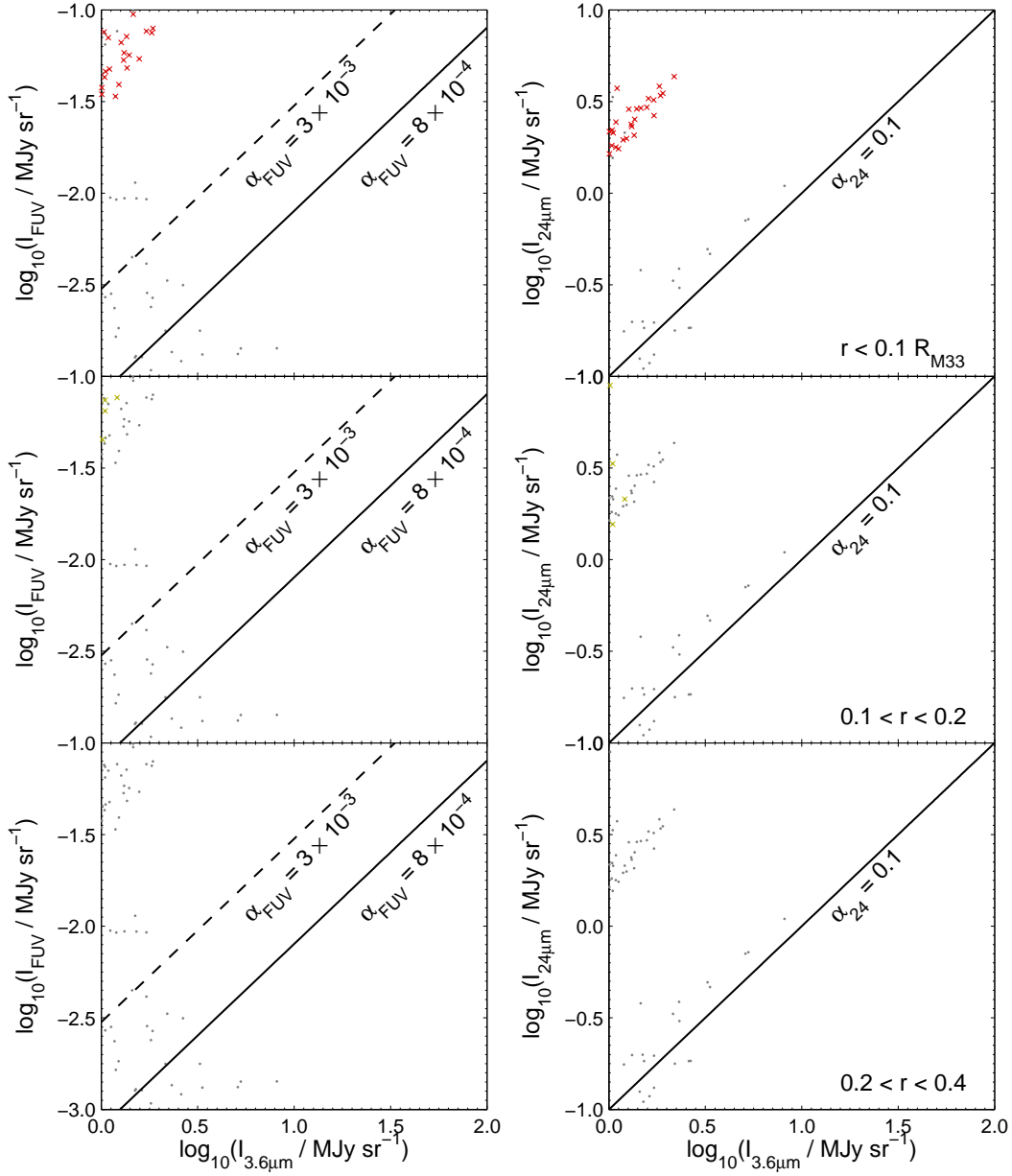
Figure B.3 FUV (left) and 24 μm (right) vs 3.6 μm emission for the outer three annuli in M31 (see Figure B.1). The black dashed trendlines in the left column indicate the correction for the old stellar population used in Leroy et al. (2008), based on $I_{FUV}/I_{3.6}$ found in ellipticals. The solid trendlines are the best fit to FUV vs 3.6 μm in the inner regions of M31 ($r < 0.1\,R_{M31}$). The solid trendlines in the right column are the best fit to 24 μm vs 3.6 μm in the inner regions. This agrees with the Leroy et al. (2008) value.
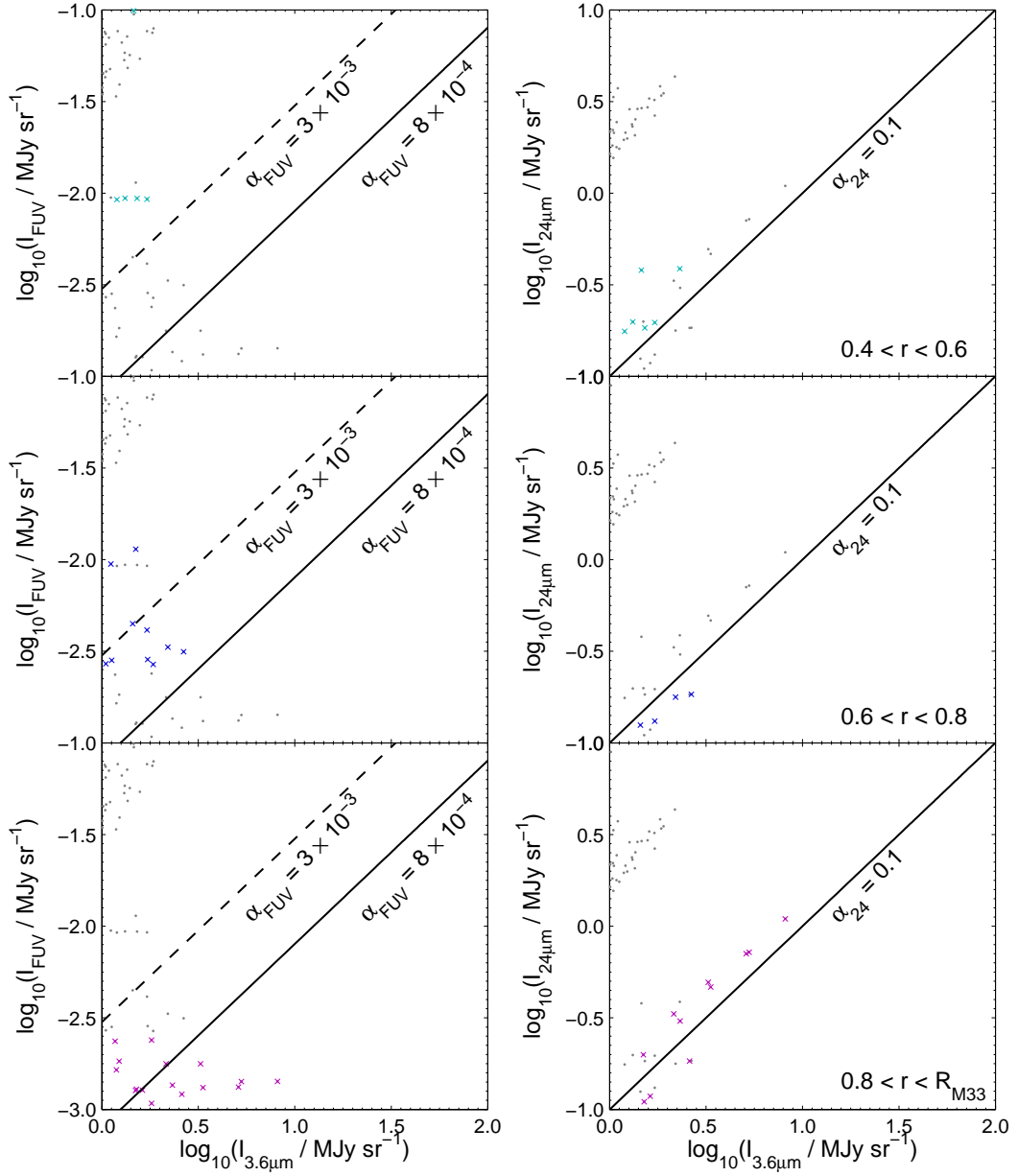
Figure B.4 FUV (left) and 24 μm (right) vs 3.6 μm emission for the central three annuli in M33 (see Figure B.1). The black dashed trendlines in the left column indicate the correction for the old stellar population used in Leroy et al. (2008), based on $I_{FUV}/I_{3.6}$ found in ellipticals. The solid trendlines are the best fit to FUV vs 3.6 μm in the inner regions of M33 ($r < 0.1\,\mathrm{R_{M33}}$). The solid trendlines in the right column are the best fit to 24 μm vs 3.6 μm in the inner regions of M31.

Figure B.5 FUV (left) and 24 μm (right) vs 3.6 μm emission for the outer three annuli in M33 (see Figure B.1). The black dashed trendlines in the left column indicate the correction for the old stellar population used in Leroy et al. (2008), based on $I_{FUV}/I_{3.6}$ found in ellipticals. The solid trendlines are the best fit to FUV vs 3.6 μm in the inner regions of M33 ($r < 0.1 R_{M33}$). The solid trendlines in the right column are the best fit to 24 μm vs 3.6 μm in the inner regions of M31.
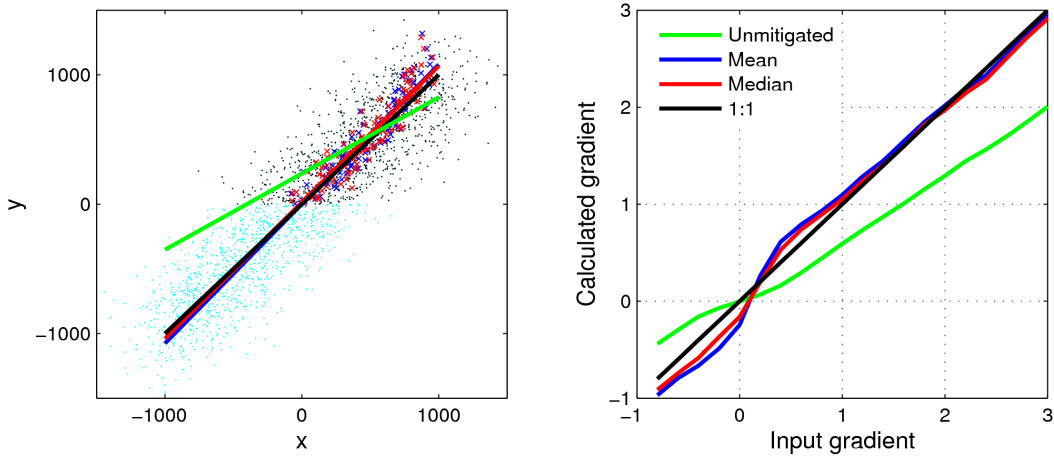
binning is not attempted here.

Figure B.6 Simulated Kennicutt-Schmidt index fitting. Left: Example simulated dataset with input gradient of 1.0. Black points are the selected data, cyan points are those that have been discarded before performing the fit. Right: Input gradient versus measured gradient for a range of input gradients and fitting methods. In both plots, green represents the unmitigated fit; blue represents the mean of binned data; red, the median. The black trendlines represent the input gradient.